Dissertation ETH Nr. 16858

Precision measurements of W and Z boson production and their decays to electrons at hadron colliders

A dissertation submitted to the

Swiss Federal Institute of Technology Zürich

for the degree of

Dr. Sc. ETH Zürich

presented by

Jan Hans Hermann Ehlers

Dipl.-Phys. Ruprecht-Karls University Heidelberg

born 4th June 1975 in Berlin, German

Prof. Günther Dissertori (examiner)

Prof. Felicitas Pauss (co-examiner)

- 2006 -

Abstract

For many measurements at hadron colliders, such as cross sections and branching ratios, the uncertainty of the integrated luminosity is an important contribution to the error of the final result. In 1997, the ETH Zurich group proposed a new approach to determine the integrated luminosity via a counting measurement of the W and Z bosons through their decays to leptons. In this thesis this proposal has been applied on real data as well as on simulation for a future experiment.

The first part of this thesis describes a dedicated data analysis to precisely measure the luminosity at the CDF experiment at the Tevatron collider (USA) through the production of Z bosons and their decay to electrons. An integrated $p\bar{p}$ luminosity of $L_{\text{counting}} = 221.7 \pm 2.8\,(\text{stat.}) \pm 11.2\,(\text{sys.})\,\text{pb}^{-1}$ has been measured for the data taking period from March 2002 to February 2004. This is in very good agreement with the traditional measurement at CDF of $L_{\text{CLC}} = 222.2 \pm 12.9\,\text{pb}^{-1}$, using Cherenkov Luminosity Counters at large angles. Both measurements are complementary and feature systematic uncertainties of similar size. Recent theoretical calculations for the Z production cross section up to next-to-next-to-leading-order (NNLO) in QCD perturbation theory allow for differential measurements for the first time. These calculations are used for this analysis and a rapidity-dependent luminosity measurement is presented in addition. The measured rapidity-dependence agrees with the theoretical predictions for on-shell Z boson production.

The analysis in the second part of this thesis was performed with Monte Carlo simulations for the CMS experiment at the future LHC collider at CERN (Switzerland). The goal is to define with the full detector simulation a first baseline selection for the channels $pp \to ZX \to ee$ and $pp \to WX \to e\nu$ and to determine potential uncertainties from detector inhomogeneities. Inclusive Z and W events with their decays to electrons are selected. The robust selection criteria lead to an essentially background-free sample of $Z \to e^+e^-$ events. The straightforward selection criteria can be considered as especially useful for the startup phase at CMS. A Z boson selection efficiency of approximately 60 % is obtained for electrons detected in the central pseudorapidity region of $|\eta| < 1.4$, and simultaneously a W selection efficiency of about 25 % is obtained. Inactive regions from the gaps between the supermodules of the electromagnetic calorimeter have been studied and an overall efficiency loss of roughly 1 % is determined. An integrated luminosity equivalent of about $200\,\text{pb}^{-1}$ of $Z \to e^+e^-$ Monte Carlo events have been analyzed. This amount of available statistics appears to be already sufficient to monitor the losses due to gaps and other potentially inefficient regions. No obstacle has been found which prevents the goal of a 1 % accuracy for counting the efficiency corrected number of centrally produced Z and W events decaying to electrons.

Zusammenfassung

An Hadronbeschleunigern hängt die Genauigkeit vieler Messungen, z.B. die von Wirkungsquerschnitten oder Verzweigungsverhältnissen, davon ab, wie präzise die integrierte Luminosität bestimmt werden kann. 1997 wurde von der ETH Zürich Gruppe eine neue Methode zur Bestimmung der integrierten Luminosität vorgeschlagen, indem man die Anzahl der erzeugten W und Z Bosonen im Beschleuniger durch ihren Zerfall in Leptonen mißt. In dieser Doktorarbeit wird diese neue Methode auf Daten eines laufenden Experiments angewandt sowie auf die bereits existierenden Simulationen eines zukünftigen Experiments.

Beim ersten Teil der Doktorarbeit handelt es sich um eine Datenanalyse am CDF Experiment, welches sich am Tevatron-Beschleuniger (USA) befindet, um die Luminosität mit Hilfe der dort produzierten Z Bosonen und deren Zerfall in Elektronen genau zu messen. Die integrierte Proton-Antiproton-Luminosität wurde in der Periode von März 2002 bis Februar 2004 zu $L_{\text{counting}} = 221.7 \pm 2.8\,(\text{stat.}) \pm 11.2\,(\text{sys.})$ pb^{-1} bestimmt, was in sehr guter Übereinstimmung mit der herkömmlichen Luminositätsbestimmung in CDF ist. Hierbei werden Cherenkov Luminosity Counters bei großen Winkeln benutzt, welche die Luminosität in der gleichen Zeitperiode mit $L_{\text{CLC}} = 222.2 \pm 12.9\,\text{pb}^{-1}$ gemessen haben. Beide Messungen sind unabhängig voneinander und besitzen einen ungefähr gleich großen systematischen Fehler. Unlängst wurde in der QCD Störungsrechnung der Produktionwirkungsquerschnitt von Z Bosonen bis next-to-next-to-leading order (NNLO) errechnet, was zum ersten Mal den Vergleich mit differentiellen Messungen erlaubt. Diese Berechnungen wurden benutzt, um eine rapiditätsabhängige Luminositätsmessung auszuführen. Die gemessene Rapiditätsverteilung stimmt mit den theoretischen Voraussagen für die Produktion von on-shell Z Bosonen überein.

Der zweite Teil dieser Arbeit nutzt die Monte Carlo Simulation des CMS Experiments, welches sich am zukünftigen LHC-Beschleuniger am CERN (Schweiz) befindet. Das Ziel hier ist es, unter Verwendung der vollständigen Detektorsimulation eine erste grundlegende Selektion der $\text{pp} \to \text{ZX} \to \text{ee}$ und $\text{pp} \to \text{WX} \to \text{e}\nu$ Prozesse zu definieren und potentielle Meßungenauigkeiten, verursacht durch einen inhomogenen Detektor, zu identifizieren. Gleichzeitig wird eine Größenabschätzung dieser Fehler gegeben. Eine robuste und unkomplizierte Selektion von inklusiven Z und W Bosonen mit anschließendem Zerfall in Elektronen wurde auch deshalb benutzt, da dies bei der Inbetriebnahme des CMS-Detektors als besonders nützlich angesehen werden kann. Außerdem führt diese Selektion zu einem quasi untergrundfreien Datensatz von $\text{Z} \to \text{e}^+\text{e}^-$ Ereignissen. Die Effizienz, Z Bosonen durch Elektronen in der zentralen Pseudorapiditätsregion ($|\eta| < 1.4$) zu detektieren, beträgt ungefähr 60 %. Für W Bosonen liegt die Effizienz bei zirka 25 %. Inaktives Material zwischen den Supermodulen des elektromagnetischen Kalorimeters im CMS Experiment führt zu einem Effizienzverlust von etwa 1 %. Es wurde ein Äquivalent von ungefähr $200\,\text{pb}^{-1}$ an $\text{Z} \to \text{e}^+\text{e}^-$ Ereignissen analysiert. Diese Statistik scheint bereits auszureichen, um den Effizienzverlust in den inaktiven Regionen oder anderen möglichen ineffizienten Bereichen des Detektors zu kontrollieren. Die ausgeführte Analyse deutet darauf hin, daß die effizienzkorrigierte Anzahl von zentral produzierten Z und W Bosonen

und ihren Zerfällen in Elektronen mit einer Genauigkeit von 1 % bestimmt werden kann.

dedicated to
my family

Contents

Abstract **i**

Zusammenfassung **iii**

Introduction **1**

1 Theoretical background **3**

1.1 The Standard Model 3

1.2 The elementary particles 3

1.3 The fundamental forces 6

2 The CDF detector at the Tevatron **15**

2.1 The Tevatron 15

2.2 The CDF detector 17

3 The CMS detector at the LHC **29**

3.1 The LHC 29

3.2 The CMS detector 31

4 Theory of Z and W production at hadron colliders **45**

4.1 The inclusive cross section 47

4.2 The differential cross section 49

4.3 The luminosity method 53

4.4 The parton luminosity 55

5 Luminosity measurement at CDF with $Z \to e^+ e^-$ events **57**

5.1 Data and Monte Carlo event samples 57

5.2 Selection of $Z \to e^+ e^-$ events 59

5.3 Efficiencies, backgrounds and counting of signal events 64

5.4 Determination of the luminosity 71

5.5 Systematic uncertainties and detector stability checks 73

5.6 Study of the rapidity-dependence of Z production 80

5.7 Summary 87

6 The counting of Drell-Yan Z and W events at CMS by using their decays to electrons **91**

6.1 Event simulation 91

6.2 Electron selection 99

6.3 Z event selection 101

6.4 W event selection 108

6.5 Summary 121

7 Conclusions and Outlook **123**

A List of Figures **127**

B List of Tables **137**

References **139**

Acknowledgement **147**

Introduction

This thesis is split into two different parts, both dealing with precision measurements of vector boson production and their subsequent decay to electrons. The first part copes with the task of accurately measuring the integrated luminosity at the Collider Detector at Fermilab (CDF) during a two year period of data taking (March 2002 - February 2004). In the second part, a first baseline selection for the processes $pp \rightarrow ZX \rightarrow ee$ and $pp \rightarrow WX \rightarrow e\nu$ at the Compact Muon Solenoid (CMS) experiment at CERN is proposed.

The layout of this thesis is specified in the following. Chapter 1 gives a brief overview of the Standard Model of particle physics, which currently is the best model for describing the interactions of elementary particles. After a short review of the particle classes and their members, the fundamental forces, governing the interactions between theses particles, are briefly discussed. In addition, the Higgs mechanism is presented in a nutshell in section 1.3.2, since the aim of finding the Higgs boson is one of the main reasons why the LHC is being built.

In the second chapter, the experimental setup for the CDF experiment is presented. It starts with a description of the Fermilab accelerator complex (section 2.1). Protons and antiprotons are circulating in opposite direction with a center of mass energy of $\sqrt{s} = 1.96\,\text{TeV}$ and are brought to collision at the two experiments - CDF and DØ. In section 2.2 the CDF detector is described. It is an all-purpose detector with 4π coverage. Although all major detector parts are presented, emphasis is put on those detector elements important for the analysis.

Chapter 3 is similarly structured as the second chapter. It characterizes the experimental setup for the CMS experiment. First, the CERN accelerator chain is explained. At LHC protons will collide with protons at a center of mass energy of $\sqrt{s} = 14\,\text{TeV}$. One of the four interaction points is located inside the CMS detector, which is one of the four detectors and one of the two multi-purpose detectors at the LHC. In the following, section 3.2, all detector sub-components are described.

In the next chapter, chapter 4, the theory of Z and W production at hadron colliders is presented. It is thought as a preparation for the succeeding analyses in this thesis and as a more detailed motivation of why these measurements are of particular importance at hadron colliders. Current theoretical limitations in the accuracy of calculating the Drell-Yan inclusive and differential cross section are discussed (section 4.2). Finally, in section 4.4, a method is pointed out of how the systematic uncertainties of the parton distribution functions could be reduced to the percent level.

The next two chapters present two different analyses. They are also both summarized in a CDF note [EHD05] and a CMS note [EHD06].

In chapter 5, the integrated luminosity at the CDF experiment is determined via the counting of $Z \rightarrow e^+e^-$ events during a two year period of data taking. The data and Monte Carlo simulation event samples are specified. In section 5.2, the selection of Z boson events is defined through a classification of electrons. Thereafter, the

method of background subtraction is discussed as well as various detector efficiencies and corrections to them. Together with the theoretical predictions in chapter 4, the experimental and theoretical uncertainties are discussed and evaluated. Besides the luminosity determination also the rapidity-dependence of Z boson production is examined and compared to the theory.

The second analysis chapter, chapter 6, comprises a baseline selection for $Z \rightarrow e^+e^-$ and $W \rightarrow e\nu$ events at the CMS experiment. This selection is aimed to be essentially background-free. In order to be able to use it already in the LHC startup phase, emphasis is put on straightforwardness and simplicity. First, the simulated event samples are described. This is followed by the selection of electrons. Section 6.3 and 6.4 deal with the identification of Z and W events and the contamination of backgrounds. In the last part of this chapter the results and future realistic analysis strategies, once data taking has started, are discussed.

Chapter 7 summarizes the work presented in this thesis. Conclusions are drawn on the pursued analyses and an outlook for future work is given.

This thesis is a follow-up of Anne-Sylvie Nicollerat's thesis [NIC04], using the basics of her analysis strategy for the integrated luminosity determination at CDF and her electron selection for the counting of Z and W events at CMS.

Chapter 1

Theoretical background

1.1 The Standard Model

Today's understanding of the fundamental constituents of matter and their interactions is described by a model called the Standard Model of particle physics. It is an effective field theory accurately describing all particle physics phenomena down to scales of about 10^{-18} m. Within the framework of this theory, matter is composed of elementary particles that are subject to interactions via the exchange of intermediate particles, called gauge particles. While in the past the Standard Model withstood all attempts to disprove it experimentally, it nevertheless appears in many ways unsatisfactory. The absence of gravity in the theoretical framework may be the most striking one, but also the family structure of the 12 different elementary particles may hint to a more fundamental theory. The Standard Model in its present form is based on the theoretical approach formulated in the 1960's and 1970's. It is a gauge field theory that comprises the Glashow-Salam-Weinberg model [GSW61] of the weak and electromagnetic interactions and Quantum Chromodynamics (QCD) [GGW73], the theory of strong interactions. In 1983, the W and Z bosons were discovered at the UA1 and UA2 experiments at CERN and provided a direct confirmation of the unification of the weak and the electromagnetic force.

1.2 The elementary particles

All fundamental particles are classified into two groups according to their spin. The matter particles (and antiparticles[1]) are spin-$\frac{1}{2}$ particles and are called fermions. These fermions are further subdivided into two groups - the quarks and leptons. The other species of fundamental particles are the force particles, which have a spin of 1 and are therefore called bosons.

[1] To each particle, there is an antiparticle associated with the same mass but opposite charge.

1.2.1 The leptons & quarks

There is a classification of leptons into three generations. Each generation differs from the previous one by an increased mass while many other properties remain the same. The electrically charged members of the generations are called electron e^- (first generation), muon μ^- (second generation) and tau τ^- (third generation) and have negative electric charge (-1) in units of the elementary charge, e. They can interact electromagnetically with all charged particles like for example their antiparticles e^+, μ^+ and τ^+, which have positive electric charge (+1), as well as weakly, for example with their corresponding neutrinos ν_e, ν_μ and ν_τ.

In the past years, a topic of great interest has been the mass of neutrinos. Originally, they were formulated as massless particles within the Standard Model to account for their apparent single helicity[2] state. Recently, evidence for neutrino oscillation was found [SKK04], which requires a mass different from zero. The possibility of oscillation from one weak eigenstate to another (e.g. from ν_e to ν_μ) needs the presence of different masses for those eigenstates.

Quarks are similarly organized - six particles are subdivided into three generations and are known as up (u), down (d), charm (c), strange (s), top (t) and bottom (b). These are the so-called flavors. Each flavor occurs in one of the three different color charges - red, green or blue. It is the charge of the strong force. Observable particles made out of quarks (hadrons) are always color-neutral, like for example baryons. They are composed of three quarks (or antiquarks), forming a color-neutral object. The most prominent representatives of baryons are the proton and the neutron. The other type of observable particles are mesons, where a quark-antiquark pair is carrying color and corresponding anticolor. Pions and kaons for example belong to this group. Figure 1.2.1 shows a summary of the leptons' and quarks' properties. Most recent values can be found in ref. [PDG06].

1.2.2 The bosons

The particles described above are interacting among each other via an exchange of a boson. Particles possessing an electric charge different from zero will interact with each other through an exchange of a photon, γ. This is the electromagnetic force. The particles, which feature a non-zero weak isospin, can interact with each other by exchanging a W^+, W^- or Z boson - the weak force. If a particle carries color charge, namely quarks or antiquarks, they are also able to interact through the strong force by exchanging one of eight different types of gluons. Figure 1.2.2 and Figure 1.2.3 give an overview of the vector bosons and the corresponding interactions.

Due to the fact that gluons by themselves carry color charge in pairs of color and anticolor, they are able to interact among each other. Similar to this, W^+ and W^- carry a weak isospin and are also able to self-interact and to interact with the Z. The third component of the weak isospin is zero for the Z, and therefore it can not interact with itself. Neither the photon can, since it has no electric charge.

[2]The helicity is the projection of the spin onto the direction of motion.

FERMIONS matter constituents spin = 1/2, 3/2, 5/2, ...

Leptons spin = 1/2

Flavor	Mass GeV/c^2	Electric charge
ν_e electron neutrino	$<1\times10^{-8}$	0
e electron	0.000511	–1
ν_μ muon neutrino	<0.0002	0
μ muon	0.106	–1
ν_τ tau neutrino	<0.02	0
τ tau	1.7771	–1

Quarks spin = 1/2

Flavor	Approx. Mass GeV/c^2	Electric charge
u up	0.003	2/3
d down	0.006	–1/3
c charm	1.3	2/3
s strange	0.1	–1/3
t top	175	2/3
b bottom	4.3	–1/3

Figure 1.2.1: Summary table for all fermions. The three generations are indicated in colors and are arranged with increasing mass from top to bottom.

BOSONS force carriers spin = 0, 1, 2, ...

Unified Electroweak spin = 1

Name	Mass GeV/c^2	Electric charge
γ photon	0	0
W^-	80.4	–1
W^+	80.4	+1
Z^0	91.187	0

Strong (color) spin = 1

Name	Mass GeV/c^2	Electric charge
g gluon	0	0

Figure 1.2.2: Summary table for the properties of the bosons.

PROPERTIES OF THE INTERACTIONS

Property \ Interaction	Gravitational	Weak (Electroweak)	Electromagnetic (Electroweak)	Strong: Fundamental	Strong: Residual
Acts on:	Mass – Energy	Flavor	Electric Charge	Color Charge	See Residual Strong Interaction Note
Particles experiencing:	All	Quarks, Leptons	Electrically charged	Quarks, Gluons	Hadrons
Particles mediating:	Graviton (not yet observed)	W^+ W^- Z^0	γ	Gluons	Mesons
Strength relative to electromag for two u quarks at: 10^{-18} m	10^{-41}	0.8	1	25	Not applicable to quarks
Strength relative to electromag for two u quarks at: 3×10^{-17} m	10^{-41}	10^{-4}	1	60	
for two protons in nucleus	10^{-36}	10^{-7}	1	Not applicable to hadrons	20

Figure 1.2.3: Summary table for the properties of the forces.

1.3 The fundamental forces

1.3.1 Electroweak Theory

The unified description of the electromagnetic and the weak force is called the electroweak theory. The gauge group on which it is based is a combination of the (non-Abelian) weak isospin group $SU(2)_L$ and the Abelian hypercharge group $U(1)_Y$. For the weak force, there is a distinction between left-handed and right-handed[3] components of fermions. Usually, the electroweak gauge group is denoted as $SU(2)_L \times U(1)_Y$, where L stands for left-handed fermions and Y for the hypercharge. Mathematically spoken, the handedness is defined by means of the chirality operator γ_5. It follows for the electron field:

$$e_L^- = \frac{1}{2}(1-\gamma_5)e^- \tag{1.3.1}$$

$$e_R^- = \frac{1}{2}(1+\gamma_5)e^- \tag{1.3.2}$$

The field e_L^- can be written as a superposition of eigenstates of the helicity operator $h = \frac{\vec{s}\cdot\vec{p}}{|\vec{p}|}$, where $\vec{s}$ denotes the electron spin operator and $\vec{p}$ the momentum operator. In the case of vanishing mass, the left-handed chiral state e_L^- is also an eigenstate of h with eigenvalue -1.

Left-handed fermions transform as doublets under $SU(2)_L$,

$$f_L \to e^{i\vec{T}\vec{\Theta}} f_L \,, \quad \text{where} \quad f_L = \begin{pmatrix} \nu_L \\ e_L \end{pmatrix}, \begin{pmatrix} u_L \\ d_L \end{pmatrix}, \ \ldots \tag{1.3.3}$$

whereas right-handed fermions transform as singlets

[3]Handedness or chirality is defined in the limit of small masses as follows: The chirality of a particle is right-handed if the direction of its spin is the same as the direction of its motion. It is left-handed if the directions of spin and motion are opposite.

quark	T	T_3	Q	Y	lepton	T	T_3	Q	Y
u_L	$\frac{1}{2}$	$\frac{1}{2}$	$\frac{2}{3}$	$\frac{1}{3}$	ν_e	$\frac{1}{2}$	$\frac{1}{2}$	0	-1
d_L	$\frac{1}{2}$	$-\frac{1}{2}$	$-\frac{1}{3}$	$\frac{1}{3}$	e_L^-	$\frac{1}{2}$	$-\frac{1}{2}$	-1	-1
u_R	0	0	$\frac{2}{3}$	$\frac{4}{3}$	e_R^-	0	0	-1	-2
d_R	0	0	$-\frac{1}{3}$	$-\frac{2}{3}$					

Table 1.3.1: The weak isospin, the hypercharge and the electric charge for fermions [HAL84].

$$f_R \rightarrow f_R \ , \quad \text{where} \quad f_R = e_R, u_R, d_R, \ ... \tag{1.3.4}$$

The vector $\overrightarrow{T}$ denotes a vector of matrices with its components $T_i = \frac{\sigma_i}{2}$ as the three generators of the $SU(2)_L$ group. σ_i (i=1,2,3) are the Pauli matrices. The generator of $U(1)_Y$, Y, commutes with T_i. The fermion quantum numbers satisfy the relation

$$Y \ = \ 2(Q + T_3) \tag{1.3.5}$$

The third component of the particle's weak isospin is indicated as T_3, and Q is the electric charge operator. Table 1.3.1 shows the weak isospin, hypercharge and electric charge for leptons and quarks.

Quarks of different families can interact with each other via the weak force less likely than they interact with each other within the same generation. The eigenstates of the weak interaction (d', s', b') are related to the physical quarks or mass eigenstates (d, s, b) via the 3×3 Cabibbo-Kobayashi-Maskawa matrix (CKM matrix):

$$\begin{pmatrix} d' \\ s' \\ b' \end{pmatrix} = \begin{pmatrix} V_{ud} & V_{us} & V_{ub} \\ V_{cd} & V_{cs} & V_{cb} \\ V_{td} & V_{ts} & V_{tb} \end{pmatrix} \begin{pmatrix} d \\ s \\ b \end{pmatrix} \tag{1.3.6}$$

If the matrix would be diagonal, then flavors would be exactly conserved in the weak process. However, the experimental values of the matrix elements do show cross generation interactions [PDG05]:

$$\begin{pmatrix} 0.9739 \text{ to } 0.9751 & 0.221 \text{ to } 0.227 & 0.0029 \text{ to } 0.0045 \\ 0.221 \text{ to } 0.227 & 0.9730 \text{ to } 0.9744 & 0.039 \text{ to } 0.044 \\ 0.0048 \text{ to } 0.014 & 0.037 \text{ to } 0.043 & 0.9990 \text{ to } 0.9992 \end{pmatrix} \tag{1.3.7}$$

The diagonal elements are, as expected, close to unity and the elements for interactions between two generations are considerably smaller than the elements for the interaction within one generation.

In absence of gauge fields, the dynamics of fermions are described by the Dirac equation with the corresponding Lagrangian as

$$\mathcal{L}_{\text{Dirac}} = \bar{\Psi}(x)(i\partial\!\!\!/ - m)\Psi(x) \ , \quad \text{with } \partial\!\!\!/ \equiv \partial_\mu \gamma^\mu \ , \tag{1.3.8}$$

where $\Psi(x)$ are the fermion fields. Requiring the Lagrangian to be invariant under local $\mathrm{SU(2)_L}$ transformations necessitates the introduction of a weak isospin triplet of gauge fields, W_μ^i $(i = 1, 2, 3)$. In addition, also the $\mathrm{U(1)_Y}$ invariance under transformations is imposed, leading to the conservation of the weak hypercharge, Y. This local gauge invariance under the $\mathrm{U(1)_Y}$ transformation directs to the introduction of a weak hypercharge singlet gauge field, B_μ. The gauge symmetry $\mathrm{SU_L(2) \times U(1)_Y}$ is then promoted by the electroweak covariant derivative

$$D_\mu \equiv \left(\partial_\mu - ig\vec{T}\vec{W}_\mu - ig'\frac{Y}{2}B_\mu \right) \ , \tag{1.3.9}$$

where g and g' are the coupling constants related to $\mathrm{SU(2)_L}$ and $\mathrm{U(1)_Y}$, respectively. The electroweak Lagrangian includes kinematic terms for the gauge fields like

$$-\frac{1}{4}W_{\mu\nu}^i W_i^{\mu\nu} - \frac{1}{4}B_{\mu\nu}B^{\mu\nu} \ , \tag{1.3.10}$$

where the field strength tensors are

$$W_{\mu\nu}^i = \partial_\mu W_\nu^i - \partial_\nu W_\mu^i + g\epsilon^{ijk}W_{\mu j}W_{\nu k} \ , \tag{1.3.11}$$

with ϵ^{ijk} as the total antisymmetric tensor, and

$$B_{\mu\nu} = \partial_\mu B_\nu - \partial_\nu B_\mu \ . \tag{1.3.12}$$

Thus, the Lagrangian contains self-interaction terms among the three W_μ^i gauge bosons, as it corresponds to the non-Abelian $\mathrm{SU(2)_L}$ group. These gauge fields can then be rewritten as a linear combination of the electroweak interaction eigenstates to

$$W_\mu^\pm = \frac{1}{\sqrt{2}}\left(W_\mu^1 \mp \mathrm{i}W_\mu^2\right) , \tag{1.3.13}$$

$$Z_\mu = W_\mu^3 \cos\theta_\mathrm{W} - B_\mu \sin\theta_\mathrm{W} , \tag{1.3.14}$$

$$A_\mu = W_\mu^3 \sin\theta_\mathrm{W} + B_\mu \cos\theta_\mathrm{W} , \tag{1.3.15}$$

where $W_\mu^\pm$, Z_μ and A_μ represent the physical gauge bosons. θ_W is the weak mixing angle, which defines the rotation in the neutral sector. Furthermore, the elementary charge e is linked via the weak mixing angle and the coupling constants of the weak isospin and hypercharge by

$$e = g \sin\theta_\mathrm{W} = g' \cos\theta_\mathrm{W} . \tag{1.3.16}$$

Experimentally, the weak mixing angle is measured to [PDG06]

$$\sin^2\theta_\mathrm{W} = 0.23122 \pm 0.00015 . \tag{1.3.17}$$

The problem, however, is that unlike in Quantum Electrodynamics (QED)[4] the observed intermediate vector bosons $\mathrm{W}^\pm$ and Z are massive, whereas mass terms like $m_W^2 W_\mu W^\mu$ and $\frac{1}{2}m_Z^2 Z_\mu Z^\mu$ violate the $\mathrm{SU(2)_L} \times \mathrm{U(1)_Y}$ gauge invariance. The gauge boson masses must be thus generated in a gauge invariant way [HIG64].

1.3.2 Spontaneous Symmetry Breaking

The symmetry of a system is said to be spontaneously broken if its ground state does not exhibit the symmetry governing its dynamics. Choosing a particular ground state produces Spontaneous Symmetry Breaking (SSB). In quantum field theory SSB occurs if the ground state of a system (the vacuum) does not share the symmetry of its Lagrangian. One feature of SSB is the appearance of massless modes, the Nambu-Goldstone bosons, or simply Goldstone bosons. The Higgs mechanism operates when SSB occurs in a gauge theory. In this case the Goldstone bosons are absorbed as the third degree of freedom of massless vector fields, which, as such, acquire mass.

In the electroweak theory SSB must break the gauge group $\mathrm{SU(2)_L} \times \mathrm{U(1)_Y}$ down to $\mathrm{U(1)_Q}$, giving mass to the W and Z bosons while keeping the photon massless, as $\mathrm{U(1)_Q}$ is a valid symmetry of the vacuum. The process leads to the introduction of a new field, the Higgs field. The simplest field structure that fulfills all requirements for SSB in the electroweak theory consists of two complex fields that form a doublet with respect to the weak isospin,

$$\Phi = \begin{pmatrix} \phi^+ \\ \phi^0 \end{pmatrix} \quad \text{with} \quad T = \frac{1}{2} \quad \text{and} \quad Y = 1 . \tag{1.3.18}$$

[4] QED is the description of the electromagnetic force which is governed by the gauge symmetry $\mathrm{U(1)_Q}$. This symmetry is generated by the electric charge Q, such that all interactions are based upon an exchange of photons.

The Lagrangian of this field is

$$(D_\mu \Phi)^\dagger (D^\mu \Phi) - V(\Phi) \tag{1.3.19}$$

with the potential

$$V = -\mu^2 \Phi^\dagger \Phi + \lambda (\Phi^\dagger \Phi)^2 \text{ and } \lambda > 0 \tag{1.3.20}$$

With $-\mu^2 < 0$, the minimum of the potential V is

$$|\Phi|^2 = \frac{\mu^2}{2\lambda} \neq 0\,. \tag{1.3.21}$$

Figure 1.3.1 [HOL02] shows the potential for $-\mu^2 < 0$.

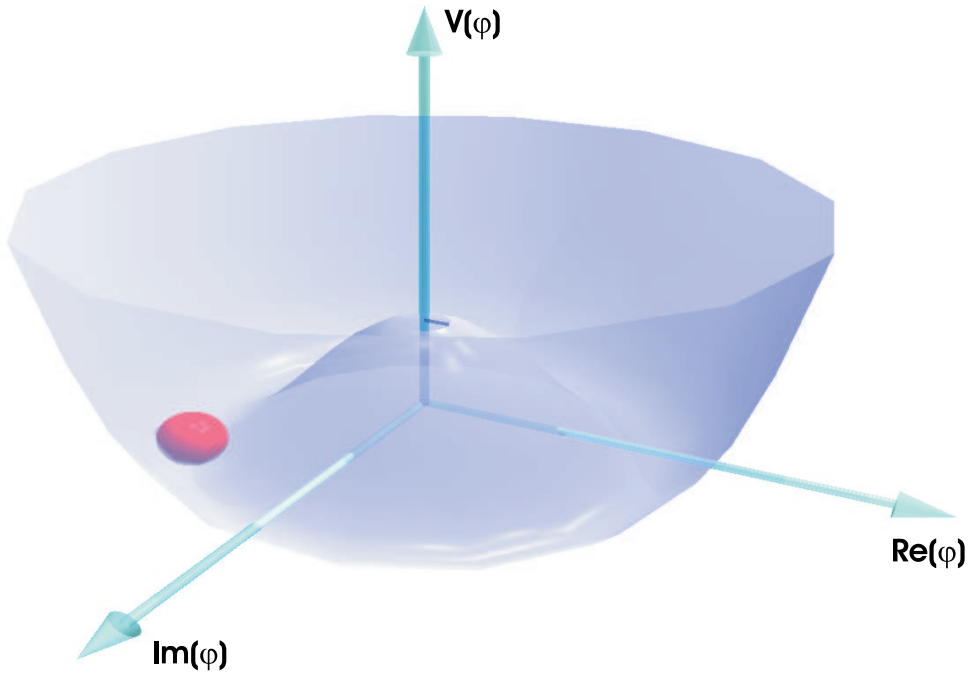

Figure 1.3.1: The Higgs potential $V = -\mu^2 \Phi^\dagger \Phi + \lambda (\Phi^\dagger \Phi)^2$ for $-\mu^2 < 0$.

This ground state is degenerate through an arbitrary phase φ and thus has no preferred direction in the weak isospin space. However, once a specific ground state is chosen SSB occurs. For instance, choosing

$$\phi_0 = \frac{1}{\sqrt{2}} \begin{pmatrix} 0 \\ v \end{pmatrix} \text{ with } v = \sqrt{\frac{\mu^2}{\lambda}} \tag{1.3.22}$$

breaks $SU(2)_L \times U(1)_Y$ leaving $U(1)_Q$ as a symmetry of the vacuum. Feynman calculus is based on perturbation theory, where fields are treated as fluctuations around the ground state. Expanding ϕ around the chosen ground state yields a Lagrangian where the Goldstone bosons are absorbed by the gauge fields. This Lagrangian also contains a new field, the Higgs field, corresponding to a massive scalar particle, the Higgs boson. Through an additional term in the complete Standard Model Lagrangian, the Yukawa term, the fermions of the theory acquire mass via the coupling to the Higgs field. As just one physical Higgs boson occurs in this theory, it is often referred to as Higgs boson of the minimal Standard Model. In nature the Higgs mechanism could be related to a more complex structure with several Higgs bosons (five in the case of a supersymmetric extension of the Standard Model). While all couplings to bosons and fermions are known as a function of the Higgs mass, the mass itself is a free parameter of the theory. One experimentally verifiable prediction of this minimal model is the ratio of the W and Z bosons

$$\frac{M_W}{M_Z} = \cos\theta_W \tag{1.3.23}$$

with

$$M_W = \frac{1}{2} g v \tag{1.3.24}$$

and

$$M_Z = \frac{1}{2}\sqrt{g^2 + g'^2}\, v \tag{1.3.25}$$

while the photon stays massless.

Despite all efforts undertaken to find the Higgs boson, it still eludes detection. At the Large Electron Positron Collider (LEP) a lower mass limit of 114.4 GeV, at the 95 % confidence level, could be set. Ref. [HHG00] provides detailed remarks to all features of a Higgs boson in this minimal model and also more complicated models with several Higgs bosons.

1.3.3 Quantum Chromodynamics

Like in QED, where the $U(1)_Q$ symmetry conserves the electric charge, the $SU(3)_C$ symmetry of QCD requires the color charge to be conserved. QCD is based on a non-Abelian gauge group and causes gluons to carry color charge. Therefore, gluon-gluon interactions become possible. This causes the strength of the strong coupling constant (α_s) to decrease with increasing energies, whilst the strength of all other coupling constants increases with rising energies. Consequently, at large momentum transfers (Q^2) or very short distances the quarks can be considered as quasi-free, so-called asymptotic freedom. Reversely, with increasing distances the potential energy of the color field rises until it becomes so large, that the energy is sufficient to create

new quark-antiquark pairs. This is assumed to explain the quark confinement and the observation of only color-neutral objects. In addition, the large value of α_s at low Q^2 is responsible for the break down of perturbation theory below $Q^2 \sim 1\,\mathrm{GeV}$.

Quarks can occur with color charges red (r), green (g) or blue (b) while antiquarks appear in antired ($\bar{\mathrm{r}}$), antigreen ($\bar{\mathrm{g}}$) or antiblue ($\bar{\mathrm{b}}$). Gluons form a SU(3) color octet and are for example available in the following orthogonal color-states:

$$\mathrm{r\bar{b}},\ \mathrm{r\bar{g}},\ \mathrm{b\bar{g}},\ \mathrm{b\bar{r}},\ \mathrm{g\bar{r}},\ \mathrm{g\bar{b}},\ \frac{\mathrm{r\bar{r}} - \mathrm{b\bar{b}}}{\sqrt{2}} \text{ and } \frac{\mathrm{r\bar{r}} + \mathrm{b\bar{b}} - 2\mathrm{g\bar{g}}}{\sqrt{6}} \tag{1.3.26}$$

Figure 1.3.2 shows an example of the interaction between two quarks via an exchange of a gluon.

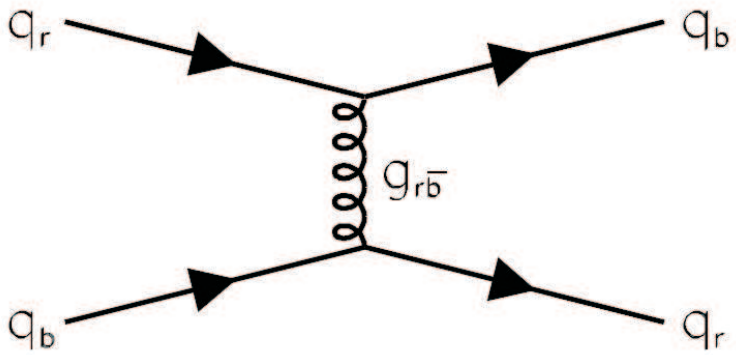

Figure 1.3.2: An example of quark-quark scattering by the exchange of a gluon. The colors are indicated.

Colored objects are not observed in nature, only color singlets (color-neutral particles) are detected. The lowest energy configuration of color singlets are baryons (quark-quark-quark) and mesons (quark-antiquark). Although colored objects can not be measured directly, the number of colors is determinable, for example, via electron-positron annihilation. The cross section ratio of their decay to hadrons to their decay to muons has been measured (cf. [PER87]),

$$R = \frac{\sigma_{\mathrm{e^+e^-} \to \mathrm{hadrons}}}{\sigma_{\mathrm{e^+e^-} \to \mu^+\mu^-}} = N_\mathrm{c} \sum_{\mathrm{flavors}} q_i^2\,, \tag{1.3.27}$$

where N_c is the number of colors, q_i the electric charge of the quark flavor i and the sum adds up all flavors, which are less massive than half of the center of mass energy of the reaction. Indeed, all measurements indicate that the number of quark colors is three.

The inter-quark potential has been shown to follow this equation [EIC75]:

$$V_\mathrm{s} = -\frac{\alpha_\mathrm{s}}{r} + kr \tag{1.3.28}$$

Here, k is a constant, r the distance between the quarks and the strong coupling constant α_s is in the order of 1 [5]. In this region where $\alpha_s \sim 1$ (at low energies and short distances), higher order diagrams contribute significantly to the calculation, such that a perturbative expansion is not useful. This is called the non-perturbative regime of QCD. In the region where $\alpha_s \ll 1$, the perturbative Feynman calculus can be applied, hence this region is called perturbative QCD. The strong coupling constant can then be approximated to

$$\alpha_s(Q^2) = \frac{4\pi}{\left(11 - \frac{2}{3}N_f\right)\ln\left(\frac{Q}{\Lambda_{QCD}}\right)^2} + \text{(higher order terms)}\,, \tag{1.3.29}$$

where N_f equals the number of quark flavors accessible at the scale Q^2 and Λ_{QCD} indicates qualitatively the magnitude of the scale at which $\alpha_s(Q^2)$ becomes large. Experimentally, Λ_{QCD} is determined to be about 0.2 GeV.

In QCD the gauge invariant Lagrangian is built similarly to the one in QED. The QCD covariant derivative

$$D_\mu q \equiv \left(\partial_\mu - \mathrm{i}g_s\left(\frac{\lambda_\alpha}{2}\right)A_\mu^\alpha\right)q\,, \quad \text{where} \quad q = \begin{pmatrix} q_1 \\ q_2 \\ q_3 \end{pmatrix} \tag{1.3.30}$$

is introduced to ensure local gauge invariance. Here, q are the quark fields and $\frac{\lambda_\alpha}{2}$ are the $SU(3)_C$ generators given by 3×3 traceless hermitian matrices. A_μ^α are the eight gluon fields, $\alpha = 1,...,8$.

The QCD Lagrangian is then

$$\mathcal{L}_{QCD} = \sum_q \bar{q}(x)(\mathrm{i}\not{D}_\mu - m_q)q(x) - \frac{1}{4}F_{\mu\nu}^\alpha(x)F_\alpha^{\mu\nu}(x) \tag{1.3.31}$$

with the gluon field strength tensor

$$F_{\mu\nu} = \partial_\mu A_\nu^\alpha(x) - \partial_\nu A_\mu^\alpha(x) + g_s f^{\alpha\beta\gamma}A_{\mu\beta}A_{\nu\gamma} \tag{1.3.32}$$

containing a bilinear term, which provides the gluon self-interaction. $f^{\alpha\beta\gamma}$ denotes the structure constants. A detailed description of QCD can be found in ref. [DIS03].

[5] $\alpha_s \sim 1$ has to be compared with the electroweak coupling constant $\alpha_{ew} \sim \frac{1}{137}$.

Chapter 2

The CDF detector at the Tevatron

The measurements presented in the first part of this thesis are performed on data of the **C**ollider **D**etector at **F**ermilab (CDF). This multi-purpose detector is located at one of the two interaction points at the Tevatron collider at Fermilab, where proton-antiproton collisions are recorded. In this chapter the different accelerator stages and the different parts of the detector are described.

2.1 The Tevatron

The Tevatron is a synchrotron of 1 km in radius and consists of an accelerator chain in five stages, leading finally to collisions of protons and antiprotons with a center of mass energy of $\sqrt{s} = 1.96\,\text{TeV}$. Superconducting magnets are used to create a magnetic field of 4.2 T to bend the particles at such energies. Figure 2.1.1 shows a simplified sketch of the accelerator complex.

In a first stage a Cockroft-Walton accelerator accelerates H^- ions to initially 750 keV. Subsequently, the ions are driven into the linear accelerator (LINAC) where they reach energies of 400 MeV and are passed through a thin carbon foil to strip off the electrons. The resulting protons are fed into the Booster, a small synchrotron of 300m in diameter, and brought up to 8GeV while also being bunched. These bunches of protons are then taken over by the Main Injector, which boosts the protons to 150 GeV and injects them into the Tevatron. Here, the protons are accelerated to 980 GeV.

Antiprotons are generated by driving the 120 GeV protons from the Main Injector onto a nickel target. A shower of particles, containing antiprotons, is produced. Antiprotons of around 8 GeV in energy are selected, debunched and collected in the Accumulator Ring. There, they are stochastically cooled down to minimize their energy dispersion. Having collected a certain amount of antiprotons, so-called stack, they are sent back to the Main Injector and follow the same acceleration procedure as the protons, just circulating in opposite direction.

Protons and antiprotons are circulating in 36 bunches with a separation of 396 ns around the Tevatron. Each bunch consists of 200×10^9 and 20×10^9 particles, respec-

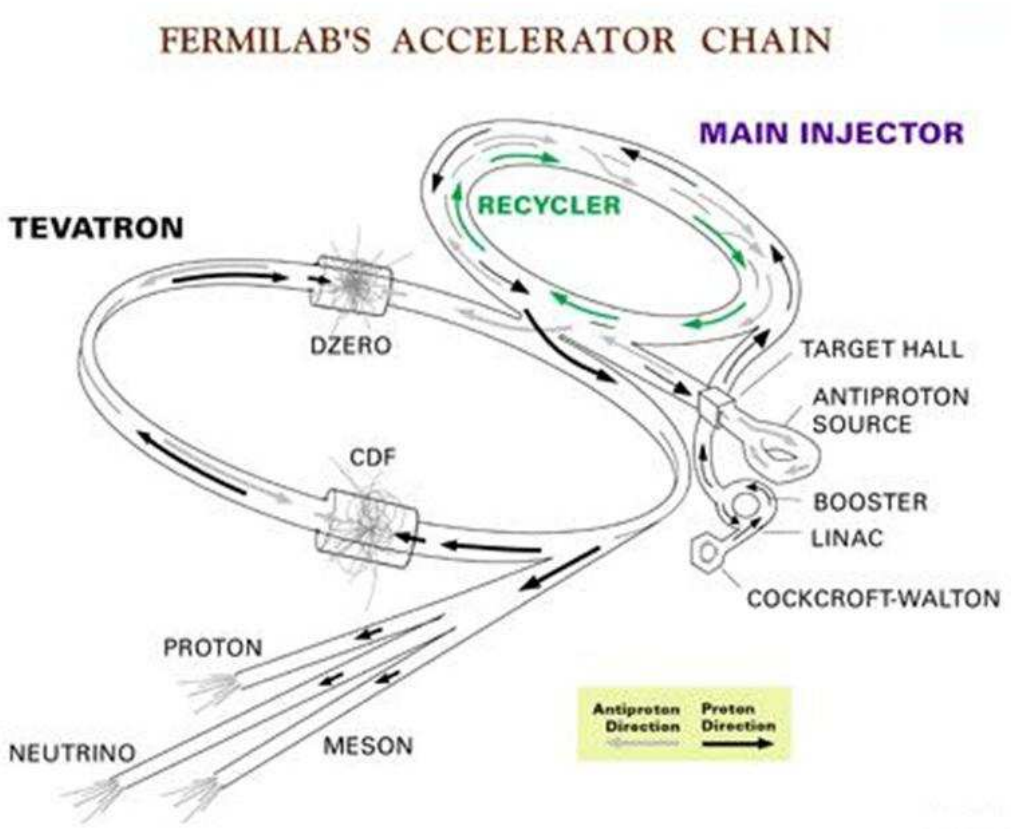

Figure 2.1.1: Schematic view of the accelerator chain at Fermilab.

tively. At maximum energy the two trains of particles and antiparticles are forced to cross each other. One of the two interaction points at the Tevatron is located in the center of the CDF detector. The other one is located in the DØ detector, another multi-purpose detector with similar capabilities as CDF. The interactions occur in a luminous region of 30 μm in the transverse plane to the beam direction and 30 cm along the beam direction due to a Gaussian dispersion.

When the upgrade of the accelerator machine and the CDF detector in April 2001 was completed, the so-called Run II started. Until February 2006, an integrated total luminosity of $\sim$ 1 fb^{-1} was recorded, as seen in Figure 2.1.2. During time also the performance of the Tevatron increased, so that meanwhile an instantaneous luminosity at the beginning of a 'store' of about 130nb^{-1}/s is achieved. The evolution of the instantaneous peak luminosity is shown in Figure 2.1.3.

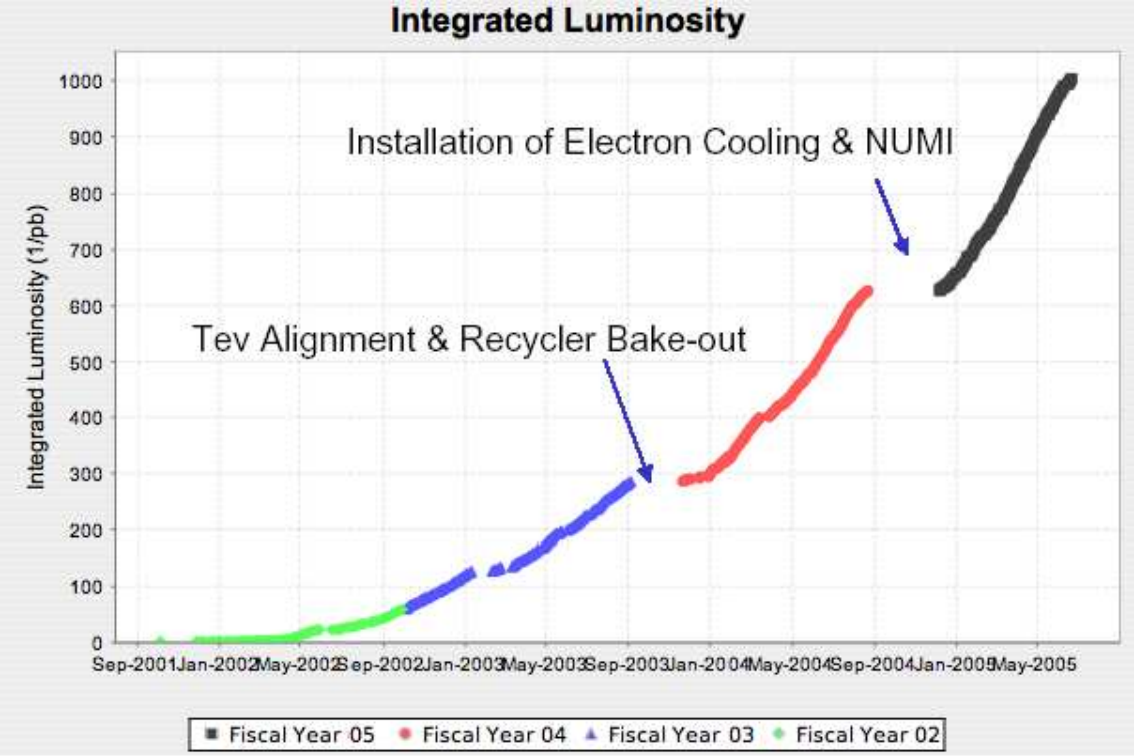

Figure 2.1.2: The integrated luminosity in inverse pico barn is shown for the years 2002 to 2005. Indicated are also the shutdown periods in the end of 2003 and 2004, where works at the Tevatron, the Recycler and a new neutrino experiment (NUMI) were carried out.

2.2 The CDF detector

The Tevatron was operated in Run I during 1992 - 1996 at a center of mass energy of $\sqrt{s} = 1.8\,\mathrm{GeV}$. After its end in 1996, the Tevatron as well as the CDF detector had undergone a major upgrade resulting in an increased center of mass energy, a higher collison rate, improved detector components and an extended angular coverage. Figure 2.2.1 shows the side-view of the CDF detector as it is now in operation. An exhausting description of all detector parts can be found in ref. [CDF96].

All detector sub-components are arranged cylindrically around the interaction point. From inside out there are layers of silicon providing high-precision tracking and vertexing, a wire drift chamber for track reconstruction, both incorporated in a solenoid magnet, followed by the electromagnetic and hadronic calorimeter to identify and measure for example electrons, photons and jets, and finally the muon chambers on the far outside. In addition, there are also other systems like the Cherenkov Luminosity Counters which are very close to the beam-pipe and very forward.

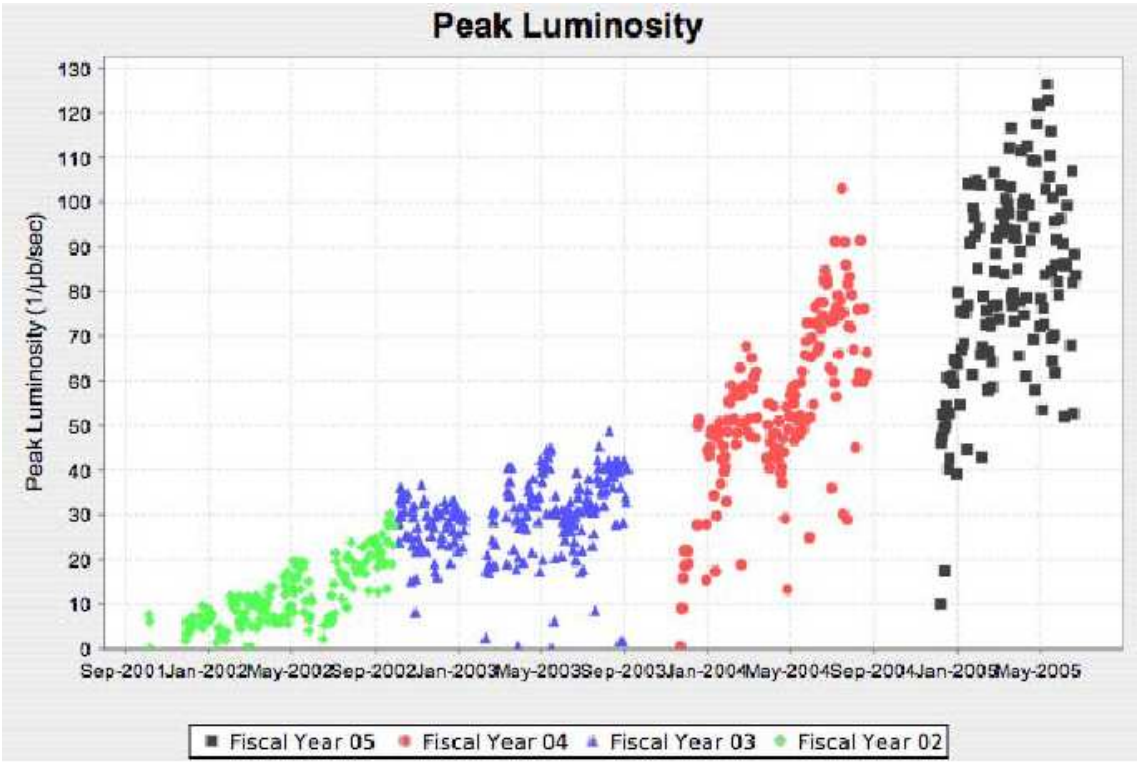

Figure 2.1.3: The peak luminosities for the different stores from the year 2002 to 2005 are presented in inverse micro barn per second.

2.2.1 Coordinate System

The overall geometry in CDF is measured in cylindrical coordinates (θ, ϕ, z) with the nominal interaction point as the center and the beam-line as the z-direction. The positive z-direction is defined with the direction of motion of the protons (eastwards), the azimuthal angle ϕ is measured in the xy-plane (transverse to the beam-direction), where y is pointing upwards and x is pointing away from the center of the Tevatron ring. $\phi = 0$ is chosen along the positive direction of the x-axis. The polar angle θ is measured from the positive direction of the z-axis. Figure 2.2.2 illustrates the CDF coordinate convention.

In the following, the polar angle will be replaced by a commonly used variable called *pseudorapidity*, η.

$$\eta = -\log\left(\tan\frac{\theta}{2}\right) \tag{2.2.1}$$

In the limit of massless particles, the pseudorapidity equals a quantity, which is called *rapidity*, Y.

$$Y = \frac{1}{2}\log\left(\frac{E + p_z}{E - p_z}\right) \tag{2.2.2}$$

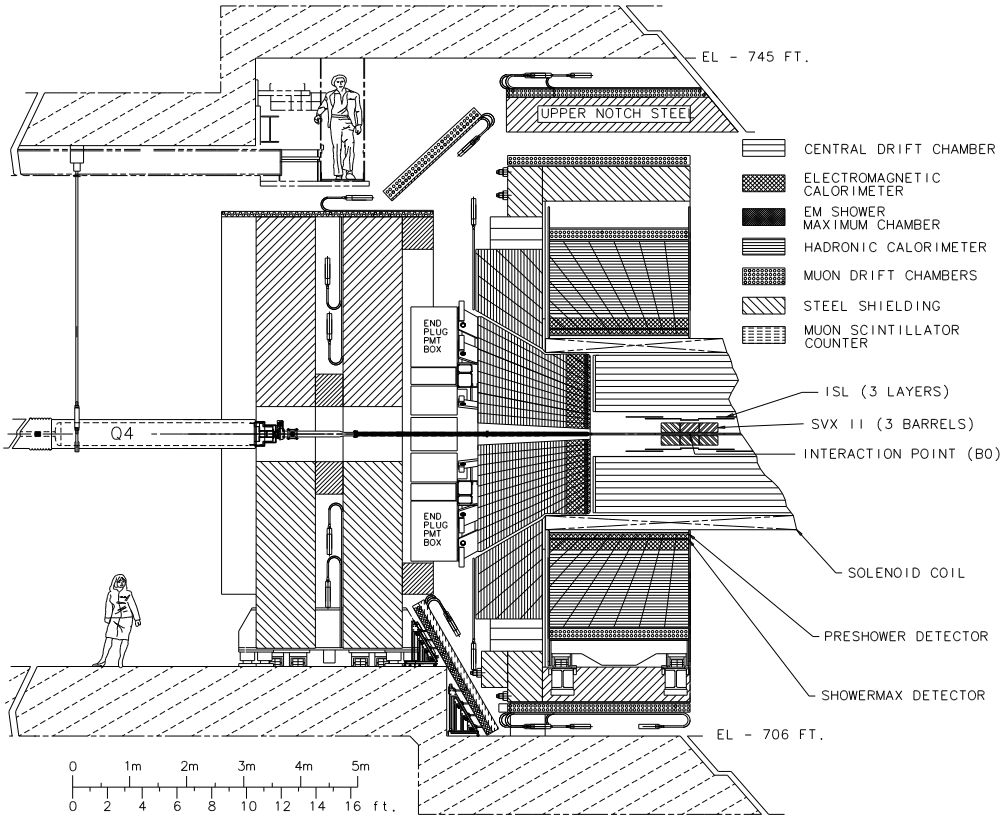

Figure 2.2.1: A sketch of the CDF detector with all its detector components. The length scale indicates its size.

A Lorentz boost along the z-direction of a particle adds a constant to the rapidity. Rapidity differences, therefore, are invariant under Lorentz boosts. Since physics processes are rotational invariant, ϕ is a natural choice and distributions of generated particles in the collisions are flat in ϕ-space. This is not necessarily the case in θ. Although protons and antiprotons carry the same momentum in the lab frame, their partons only have a fraction of it. This might result in a net-momentum in z-direction. Therefore, the rapidity or the pseudorapidity are plausible and handy variables to work with. In the following, a brief description of the detector subsystems is given with an emphasis on those detector parts, which are relevant for the analysis carried out in this thesis.

2.2.2 Tracking System

A combination of silicon strip detectors and drift chambers is used for the tracking system, all incorporated in a superconducting solenoid magnet of 1.5 m in radius that creates a magnetic field of 1.4 T parallel to the beam axis. It performs charged-particle track reconstruction and vertex finding. Figure 2.2.3 shows a sketch of the

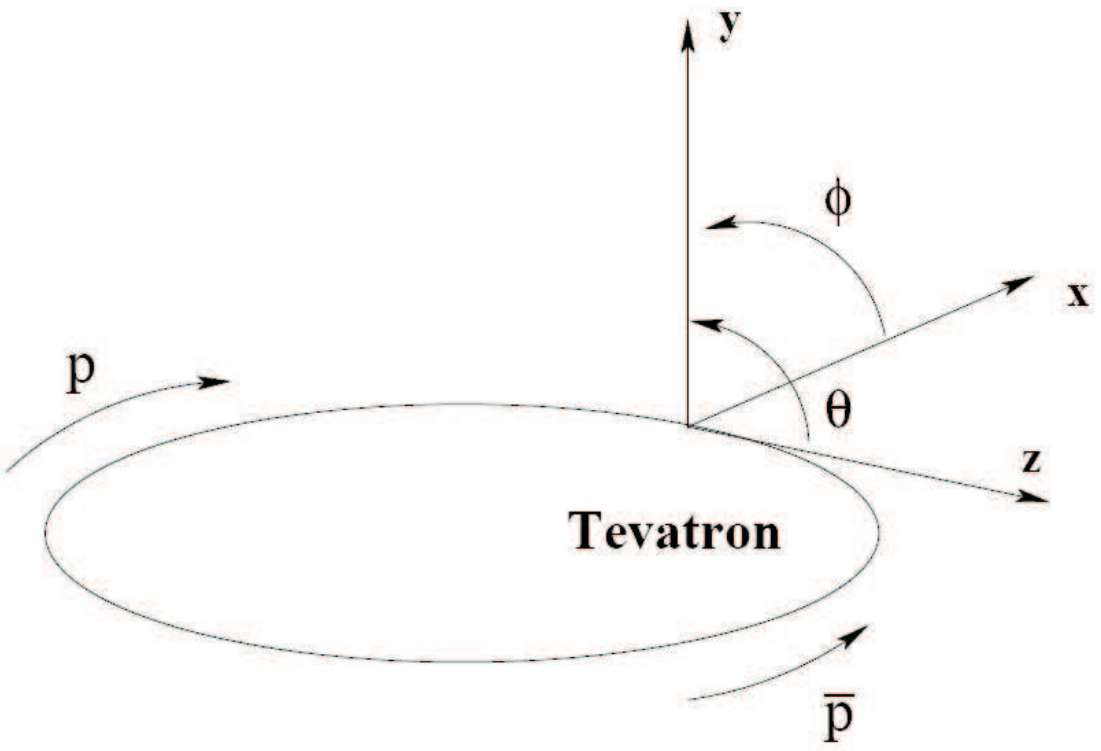

Figure 2.2.2: The CDF coordinate system with respect to the Tevatron in x, y, z, ϕ and θ.

tracking system.

Silicon Tracking (Layer00, SVX, ISL) The inner tracking consists of three different sub-components [AMI94], [CIH95]. 'Layer00' denotes a layer of single-sided silicon strip detectors directly mounted on the beam-pipe. It was added in Run II to improve the impact parameter resolution for high momentum tracks up to 25 μm.

At a distance of 2.5 cm to 10.7 cm from the beam-pipe the silicon vertex detector (SVX) is positioned. It comprises five layers of stereo-sided silicon sensors, where the sensors are oriented alternately in a small-angle (1.2°) and 90° . This enables to obtain three-dimensional information and an enhanced secondary vertex resolution in the z-coordinate.

The Intermediate Silicon Layers (ISL) consist of a silicon layer at 22 cm from the beam-pipe in the region $-1 < \eta < 1$. Additionally, there are two layers at 20 cm and 28 cm at higher pseudorapidities, namely $1 < |\eta| < 2$. Figure 2.2.4 shows the inner tracking system.

A resolution of 40 μm is achieved for the impact parameter of charged particle tracks (including beam uncertainties), and a resolution of 70 μm along the z-direction is obtained.

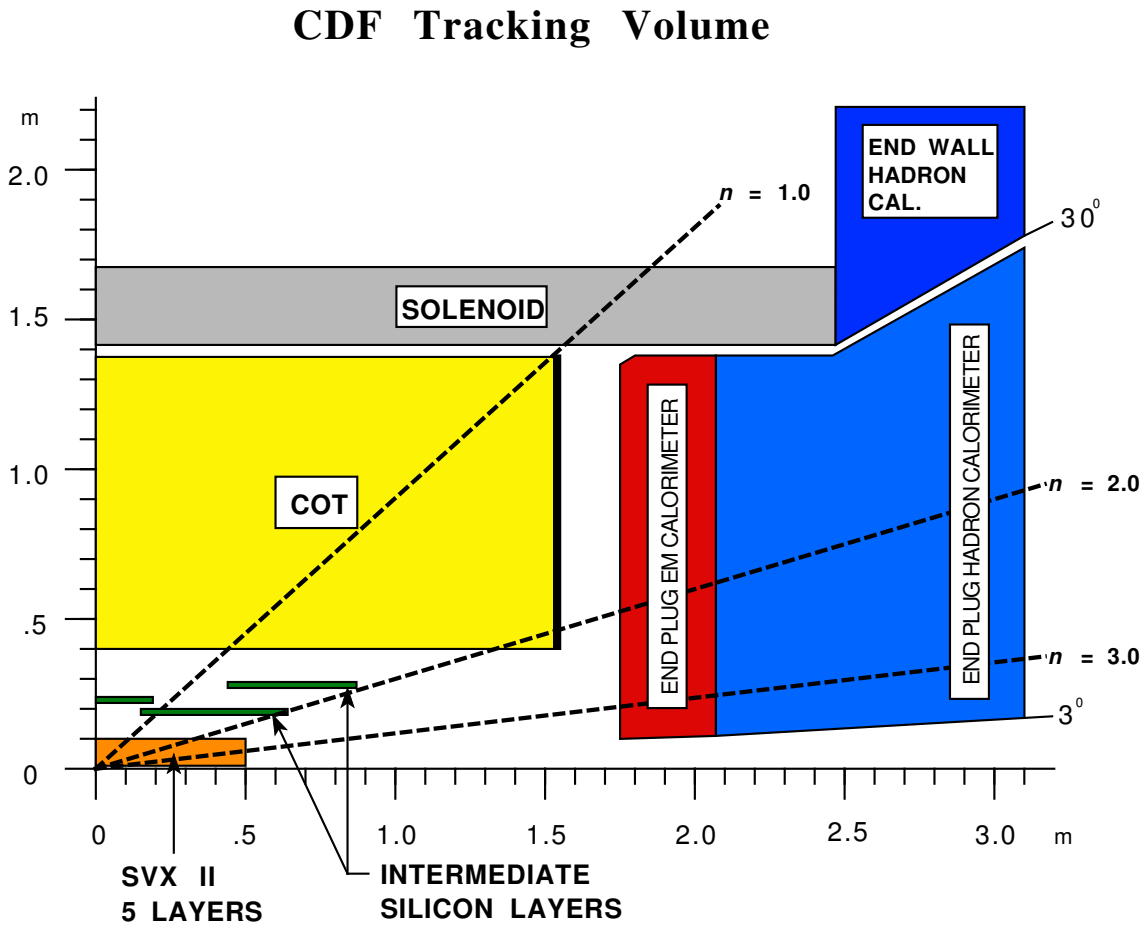

Figure 2.2.3: Shown are all components of the CDF tracking system. In addition, the magnet and parts of the calorimeter are also sketched. The range in pseudorapidity is indicated.

Drift Chamber (COT) The central outer tracker [AFF04] is a $\sim 3\,\mathrm{m}$ long open cell drift chamber with a maximum drift time of 100 ns. It covers a distance of 43 cm to 133 cm from the beam-pipe. 96 layers are arranged in 8 superlayers à 12 layers of sense wires, as shown in Figure 2.2.5.

Four axial and four $\pm 2°$ (with respect to the z-direction) stereo superlayers are arranged alternately. As a gas mixture Ar-Ethane-CF_4 (50 : 35 : 15) was chosen. Since 2004, also a small amount of oxygen is added. In the innermost layers of the COT aging effects were observed and partially reversed by supplementing the design mixture with a small fraction of O_2. In the region $|\eta| < 1.1$ a track reconstruction efficiency for isolated high-p_T tracks of almost 100 % is achieved. At the position $z = 0$ a spacer bar is located which serves structural purposes and results in lower tracking trigger efficiencies at $\eta = 0$. A single hit spatial resolution of about 140 μm is observed and translates to a momentum resolution of $\delta p_T/p_T \sim 0.15\% \cdot p_T\,[\mathrm{GeV/c}]$. Additionally, the specific energy loss by ionization (dE/dx) information of the COT can be used for particle identification.

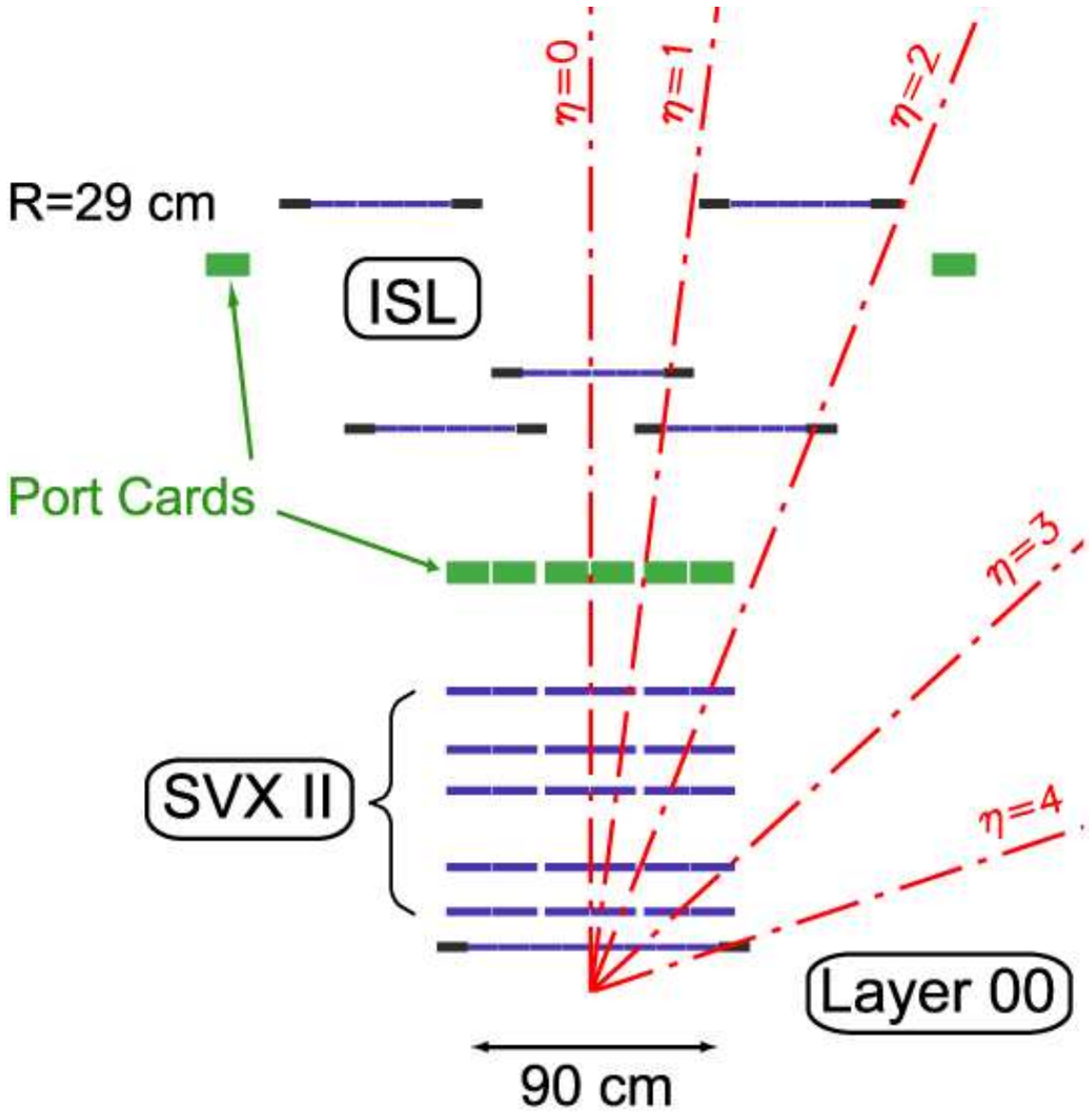

Figure 2.2.4: The geometrical arrangement in the yθ-plane of the three sub-systems of the inner tracking chamber. The z-coordinate is compressed.

As mentioned before, the whole tracking system is surrounded by the superconducting coil. In between the magnet and the COT, there is also a scintillator employed - the time of flight chamber (TOF) [GRO01] - to tag charged kaons in a p_{T}-range from 0.6 GeV to 1.6 GeV.

2.2.3 Calorimeter System

It could be seen already in Figure 2.2.1 that the calorimeters are physically separated in η. The central region stretches approximately from $\eta = -1.1$ to $\eta = +1.1$,

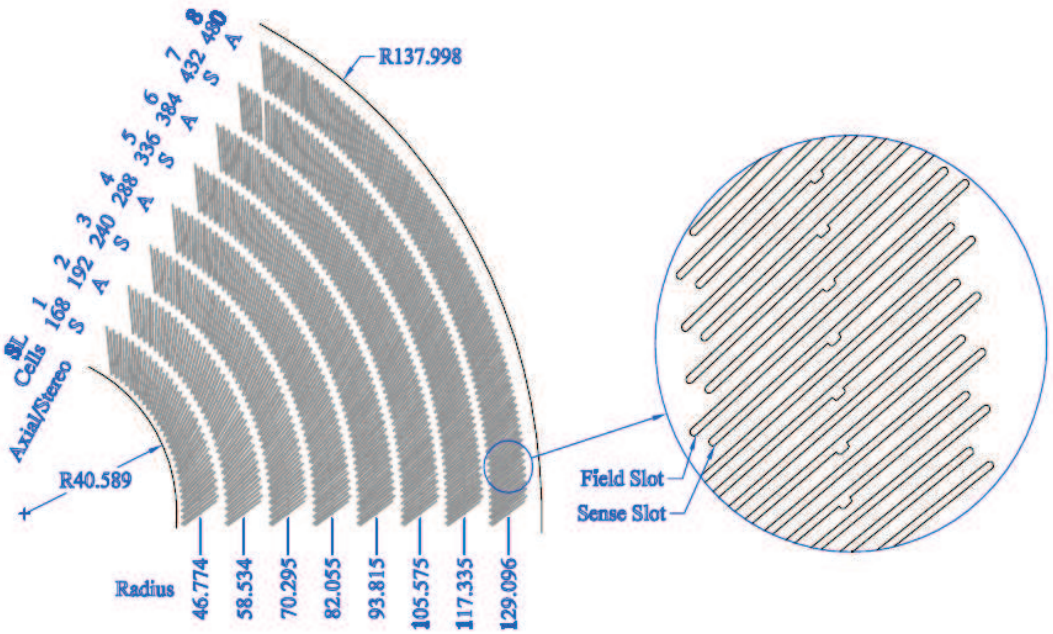

Figure 2.2.5: The rϕ-plane of the COT is presented. The sketch shows one sixth of the east endplate. For each superlayer the average radius (in centimeter), the wire orientation (axial and stereo) and the total number of supercells are given. The zoom shows the sense and field sheet slot geometry.

whereas the forward calorimeters (also called plug calorimeters) cover the region $1.1 < |\eta| < 3.6$. The calorimeter system consists of two main instruments - an inner electromagnetic calorimeter and an outer hadronic calorimeter.

Polystyrene scintillator sampled with layers of lead clad in aluminum are the principal components of the central electromagnetic calorimeter (CEM) [BAL88]. Behind the eighth sample of the CEM proportional chambers are located, called the central shower maximum chambers (CES). Typically, the showers in the electromagnetic calorimeter reach their maximum in the transverse extent at this depth. Thus, it is possible to better distinguish between π^0's and electrons.

Directly attached at the outer part of the CEM follows the central hadronic calorimeter (CHA) [BER88]. It consists of steel layers interleaved each 2.5 cm by scintillator material. To fill the gap between the CHA and the plug hadronic calorimeter (PHA) the wall hadronic calorimeter (WHA) is inserted. Of the same tower structure as the CHA, it features a reduced sampling every 5 cm. The towers for the electromagnetic and the hadronic central calorimeters are segmented into blocks of $\Delta\phi = 15°$ and $\Delta\eta = 0.11$. Between the CEM and the superconducting coil is the central preradiator (CPR) situated. Its purpose is to support the separation of electrons and photons, where the latter ones are originating from pion decays.

The basic structure of the central parts of the calorimeter is also found in the plug components. Like the CEM the plug electromagnetic calorimeter (PEM) is made of

	coverage	absorber material	thickness	energy resolution
CEM	$0 < \|\eta\| < 1.1$	Pb	0.33 cm 19 X_0, 1 λ_I	$\frac{13.5\,\%}{\sqrt{E_T}} \oplus 1.7\,\%$
PEM	$1.3 < \|\eta\| < 3.6$	Pb	0.46 cm 21 X_0, 1 λ_I	$\frac{16\,\%}{\sqrt{E_T}} \oplus 1\,\%$
CHA	$0 < \|\eta\| < 0.9$	Fe	2.5 cm 4.5 λ_I	$\frac{75\,\%}{\sqrt{E_T}} \oplus 3\,\%$
PHA	$1.3 < \|\eta\| < 3.6$	Fe	5.0 cm 7 λ_I	$\frac{80\,\%}{\sqrt{E_T}} \oplus 5\,\%$
WHA	$0.7 < \|\eta\| < 1.3$	Fe	5.0 cm 4.5 λ_I	$\frac{80\,\%}{\sqrt{E_T}}$

Table 2.2.1: Overview of the electromagnetic and hadronic calorimeter properties.

a stack of lead and scintillator material. It incorporates a shower-maximum detector (PES), located after about six radiation lengths into the PEM. Similar to the central pendant, the CES, the PES provides better spatial resolution than the PEM and is therefore also used to match cluster and tracks as well as measuring the shower shape. The towers for the electromagnetic and the hadronic forward calorimeters are segmented into blocks of $\Delta\phi = 7.5°$ at lower pseudorapidities and $\Delta\phi = 15°$ at higher pseudorapidities. In ϕ they range between $\Delta\eta = 0.64$ and $\Delta\eta = 0.09$.

Like the CPR, the plug pre-radiator (PPR), which is the first layer of the PEM and is read out separately, supports the separation of electrons and photons by measuring the shower shape already at this first stage. The characteristics of the most important calorimeter components are collected in Table 2.2.1.

2.2.4 Muon System

There are four muon sub-systems [ART04] employed in CDF - the central muon detector (CMU), the central muon upgrade (CMP), the central muon extension detector (CMX) and the intermediate muon detector (IMU). All these systems form the most outer parts of the spectrometer. The CMU and the CMP cover the pseudorapidity region $|\eta| < 0.6$, the CMX covers $0.6 < |\eta| < 1.0$, and the IMU extends from $|\eta| = 1.0$ to $|\eta| = 1.5$. Sets of staggered drift chambers and scintillators are chosen to detect the muons. The return yoke of the magnetic field and steel walls are located in front of the muon-system. In coincidence with the track information from the COT relevant muons are detected. Since this analysis does not use the information of the muon chambers, the interested reader is referred to ref. [CDF96] for a more detailed description.

2.2.5 Trigger System

Three trains à twelve proton and antiproton bunches are crossing every 396 ns in the CDF detector. With a rate of one interaction per crossing, this makes 2.5 million events per second. An event rate of 2.5 MHz is a challenging task, especially if the maximum disk recording rate is around 75 Hz. This limitation is on the one hand due to the disk space one event requires, namely 250 KB, and on the other hand due to the fact, that it takes 2 ms to read out all detector components. To overcome this hurdle and optimize the output rate, an elaborate trigger system in several stages is required to extract the relevant physics events and discard the vast majority of less interesting events. At CDF the data acquisition system (DAQ) organizes the triggers in three different levels.

Level 1 In order to reduce the trigger rate from 2.5 MHz to about $(30 - 50)$ kHz, a pure hardware trigger was implemented. Three parallel streams are used and can also be combined for this purpose. The trigger information is based on the energy deposit from the calorimeter towers to identify electrons, photons and jets or variables like missing transverse energy and total energy, on roughly reconstructed two-dimensional tracks found by the extremely fast tracker (XFT) from hits in the COT, and on signatures seen in the muon chambers in combination with matching tracks from the COT. A 42 stage deep pipeline at all front-end electronics with a clock cycle of 132 ns makes a maximal latency of 5.544 μs possible.

Level 2 Taking over the events from the L1 trigger, the L2 trigger proceeds to reduce the event rate further down to $(300 - 350)$ Hz. Also Level 2 is purely implemented via hardware. It is more sophisticated than the L1 trigger and features additional two-dimensional tracking information from the SVX, including impact parameter calculations. Basic clustering in the calorimeters is processed and more strict requirements on the objects already used by the L1 trigger are applied. The latency here is $\sim 20\,\mu$s. In case that the four spots in the buffer are already filled up, no further event can be accepted. This is the so-called 'dead-time'.

Level 3 The information of all accepted L2 events is collected and passed over to the event builder (EVB). These event fragments are assembled there into complete events and are then sent to the L3 processing farm. This farm runs the full offline reconstruction code by reconstructing three-dimensional tracks and makes this information available to the final trigger decision. The process to reconstruct a full event is allowed to take up to one second which makes it already possible to apply some calibrations. The events are then written onto tape which allows for a final event recording rate of 75 Hz.

2.2.6 Cherenkov Luminosity Counter

For the luminosity measurement CDF uses Cherenkov Luminosity Counters (CLC) [ACO01], which measure the average number of inelastic proton-antiproton interactions per bunch crossing, μ. The instantaneous luminosity L is then obtained by using the following formula

$$\mu \cdot f_{\mathrm{bc}} = \sigma_{\mathrm{p\bar{p}}}^{\mathrm{in}} \cdot L \,, \tag{2.2.3}$$

where $\sigma_{\mathrm{p\bar{p}}}^{\mathrm{in}}$ is the inclusive inelastic proton-antiproton cross section at $\sqrt{s} = 1.96\,\mathrm{TeV}$ and f_{bc} the rate of bunch crossings in the Tevatron. Figure 2.2.6 shows a schematic view of the luminosity monitors.

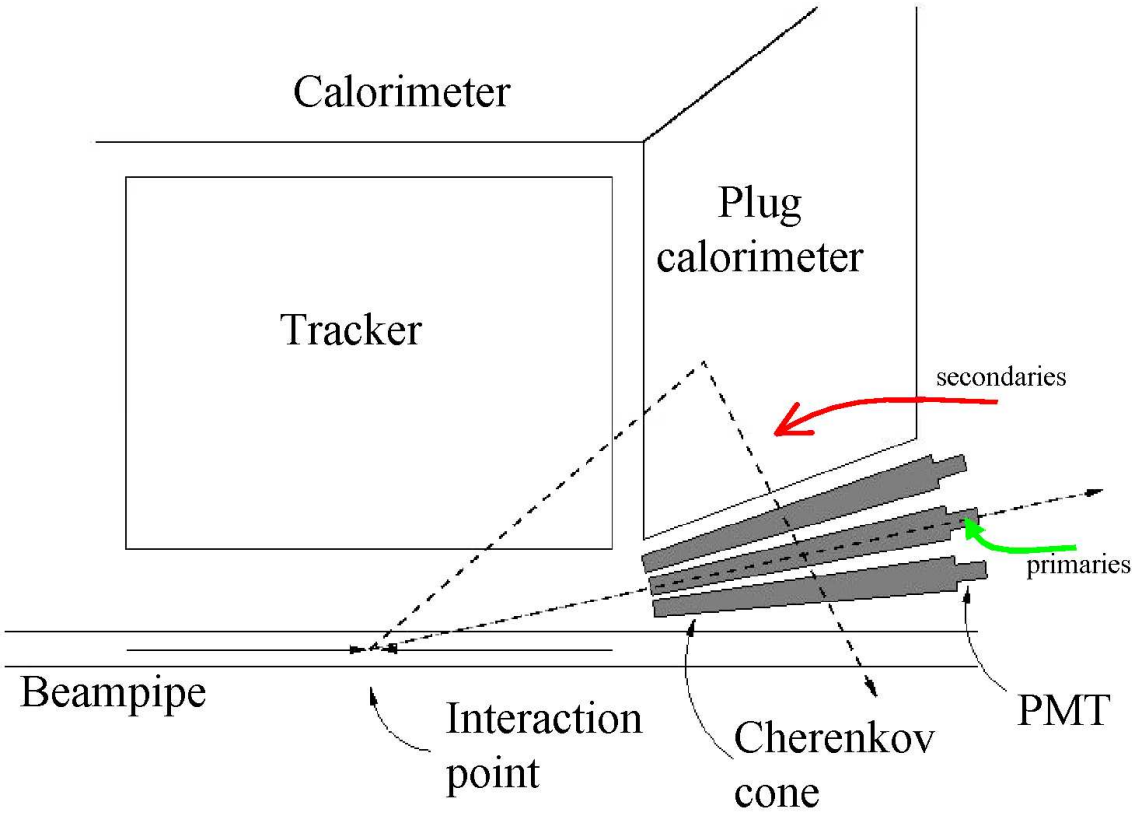

Figure 2.2.6: Parts of the detector and the position of the Cherenkov Luminosity Counter are shown. The CLC is located at large pseudorapidities close to the beam-pipe. Primary and secondary particles traversing the detector are indicated.

The CLC is designed in such a way, that it can measure the average number of inelastic proton-antiproton interactions per bunch within a few percent, since μ is directly proportional to the average number of hits in the luminosity monitors per bunch crossing. There are two CLC modules employed at small angles close to the beam-pipe. In this pseudorapidity region the inelastic cross section is largest. Both modules cover pseudorapidities of $3.75 < |\eta| < 4.75$ on the east and west side, respectively. Pointing towards the interaction point, the luminosity counters are consisting of 48 thin, long, conical and gas-filled Cherenkov counters. Each individual counter is composed of aluminum mylar sheets with a thickness of only 0.1 mm and a diameter of 2 cm to 6 cm. They are arranged in three concentric layers around the beam-pipe. Each layer possesses 16 counters. Whereas the inner layer has counters of 110 cm in length, the two outer ones consist of 180 cm long

source	uncertainty
geometry	$< 3.0\%$
generator	$< 2.0\%$
beam	$< 1.0\%$
$\sigma^{\text{in}}_{\text{P}\bar{\text{P}}}$	4.0%
total	5.8%

Table 2.2.2: Estimate of the systematic uncertainties on the luminosity measurement of the CLC in 2004. [ROS04]

counters. Particles produced in the proton-antiproton interaction, called primary particles, traverse the full length of the counters, which are mounted inside a pressure vessel made of aluminum and filled with isobutan. Exceeding the speed of light in the medium under this condition, these particles generate photons along their way, which are collected and amplified at the end of the counters in photo multiplier tubes (PMT). Secondary particles, particles produced inside the beam-pipe or surrounding material, on the other hand enter the counters in an angle different from the primary particles and lead to a much smaller light yield.

The luminosity is computed via this equation:

$$L = \frac{R_{\text{P}\bar{\text{P}}}}{\epsilon_{\text{CLC}} \cdot \sigma^{\text{in}}_{\text{p}\bar{\text{p}}}} \tag{2.2.4}$$

The rate of the inelastic proton-antiproton events measured by the CLC monitors is denoted as $R_{\text{p}\bar{\text{p}}}$, and ϵ_{CLC} marks the efficiency to detect these events. The two major uncertainty sources of this luminosity measurement are given by the error of the inelastic proton-antiproton cross section and the error of the geometrical acceptance of the CLC counters. The geometrical acceptance enters into the efficiency determination. Table 2.2.2 shows the systematic uncertainties of this measurement.

Chapter 3

The CMS detector at the LHC

The **C**ompact **M**uon **S**olenoid (CMS) detector is a general-purpose detector located 100 m deep underground at the **L**arge **H**adron **C**ollider (LHC) at CERN. The first proton-proton collisions are anticipated for the end of 2007 which will usher in a new era of high-energy physics.

3.1 The LHC

The LHC [LHC94] is currently constructed in the previous Large Electron Positron Collider (LEP) tunnel of 27 km in circumference, where proton-proton collisions will take place at a center of mass energy of $\sqrt{s} = 14\,\text{TeV}$. It is foreseen to start with an initial instantaneous luminosity for the first years of $L \cong 2 \times 10^{33}\,\text{cm}^{-2}\text{s}^{-1}$, referred to as 'low luminosity' run, and then to increase it to the design instantaneous luminosity of $10^{34}\,\text{cm}^{-2}\text{s}^{-1}$, the 'high luminosity' run.

Similar to Fermilab, the protons at CERN are initially accelerated by a Linac, transferred to the Booster and then injected into the Proton Synchrotron (PS). After these three acceleration steps, the protons gained an energy of 26 GeV. In a further step, the Super Proton Synchrotron (SPS) delivers 450 GeV protons to the LHC, which finally brings them up to an energy of 7 TeV. Figure 3.1.1 shows the full accelerator complex at CERN.

Unlike the Tevatron, the LHC collides protons with protons. This decision was made in order to reach the design luminosity, since it is very difficult to produce sufficient antiprotons to achieve this high luminosity regime. At LHC energies, the dominant contribution for many processes is made by gluon interactions and their distribution functions are the same for proton and antiproton. Still, this decision implies some consequences for the design of the accelerator. Whereas at the Tevatron particles and antiparticles can be accelerated in the same beam pipe in opposite direction due to their opposite charge, this is not possible anymore at LHC. To overcome this problem a so-called '2-in-1' magnet was designed, which means that the two different proton beams are circulating in two parallel vacuum tubes embedded in one magnet system. Figure 3.1.2 shows such a LHC dipole. The magnetic field in each tube is of opposite

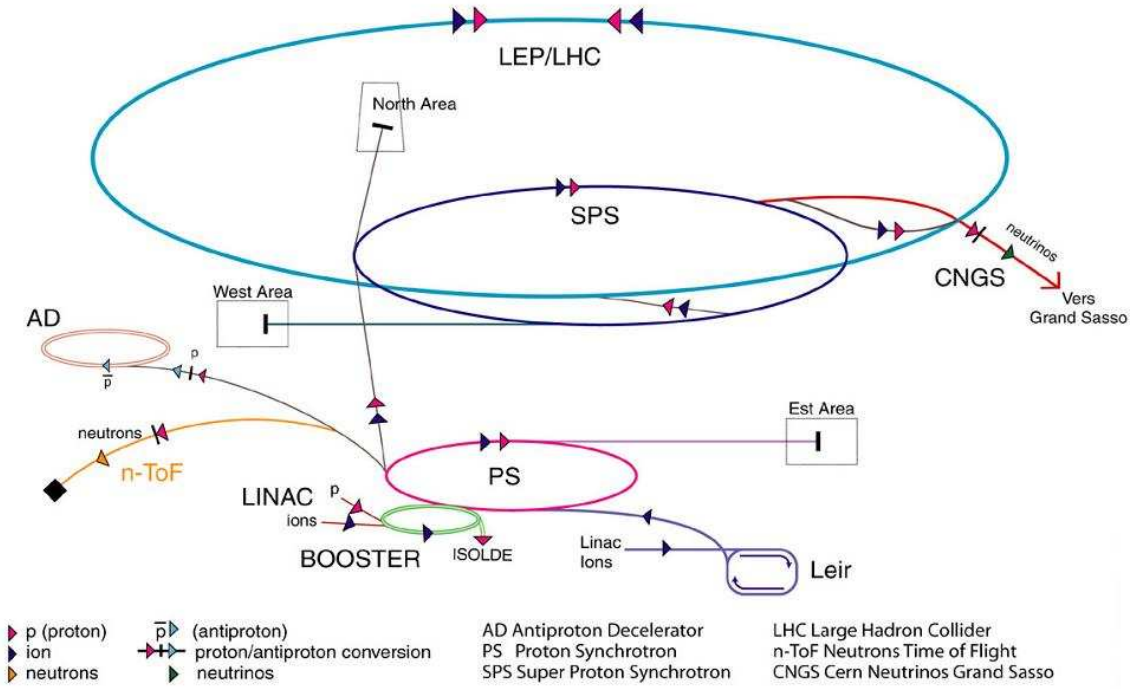

Figure 3.1.1: Schematic view of the complete accelerator chain at CERN - from the Linac to the LHC. Other accelerator parts are also shown.

direction to bend the respective particles in the right direction. 1232 of these main dipoles will be installed around the LEP tunnel and about 400 quadrupoles to keep the particles trajectories close to each other and along the predefined direction of the beam pipe. With a radius of 4.3 km and a given energy of 7 TeV, the necessary magnetic field is calculated to be about 8.3 TeV to keep the protons on this constant radius. Such a high field strength requires superconductive dipole magnets, which are hence cooled down to very low temperatures. The cryogenic system uses super-fluid helium at temperatures of 1.9 K .

At nominal beam conditions, there will be 2835 bunches, each consisting of about 10^{11} protons. The acceleration is provided by sixteen 400 MHz radio-frequency cavities assembled around the ring in four modules. Every 25 ns the beams are brought to collision, which can be done at the four interaction points, namely at the location of the four different experiments. Figure 3.1.3 shows the geographical position of these detectors.

ATLAS (A Toroidal LHC ApparatuS) and CMS (Compact Muon Solenoid) are multi-purpose detectors. Their main focus will be the discovery of the expected Higgs particle and generally new phenomena at high masses. LHCb is a detector dedicated to a large variety of b(ottom)-physics, especially CP-violation. Finally, ALICE (A

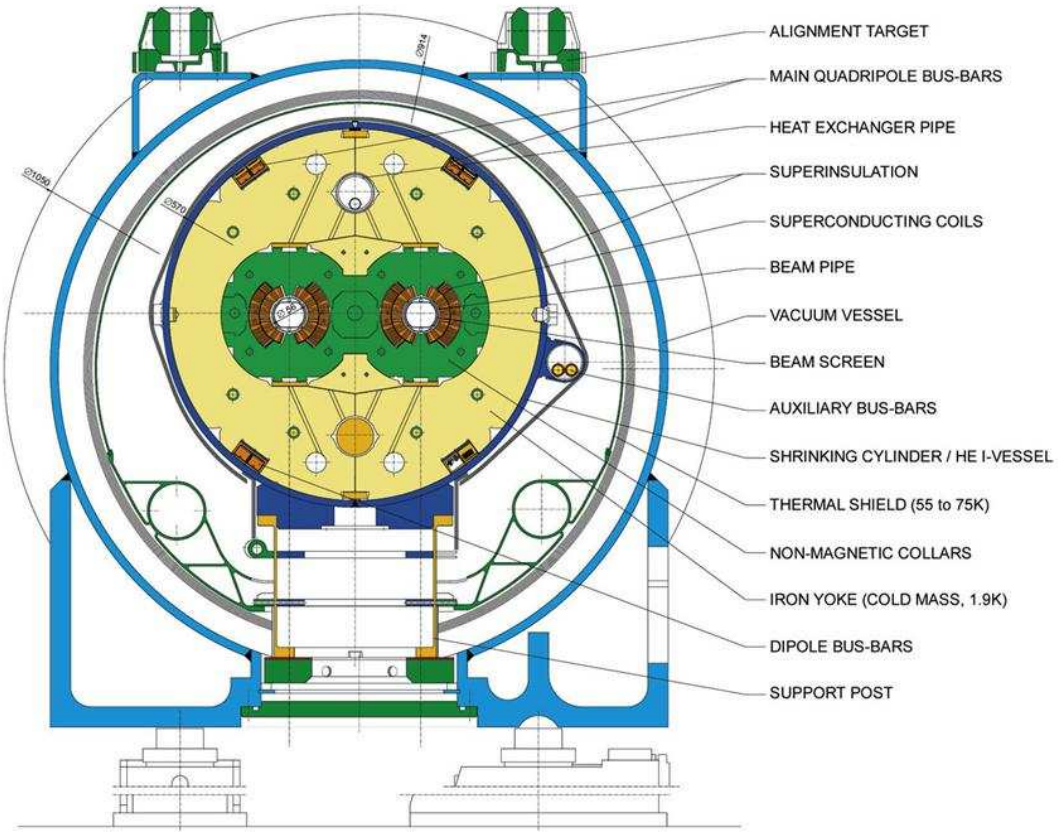

Figure 3.1.2: Cross section of a standard LHC dipole.

Large Ion Collider Experiment) will study heavy ion collisions. For this purpose, dedicated runs with lead-nuclei at a center of mass energy of 5.4 TeV will be pursued at the LHC.

3.2 The CMS detector

The structure and the components of the CDF and CMS detectors are similar to each other. However, the emphasis of the CMS detector is, as the name already suggests, a compact design with a good muon system and a strong magnetic field. Besides, the excellent electromagnetic calorimeter marks the cornerstone of the detector. A detailed description can be found in ref. [CMS94]. A schematic view of the complete detector is depicted in Figure 3.2.1.

Even though the word 'compact' enters into the name of CMS, the detector measures a length of 21.6 m with a diameter of 15 m and a total weight of 12000 tons. Indeed, the main share of weight arises from the return yoke of the magnet, which is made out of iron. It also serves structural purposes and supports all other components.

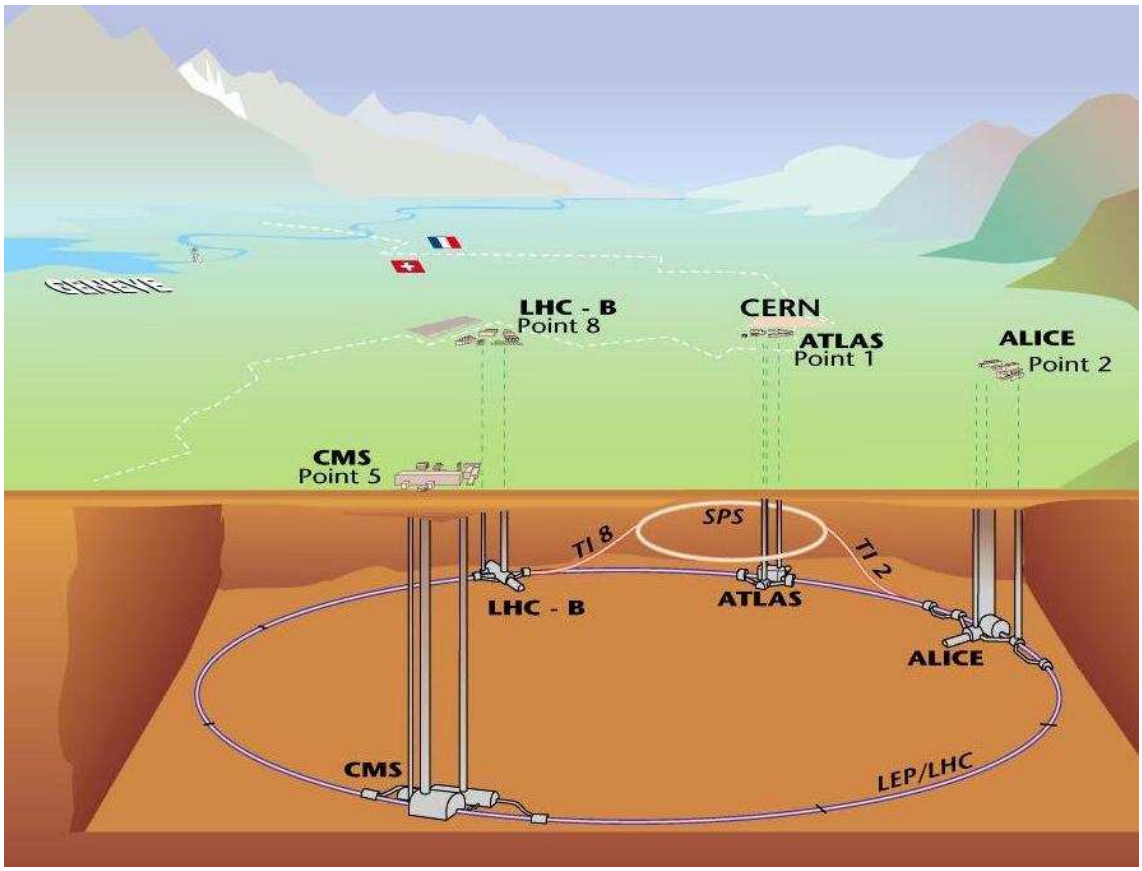

Figure 3.1.3: The four experiments at LHC. The LHC tunnel lies at a depth varying between 50 and 150 meters.

CMS is mechanically sub-divided into three major parts, namely into a barrel and two endcaps located on both ends of the barrel structure. The barrel covers the region of $0 \lesssim |\eta| \lesssim 1.5$ and the endcaps range from $1.5 \lesssim |\eta| \lesssim 3.0$. Figure 3.2.2 shows the longitudinal view of CMS. The barrel part is arranged coaxial to the beam pipe in cylindrical shape. The endcap components are perpendicular to the beam pipe.

3.2.1 The CMS Tracker

When LHC will run at nominal luminosity, about 20 collisions per bunch crossing are expected to produce approximately 1000 charged particles in the acceptance of the tracking detector ("tracker"). This is extremely challenging, especially for the sub-detectors closest to the beam pipe. Therefore, the tracker has to be very radiation hard as well as to offer high granularity. A combination of pixel layers and silicon micro-strip layers was chosen [TRA98].

Pixel Detector Closest to the beam pipe are the three barrel layers of the pixel detector at an average distance of 4.4 cm, 7.3 cm and 10.2 cm. They stretch 53 cm

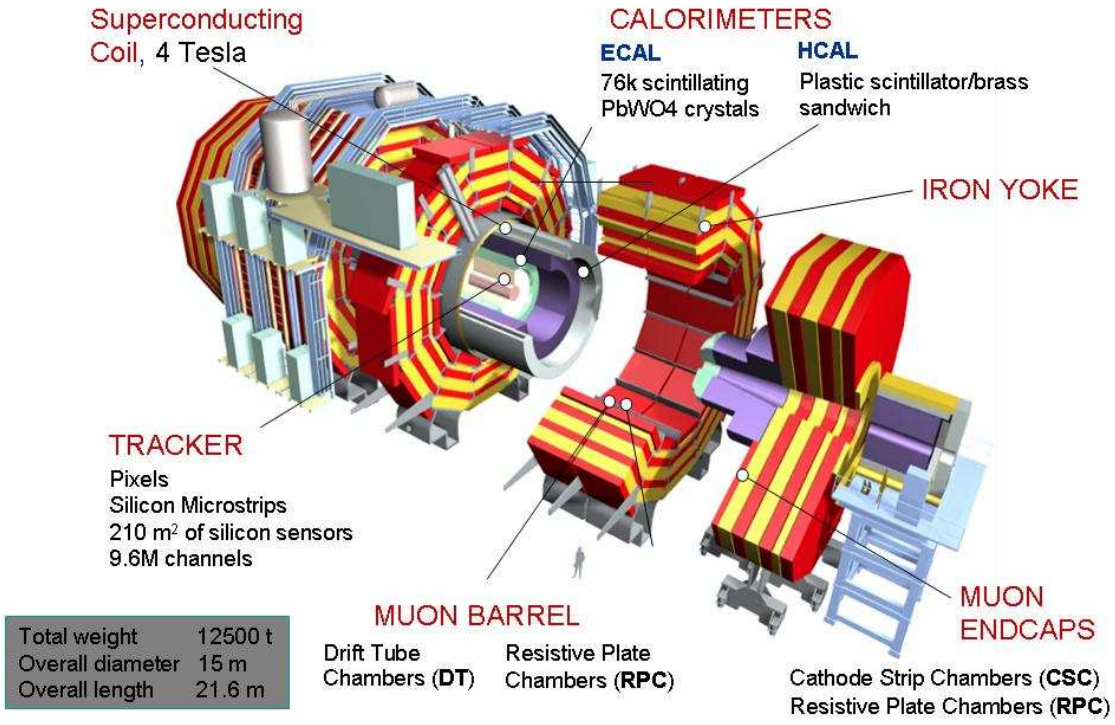

Figure 3.2.1: The CMS detector with all its sub-components is displayed in this drawing.

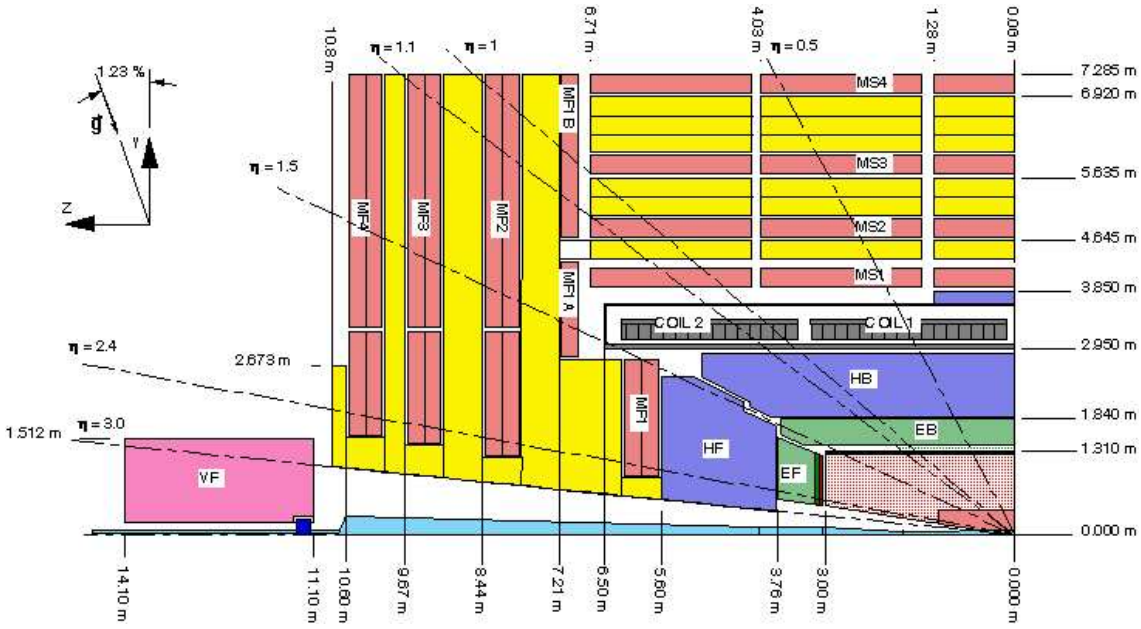

Figure 3.2.2: A sketch of one quarter of the CMS detector.

in length. Perpendicular to them, two pixel disks on each side will be positioned at $z = 34.5\,\text{cm}$ and $z = 46.5\,\text{cm}$. Each disk ranges from 6.0 cm to 15.0 cm in diameter. Figure 3.2.3 shows a three-dimensional view of the pixel detector.

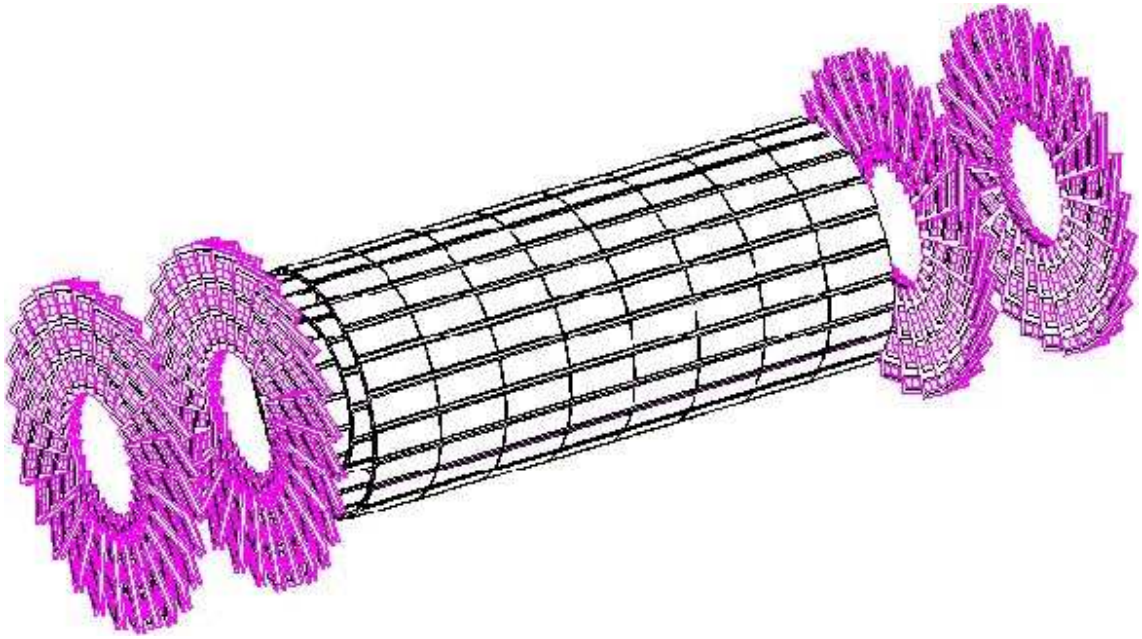

Figure 3.2.3: The CMS pixel detector (barrel and endcaps).

Each sensor of the pixel detector consists of a 52×53 array of $150 \times 150\,\mu\text{m}^2$ pixels. There are about 16000 of these sensors implemented, adding up to approximately 44 million readout channels. A hit resolution of $\sim 10\,\mu$m in the rϕ-plane and of $\sim 17\,\mu$m in the rz-plane is expected. All electronics close to the interaction point are fabricated in radiation hard quarter micron CMOS technology.

Silicon Micro-Strip Detector The outer part of the tracker is sub-divided into four parts. The Tracker Inner Barrel (TIB), consisting of the four innermost layers, and the Tracker Outer Barrel (TOB), comprising the six remaining outermost layers in the barrel region. In the endcap, there are three smaller disks, the Tracker Inner Disks (TID) and nine larger disks sub-divided into seven rings each, called the Tracker End-Cap (TEC). Figure 3.2.4 illustrates one quarter of this detector system.

These tracker components cover a volume from 20cm to 120cm in radius and -280cm to $+280\,$cm in the z-coordinate. Efficient tracking is therefore possible up to pseudo-rapidities of $|\eta| = 2.5$. Two of the four layers in the TIB are double-sided and the silicon micro-strips are tilted by 100 mrad with respect to the z-direction in order to obtain also spatial information in this coordinate. The other layers are parallel to the beam axis and provide resolution in the rϕ-plane. In the TOB, three out of six layers are double-sided in the same way as in the TIB. The strip pitch here ranges from 60 μm up to 270 μm in the TIB and from 140 μm to 210 μm in the TOB. Also the strip length is increased from 7 cm and 12.5 cm to 21 cm.

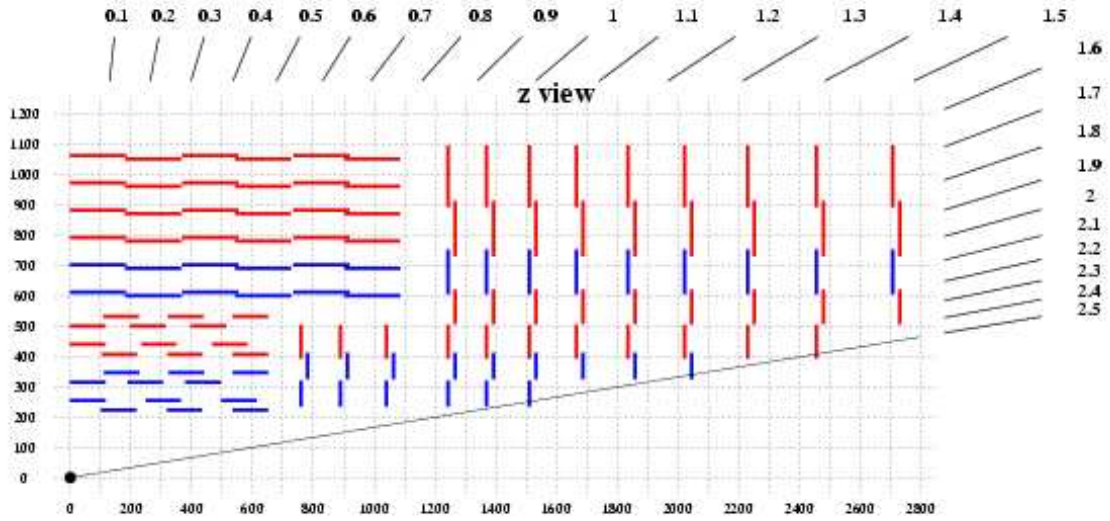

Figure 3.2.4: Layout of the Silicon Micro-Strip Detector.

TID and TEC consist of identical sensors and are just distinguished by the size of the disks. All sensors feature a wedge-structure. Three rings of the TEC are again stereo detectors and provide coordinate information in r and ϕ, the single-sided disks only in ϕ. A hit resolution of 10 μm to 60 μm in the rϕ-plane is achieved and 500 μm in the rz-plane. The momentum resolution in the region $|\eta| < 1.6$ is estimated to be $\delta p_{\mathrm{T}}/p_{\mathrm{T}}^2 = 0.015\,\%$ and degrades at $1.6 < |\eta| < 2.5$ to $\delta p_{\mathrm{T}}/p_{\mathrm{T}}^2 = 0.06\,\%$.

3.2.2 The Electromagnetic Calorimeter

The Electromagnetic Calorimeter (ECAL) [ECA97] is placed around the tracking detectors. It is made out of $\sim$ 76000 lead tungstate ($PbWO_4$) crystals and divided in a barrel and an endcap part. The crystals in the barrel (61200) measure 2.2 cm $\times$ 2.2 cm $\times$ 23 cm, in the endcap the dimensions are 2.5 cm $\times$ 2.5 cm $\times$ 22 cm. This corresponds for the barrel to a granularity in $\Delta\phi \times \Delta\eta$ of 0.0175 $\times$ 0.0175. Lead tungstate crystals were chosen since they offer the best properties for a precision electromagnetic calorimeter at the harsh radiation environment at LHC. With a high density of 8.2 g/cm^3, lead tungstate exhibits a short radiation length of only $X_0 = 0.89$cm and a small Moliere radius of R_{M}[1] $= 2.19$cm. This means the length of the crystals corresponds to 26 radiation lengths. Moreover, the scintillating process is fast. Within 15 ns, 60 % of the light is emitted, within 20 ns already 85 %. In addition, the material of the crystals possesses good radiation hardness properties. However, a drawback is the low light yield of only $\sim (5 - 10)$ photo-electrons per incident MeV. This requires amplification within the photodetector at the end of

[1]The Moliere Radius is a characteristic constant of the material and describes the lateral electromagnetic shower shape. Within a cone of 1 R_{M}, 90 % of the shower's energy is contained

the crystal. Two avalanche photo-diodes (APD's) per barrel crystal are used to collect and amplify the light signal. For the endcap crystals, one vacuum photo-triode (VPT) per crystal undertakes the photon collection since the higher irradiation in this region makes the use of photo-diodes impossible.

The light yield sensitivity to the temperature fluctuations for the $PbWO_4$ crystals amounts to $\frac{1}{LY}\frac{dLY}{dT} = -1.9\,\%/°C$, where LY indicates the light yield and T the temperature. Also the gain, G, of the APD's is temperature dependent. The temperature coefficient defined as $\frac{1}{G}\frac{dG}{dT}$ gives $-2.4\,\%/°C$. This requires a cooling system to stabilize the temperature at ± 0.1 degrees at an operating temperature of 18 degrees. Figure 3.2.5 shows the temperature dependence of the light yield and the APD gain.

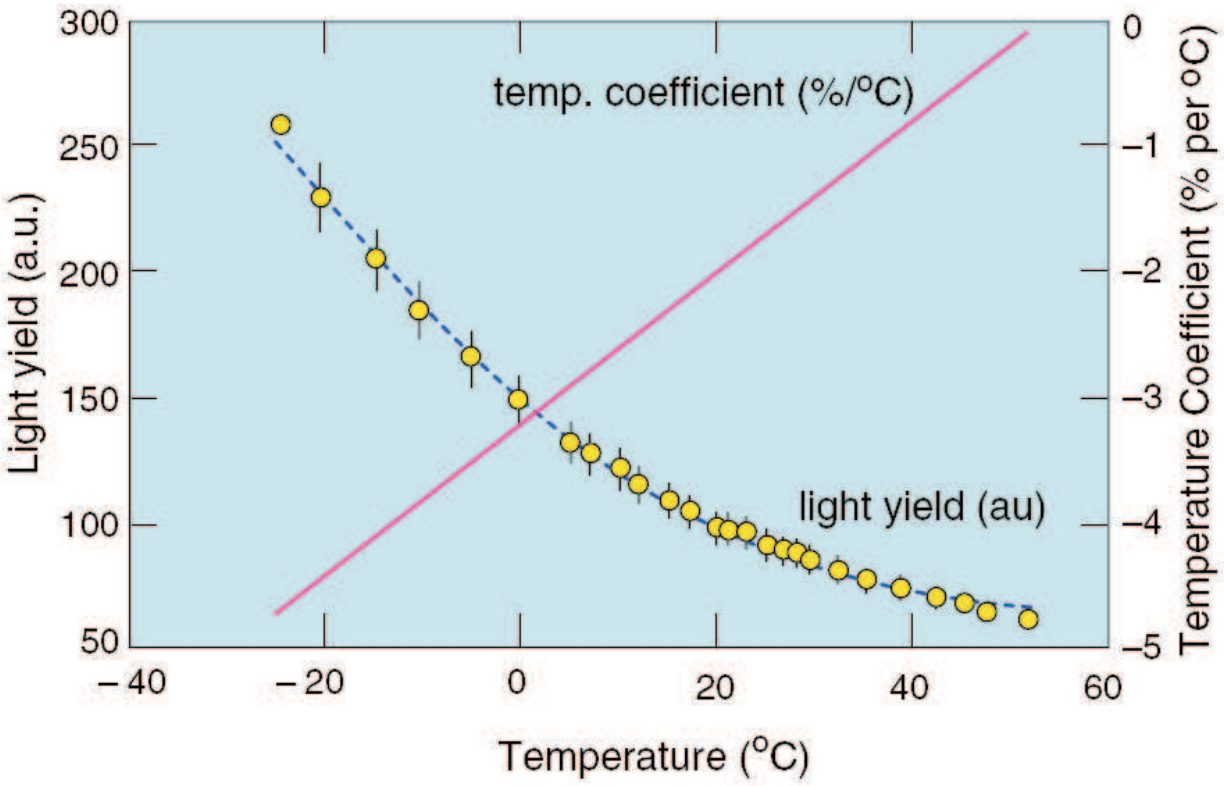

Figure 3.2.5: The light yield temperature dependence for the crystals and the temperature coefficient for the APD's are shown.

In the barrel detector, the ECAL is divided into super-modules, modules and sub-modules. One sub-module consists of 2×5 crystals, where the single crystals are supported by a fiberglass alveolar structure. A module is formed by assembling 40 or 50 of these sub-modules together. Consequently, a module consists of 400 or 500 crystals. Four of these modules are then again arranged together forming a super-module with 1700 crystals. In total, there are 36 super-modules. Figure 3.2.6 depicts the barrel ECAL structure.

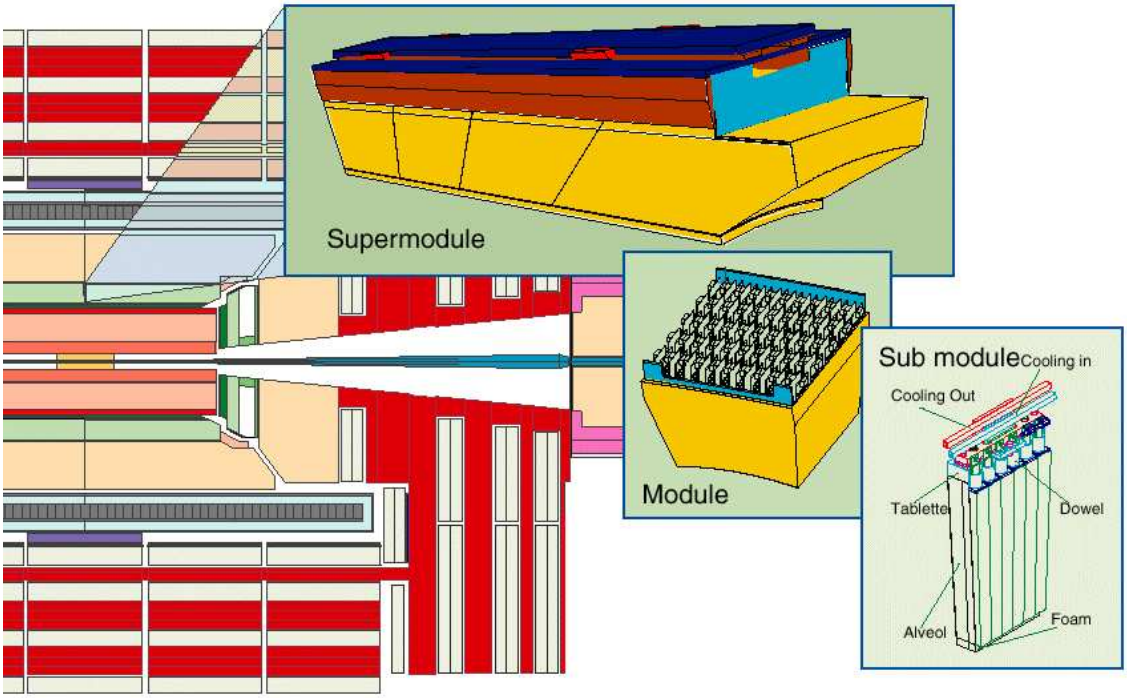

Figure 3.2.6: The arrangement of the CMS ECAL sub-modules, modules and super-modules.

All the crystals are tilted by 3 degrees in the transverse plane, such that their axes make an angle of 3 degrees with a line from the nominal vertex point. This tilt minimizes the probability that particles pass through the inactive area between crystals and is achieved by using 17 different crystal shapes. In addition, the crystals are also tilted in the η-direction by 3 degrees for the same reason. Within a sub-module a maximum distance of 0.4 mm between the crystals is achieved and between the sub-modules a distance of 0.6 mm. Across the modules a gap between 6.8 mm and 7.8 mm is estimated and from one super-module to the next one a gap of about 6 mm is expected. The endcap crystals are arranged in 5 by 5 towers. Also these crystals are positioned in a way, that a particle unlikely traverses the inactive material between the crystals. Their center points 1.3 cm away from the interaction point and thus orientates the crystals similarly to the ones in the barrel ECAL. Figure 3.2.7 shows an artistic view of the ECAL endcap.

The energy resolution can be parametrized as a function of the energy as

$$\frac{\sigma_{\mathrm{E}}}{E} = \frac{a}{\sqrt{E}} \oplus b \oplus \frac{c}{E}\,, \tag{3.2.1}$$

where a is the so-called *stochastic* term, which takes into account the statistical fluctuations of the shower and the detector response. The *constant* term b arises from non-uniformities as well as calibration pecision and energy leakage of the crystals, and c represents the *noise* term, which contributes as a result of electronics noise

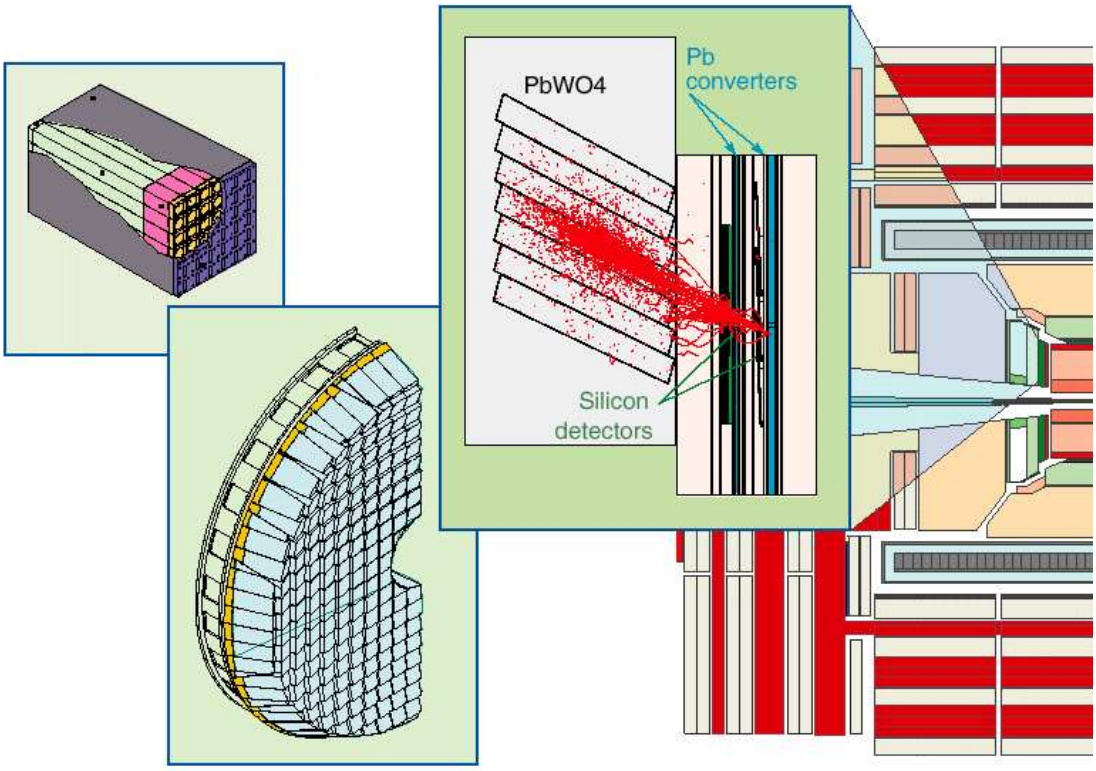

Figure 3.2.7: Artistic view of the endcap ECAL. The preshower detector is also indicated.

and pile-up events. It is aimed to reach for a stochastic term of $a = 2.7\,\%$ (barrel) and $a = 5.7\,\%$ (endcap), for a constant term of $b = 0.55\,\%$ and for a noise term of $c = 210\,\text{MeV}$ (barrel) and $c = 245\,\text{MeV}$ (endcap) at high luminosities. Current test beam data for a matrix of 3×3 barrel crystals measure for the stochastic term $a = 2.83\,\% \pm 0.3\,\%$, for the constant term $b = 0.26\,\% \pm 0.04\,\%$ and for the noise term $c = 124\,\text{MeV}$ [ZAB05], as can be seen in Figure 3.2.8. In 2004, the data was taken at a series of beam momenta corresponding to the energies of 20, 30, 50, 80, 120, 180 and 250 GeV. The energy resolution as a function of the energy is extracted by fitting it using the Equation 3.2.1.

In front of the endcap calorimeter the preshower detector is located. It consists of two alternating layers of lead and silicon micro-strip sensors. The lead layers feature a thickness of one and two radiation lengths, respectively. The silicon micro-strip detectors in between consist of a plane of orthogonal orientated strips. With this setup it is possible to better distinguish between two photons from neutral pions and single photons by measuring their lateral shower shape. Also the isolation of particles can be improved with this detector element. For example, the photons from a π^0 with an energy of 50 GeV are expected to be measured with an accuracy of about 300 μm or 0.1 mrad. Assuming the pion decays into two photons close to the interaction point, their opening angle is around 2 mrad.

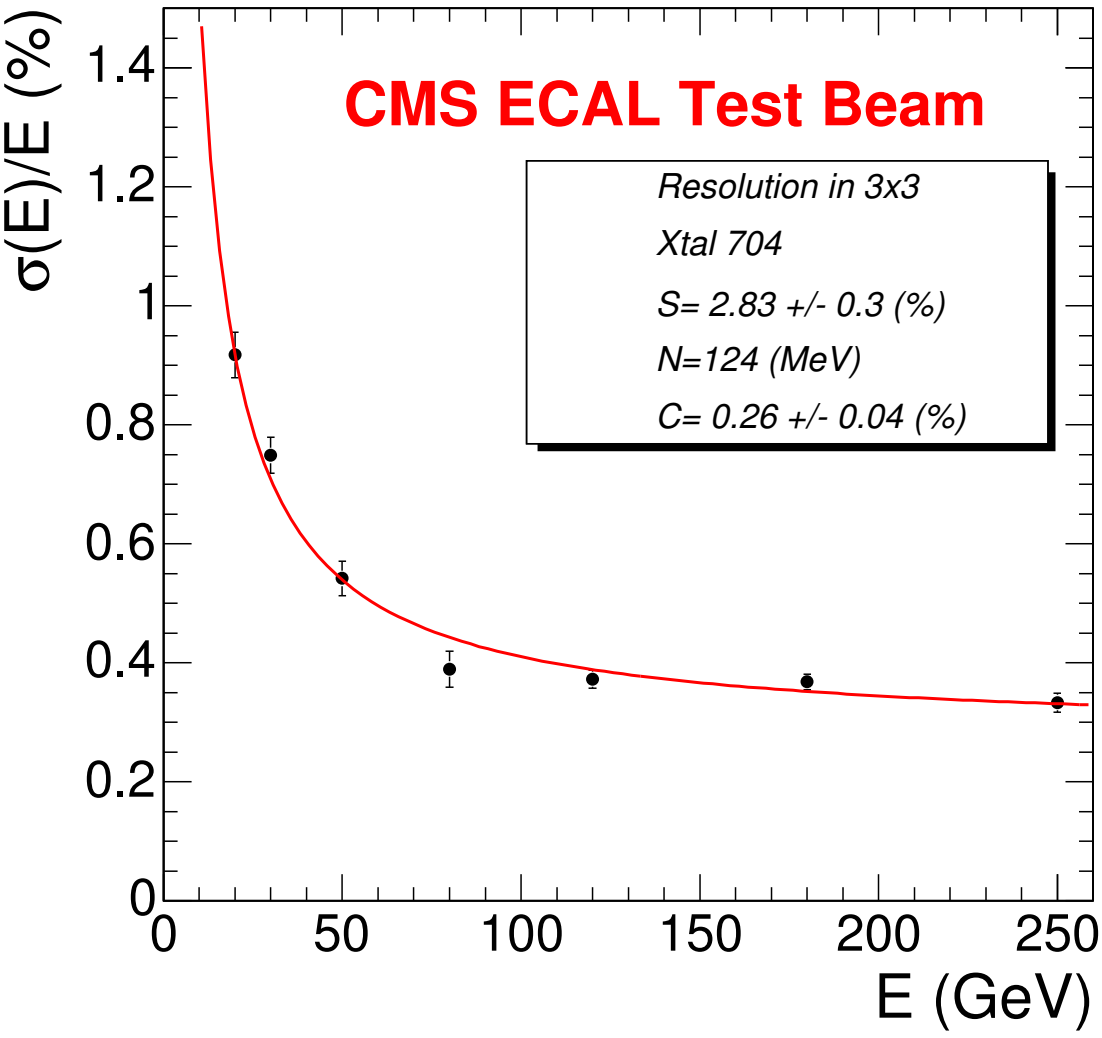

Figure 3.2.8: The energy resolution as a function of the reconstructed energy in a 3×3 crystal matrix, centered on crystal number 704.

3.2.3 The Hadronic Calorimeter

The electromagnetic calorimeter is enclosed by the hadronic calorimeter (HCAL) [HCA97], which is again sub-divided into a barrel detector (HB) and two endcap hadronic calorimeters (HE). Together they cover a pseudorapidity region of $|\eta| < 3.0$. The diameter of the barrel part ranges from 2 m to 3 m over a length of 9 m. This corresponds to a pseudorapidity of $|\eta| < 1.48$. The region $1.48 < |\eta| < 3.0$ is covered by the two HE. The two endcap wheels of the HCAL measure 40 cm at the inner radius and 3 m at the outer radius. Figure 3.2.9 presents the side view of one quarter of the HCAL detector.

There is also a very forward hadronic calorimeter (VF) on each side of the endcaps, 11 m away from the interaction point. With its size of 12.5 cm inner radius and 1.5 m

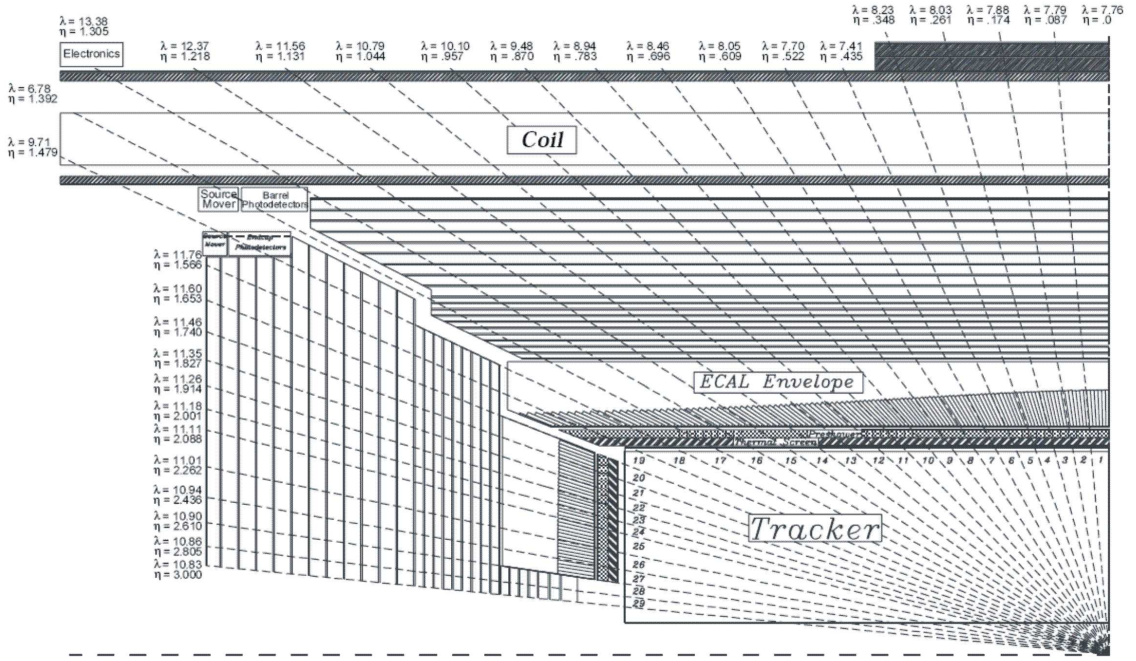

Figure 3.2.9: Sketch of one quarter of the CMS detector. The HCAL is located in between the magnetic coil and the ECAL and reaches up to rapidities of $|\eta| = 3$.

outer radius it covers a pseudorapidity region of $3.0 < |\eta| < 5.0$. This coverage up to high pseudorapidities provides a good measurement of missing energy.

The HCAL in the barrel and endcap region consists of brass absorber plates interleaved with wavelength shifting plastic scintillator tiles. A high granularity of the tiles ensures that even strongly boosted di-jet events can still be separated. An energy resolution of about

$$\frac{\sigma_{\mathrm{E}}}{E} = \frac{120\,\%}{\sqrt{E}} \oplus 5\,\% \tag{3.2.2}$$

is achieved. In the very forward region the calorimeter (VF) is made out of quartz fibers as active elements embedded in a steel absorber matrix. Quartz is more radiation hard than plastic which becomes more important at large pseudorapidities.

In the pseudorapidity region $|\eta| < 2$, a granularity of $\Delta\eta \times \Delta\phi = 0.087 \times 0.087$ has been realized in order to match the trigger granularity of the ECAL and the muon chambers. The thickness of the HB in nuclear interaction lengths is too low for a full shower containment. To monitor possible resulting energy losses, the hadron outer calorimeter (HO) is installed beyond the solenoid magnet coil in the pseudorapidity region of $|\eta| < 1.4$. It just consists of one single scintillator layer and uses the coil and the first muon absorber plate as additional absorbers.

3.2.4 The Superconducting Magnet

The superconducting solenoid magnet [CMS97] extends 13 m in length with an inner diameter of 5.9 m. A field of 4 T is created by a 20000 A current and extends around the whole tracking and calorimetric system. Its strong magnetic field enables a good track momentum measurement of charged particles, since the resolution of the track momentum is inversely proportional to the magnetic field strength. The magnetic flux is returned by the return yoke. This is a ~ 1.8 m thick and ~ 9 m long saturated iron yoke, which contains the muon chambers and serves structural purposes. The field here amounts to 2 T and provides also track momentum measurements for the muon candidates traversing the iron. Muons can be efficiently detected up to $|\eta| < 2.4$. Figure 3.2.10 shows, among other particles, a muon bent due to the magnetic field.

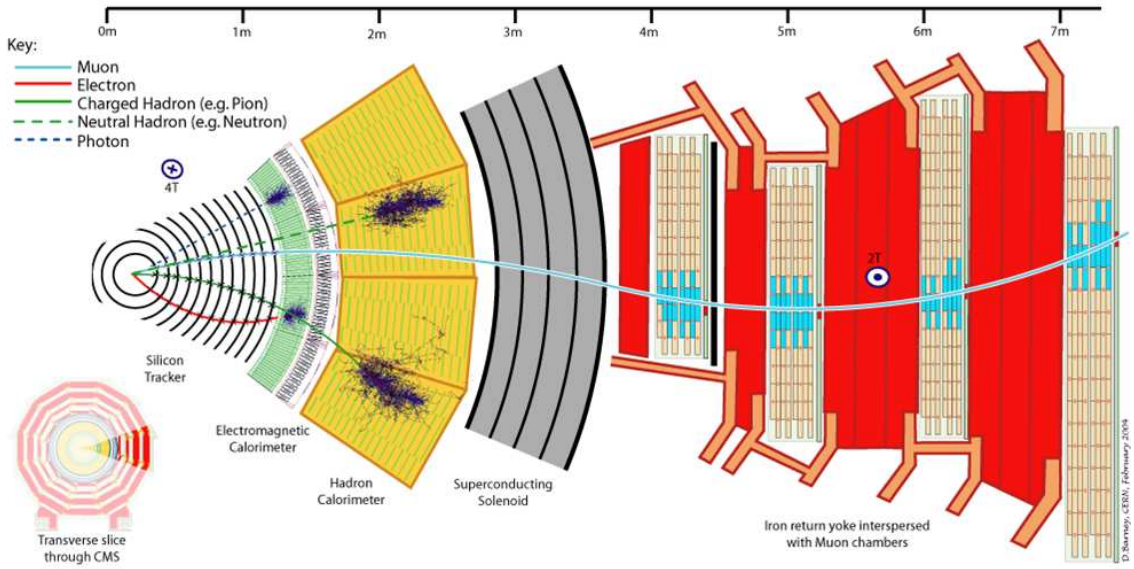

Figure 3.2.10: Transverse slice through the CMS detector. Different charged particles are indicated which follow bent trajectories due to the magnetic field.

3.2.5 The Muon System

The muon system forms the outermost part of the CMS detector, consisting of three different types of muon detectors [MUO97]. All are incorporated into the return yoke of the magnet. Muons are, owing to their long lifetime and due to the fact that they emit only little bremsstrahlung, one of the cleanest measurable objects in the detector. Therefore, the muon chambers are installed to identify muons, to measure the muon momentum and to trigger on events which contain muons.

Drift Tubes (DT's) and Resistive Plate Chambers (RPC's) are used in the muon barrel region, which is defined by $|\eta| < 1.2$. In the endcap region ($0.9 < |\eta| < 2.4$)

the muons are detected with RPC's and in addition with cathode strip chambers (CSC's). The spatial resolution of the resistive plate chambers is lower compared to the DT's and CSC's, but they provide a good time resolution of 2 ns to 3 ns and thus are used to trigger on muons. Figure 3.2.11 shows a longitudinal view of the muon system.

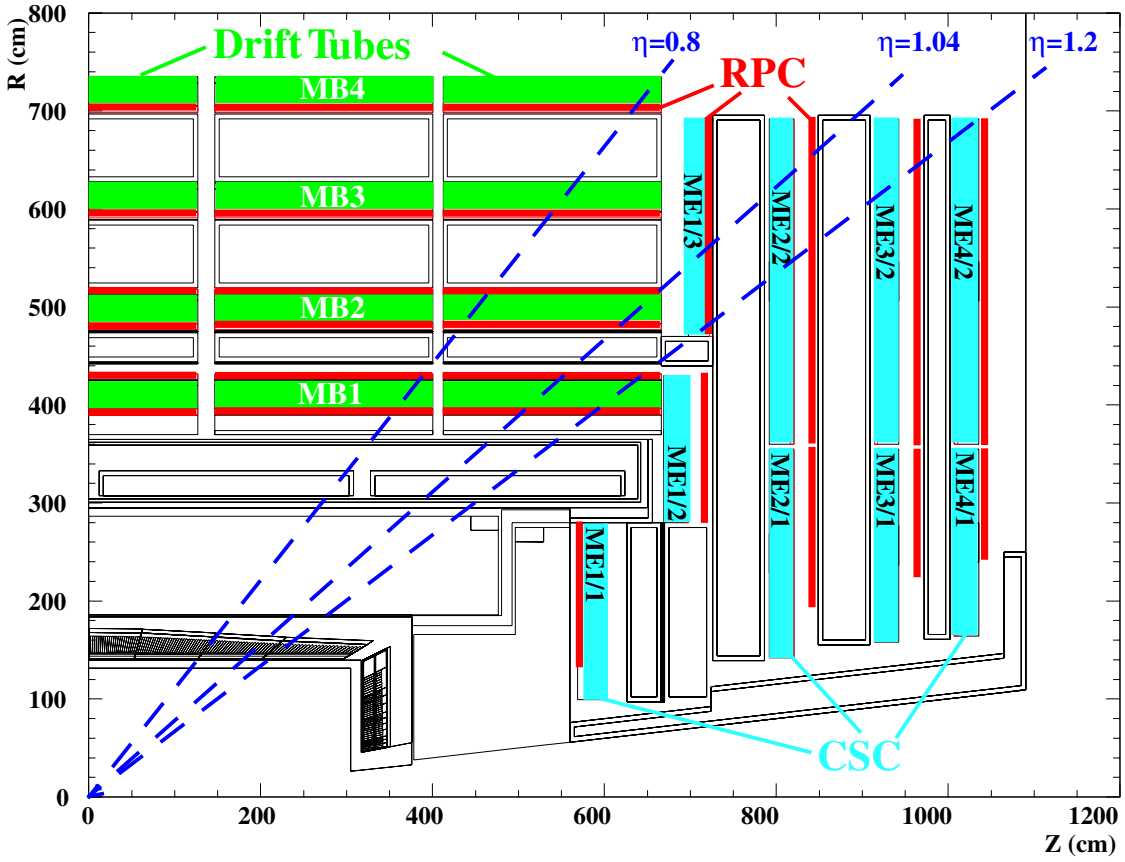

Figure 3.2.11: Longitudinal view of one quarter of the CMS muon system.

Drift Tubes Installed only in the barrel region, the DT's are able to deliver precise track information in the pseudorapidity region $|\eta| < 1.3$. Relatively low particle rates of less than $10\,\mathrm{cm}^{-2}\mathrm{s}^{-1}$ and the low magnetic field (the magnetic flux is largely contained inside the iron yoke) make the drift tube technology applicable in this region. A single drift tube consists of aluminum cathodes, which are 1.2 mm thick and 9.6 mm long. A wire of stainless steel in the center of the tube acts as an anode. The drift tube measures a volume of 1 cm × 4 cm × 2 m and is filled with an Ar-CO_2 mixture. Twelve layers of these drift tubes compose one superlayer and three of these superlayers are then integrated into one barrel muon chamber. In two of the superlayers the wires are oriented in z-direction and thus measure the ϕ-coordinate. The remaining superlayer is rotated by 90°, such that information about the z-coordinate is also available. The innermost barrel modules stretch about 2.5 m in z, 2 m in r/ϕ

and are approximately 0.4 m thick. The size in r/ϕ increases towards the outermost layer up to 4 m. In total about 250 of these modules are employed in the barrel muon system. An angular resolution in the transverse plane of $\sim$ 1 mrad should be possible.

Resistive Plate Chambers As already mentioned before, the RPC's are installed in the barrel region as well as in the endcaps. In the barrel region, they are attached on both sides of the drift tube chambers for the two innermost muon stations, and one RPC is attached to the inner side for each of the two outermost muon stations. In the endcap region, the resistive plate chambers are attached to the inner side of the CSC's up to pseudorapidities of $|\eta| = 2.1$. The RPC itself is composed of two parallel plates with a small gap, in the order of millimeters, filled with gas. The plates are made up of phenolic resin with a high bulk resistivity and are coated with a thin layer of conductive graphite paint, which serves as the electrodes. A muon passing the RPC leaves ionization electrons in the gas which are drifting towards the anode and are amplified with an electric field. The drift of electrons towards the anode induces then a fast signal (charge) on the other electrode. Since the RPC's give a fast time response and are highly segmented, they are well suited for the bunch crossing of only 25 ns at LHC and thus serve trigger purposes.

Cathode Strip Chambers Besides the RPC's, the cathode strip chambers are employed in the endcaps. CSC's are chosen, since they are better suited to cope with a higher and more inhomogeneous magnetic field and higher particle rates compared to the barrel. The cathode strip chambers are multi wire proportional chambers (MWPC's) with a cathode strip readout. The anode is a gold-plated wire parallel to the cathode plane and perpendicular to the strips. The anode-cathode spacing is equal to the anode wire pitch. A complete cathode strip chamber is of trapezoidal shape, with the cathode strips running radially outwards from the beam line and the anode wires run azimuthally. Each chamber features six layers of strips and wires and is filled with a gas mixture of Ar-CO_2-CF_4. The largest chambers are 3.4 m long and on average 1.5 m wide. In total, there are 500 chambers in the two endcap muon modules with more than two million anode wires.

3.2.6 The Trigger System

At LHC, on average 20 interactions per bunch crossing are expected every 25 ns for a design luminosity of $10^{34}\,\mathrm{cm}^{-2}\,\mathrm{s}^{-1}$. This makes almost one billion interactions per second. Moreover, CMS possesses almost one hundred million detector channels. Estimating an event size of about 1 MB, this would lead to a data stream of 1 PB per second. Evidently, neither storage nor data handling of such an amount of data is feasible or meaningful. Since anyway most of the events are background events, it is the challenging task of the trigger system to preselect only the relevant events and reject at first stage already the huge amount of dispensable events which are of no purpose for physics analyses. A reduction factor of $\sim 10^7$ is required to achieve a final trigger rate of $\sim$ 100 Hz or $\sim$ 100 MB/s. This is the maximum rate the data

acquisition (DAQ) can cope with [TRI00]. Overall, the trigger rate is decreased by passing through three levels.

Level-1 Trigger (L1) Purely hardware-based, the Level-1 trigger is fast and allows for the first rough estimation of relevant events. To be able to keep up with the high frequency of the bunch crossings, it can only master a small fraction of data available. Rough information from the pattern recognition of the muon chambers and coarse energy measurements from the calorimeters are used to define the first candidate events. In more detail, the four most energetic objects for each of the following candidates are investigated. - Muons, isolated electrons/photons, non-isolated electrons/photons, central jets, forward jets and specific τ-jets. To achieve an output L1 trigger rate of not more than 100 kHz in the high luminosity regime and 50 kHz in the low luminosity regime, threshold cuts are applied for example on the transverse momentum and the isolation. After 3.2 μs, it is decided whether the event passes the Level-1 trigger or is rejected. This time includes the information transfer back and forth from the front-end electronics and the L1 processing elements. Actually, there is only about 1 μs to process the data. While waiting for the decision, the complete detector information for each event is stored in a pipeline. If required, this information is read out and passed on to the next level.

Level-2 Trigger (L2) From Level-2 on, the trigger decisions are made by a processor farm with standard CPU's. This makes a more elaborate trigger decision possible. On average, the L2 obtains an event every 10 μs and thus enables a fast physics selection algorithm to combine more accurate position knowledge with a more precise energy measurement. In addition, primary tracking information from the pixel detectors is taken into account (Level-2.5). A rate reduction factor of 10 is accomplished that way.

Level-3 Trigger (L3) The final step of the trigger decision utilizes full event reconstruction. Level-2 together with Level-3 are also called High Level Trigger (HLT). The entire information of the full tracker is available and thus enables to acquire the fully reconstructed physics event. This decreases the output rate of L3 compared to the input rate by a factor of 100. Consequently, the final required output rate of 100 Hz is obtained.

Chapter 4

Theory of Z and W production at hadron colliders

Z and W boson production in $p\bar{p}$ collisions at the Tevatron and in pp collisions at the LHC occur through the Drell-Yan process [DYA70]. Figure 4.0.1 shows the leading order Feynman diagram for this process.

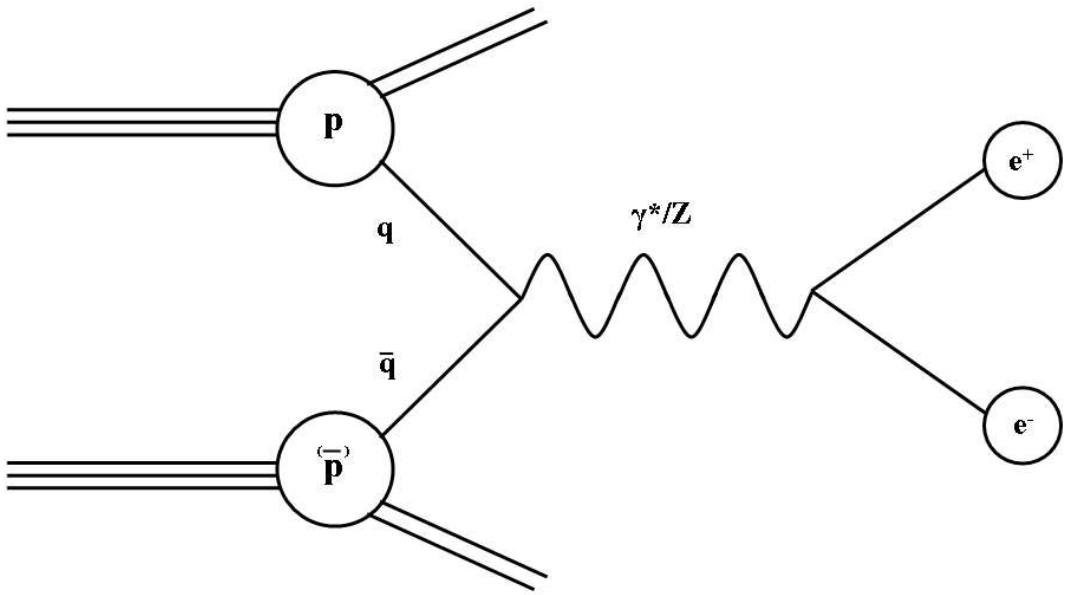

Figure 4.0.1: Leading order Feynman diagram for Drell-Yan electron pair production.

Some next-to-leading order (NLO) diagrams are presented in Figure 4.0.2.

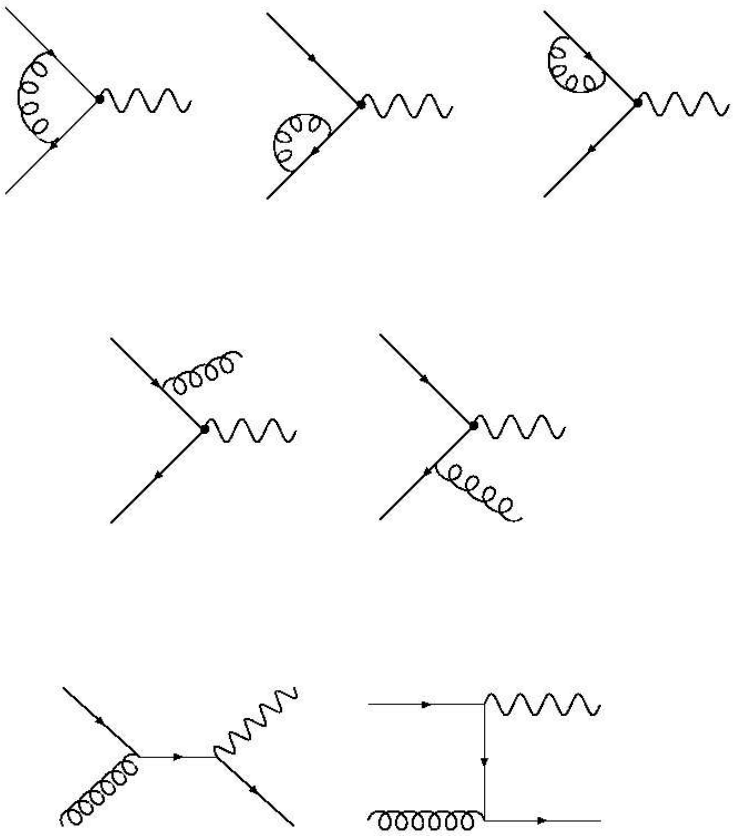

Figure 4.0.2: Next-to-leading order (NLO) contributions for Drell-Yan electron pair production. The electron pair from the γ^*/Z decay is not shown here.

Both, γ^* and Z exchange contribute to lepton pair production and the interference term of both has to be taken into account as well. However, in this thesis events close to the Z pole are investigated and therefore the Z exchange is the dominant process. The diagrams for the Drell-Yan W production process with a subsequent decay to lepton and neutrino look similar. - There is a quark and an antiquark, both of different flavor, in the initial state, the γ^*/Z has to be replaced by a W and one electron by a neutrino.

At energies of the Tevatron or of the LHC, the squared momentum transfer Q^2 of the process can be very high, such that the partons of the protons and antiprotons can be considered as asymptotically free. It follows that the process can be calculated perturbatively. Nevertheless, the protons and antiprotons as initial states consist of confined partons instead of free constituents. Hence, the measured cross section is sensitive to the so-called parton distribution function (PDF), which, as a parameterization of the (anti-)proton's quark/gluon structure, are the link between the colliding (anti-)protons and their partons.

4.1 The inclusive cross section

The cross section σ_{X} for a process pp $\rightarrow$ X, where the protons have the momenta P_1 and P_2, can be expressed as follows [ELL96][1]:

$$\sigma_{\mathrm{X}}(P_1, P_2) \;=\; \sum_{a,b} \int_0^1 dx_1 dx_2 \; f_a(x_1, \mu^2) f_b(x_2, \mu^2) \times \hat{\sigma}_{ab\rightarrow \mathrm{X}}(p_1, p_2, \alpha_{\mathrm{S}}(\mu^2), Q^2/\mu^2) \,, \tag{4.1.1}$$

where x_1 and x_2 are the momentum fractions carried by the colliding partons within the incident protons, $x_i = \frac{p_i}{P_i}$. The involved parton flavors are denoted as a and b, with f_a and f_b the corresponding parton distribution functions, which are interpreted as the probability of finding the parton with its momentum fraction inside the proton at the factorization scale μ^2. The strong coupling constant is indicated as α_{s}, and $\hat{\sigma}_{ab\rightarrow \mathrm{X}}$ denotes the partonic Drell-Yan cross section. For Z boson production from quarks, the leading order cross section is given by [ELL96]

$$\hat{\sigma}_{\mathrm{q\bar{q}} \rightarrow \mathrm{Z}} \;=\; \frac{\pi}{3} \sqrt{2} G_{\mathrm{F}} M_{\mathrm{Z}}^2 (g_{\mathrm{V}}^2 + g_{\mathrm{A}}^2) \delta(\hat{s} - M_{\mathrm{Z}}^2) \,, \tag{4.1.2}$$

where G_{F} stands for the Fermi constant ($G_{\mathrm{F}} = 1.166 \times 10^{-5}\,\mathrm{GeV}^{-2}$)[2], M_{Z} is the mass of the Z boson, $g_{\mathrm{V}} = T_3 - 2\,Q \sin^2\theta_{\mathrm{W}}$ and $g_{\mathrm{A}} = T_3$ are the vector and axial vector couplings, with θ_{W} as the weak mixing angle and $\hat{s}$ as the energy available for this process. It is defined as

$$\hat{s} \;=\; x_1 x_2 s \,. \tag{4.1.3}$$

Here, s is the total proton-proton center-of-mass energy squared.

The cross sections $\sigma_{\mathrm{pp} \rightarrow \mathrm{Z}}$ and $\sigma_{\mathrm{p\bar{p}} \rightarrow \mathrm{Z}}$ have been calculated perturbatively up to next-to-next-to-leading order (NNLO) and the perturbation series are found to converge quickly [NEE91]. The largest theoretical uncertainty of the cross section origins from the parton distribution functions. They depend on the soft processes that determine the structure of the proton (antiproton) as a bound state of quarks and gluons. There the strong coupling constant α_{s} becomes large and thus calculations using perturbative QCD can not be performed. The PDF's have to be extracted from data.

Several theoretical groups, for instance Alekhin [ALE03], CTEQ [CTE04] or MRST [MRS04], use the experimental data from deep inelastic scattering (DIS) like BCDMS [BEN89], E665 [ADA96], H1 [ADL00], NMC [ARN97], SLAC [WHI92] or ZEUS [BRE00] to extract the PDF's. Also the Drell-Yan process from E605 [MOR91], E866 [TOW01] and measurements of high transverse momentum jets in CDF [ABE98], DØ [ABB01] are used, as well as measurements of the W rapidity asymmetry [AFF01].

[1] For clarity, only proton-proton collisions will be taken as an example.

[2] Planck's constant $\hbar$ and the speed of light c are both set to 1.

Depending on how these data are fitted, which data are included into the calculations, how the experimental errors are treated, the choice of the factorization and renormalization scale etc. leads to different extractions of the parton distribution functions and thus to uncertainties in the PDF knowledge. In Figure 4.1.1 the Drell-Yan lepton pair production cross section measurements and theoretical calculations are presented.

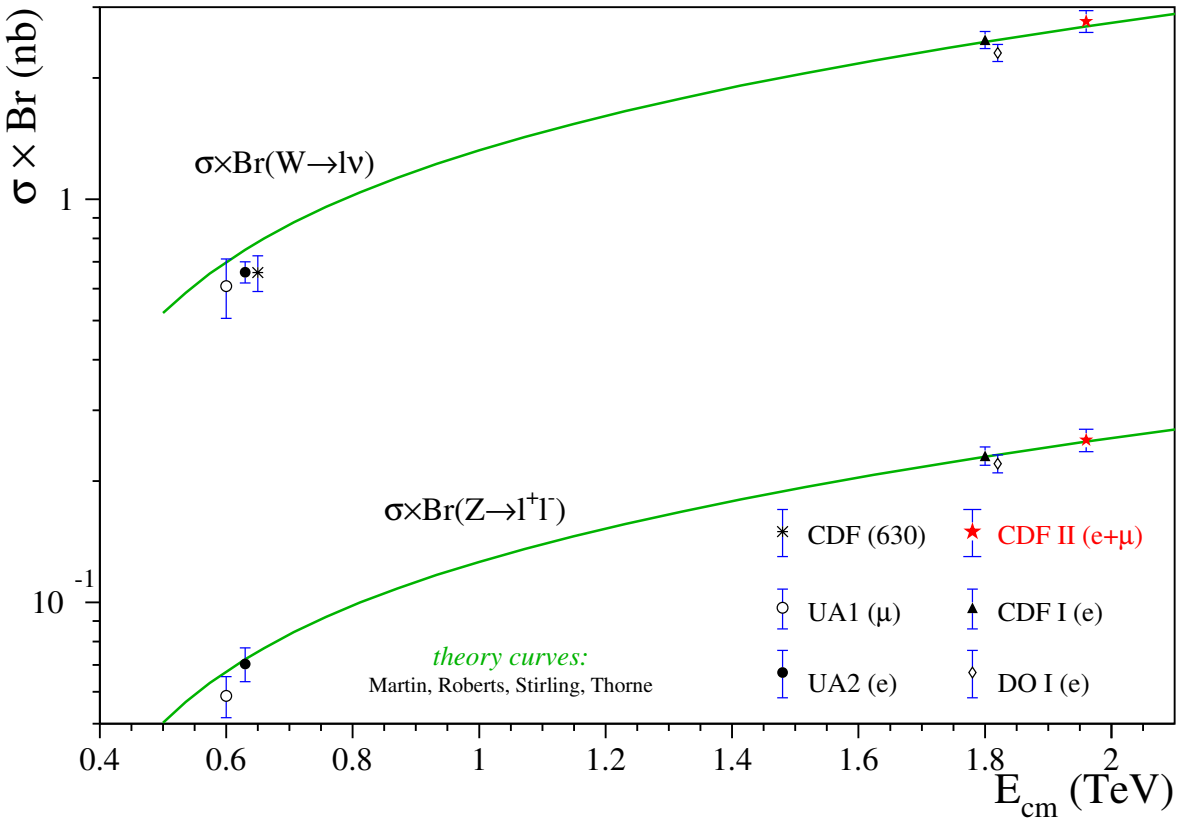

Figure 4.1.1: The inclusive Drell-Yan lepton pair production cross sections ($p\bar{p} \rightarrow \gamma^*/Z \rightarrow l^+l^-$ and $p\bar{p} \rightarrow W \rightarrow l\nu$) are shown with respect to the center of mass energy. The lines represent the theoretical NNLO calculations for the individual processes, the points with the error bars indicate the measurement of the corresponding experiments and their uncertainties.

For the CDF Run II experiment, cross section measurements of

$$\sigma_{Z \rightarrow e^+e^-} = 255.8 \pm 16.8\,\text{pb} \tag{4.1.4}$$

and

$$\sigma_{W \rightarrow e\nu} = 2780 \pm 178\,\text{pb} \tag{4.1.5}$$

are obtained, while the theoretical calculations give

Z decay mode	branching fraction	W decay mode	branching fraction
e^+e^-	$3.363 \pm 0.004\%$	$e\nu$	$10.75 \pm 0.13\%$
$\mu^+\mu^-$	$3.366 \pm 0.007\%$	$\mu\nu$	$10.57 \pm 0.15\%$
$\tau^+\tau^-$	$3.370 \pm 0.008\%$	$\tau\nu$	$11.25 \pm 0.20\%$
invisible	$20.00 \pm 0.06\%$	invisible	$1.4 \pm 2.8\%$
hadrons	$69.91 \pm 0.06\%$	hadrons	$67.60 \pm 0.27\%$

Table 4.1.1: The largest branching fractions for the Z and W decay modes [PDG06].

$$\sigma^{\mathrm{NNLO}}_{\mathrm{Z}\to \mathrm{e^+e^-}} \;=\; 251.3 \;\pm\; 5.0\,\mathrm{pb} \tag{4.1.6}$$

and

$$\sigma^{\mathrm{NNLO}}_{\mathrm{W}\to \mathrm{e}\nu} \;=\; 2687 \;\pm\; 54\,\mathrm{pb}\,, \tag{4.1.7}$$

see ref. [ACO04]. For comparison, at the LHC the cross sections are about

$$\sigma^{\mathrm{NNLO}}_{\mathrm{Z}\to \mathrm{e^+e^-}} \;\sim\; 1500\,\mathrm{pb} \tag{4.1.8}$$

and

$$\sigma^{\mathrm{NNLO}}_{\mathrm{W}\to \mathrm{e}\nu} \;\sim\; 15000\,\mathrm{pb}\,. \tag{4.1.9}$$

The branching fractions for the Z and W decay modes are listed in Table 4.1.1.

4.2 The differential cross section

Besides the knowledge of the inclusive cross section, it is essential to understand also its differential behavior in kinematic variables like the invariant mass, W/Z transverse momentum or rapidity. In order to look for new physics $\frac{d\sigma}{dM}$ has been investigated, $\frac{d\sigma}{dp_{\mathrm{T}}}$ can be used as a test of modeling soft QCD initial-state radiation and $\frac{d\sigma}{dY}$ to constrain the parton distribution functions (see section 4.4). The latter measurement is also important to tune the Monte Carlo event generators. Thereby, the systematic uncertainties in many measurements can be reduced. In addition, the differential cross section measurement with respect to the rapidity is complementary to the constraints on the PDF's from deep inelastic scattering experiments. NNLO calculations for electroweak gauge boson production have been carried out for this quantity [ANA04]. Figure 4.2.1 and Figure 4.2.2 show the rapidity distribution of the cross section for on-shell Z boson production at the Tevatron and the LHC.

The error bands are due to the variation of the renormalization and factorization scale only and thus do not include the uncertainties from the parton distribution

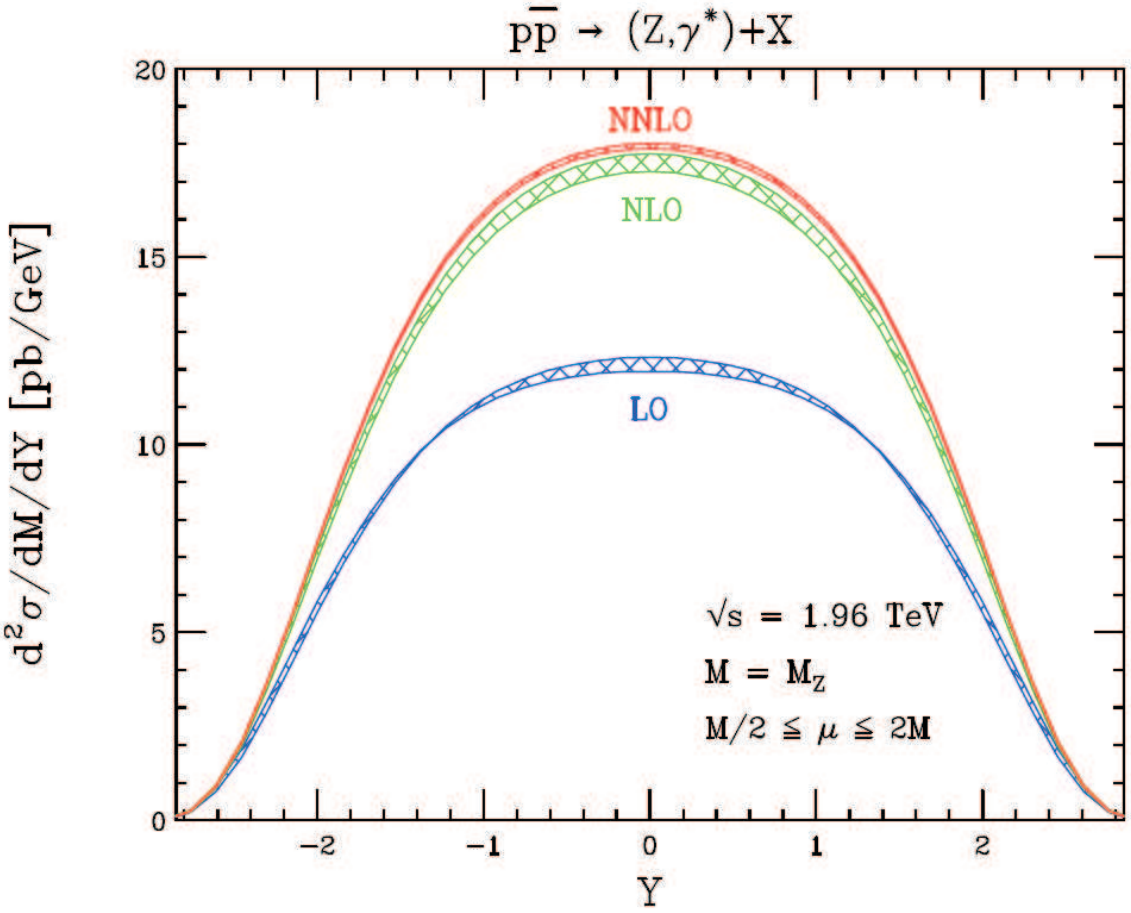

Figure 4.2.1: The LO, NLO and NNLO results for the rapidity distribution of the cross section for on-shell Z bosons at the Tevatron. The error bands indicate the variation of the renormalization and factorization scale in the range $M_Z/2 < \mu < 2M_Z$ [ANA04].

functions. Nevertheless, the error on the PDF's accounts for the largest contribution to the uncertainty. From LO to NLO, the magnitude of higher order corrections is about 30 % (45 %) for central rapidities and 15 % (15 %) for larger rapidities at the LHC (Tevatron). At NNLO, the results stabilize with a decrease of 1 % to 2 % for the LHC and a further increase by 3 % to 5 % for the Tevatron. However, the shapes are not affected. In particular, this was the first NNLO calculation which allowed to compute not only the inclusive cross section, but also to obtain the cross section as function of the boson rapidity. In the meantime, also Higgs production has been computed at NNLO accuracy [ANA05], in this case even the full differential information on the Higgs momentum and its decay products is available. The calculation of the differential Drell-Yan cross section is implemented in a software package called VRAP [DIX05], which has been complemented by a user-friendly interface [GDH04].

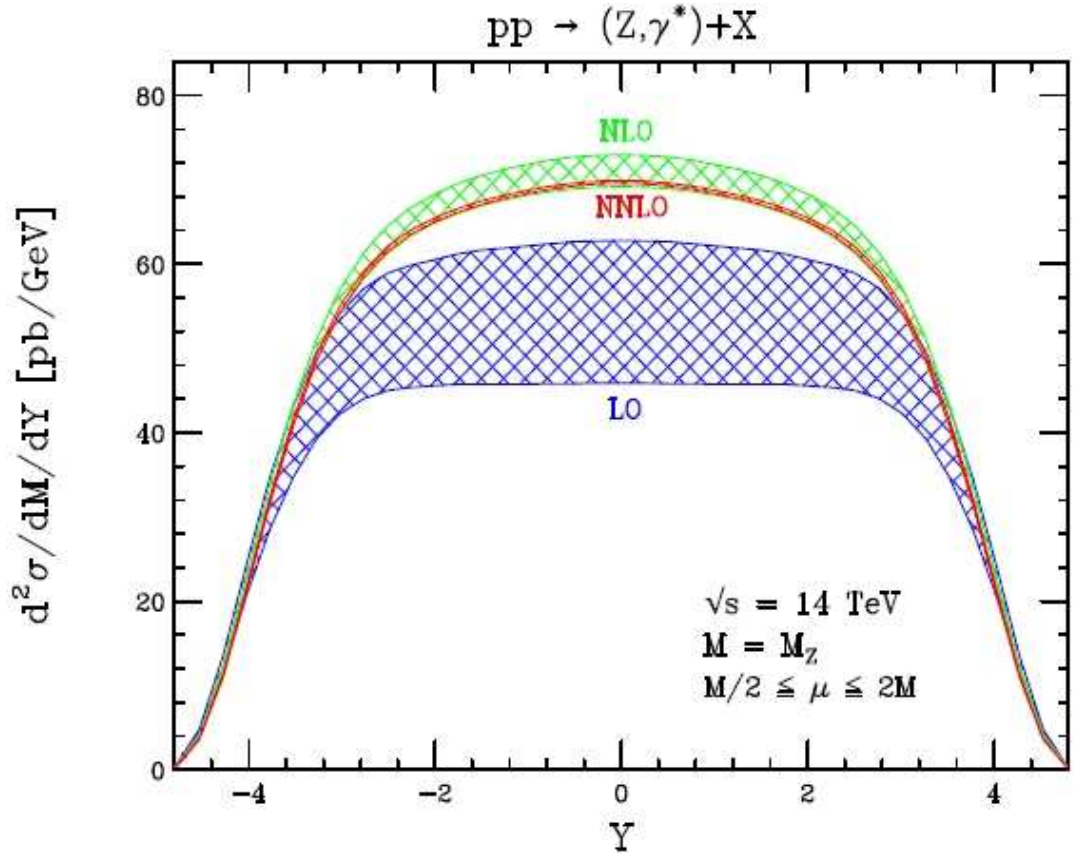

Figure 4.2.2: The LO, NLO and NNLO results for the rapidity distribution of the cross section for on-shell Z bosons at the LHC. The error bands indicate the uncertainties from the variation of the renormalization and factorization scale in the range $M_Z/2 < \mu < 2M_Z$ [ANA04].

The code has several options to be chosen by the user, such as the collider type (e.g. TEVATRON or LHC), which sets the correct beam particles and energies, the vector boson produced (W^+, W^-, Z, γ), with or without Z/γ interference terms, the PDF set (for more details on the available PDF sets, see [ANA04]), renormalization and factorization scales, size and number of rapidity slices to be computed, as well as the boson mass range to be integrated over.

The Drell-Yan Z boson production cross section was computed with the above code for the rapidity bins as indicated in Table 4.2.1 for the Tevatron and in Table 4.2.2 for the LHC. The cross section has been obtained by integrating over a mass region for the exchanged Z boson of $M_Z - 3\,\Gamma_Z < m < M_Z + 3\,\Gamma_Z$, corresponding to the definition of the Z signal in the following analyses as outlined in section 5.3.1 for CDF and section 6.3 for CMS. The default results have been obtained with the MRST01-NNLO PDF set [STI02], taking Z boson exchange only and the renormalization and factorization scales fixed at $\mu_R = \mu_F = M_Z$. The thus obtained inclusive cross section for a Z rapidity range of $-2 < Y < 2$ at CDF amounts to 209.41 pb and the

Y_{low}	Y_{high}	σ [pb]	Δ_{PDF} [pb]	Δ_{scaling} [pb]	Δ_{tot} [pb]	Δ_{relative} [%]
-2.0	-1.6	13.659	0.971	0.088	0.975	7.138
-1.6	-1.1	24.525	1.273	0.153	1.282	5.227
-1.1	-0.6	29.183	1.174	0.175	1.187	4.067
-0.6	-0.1	31.053	1.134	0.180	1.147	3.694
-0.1	+0.1	12.565	0.455	0.075	0.462	3.677
+0.1	+0.6	31.053	1.134	0.180	1.147	3.694
+0.6	+1.1	29.183	1.174	0.175	1.187	4.067
+1.1	+1.6	24.525	1.273	0.153	1.282	5.227
+1.6	+2.0	13.659	0.971	0.088	0.975	7.138

Table 4.2.1: Results of the theoretical on-shell Z boson cross section calculations as a function of rapidity (lower and upper bin limits are given) for the Tevatron. The errors on these calculations from PDF uncertainties and scale variations are listed as well as the total (quadratic sum of both) and the relative error.

Y_{low}	Y_{high}	σ [pb]	Δ_{PDF} [pb]	Δ_{scaling} [pb]	Δ_{tot} [pb]	Δ_{relative} [%]
-2.50	-1.44	241.674	10.268	2.254	10.512	4.350
-1.44	+1.44	694.803	14.181	5.790	15.317	2.205
+1.44	+2.50	241.674	10.268	2.254	10.512	4.350

Table 4.2.2: Results of the theoretical on-shell Z boson cross section calculations as a function of rapidity (lower and upper bin limits are given) for the LHC. The errors on these calculations from PDF uncertainties and scale variations are listed as well as the total (quadratic sum of both) and the relative error.

inclusive cross section for a Z rapidity range of $-2.5 < Y < 2.5$ at CMS amounts to 1178.15 pb.

In order to obtain an estimate of the theoretical uncertainties, the NNLO cross section predictions have been re-computed with several different parameter choices. The renormalization and factorization scales have been varied independently between $0.5\,M_{\text{Z}}$ and $2\,M_{\text{Z}}$. The maximum variation for the inclusive cross section, integrated over a rapidity range of $-2 < Y < 2$ ($-2.5 < Y < 2.5$), turns out to be only 0.6 % (0.9 %) at CDF (CMS). Several other PDF sets have been employed, such as minor variations of the MRST01-NNLO set (cf. [ANA04]) as well as the NNLO set by Alekhin [ALE03]. Comparing the MRST and Alekhin PDF sets gives the dominant systematic uncertainty of 4.5 % at CDF and 3.1 % at CMS. Further stability checks, such as changing the running of the electromagnetic coupling or including also photon exchange result in variations well below the per cent level. Regarding photon exchange it should be noted that actually this contribution is experimentally eliminated to first order by using a side-band subtraction method, which is described in section 5.3.

From the definition of the rapidity in section 2.2.1 and the leading order Drell-Yan process in Figure 4.0.1, it follows that the momentum fractions of the participating partons and the boson rapidity are directly related via the following equation:

$$x_{1/2} = \frac{M_{\mathrm{ee}}}{\sqrt{s}} \mathrm{e}^{\pm Y} \tag{4.2.1}$$

Here, M_{ee} denotes the invariant mass of the di-electron pair. As a consequence of this relation, a Z boson produced at large rapidities requires an interaction of one parton with a high momentum fraction and one parton with a low momentum fraction. Therefore, the differential cross section with respect to the rapidity, $\left(\frac{d\sigma}{dY}\right)$, allows to probe the low momentum region of the PDF's. This is especially interesting, since the predictions for the different PDF sets differ most at large rapidities. In CDF for example, the rapidity coverage of the electromagnetic and hadronic calorimeter exceeds the one of the muon chambers, which makes the Drell-Yan process to electrons and positrons a favorable channel.

In addition, the PDF's depend not only on x but also on Q^2. Figure 4.2.3 shows the range of x and Q^2 accessible at HERA[3] and at the LHC.

Since the branching ratio of $\mathrm{Z} \rightarrow \mathrm{e^+e^-}$ and $\mathrm{W} \rightarrow \mathrm{e}\nu$ has been measured with high precision at the Large Electron Positron Collider (LEP) [PDG06], a cross section determination of the process $\mathrm{pp}(\mathrm{p\bar{p}}) \rightarrow \mathrm{Z} \rightarrow \mathrm{ee}$ and $\mathrm{pp}(\mathrm{p\bar{p}}) \rightarrow \mathrm{W} \rightarrow \mathrm{e}\nu$ can also be interpreted as a cross-check of the PDF evolution from their measured scales at DIS experiments ($Q^2 \sim 10^{1-2}\,\mathrm{GeV}^2$) to the scale of the process ($Q^2 \sim 10^4\,\mathrm{GeV}^2$).

4.3 The luminosity method

The number of events per unit time and area is characterized by the luminosity L. It is defined by the number of events per cross section which take place in a certain area hit by the beam per time unit. In the easiest case, every colliding beam consists of only one homogeneous bunch of particles with an area A which collide head on. If the bunches collide with a frequency f and consist both of N_i particles, then the luminosity at the interaction point is given by

$$L = \frac{N_1 N_2 f}{A}\,. \tag{4.3.1}$$

In the following, the term luminosity denotes the integrated luminosity for a defined period in time. Conventionally, the luminosity is obtained by counting the total number of inelastic interactions of the colliding particles. Equation 2.2.3 in section 2.2.6 shows the relation between luminosity and the number of inelastic interactions. A complementary luminosity measurement for hadron colliders was then proposed

[3]The Hadron-Elektron-Ringanlage (HERA) is an electron-proton collider at the Deutsches Elektronen Synchrotron (DESY), Hamburg, Germany.

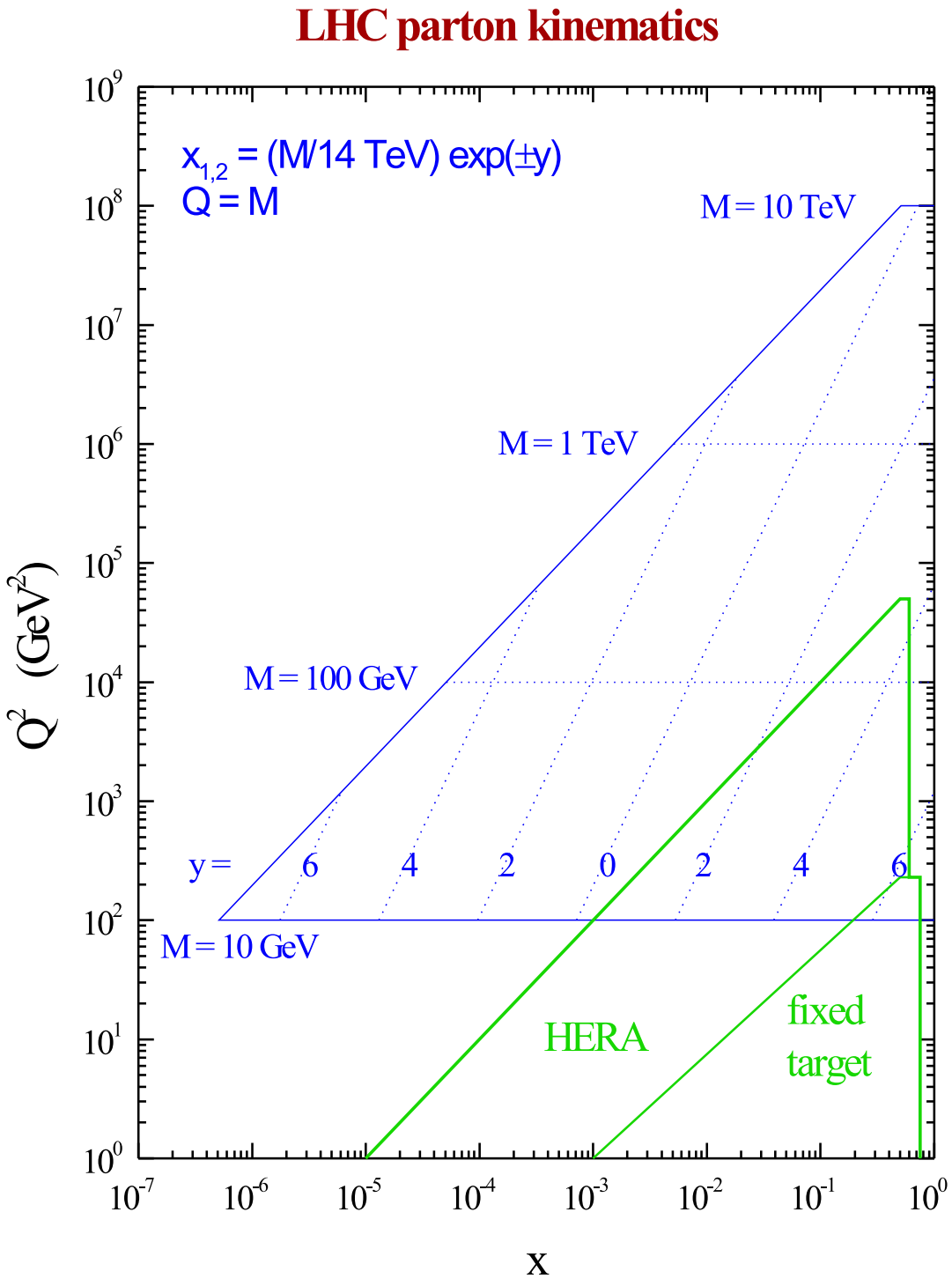

Figure 4.2.3: The region of the parton kinematics x and Q^2 is shown, which is covered by the deep inelastic scattering experiments at HERA and the region accessible with the LHC [STI04].

by [DPZ97] and also investigated with CDF data in more detail by [MDA03] and [EHD05]. In this case the master equation is given by

$$\sigma_{\text{partons}\to\text{Z}} \times \text{PDF}\left(x_1, x_2, Q^2\right) \times L_{\text{p}\bar{\text{p}}} = \frac{S_\text{Z}}{\epsilon}\,, \tag{4.3.2}$$

where $\sigma_{\text{partons}\to\text{Z}}$ is the theoretically calculated parton-parton cross section for Z boson production. As seen in section 4.2, it is calculated up to next-to-next-to-leading order perturbation theory by Anastasiou et al. [ANA04]. The number of counted Z bosons is S_Z and the detector efficiency to detect the produced Z bosons is indicated by ϵ. As its cross section is calculated with a good precision, the counting of Z events is an interesting alternative way to determine the hadron-hadron luminosity and, in a further step, to constrain the PDF's, leading to the parton-parton luminosity.

4.4 The parton luminosity

As already discussed in the previous sections of this chapter, the precision of the theoretical cross section calculations is constrained by the uncertainty of the parton distribution functions. The error of the PDF's are in the order of 5 %, depending on the process type and the center-of-mass energy. On the other hand, the experimental accuracy of measuring the cross section at hadron colliders is primarily limited by the accuracy of the luminosity determination, which is expected to be less than 5 %. Note, that the statistical uncertainty only plays a subordinate role at the Tevatron and will be negligible at the LHC.

For a specific process, the number of signal events $N_\text{signal} = N_\text{observed} - N_\text{background}$, the measurable proton-proton cross section $\sigma_{\text{pp}\to\text{X}}$ and the proton-proton luminosity L_pp are linked via the following relation:

$$N_\text{signal} = N_\text{observed} - N_\text{background} = \sigma_{\text{pp}\to\text{X}} \times L_\text{pp} \times \epsilon\,, \tag{4.4.1}$$

where ϵ denotes the efficiency for detecting pp $\to$ X events.

A possibility to reduce the uncertainties of the PDF's and of the luminosity is to measure directly the different parton luminosities using the single W and Z boson production identified through their leptonic decays. The number of signal events can then be expressed in the following way:

$$N^{\text{W/Z}}_\text{signal} = N^{\text{W/Z}}_\text{observed} - N^{\text{W/Z}}_\text{background} = \sigma_{\text{partons}\to\text{W/Z}} \times L_\text{partons}(x_1, x_2, Q^2) \times \epsilon_{\text{W/Z}} \tag{4.4.2}$$

$L_\text{partons}(x_1, x_2, Q^2)$ denotes the *parton luminosity*, which predicts the frequency at which two partons of given type, given momenta and at a defined energy scale will interact with each other. Apart from the machine parameter, this depends on the following physics parameters: The parton types (quarks, antiquarks or gluons), the

parton momentum fractions (x_1 and x_2) and the energy scale of the process (Q^2). Since the theoretical estimates for high Q^2 processes are based on the interaction of quarks, antiquarks and gluons, parton luminosities appear to be a natural quantity [DPZ97]. The u, $\bar{\text{u}}$, d, $\bar{\text{d}}$ parton distribution functions can be studied using the following processes: $\text{u}\bar{\text{u}}(\text{d}\bar{\text{d}}) \rightarrow \text{Z} \rightarrow \text{ll}$, $\text{u}\bar{\text{d}} \rightarrow \text{W}^+ \rightarrow \text{l}^+\nu$ and $\bar{\text{u}}\text{d} \rightarrow \text{W}^- \rightarrow \text{l}^-\bar{\nu}$. This is attractive due to the following reasons.

- The branching ratio of W and Z bosons decaying into leptons is precisely measured from LEP data.
- There is lepton universality.
- The W/Z production occurs at a defined mass. Equation 4.1.3 thus fixes the product of x_1 and x_2 to a certain value.
- The rapidity distribution of the weak bosons is directly related to the momentum fractions of the partons (see equation 4.2.1).
- Therefore the pseudorapidity distributions of the charged leptons are also constrained by the momentum fraction of the partons.

It follows that the key to precisely measure the PDF's and parton luminosities is the accurate knowledge of the pseudorapidity shape and rate of the charged leptons.

An interesting example, where the W/Z production is used as a normalization process, is the production of vector boson pairs, which depend on the $\text{q}\bar{\text{q}}$ luminosities at different values of Q^2. Normalizing their cross sections to the cross section of single produced vector bosons might eventually result in systematic uncertainties for the event rate of boson pair-production at the percent level [DPZ97]. For example

$$N_{\text{pp}\rightarrow\text{W}} = L_{\text{pp}} \times \text{PDF}(x_1, x_2, Q^2) \times \sigma_{\text{partons}\rightarrow\text{W}} \tag{4.4.3}$$

$$N_{\text{pp}\rightarrow\text{WW}} = L_{\text{pp}} \times \text{PDF}(x_1', x_2', Q'^2) \times \sigma_{\text{partons}\rightarrow\text{WW}} \tag{4.4.4}$$

$$\frac{N_{\text{pp}\rightarrow\text{WW}}}{N_{\text{pp}\rightarrow\text{W}}} = \frac{\sigma_{\text{partons}\rightarrow\text{WW}}}{\sigma_{\text{partons}\rightarrow\text{W}}} \times \frac{\text{PDF}(x_1', x_2', Q'^2)}{\text{PDF}(x_1, x_2, Q^2)}\,, \tag{4.4.5}$$

where the proton-proton luminosity cancels out.

Chapter 5

Luminosity measurement at CDF with $Z \rightarrow e^+ e^-$ events

For the data recorded from March 2002 to February 2004 at the CDF experiment, the production of $Z \rightarrow e^+e^-$ events has been analyzed in order to estimate the luminosity via Z boson counting. With this method a proton-antiproton luminosity for this time period is obtained. Recent theoretical calculations for the Z production cross section up to next-to-next-to-leading order allow for a comparison between theory and differential measurements as a function of rapidity for the first time. These calculations are used for this analysis and a rapidity-dependent luminosity measurement is presented in addition.

5.1 Data and Monte Carlo event samples

Originating from stream b[1], the dataset bhel0d was used. This dataset of high p_T electrons and positrons[2] was reprocessed with the CDF reconstruction software version 5.3.1 and analyzed with Stntuple[3] version 5.3.3 [MUR04]. The dataset corresponds to a time period from March 2002 until February 2004. Only the good runs [MAR04] were taken (run number 141544 to run number 179056) which is equivalent to an integrated luminosity of $222.2\,\mathrm{pb}^{-1}$ as estimated from the Cherenkov Luminosity Counters (CLC). In addition, the dataset was divided into twelve subsets of more or less equal luminosity, each set comprising the same amount of runs as shown in Table 5.1.1.

Since the data from stream b was taken, two trigger conditions have been analyzed. For the selection of Z events the ELECTRON_CENTRAL_18 trigger was examined. Due to the fact that the Z_NOTRACK trigger was not implemented in the beginning

[1]Stream b provides the datasets with those events, which include candidates for electrons with a high transverse momentum ($p_T > 18\,\mathrm{GeV}$).

[2]For simplicity, "electrons" will be used in the following for both electrons and positrons.

[3]The Stntuple data format is basically a standard ROOT tree [BRU96]. It is a container which simplifies and standardizes the data access.

Dataset	Run number	CLC luminosity [pb^{-1}]
1	141544 - 148674	26.6
2	148774 - 151870	19.4
3	151871 - 152967	14.3
4	153051 - 155312	8.5
5	155313 - 160314	12.5
6	160346 - 161786	14.9
7	161787 - 163462	13.3
8	163463 - 165271	14.9
9	165297 - 167139	18.2
10	167186 - 175289	21.9
11	175292 - 178165	29.0
12	178255 - 179056	28.8

Table 5.1.1: The data divided into several time periods. The run numbers and the corresponding CLC luminosity estimates are indicated.

of the data taking period, the W_NOTRACK trigger was used to obtain the trigger efficiency. Whereas the ELECTRON_CENTRAL_18 trigger requires a cluster in the central calorimeter of $p_{\mathrm{T}} > 18$ GeV and a matching track of $p_{\mathrm{T}} > 8$ GeV, the W_NOTRACK trigger does not need any tracking and is completely independent of the ELECTRON_CENTRAL_18 trigger.

Since the dataset bhel0d is more than one Terabyte in size, a preselection filter was introduced into the analysis software in order to make the analysis faster and to store the produced Stntuples on smaller local disks. Therefore evident QCD backgrounds (mainly di-jet events) were removed, which reduced the data size down to 5 % of the original sample. The preselection was designed in such a way that all detectable $\mathrm{Z} \rightarrow \mathrm{ee}$ events are kept, if:

- each event contains at least one reconstructed track and at least one electromagnetic cluster with a transverse energy of at least 25 GeV
- there are at least two electromagnetic clusters
- the electromagnetic cluster is isolated[4]: $\frac{Iso}{Iso + E_{\mathrm{T}}} < 0.05$; its fraction of the electromagnetic energy to the hadronic energy is large: $\frac{E_{\mathrm{had}}}{E_{\mathrm{em}}} < 0.025$; the electron candidate features a good energy over momentum ratio: $0.6 < \frac{E}{p} < 1.6$

In addition - to retain the possibility to extend this analysis to $\mathrm{W} \rightarrow \mathrm{e}\nu$ events - also events were kept with the following characteristics:

[4] Iso is a variable which represents the fraction of energy within a cone of $\Delta R = \sqrt{\Delta\phi^2 + \Delta\eta^2} = 0.4$ around an electromagnetic cluster.

- there is exactly one electromagnetic cluster of at least 25GeV and no additional jet with a minimum $p_{\mathrm{T,jet}} = 10\,\mathrm{GeV}$, defined with a clustering algorithm and a cone size ΔR of 0.7,
- there is exactly one electromagnetic cluster of at least 25 GeV and one or more jets with the angle Φ smaller than 160° in the plane transverse to the beam between the highest p_{T} jet and the electromagnetic cluster.

To compare the data with signal simulation the Monte Carlo set "zewkae" from the Electroweak Group at CDF was used. The zewkae set contains $\mathrm{p\bar{p}} \rightarrow \gamma^*/\mathrm{Z} \rightarrow \mathrm{e^+e^-}$ events with a generated di-lepton mass of $M_{\mathrm{e^+e^-}} > 30\,\mathrm{GeV}$ and includes also minimum bias events. It was generated with PYTHIA 6.216 [SJO03] and reconstructed with version 5.3.2 of the CDF reconstruction software. A total of 200000 events were analyzed for this purpose.

5.2 Selection of $\mathrm{Z} \rightarrow \mathrm{e^+\,e^-}$ events

Z events provide a clean signal with a narrow mass peak above a very small background. Following the idea of a simple analysis to possibly keep the systematic error small, the following electron selection criteria were chosen: First, three different electron qualities were defined to categorize the electron candidates into three different classes. The three qualities are listed below:

a) $\frac{Iso}{Iso + E_{\mathrm{T}}} < 0.05$

b) $\frac{E_{\mathrm{had}}}{E_{\mathrm{em}}} < 0.025$

c) $0.6 < \frac{E}{p} < 1.6$

Quality a) is the so-called isofraction and denotes the fraction between the transverse energy around an electromagnetic cluster within a cone of size $\Delta R < 0.4$ and the total transverse energy. Requirement b) denotes the cluster's energy ratio of the hadron calorimeter to the electromagnetic calorimeter and c) the ratio of the cluster energy to the matched track momentum. An electron is called *golden*, if it fulfills all three requirements. *Silver* electrons have to satisfy the condition c) and either the first a) or the second b). To be a *bronze* electron only one of the three requirements has to be fulfilled. In addition, all these electron candidates are obliged to pass a transverse energy cut of $E_{\mathrm{T}} > 25\,\mathrm{GeV}$ and a so-called z-vertex cut of $|z| < 60\mathrm{cm}$. Traditionally, it is required at CDF for high p_{T} events to cut on the z-vertex coordinate (along the beam line), since high p_{T} physics should be found around the center of the CDF detector at $z = 0$. A distinction is made between the two cases that the Z boson momentum is reconstructed from two electrons where both are found in the central calorimeter, called central-central electrons, and the case where only one is detected by the central calorimeter and the other one by the plug calorimeter, called central-plug electrons. Figure 5.2.1 clarifies the two different event types.

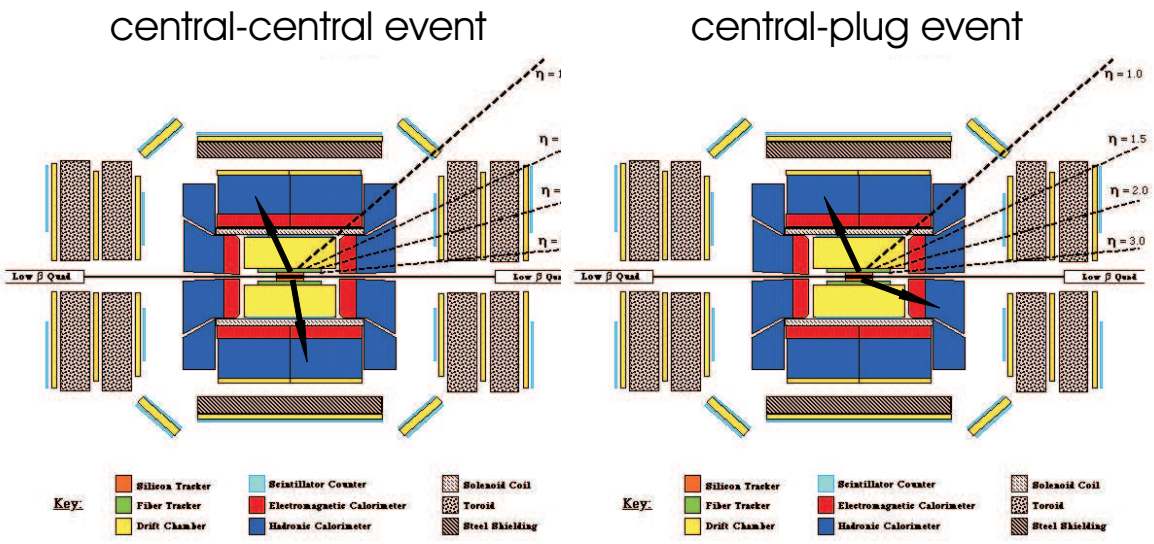

Figure 5.2.1: A schematic view of the two different event types. On the left a Z boson event with both electrons central, on the right a Z boson event with only one electron detected in the central calorimeter and the other one in the plug calorimeter. The electrons are indicated by the black arrows.

The distributions of the three basic selection variables are shown in Figure 5.2.2. Comparing the distributions of the $\frac{E_{\mathrm{had}}}{E_{\mathrm{em}}}$ variable for central-central and central-plug electrons, a higher mean value is found in the former case which is not described by the simulation. This might be an effect of the spacer bars in the central calorimeter which absorb additional electromagnetic energy and therefore cause a higher ratio of hadronic to electromagnetic energy [NIC04].

Clear signals from central-central Z bosons were obtained, if one of the electrons was identified as golden and the other electron at least as bronze. In this case, the event was accepted for the Z selection. Central-plug electron pairs showed similar quality requiring the central electron as golden or silver whereas the plug electron had to be at least bronze. The invariant mass distributions of the different electron combinations for central-central and central-plug are shown in Figure 5.2.3 and 5.2.4.

Having defined our candidate events, a Gaussian fit to the mass peaks in the central-central and central-plug cases determines the reconstructed Z mass and width (σ). In both, data and Monte Carlo, the reconstructed energy of the electrons had to be recalibrated, taking as reference the well-known mass of the Z boson. While for central electrons neither in data nor in Monte Carlo corrections had to be applied, the plug electron energy for data needed to be increased by 5 % and for Monte Carlo by 3 %. These energy corrections were determined in an iterative process. A priori it is not obvious how much the energy of the plug electrons contributes to the value of the central-plug mass peak for reconstructed Z bosons. In addition, there could have been also a difference in energy between east- and west-plug electrons. This possibility was excluded and will be discussed in section 5.5.1. To match also the

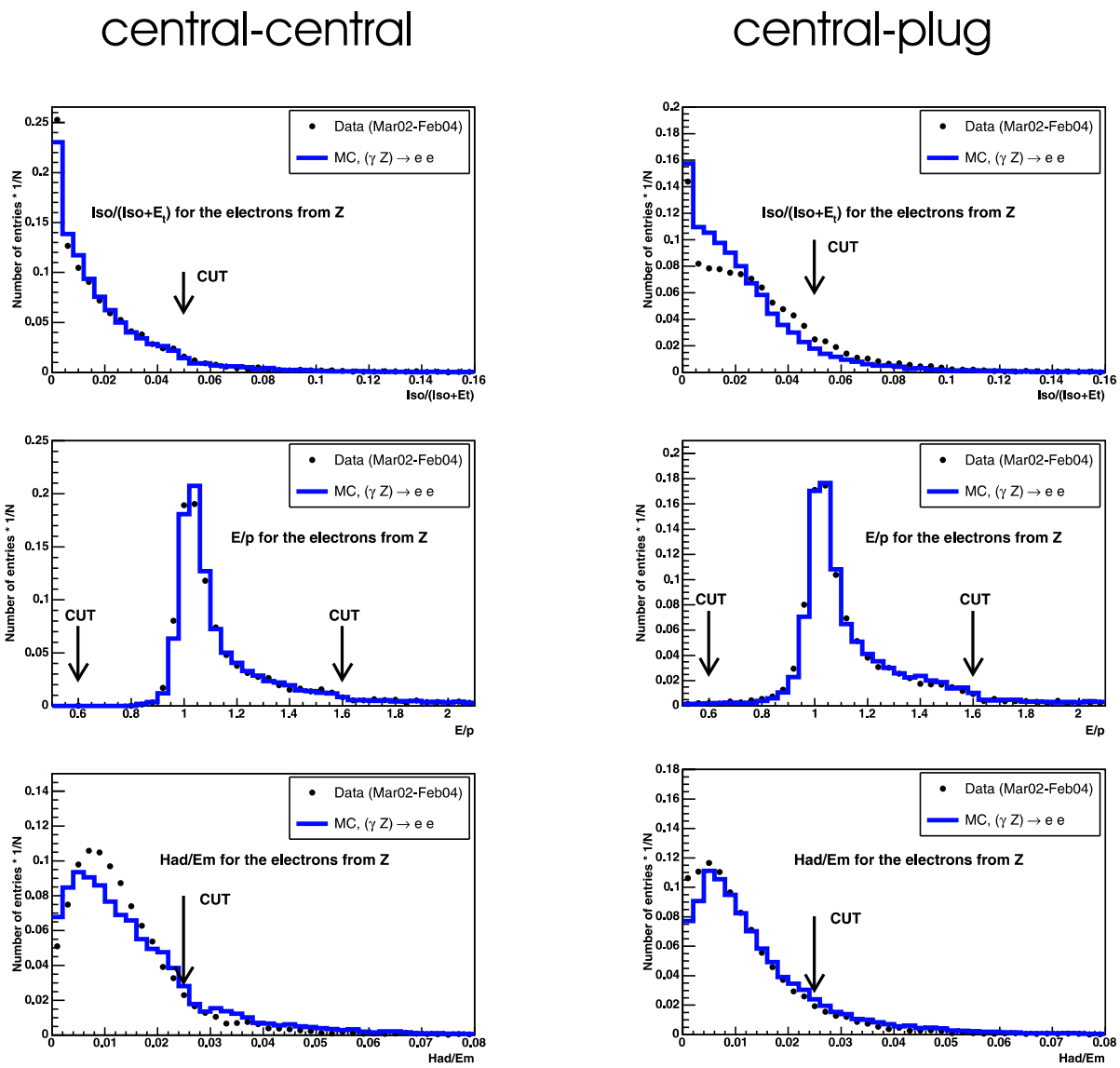

Figure 5.2.2: The normalized distributions for good electron candidates are shown, on the left for central-central electrons, on the right for central-plug electrons. Except for the plotted variable, all the cuts on the other variables are applied. Data is shown as dots, the Monte Carlo prediction as solid line.

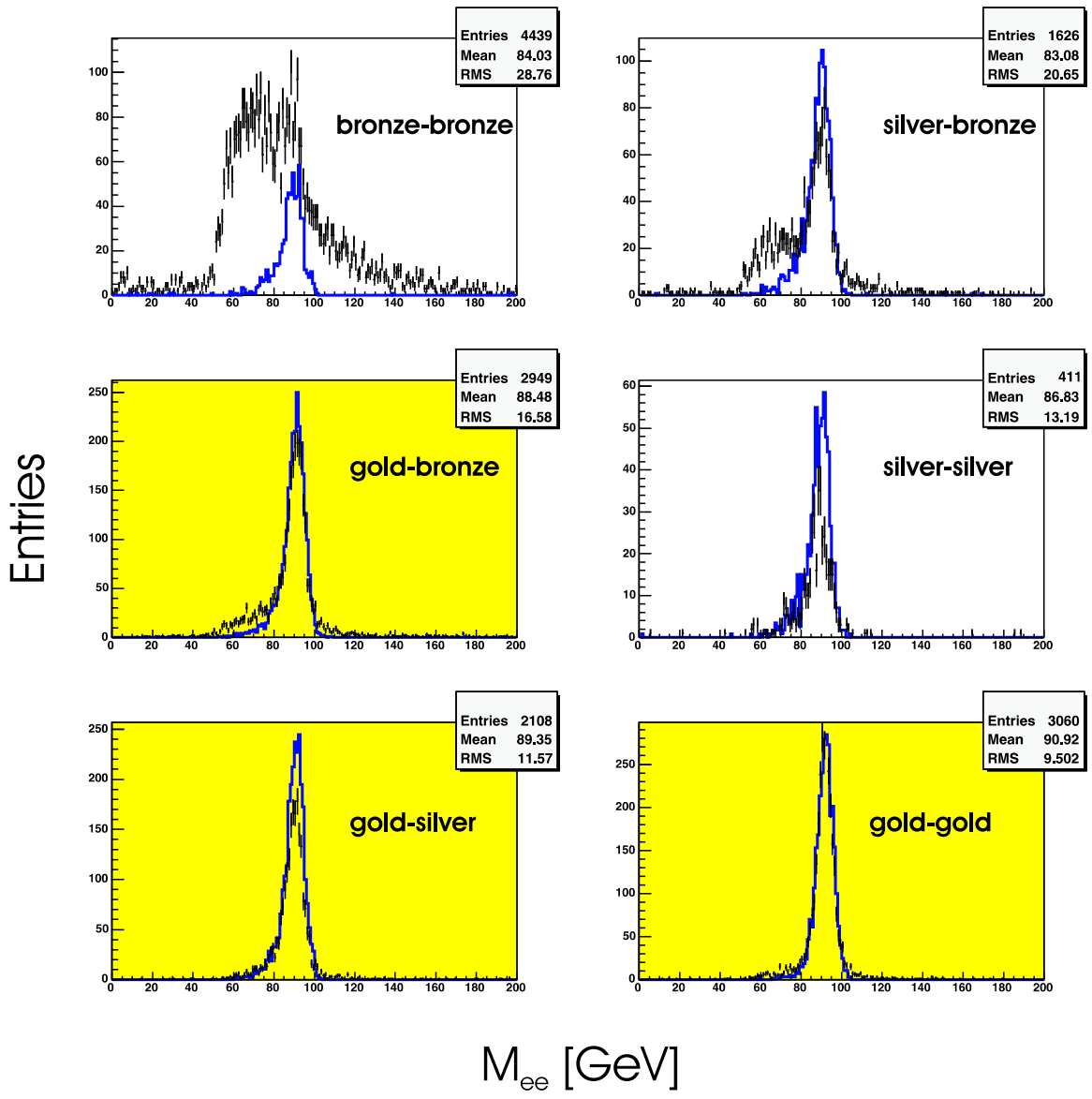

Figure 5.2.3: The invariant mass distribution of central-central electrons for various combinations of their electron quality. The data is shown with its statistical uncertainty as error bars, the simulation as solid line. Those combinations which are used to define the Z signal are highlighted, namely gold-gold, gold-silver and gold-bronze. These combinations are also used to determine the normalization factor between data and simulation.

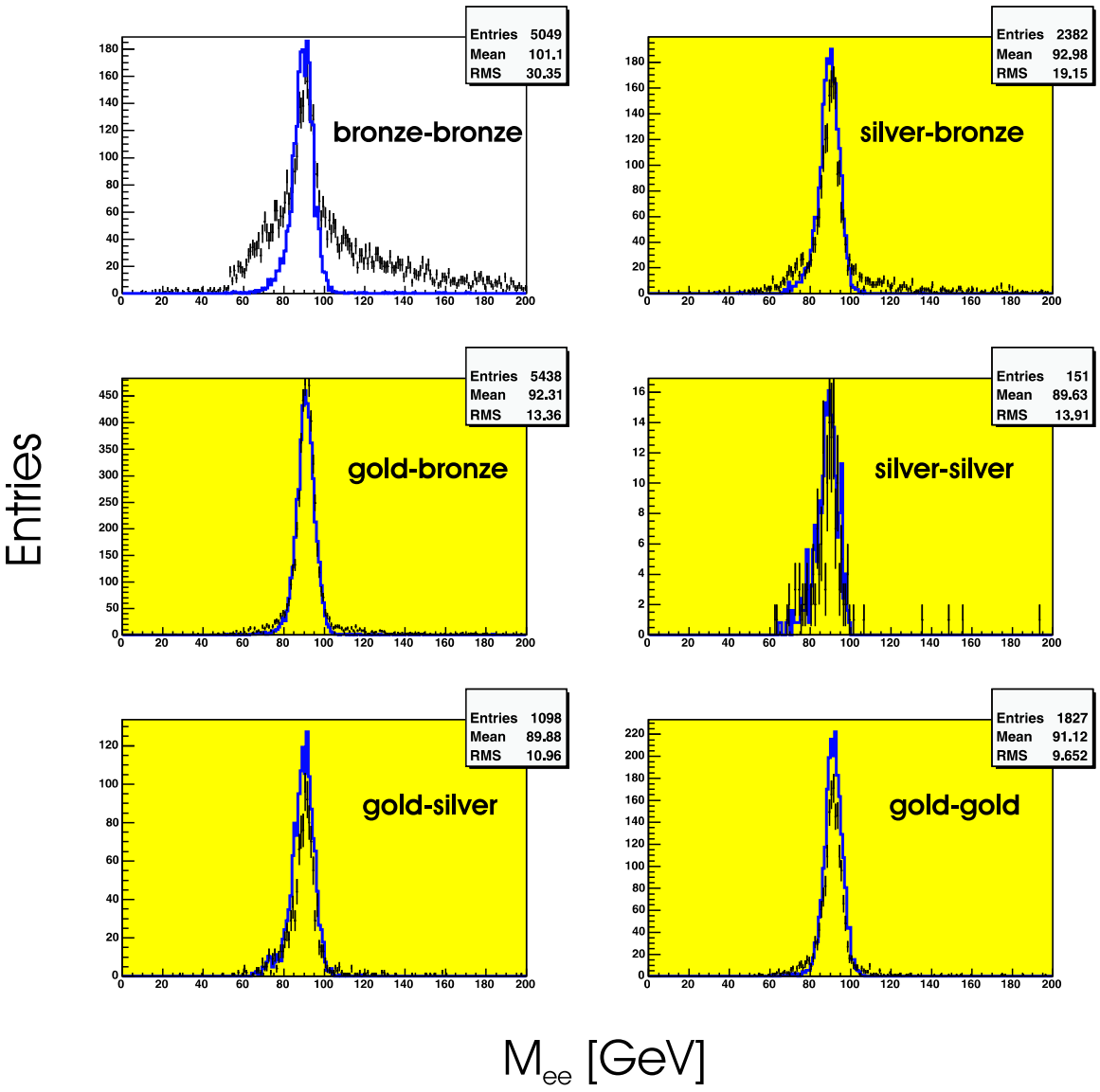

Figure 5.2.4: The invariant mass distribution of central-plug electrons with the specific combination of their electron quality. The data is shown with its statistical uncertainty as error bars, the simulation as solid line. Highlighted are the combinations which are used to define the Z signal, namely gold-gold, gold-silver, gold-bronze, silver-silver and silver-bronze. Moreover, the central electron had to be at least golden or silver. These combinations are also used to determine the normalization factor between data and simulation.

	central-central		central-plug	
	mass [GeV]	σ [GeV]	mass [GeV]	σ [GeV]
data uncorrected	90.9	4.4	88.3	4.5
data corrected	90.9	4.4	90.9	4.4
Monte Carlo uncorrected	91.0	3.9	89.2	3.8
Monte Carlo corrected	91.0	4.4	90.7	4.5

Table 5.2.1: Results obtained by the Gaussian fit of the invariant mass distributions for uncorrected and corrected data and simulation. The statistical errors for mass and width are below 100 MeV.

width of the distributions a Gaussian smearing of 2.7 % for central electrons and 5 % for plug electrons in the simulation was needed. This was also determined iteratively. Table 5.2.1 summarizes the values for adapting simulation to data.

Figure 5.2.5 shows the invariant mass distribution for central-central and central-plug electron pairs before and after calibration.

5.3 Efficiencies, backgrounds and counting of signal events

Whereas the theoretical cross section estimates are obtained for nearly "on mass-shell" Z boson production, the data contains also off-shell Z boson production and backgrounds. These measurements have to be corrected for efficiency and background in order to obtain a meaningful comparison with the prediction. For the Z signal all candidate events are counted within $\pm\, 2\,\sigma$ around the Z mass peak, as determined by a Gaussian fit. Then the background is subtracted (including γ^*/Z events), which is defined by a sideband-method, namely the number of all events found in the region between $(3 - 5)\ \sigma$ on both sides of the Z mass peak. Figure 5.3.1 illustrates the definition of signal and background regions.

Alternatively, the background was estimated by fitting the M_{ee}-distribution between 40 GeV and 160 GeV with a sum of an exponential function of the form $\gamma e^{\frac{x-x_1}{x_1}}$ and a function of the form $\alpha \left(\frac{x}{x_0}\right)^{\beta}$, where x_0 and x_1 are constants and α, β and γ are parameters of the fit. x is the invariant electron-positron (Z) mass. The constant x_0 was chosen in such a way that the fit of the background would follow the background-behavior at small invariant masses, whereas the exponential function with its constant x_1 describes the background at higher energies. This method was motivated by the fact that the electron quality combinations used for the definition of the Z signal exhibit an excess of events at around 70 GeV. Especially in the central-central case, this excess is dominating the lower quality combinations where also more background is expected. Nevertheless, the shape of the background remains the same in all combinations. Therefore, the function described above plus a Gaussian

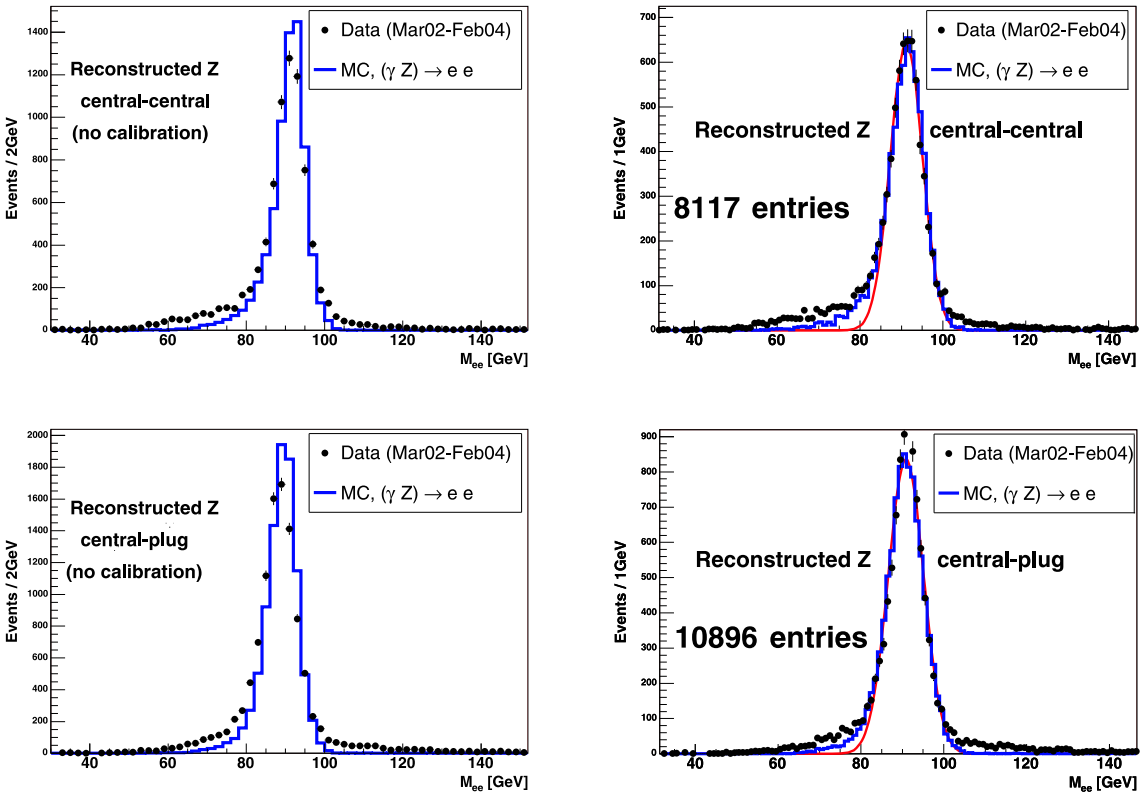

Figure 5.2.5: The invariant mass distribution of accepted electron pairs. The Gaussian fit to the data between 80 GeV and 100 GeV is shown in red for the energy corrected data. The Monte Carlo simulation is normalized to the number of events found within $\pm 2\,\sigma$ around the fitted Z mass peak.

function was fitted to the sample comprising the largest background (bronze-bronze), see Figure 5.3.2. This background-shape was then scaled and used to determine the background in the signal sample.

Figure 5.3.3 shows the result of the fit for the background (without the Gaussian function) in the signal sample used for counting Z bosons.

Depending on the background estimation - either by the sideband-technique or the fitting-method - the final results on the luminosity differ by 2.8%. Since the luminosity estimate for the sideband-method is more robust under changes of the selection cuts, this analysis is carried out via the sideband-technique.

5.3.1 Reconstruction efficiency and background subtraction

The Z reconstruction efficiency is defined as follows: All events which are generated in the invariant mass range 91.2 $\pm$ 7.5 ($= 3\Gamma_Z$) GeV (nearly "on-shell") and with a rapidity of $|Y| < 2$ are counted. The efficiency then is given by the ratio between the number of all accepted events and all generated nearly on-shell Z events. This is

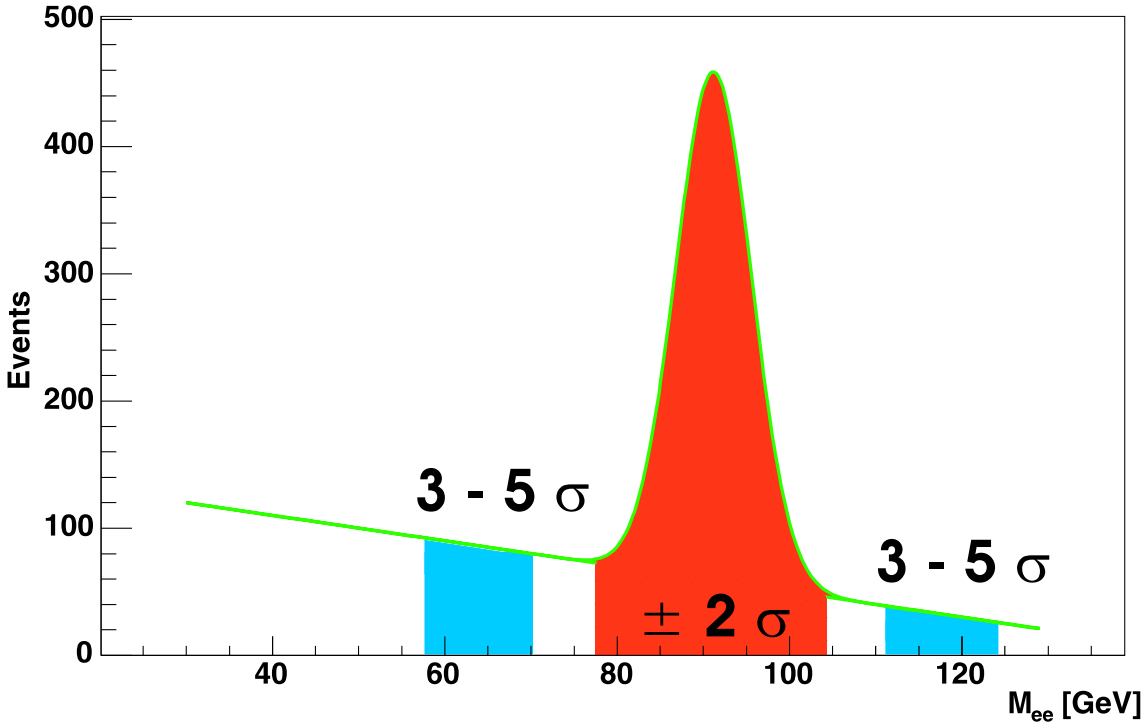

Figure 5.3.1: A sketch of the Z boson mass peak. In red the signal region with Z boson events and background, in blue the sidebands which only contain background events.

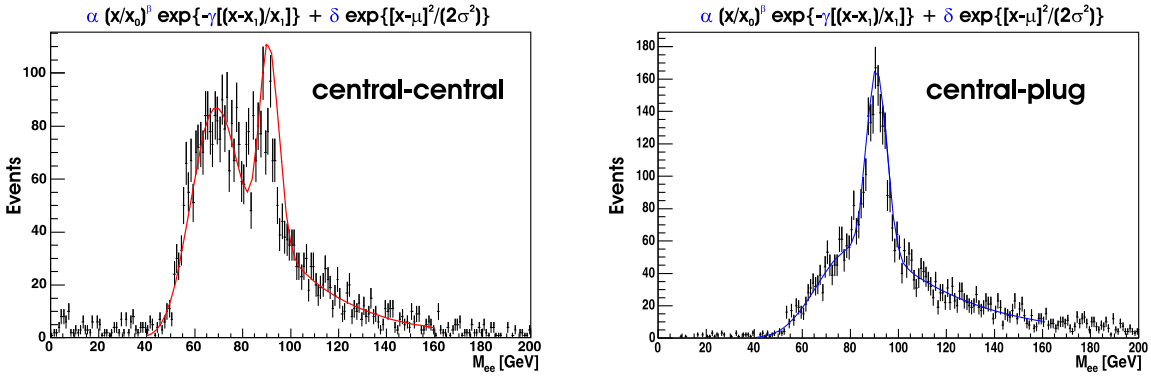

Figure 5.3.2: The bronze-bronze electron combination for central-central and central-plug Z bosons. Data is shown with its error bars and the fit as a solid line.

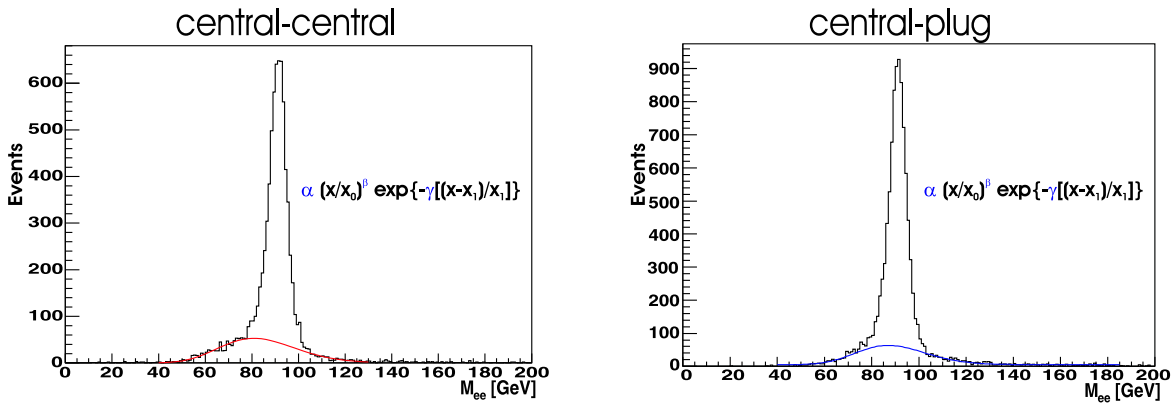

Figure 5.3.3: Z boson candidate events for central-central and for central-plug electrons. The fits of the background are indicated in red and blue with a $\frac{\chi^2_{\mathrm{cc}}}{\mathrm{n.d.f.}} = \frac{55}{47}$ and $\frac{\chi^2_{\mathrm{cp}}}{\mathrm{n.d.f.}} = \frac{60}{47}$, respectively.

done for central-central and central-plug events separately and shown in Figure 5.3.4. An average reconstruction efficiency for central-central Z bosons of 11.2 % ± 0.1 % and for central-plug Z bosons of 17.1 % ± 0.2 % was obtained.

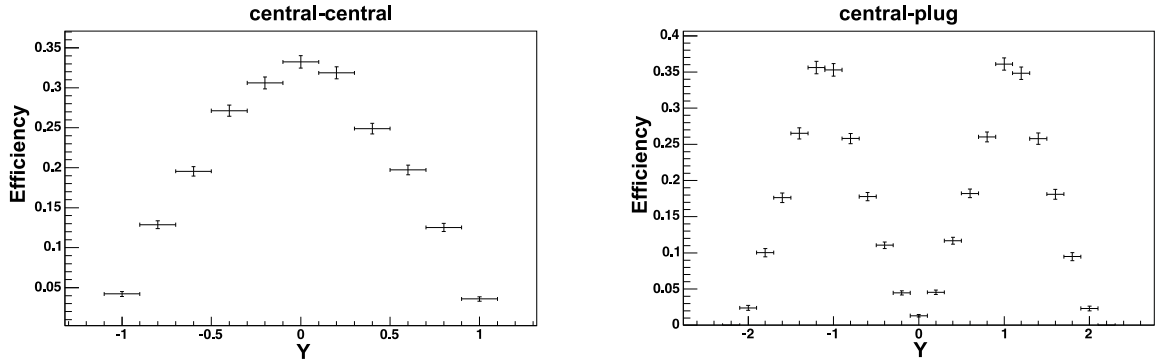

Figure 5.3.4: The shape of the Z-reconstruction efficiency as a function of rapidity for central-central and central-plug electrons, only statistical errors are plotted.

This reconstruction efficiency accounts for events, which are generated on-shell but possibly reconstructed also in the off-shell region. On the other hand, a correction for Z boson events coming from the mass-region outside the narrow width approximation is necessary, the so-called "Z-migration". For this, one has to investigate the number of events, which are generated with a Z boson mass outside the 91.2 ± 7.5 ($= 3\Gamma_Z$) GeV mass-range but reconstructed either inside the signal region or inside the sidebands. An additional 2.5 % of Z boson events are reconstructed inside the signal region, even though they are generated outside this mass-window. Figure 5.3.5 shows the distribution in this case. In Figure 5.3.6 the signal region of Figure 5.3.5 is shown as a two-dimensional plot for the generated and reconstructed mass.

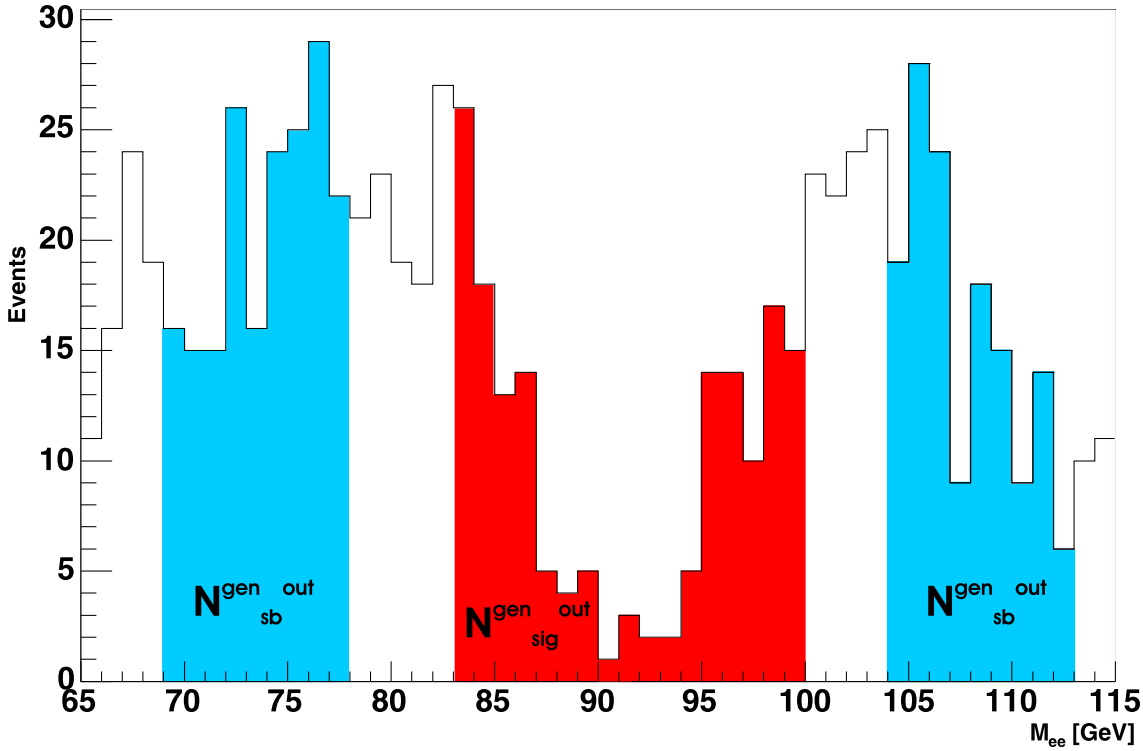

Figure 5.3.5: The distribution from simulation for reconstructed Z bosons which are generated "off-shell". In red the events which are reconstructed in the signal region, in blue those events which are reconstructed in the sidebands.

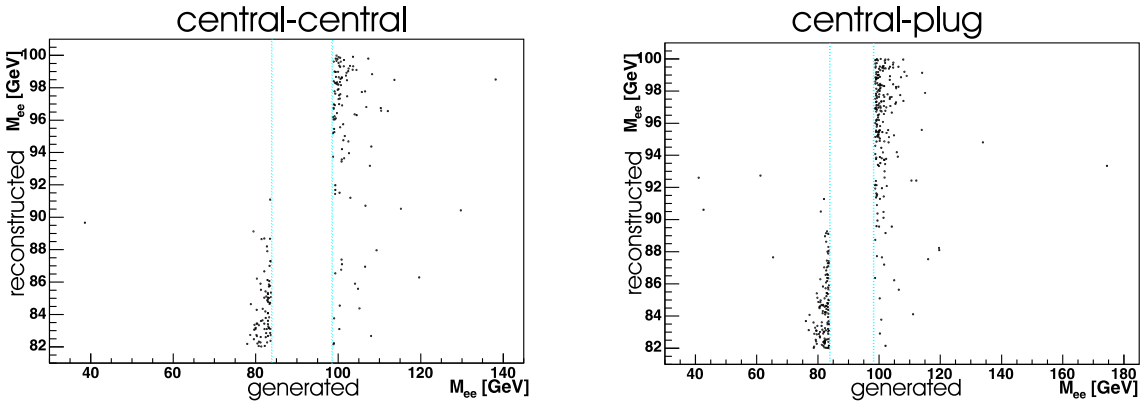

Figure 5.3.6: A two-dimensional plot for the reconstructed and generated mass of Z boson candidate events, which are generated "off-shell" but reconstructed inside the counting region. The region for "on-shell" generated Z bosons is located in between the two blue dashed lines.

Actually, it turns out that the background is overestimated, if the correction is not applied. This is calculated in the following:

$$\Delta N = N_{\mathrm{sb}}^{\mathrm{gen\,out}} - N_{\mathrm{sig}}^{\mathrm{gen\,out}} , \tag{5.3.1}$$

where ΔN is the number of additional events in the signal region after background subtraction, $N_{\mathrm{sb}}^{\mathrm{gen\,out}}$ is the number of Z boson events generated outside the $3\Gamma_{\mathrm{Z}}$-window and reconstructed inside the sidebands and $N_{\mathrm{sig}}^{\mathrm{gen\,out}}$ are the events reconstructed in the signal region. $N_{\mathrm{sb}}^{\mathrm{gen\,out}}$ can then be expressed via

$$N_{\mathrm{sb}}^{\mathrm{gen\,out}} = (1+f) N_{\mathrm{sig}}^{\mathrm{gen\,out}} , \tag{5.3.2}$$

with $f = \frac{\Delta N}{N_{\mathrm{sig}}^{\mathrm{gen\,out}}}$ or

$$\Delta N = f N_{\mathrm{sig}}^{\mathrm{gen\,out}} . \tag{5.3.3}$$

Moreover, $N_{\mathrm{sig}}^{\mathrm{gen\,out}}$ can be written as

$$N_{\mathrm{sig}}^{\mathrm{gen\,out}} = \epsilon_{\mathrm{reco}}^{\mathrm{out}} N_{\mathrm{tot}}^{\mathrm{gen\,out}} , \tag{5.3.4}$$

where $\epsilon_{\mathrm{reco}}^{\mathrm{out}}$ is the efficiency to reconstruct events in the signal region which are generated outside the $3\,\Gamma_{\mathrm{Z}}$-window, namely $N_{\mathrm{tot}}^{\mathrm{gen\,out}}$. This leads to

$$\Delta N = f \epsilon_{\mathrm{reco}}^{\mathrm{out}} N_{\mathrm{tot}}^{\mathrm{gen\,out}} . \tag{5.3.5}$$

Obviously, the total number of events which are generated, $N_{\mathrm{tot}}^{\mathrm{gen\,in/out}}$, is the sum of the events which are generated with the narrow width approximation, $N_{\mathrm{tot}}^{\mathrm{gen\,in}}$, and $N_{\mathrm{tot}}^{\mathrm{gen\,out}}$:

$$N_{\mathrm{tot}}^{\mathrm{gen\,in/out}} = N_{\mathrm{tot}}^{\mathrm{gen\,in}} + N_{\mathrm{tot}}^{\mathrm{gen\,out}} \tag{5.3.6}$$

Rewriting $N_{\mathrm{tot}}^{\mathrm{gen\,out}}$ as

$$N_{\mathrm{tot}}^{\mathrm{gen\,out}} = (m-1) N_{\mathrm{tot}}^{\mathrm{gen\,in}} , \tag{5.3.7}$$

with $m = \frac{N_{\mathrm{tot}}^{\mathrm{gen\,in/out}}}{N_{\mathrm{tot}}^{\mathrm{gen\,in}}}$ leads finally to

$$\Delta N = f \epsilon_{\mathrm{reco}}^{\mathrm{out}} (m-1) N_{\mathrm{tot}}^{\mathrm{gen\,in}} , \tag{5.3.8}$$

where all quantities can be extracted from the Monte Carlo simulation. Without Z-migration one would write:

$$N_{\mathrm{tot}}^{\mathrm{gen\,in}} = \frac{N_{\mathrm{reco}}^{\mathrm{in}} - N_{\mathrm{bkg}}^{\mathrm{in}}}{\epsilon_{\mathrm{cut}}^{\mathrm{in}}} \tag{5.3.9}$$

Here, $N^{\text{in}}_{\text{reco}}$ indicates the number of reconstructed events inside the signal region, $N^{\text{in}}_{\text{bkg}}$ the reconstructed events inside the sidebands and $\epsilon^{\text{in}}_{\text{cut}}$ the efficiency to detect these from the generated events $N^{\text{gen in}}_{\text{tot}}$. In data, there is no narrow width approximation and thus Z-migration has to be considered and the correction ΔN has to be included:

$$N^{\text{in}}_{\text{reco}} - N^{\text{in}}_{\text{bkg}} = \epsilon^{\text{in}}_{\text{cut}} N^{\text{gen in}}_{\text{tot}} + \Delta N \,, \tag{5.3.10}$$

which gives

$$N^{\text{gen in}}_{\text{tot}} = \frac{N^{\text{in}}_{\text{reco}} - N^{\text{in}}_{\text{bkg}}}{\epsilon^{\text{in}}_{\text{cut}} + f\epsilon^{\text{out}}_{\text{reco}}(m-1)} \,, \tag{5.3.11}$$

where $f\epsilon^{\text{out}}_{\text{reco}}(m-1)$ is a small but negative number in this case and accounts for the actual additional Z boson events in the signal region which were neglected before.

An additional correction for the Z counting is thus obtained, leading to an increase in the number of counted Z bosons by 1.3 % from electrons both reconstructed in the central calorimeter and by 0.5 % where one electron ends up in the plug calorimeter.

5.3.2 Correction for the main vertex distribution

A z-vertex cut of $|z| < 60\,\text{cm}$ is traditionally applied for high p_{T} physics at CDF and thus introduces an efficiency loss. This does not apply for the luminosity measurement of the CLC monitors, since they measure the interactions over the entire collision region along the beam line. However, in our analysis the z-vertex cut is applied and has to be taken into account. Due to larger inefficiencies at large z_{event} positions, in particular for trigger and tracking, events boosted inside the detector were examined. "Inside the detector" means precisely that the sign of p_{z} of the Z boson and the sign of the z-vertex value are opposite. Since these events have better acceptance, they provide a more reliable measurement and therefore reduce the error, which may occur from other inefficiencies. For the preselected data and simulation the z_{event} distribution is presented in Figure 5.3.7.

Fitting both distributions with a Gaussian function, a width $\sigma = 32.0\,\text{cm}$ for data and $\sigma = 27.6\,\text{cm}$ for Monte Carlo was obtained. Due to the broader distribution in data, an efficiency correction factor for the z-vertex cut of 0.967 was necessary. This inefficiency has to be included on top of the actual Monte Carlo z-vertex inefficiency.

5.3.3 Trigger efficiencies

As already mentioned in section 5.2, the trigger ELECTRON_CENTRAL_18 was used for this analysis. It requires one cluster in the central calorimeter with transverse energy of $E_{\text{T}} > 18\,\text{GeV}$ and an associated track with $p_{\text{T}} > 8\,\text{GeV}$. In addition, the ratio of hadronic to electromagnetic energy has to be smaller than one eighth. To estimate its efficiency the W_NOTRACK trigger was applied in coincidence with the

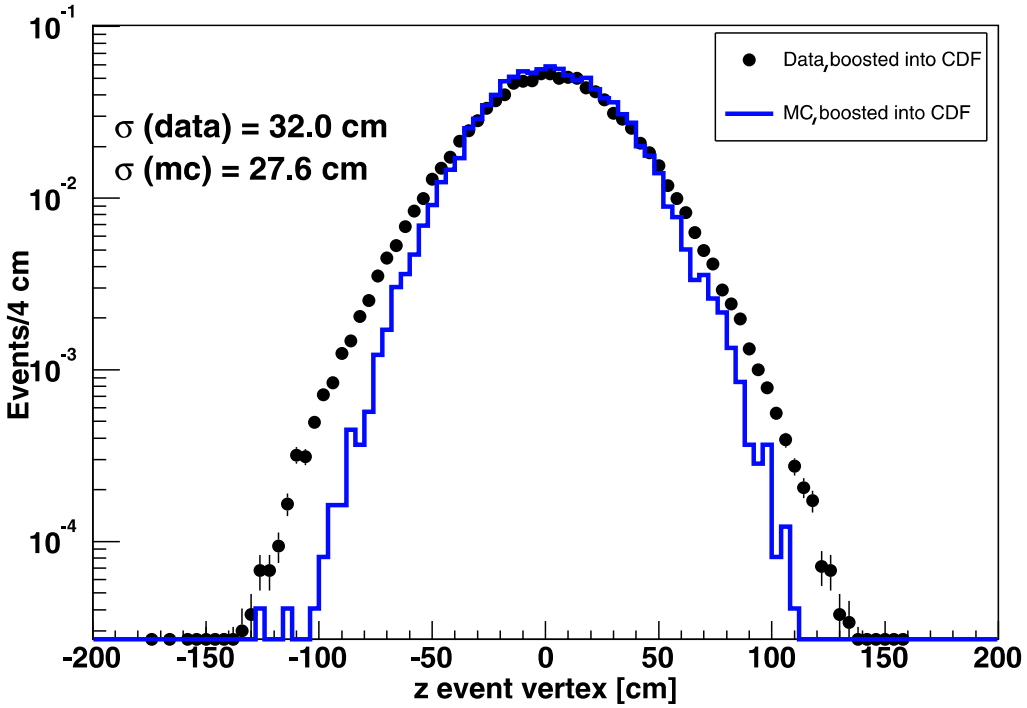

Figure 5.3.7: The z-vertex distribution for events boosted into the detector, for data and Monte Carlo simulation.

ELECTRON_CENTRAL_18 trigger. Taking the ratio between all events triggered by both and the events which are triggered only by the W_NOTRACK trigger, an overall average trigger efficiency for the ELECTRON_CENTRAL_18 trigger of 97.5% was found. The trigger efficiency depends on the electron pseudorapidity and on the quality of the electron, as shown in Figure 5.3.8, and moreover, also on the time period. Values between 93.9 % and 99.9 % for the different time periods were found and are tabulated in Table 4.2.1. Clearly visible is the drop of the efficiency for the ELECTRON_CENTRAL_18 trigger in the center of the detector. This is due to the spacer bars at $\eta = 0$ which cause track-finding inefficiencies. Since the W_NOTRACK trigger does not require any tracking, it is efficient also at $\eta = 0$.

5.4 Determination of the luminosity

The luminosity L is determined by counting signal events, N_{signal}. Both quantities are linked by the following equation:

$$L = \frac{N_{\text{signal}}}{\sigma_{\text{NNLO}} \cdot \epsilon_{\text{reco}} \cdot \epsilon_{\text{trigger}} \cdot \epsilon_{\text{corr}}} \tag{5.4.1}$$

σ_{NNLO} denotes the NNLO theoretical cross section of 209.41 pb for inclusive Z boson production at a center of mass energy $\sqrt{s} = 1.96$ TeV and for a rapidity range

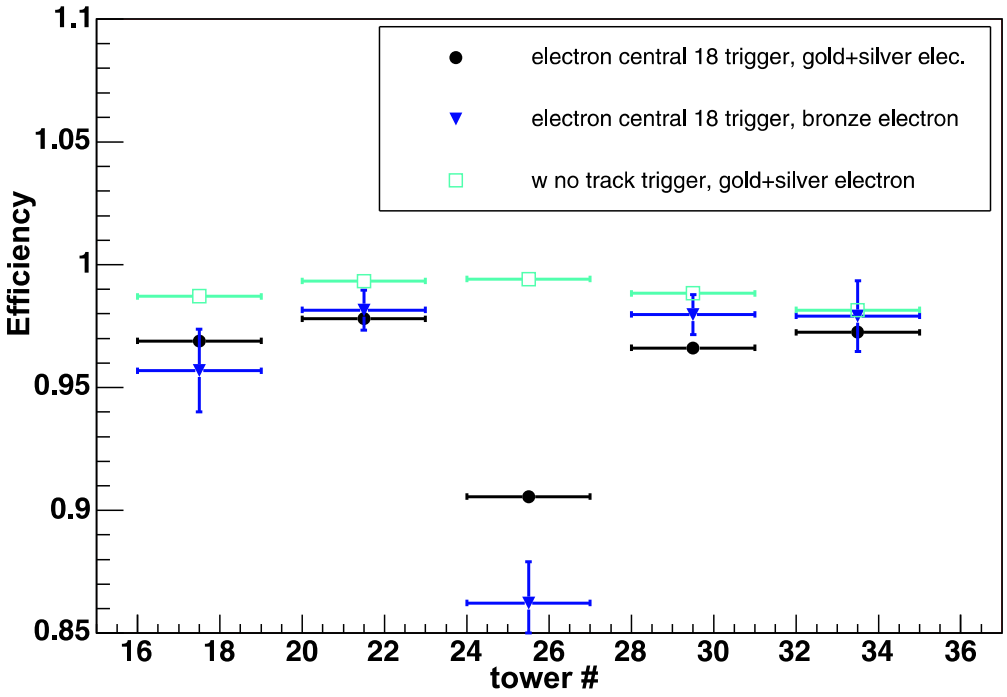

Figure 5.3.8: The trigger efficiencies with statistical errors for the electron qualities for the ELECTRON_CENTRAL_18 trigger and the W_NOTRACK trigger as a function of the calorimeter tower number in η.

$|Y| < 2$. For Z bosons originating from two central electrons, a reconstruction efficiency of $\epsilon_{\text{reco}} = 11.2\,\% \pm 0.1\,\%$ is obtained, and for Z bosons from one central electron and one plug electron one gets an efficiency of $\epsilon_{\text{reco}} = 17.1\,\% \pm 0.2\,\%$. The reconstruction efficiency is defined by the ratio of accepted events in the Monte Carlo simulation and the generated events. All events have to fulfill the two conditions that $|91.2\text{ GeV} - M_{\text{gen}}| < 3\,\Gamma_{\text{Z}}$ and $|Y| < 2$. The trigger efficiency of the ELECTRON_CENTRAL_18 trigger varies slightly over the time periods. $\epsilon_{\text{trigger}}$ was estimated in coincidence with the W_NOTRACK trigger. A mean value of 99.8 % for central-central electrons and 95.6 % for central-plug electrons is obtained. The efficiency correction ϵ_{corr} for the z-vertex cut of $|z_{\text{event}}| < 60$ cm which has to be included on top of the actual vertex inefficiency, obtained from simulation, is found to be 96.7 %. This is due to the fact that the efficiency of this cut is lower in data than in simulation. Table 5.4.1 provides an overview of luminosity estimates, signal events, background events and efficiencies for each time period as well as for the total period. Both luminosity measurements from Z bosons in the central-central and in the central-plug calorimeter agree with the luminosity estimates of the CLC monitors, taking into account the systematic uncertainty of roughly 5 % dominated by the theoretical predictions and the 6 % uncertainty on the CLC measurement.

The combined luminosity of central-central and central-plug Z bosons yields $L_{\mathrm{cc/cp}} = 221.7 \pm 2.8\,(\mathrm{stat.}) \pm 11.1\,(\mathrm{sys.})\ \mathrm{pb}^{-1}$ and shows good agreement with the CLC measurement of $L_{\mathrm{CLC}} = 222.2 \pm 12.9\,\mathrm{pb}^{-1}$. The systematic uncertainty is discussed in the following.

5.5 Systematic uncertainties and detector stability checks

As seen in equation 5.4.1, systematic uncertainties have to be examined for each of the following factors. The systematic error on N_{Signal} $\left(= \frac{S_Z}{\epsilon}\right)$ was estimated by observing the luminosity change if the signal and background region used for the counting was broadened or narrowed, including efficiency corrections. In detail, the fitted width of the Z mass peak of $\sigma = 4.4\mathrm{GeV}$ was varied between $\sigma = 3.75\mathrm{GeV}$ and $\sigma = 5.0\,\mathrm{GeV}$. Stable counting results for central-central electrons and central-plug electrons were found within 0.9 % and 2.2 % respectively. For the trigger efficiency $\epsilon_{\mathrm{trigger}}$ the systematic error was determined by its statistical error, namely the error on the number of events which were triggered by both, the ELECTRON_CENTRAL_18 trigger and the W_NOTRACK trigger. The introduced error ranges from 0.2 % up to 0.4 % in the rapidity region $-2 < Y < 2$ and is thus negligible. To estimate the systematic uncertainty on the basic selection cuts (see Figure 5.2.2) which were used to define the different electron qualities, the simulated events were weighted with respect to the data, the new efficiencies calculated and the luminosity change - after the repetition of the whole analysis - was recorded. This was done independently for Z bosons originating from both central electrons and for Z bosons where one electron is reconstructed inside the plug detector. Except for the cut on $\frac{E_{\mathrm{had}}}{E_{\mathrm{em}}}$ all the systematic errors are negligible. A luminosity variation of 0.4 % in both cases was found. The discussion of the theoretical uncertainties was presented in detail in section 4.2. Table 5.5.1 gives a summary of all studied systematic uncertainties.

A total systematic error of roughly 5 % is obtained. This error exceeds by far the combined statistical error for Z bosons from central-central electrons and central-plug electrons, which amounts to 1.2 %. Thus, the theoretical uncertainties limit the accuracy. For comparison, the total systematic error, where the measurement is based on the fit-method for the background, is around 6 %. The increase here is mainly due to the larger systematic error on N_{Signal}.

5.5.1 Stability checks

The analyzed data was divided into twelve sub-samples (see Table 5.1.1) in order to check the counting stability over time with respect to the CLC luminosity estimates. This was done for central-central and central-plug Z bosons separately. The number of Z bosons were counted in each period and divided by the CLC luminosity estimate, including the trigger efficiency corrections. Figure 5.5.1 presents the result.

data period	sample type	signal ev.	bckg. ev.	$\epsilon_{\text{trigger}}$	$L_{\text{p}\bar{\text{p}}}$(Z) [pb^{-1}]	$L_{\text{p}\bar{\text{p}}}$(CLC) [pb^{-1}]	ratio: $L_{\text{p}\bar{\text{p}}}$(Z)/ $L_{\text{p}\bar{\text{p}}}$(CLC)
1	Z cc	705	74	0.998	28.5 ± 1.1	26.6	1.07 ± 0.04
	Z cp	1046	89	0.960	27.3 ± 0.8	26.6	1.03 ± 0.03
2	Z cc	505	45	0.998	20.4 ± 0.9	19.4	1.05 ± 0.05
	Z cp	751	61	0.963	19.6 ± 0.7	19.4	1.03 ± 0.04
3	Z cc	385	30	0.998	15.5 ± 0.8	14.3	1.08 ± 0.06
	Z cp	568	40	0.957	14.8 ± 0.6	14.3	1.03 ± 0.04
4	Z cc	215	22	0.997	8.7 ± 0.6	8.5	1.03 ± 0.07
	Z cp	317	31	0.939	8.3 ± 0.5	8.5	1.03 ± 0.06
5	Z cc	327	31	0.998	13.2 ± 0.7	12.5	1.06 ± 0.06
	Z cp	461	51	0.973	12.1 ± 0.6	12.5	0.97 ± 0.04
6	Z cc	378	44	0.998	15.3 ± 0.8	14.9	1.03 ± 0.05
	Z cp	511	52	0.951	13.4 ± 0.6	14.9	0.90 ± 0.04
7	Z cc	362	32	0.998	14.6 ± 0.8	13.3	1.10 ± 0.06
	Z cp	451	46	0.954	11.8 ± 0.6	13.3	0.89 ± 0.04
8	Z cc	411	37	0.998	16.6 ± 0.8	14.9	1.11 ± 0.05
	Z cp	515	47	0.960	13.4 ± 0.6	14.9	0.90 ± 0.04
9	Z cc	406	60	0.999	16.4 ± 0.8	18.2	0.90 ± 0.04
	Z cp	690	56	0.964	18.0 ± 0.7	18.2	0.99 ± 0.04
10	Z cc	544	51	0.998	22.0 ± 0.9	21.9	1.00 ± 0.04
	Z cp	803	61	0.957	21.0 ± 0.7	21.9	0.96 ± 0.03
11	Z cc	727	74	0.998	29.4 ± 1.1	29.0	1.01 ± 0.04
	Z cp	1095	91	0.953	28.6 ± 0.9	29.0	0.99 ± 0.03
12	Z cc	745	76	0.997	30.1 ± 1.1	28.8	1.05 ± 0.04
	Z cp	1006	76	0.941	26.3 ± 0.8	28.8	0.91 ± 0.03
total	Z cc	5730	575	0.998	231.4 ± 3.1	222.2	1.04 ± 0.01
	Z cp	8223	713	0.956	214.9 ± 2.5	222.2	0.97 ± 0.01

Table 5.4.1: The data divided into several time periods. For each period there are two rows indicating events, efficiencies and luminosities for the two cases where on the one hand a Z is reconstructed from two electrons in the central calorimeter (Z cc), and on the other hand a Z is reconstructed from one central electron and one plug electron (Z cp). The corresponding CLC luminosity estimates (in pb^{-1}) are indicated as well. All given errors are of statistical nature. The statistical uncertainty of the CLC measurements are negligible.

Systematic error for:	Z cc	Z cp
N_{Signal}	0.9 %	2.2 %
$\epsilon_{\text{trigger}}$	0.4 %	0.2 %
ϵ_{cuts}	0.4 %	0.4 %
σ_{NNLO}	4.7 %	4.7 %
total	4.8 %	5.2 %

Table 5.5.1: An overview of the considered systematic errors for the inclusive luminosity measurement ($-2 < Y < +2$).

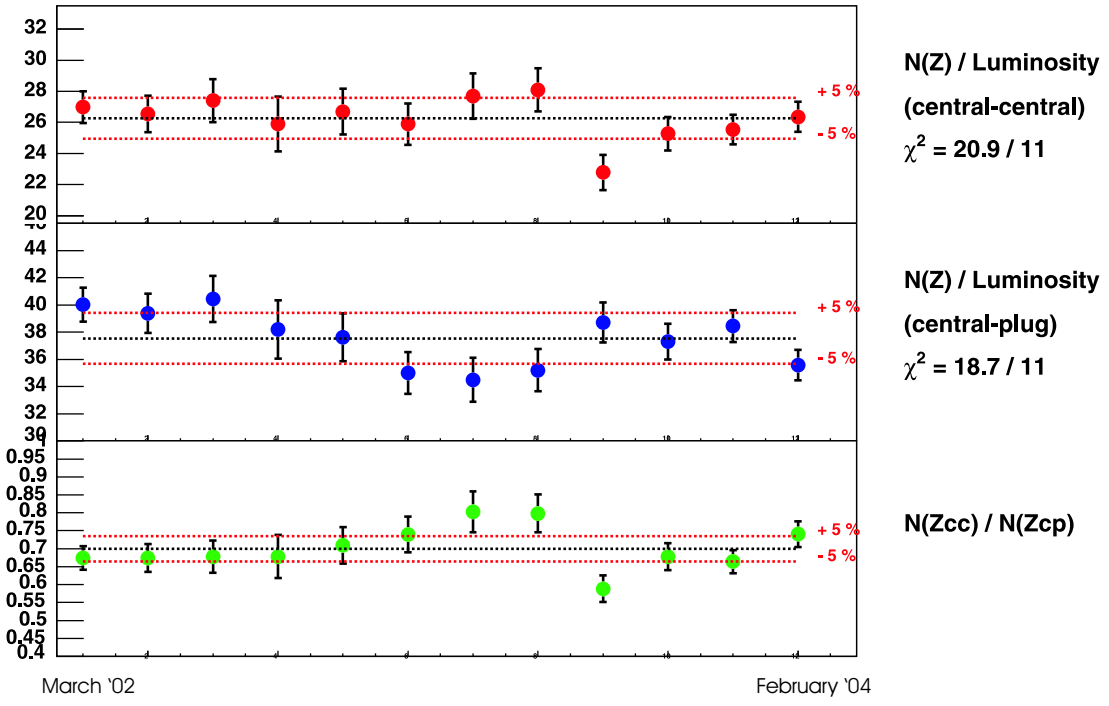

Figure 5.5.1: Ratios of the number of counted Z bosons and the corresponding CLC luminosity estimates. Indicated are also the mean values of these ratios and the $\pm 5\%$ line, which is approximately equivalent to the uncertainty of the CLC monitors. The bottom plot shows the ratio between the counting of Z bosons for central-central electrons and central-plug electrons. All error bars are purely statistical.

The data appears to be constant within $\pm 5\,\%$, corresponding approximately to the CLC monitor uncertainty. Nevertheless, in some time periods the ratio deviates more strongly from the mean value than in others, especially around the time period of April 2003. No particular reason could be found.

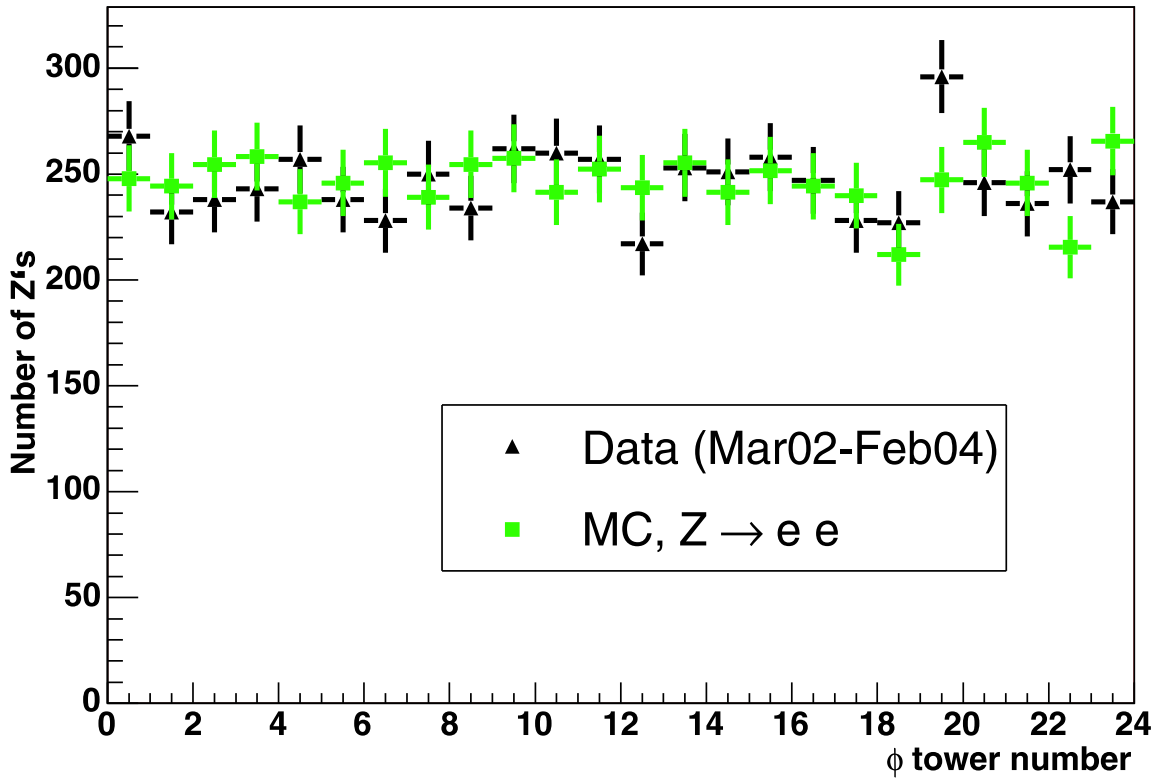

Figure 5.5.2: The number of Z bosons for data and simulation per calorimeter tower in the ϕ-direction is shown.

Also the homogeneity of the calorimeter in ϕ was checked as shown in Figure 5.5.2. Data and Monte Carlo simulation agree quite well and no evidence of significant inefficiencies were found. As expected, the number of Z bosons remains constant from tower to tower.

In order to check the energy calibration of the calorimeter in time, the uncorrected invariant mass of the two central-central and central-plug electrons for different run periods is plotted. A Gaussian fit of all candidate events between 87 GeV and 97 GeV in the respective run period is applied and the mean value taken as an estimate of the Z boson mass during this time. The result of this reconstructed Z mass scan in time is presented in Figure 5.5.3. The fluctuation of the Z boson mass estimates is within 1 GeV. To investigate the sensitivity of the analysis on the mean Z boson mass value, the Z boson counting was repeated, assuming a different mean mass value ($\pm$ 500 MeV) for the Z bosons in the whole data taking

period. The resulting luminosity change was recorded but no significant difference in the luminosity estimate was observed. In addition, the difference between the reconstructed Z mass of one central electron and one electron in the eastern plug calorimeter and the reconstructed Z mass of one central electron and one electron in the western plug calorimeter was examined, as shown in Figure 5.5.4. Only a small discrepancy of 300 MeV was found.

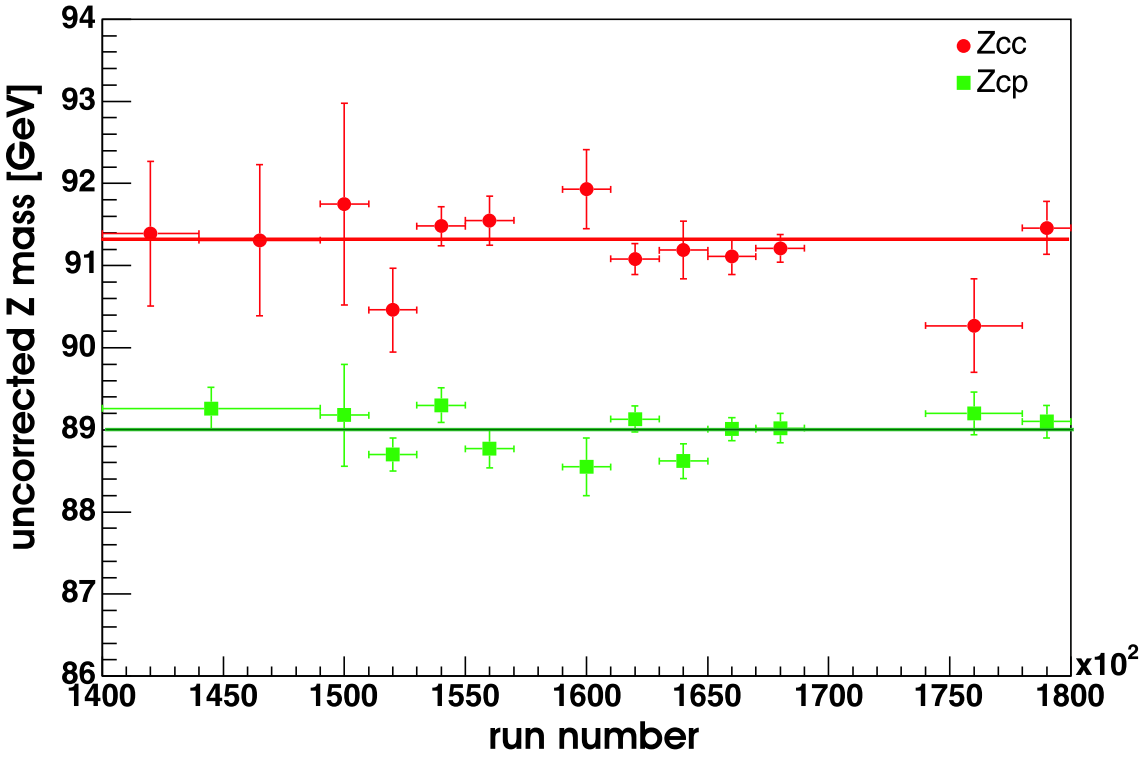

Figure 5.5.3: The change of the uncorrected invariant mass of two reconstructed electrons originating from Z boson candidate events for different run periods. The lines show the average value for central-central and central-plug electrons, respectively. The statistical uncertainties are shown as error bars.

5.5.2 Distributions of kinematic observables

In the following some kinematic variables are shown. The comparison is performed between the signal events in data and the PYTHIA predictions. For Z bosons reconstructed with central-central and central-plug electron pairs the rapidity distribution and the transverse momentum spectrum are presented in Figure 5.5.5 and Figure 5.5.7. Figure 5.5.6 and Figure 5.5.8 show the difference of the data and Monte Carlo predictions, plotting $\frac{\text{data}-\text{MC}}{\text{MC}}$. In the rapidity distribution as well as in the transverse momentum spectrum a good agreement between data and simulation is seen. To ensure that the rapidity is also well described within individual p_{T}-ranges, Figure 5.5.9 and Figure 5.5.10 display nine different spectra.

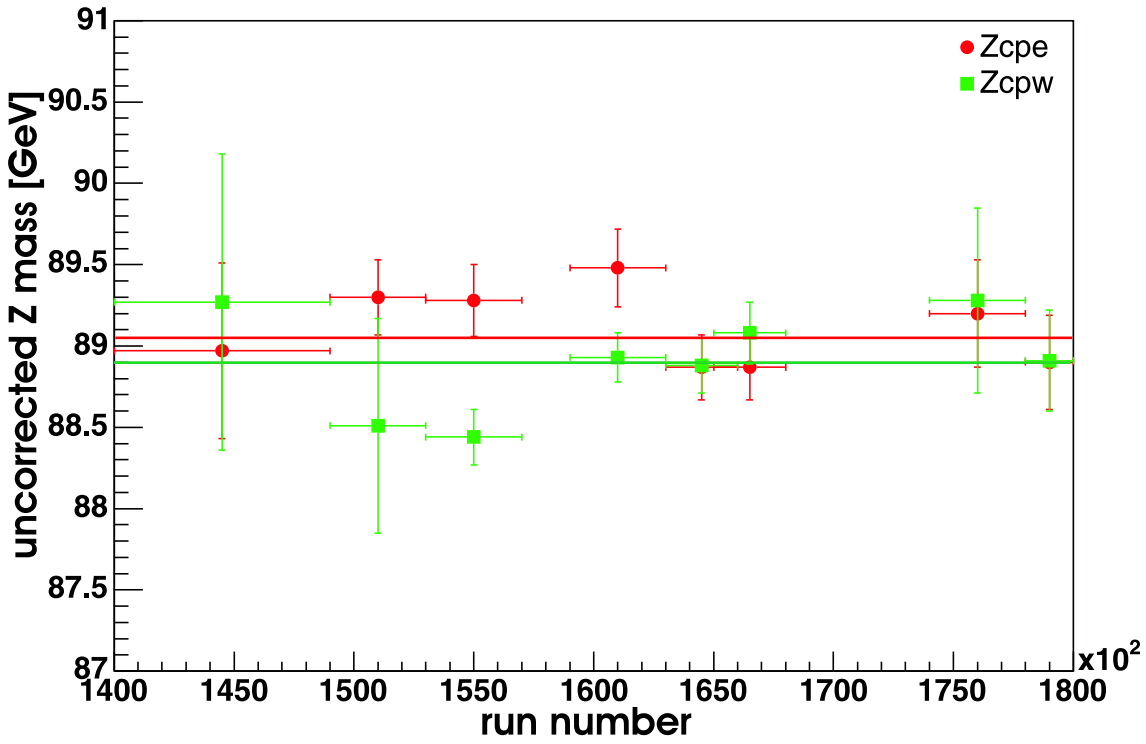

Figure 5.5.4: The difference between the uncorrected reconstructed Z boson mass for events with one central electron and one electron in the east-plug (Zcpe) on the one hand and one central electron and one electron in the west-plug (Zcpw) on the other hand, for different run periods. The lines show the average value of approximately 89.1 GeV for central-east-plug and approximately 88.8 GeV for central-west-plug electrons. The error bars indicate the statistical error.

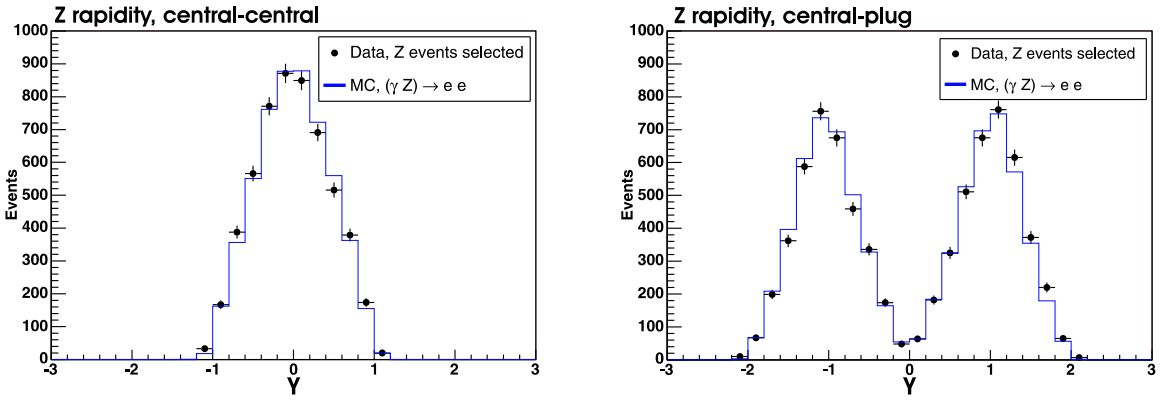

Figure 5.5.5: The rapidity distribution for Z bosons originating from central-central and central-plug electrons. The data is shown as dots with their statistical error and the Monte Carlo simulation as a blue line.

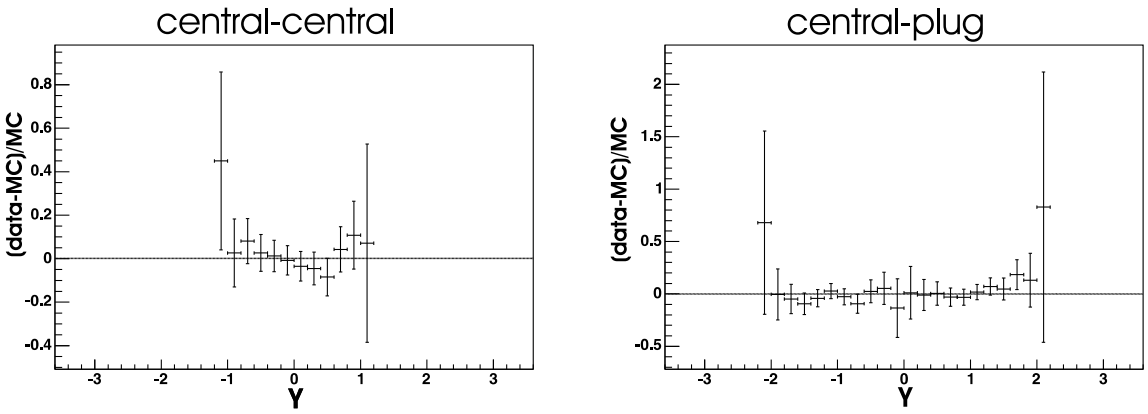

Figure 5.5.6: The relative difference in the number of reconstructed Z events between data and simulation per rapidity-bin after all cuts.

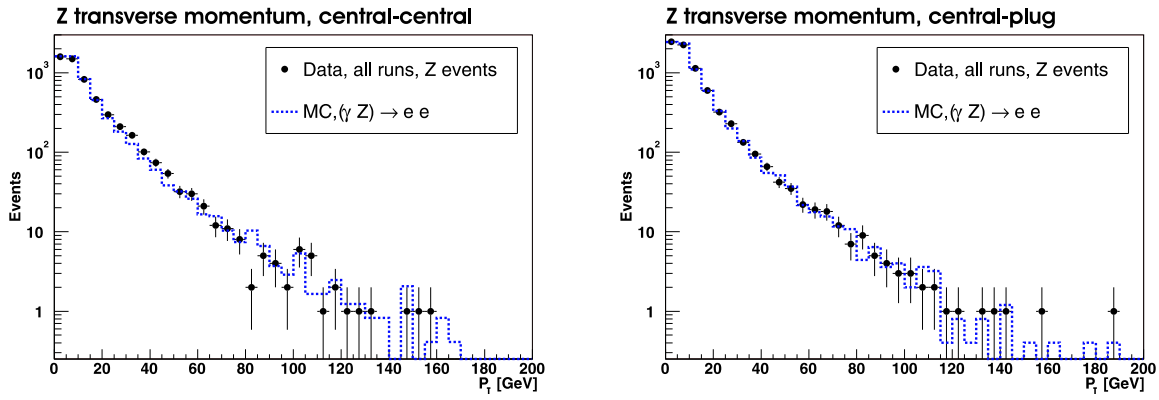

Figure 5.5.7: The transverse momentum of reconstructed Z bosons. The simulation is indicated with a dashed blue line and the data with points and their statistical error as error bars.

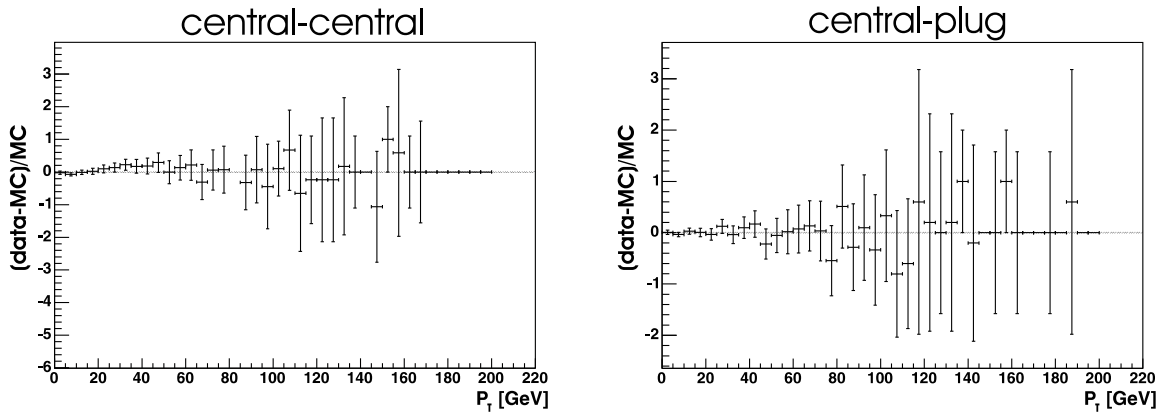

Figure 5.5.8: The relative difference in the number of reconstructed Z events between data and simulation per p_{T}-bin after all cuts.

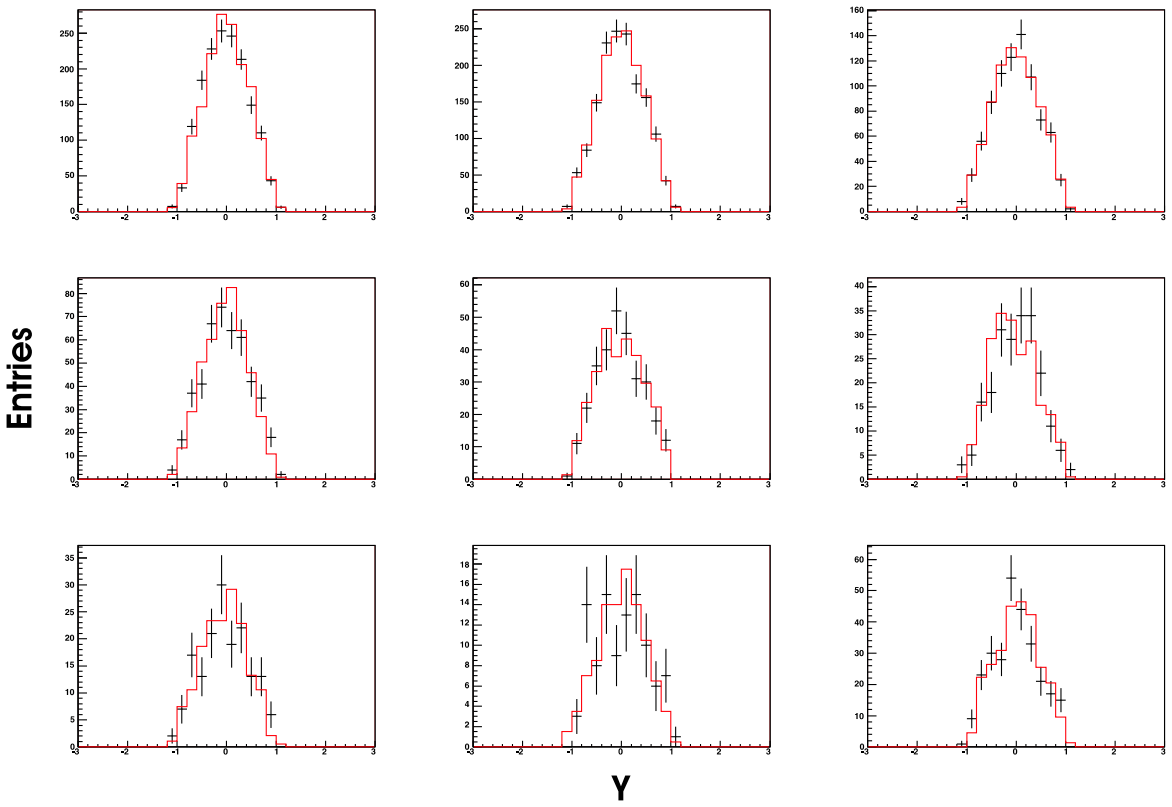

Figure 5.5.9: Rapidity distributions for central-central electrons for different p_T-regions. From the left to the right - Upper row: (0-5) GeV, (5-10) GeV, (10-15) GeV. Middle row: (15-20) GeV, (20-25) GeV, (25-30) GeV. Lower row: (30-35) GeV, (35-40) GeV , 40 GeV and above.

5.6 Study of the rapidity-dependence of Z production

Since the theoretical calculations allow for the first time to estimate the Z production as a function of rapidity, the whole analysis was repeated for single rapidity regions. The region of $-2 < Y < 2$ was divided into nine sub-regions and in each of these regions the number of Z bosons were counted with the method described above, again separately for central-central and central-plug electron pairs. The central calorimeter was divided equally into four regions and an additional part, $|Y| < 0.1$, to separate the area of the spacer bars from the rest of the calorimeter. Also the plug calorimeter was segmented into four regions. Although a higher granularity would have been preferable to determine more precisely the shape of the cross section, the number of Z boson events is not sufficient to keep a small statistical error in that case.

The method to obtain the reconstruction efficiency is the same as for the inclusive measurement. It was applied for each rapidity slice individually. As seen in section

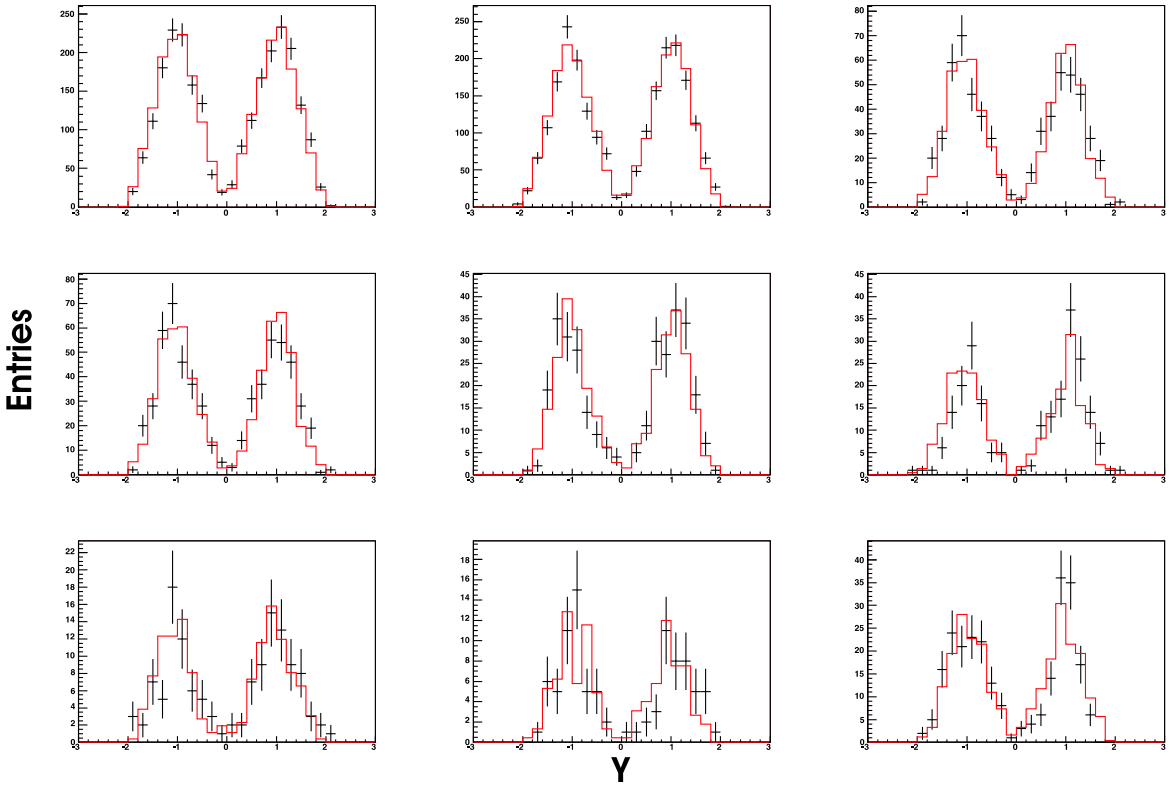

Figure 5.5.10: Rapidity distributions for central-plug electrons for different p_T-regions. From the left to the right - Upper row: (0-5) GeV, (5-10) GeV, (10-15) GeV. Middle row: (15-20) GeV, (20-25) GeV, (25-30) GeV. Lower row: (30-35) GeV, (35-40) GeV , 40 GeV and above.

5.3.1 the reconstruction efficiency depends on the mean Z boson mass. For the inclusive as well as for the differential analysis its world average value of 91.2 GeV is taken since it agrees within a few hundred MeV with the value found for the invariant mass distribution of accepted electron pairs.

Whereas the trigger efficiency for detecting Z bosons in the inclusive measurement for the full rapidity range ($|Y| < 2$) was given as an averaged result before, this trigger efficiency was measured in the differential measurement as a function of rapidity. In detail, the trigger efficiency for Z bosons in a certain rapidity region was determined by the efficiency to detect its corresponding electron or electrons, which - in most cases - will enter the calorimeter in a different rapidity region than the Z boson itself. Accordingly, the individual Z event is weighted with respect to the reciprocal efficiency of detecting its electrons in their rapidity region.

The z-vertex cut correction was applied for each rapidity region individually as well, since the corrections differ by up to 5% from region to region. However, a distinction between central-central electrons and central-plug electrons is not necessary, since a study of possible changes in the z-vertex correction showed a difference of merely 2 per mill. Figure 5.6.1 shows the z-vertex distribution for the individual rapidity

rapidity region	detector region	$\epsilon_{\text{trigger}}$	ϵ_{reco}	corr. fac.	$L_{\text{p}\bar{\text{p}}}$ $\pm \Delta_{\text{stat.}}$ $\pm \Delta_{\text{sys.}}$
$+2.0 < Y < +1.6$	central-plug	0.971	0.097	0.953	239.5 ± 13.2 ± 17.6
$+1.6 < Y < +1.1$	central-plug	0.975	0.250	0.946	232.8 ± 6.2 ± 12.3
$+1.1 < Y < +0.6$	central-central	0.999	0.085	0.968	229.2 ± 9.4 ± 9.6
	central-plug	0.967	0.259	0.968	207.2 ± 5.2 ± 8.6
$+0.6 < Y < +0.1$	central-central	0.998	0.239	0.972	217.2 ± 5.2 ± 9.8
	central-plug	0.951	0.090	0.972	204.3 ± 8.4 ± 8.7
$+0.1 < Y < -0.1$	central-central	0.997	0.308	0.963	234.1 ± 7.4 ± 9.2
	central-plug	0.951	0.013	0.963	304.7 ± 38.6 ± 18.6
$-0.1 < Y < -0.6$	central-central	0.998	0.237	0.975	227.4 ± 5.4 ± 8.6
	central-plug	0.954	0.088	0.975	207.3 ± 8.4 ± 9.3
$-0.6 < Y < -1.1$	central-central	0.999	0.088	0.965	225.9 ± 9.1 ± 10.1
	central-plug	0.967	0.251	0.965	215.1 ± 5.4 ± 8.9
$-1.1 < Y < -1.6$	central-plug	0.955	0.262	0.926	218.6 ± 5.9 ± 11.6
$-1.6 < Y < -2.0$	central-plug	0.955	0.094	0.968	215.5 ± 12.8 ± 18.1

Table 5.6.1: The data divided into several rapidity regions. The rapidity Y, the corresponding efficiencies, the correction factors for the z-vertex cut and the luminosity estimates with their statistical and systematic errors (in pb^{-1}) are indicated for central-central and central-plug Z bosons.

regions. The descrepancy between data and Monte Carlo especially in the rapidity region $1.1 < |Y| < 1.6$ could be induced by the position and energy misalignment of the plug calorimeter.

The corrections for the Z-migration of the inclusive measurement were applied also for the differential measurement. An accurate determination of this correction for the individual rapidity regions is not possible due to the statistical limitations. However, since the invariant mass of the electrons remains unchanged within its uncertainty between the individual rapidity regions, a very similar correction factor seems logical.

5.6.1 Corrections due to rapidity resolution

All efficiencies and corrections for the individual rapidity regions are listed in Table 5.6.1. Due to the finite resolution of the detector, it was taken care to correct for Z bosons, which were produced in a certain rapidity region but reconstructed in a different one. The necessary correction was obtained from Monte Carlo simulation and then applied to the data, as presented in Table 5.6.2. Figures 5.6.2 and 5.6.3 show the generated rapidity versus the reconstructed rapidity for central-central and central-plug Z bosons.

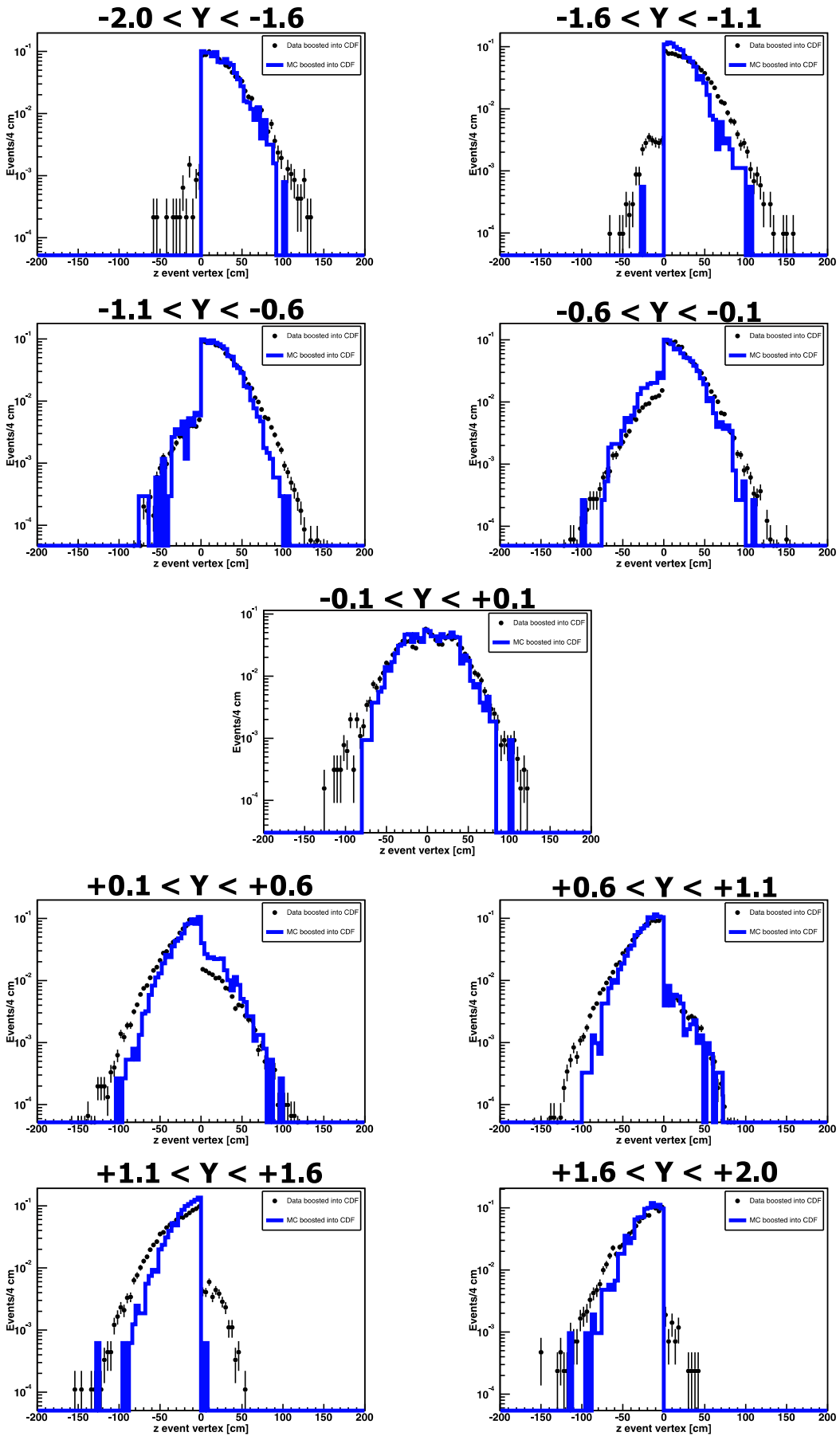

Figure 5.6.1: The z-vertex distributions for the different rapidity regions for events boosted inside the detector. The data is shown as dots with its statistical errors and the simulation as a solid line.

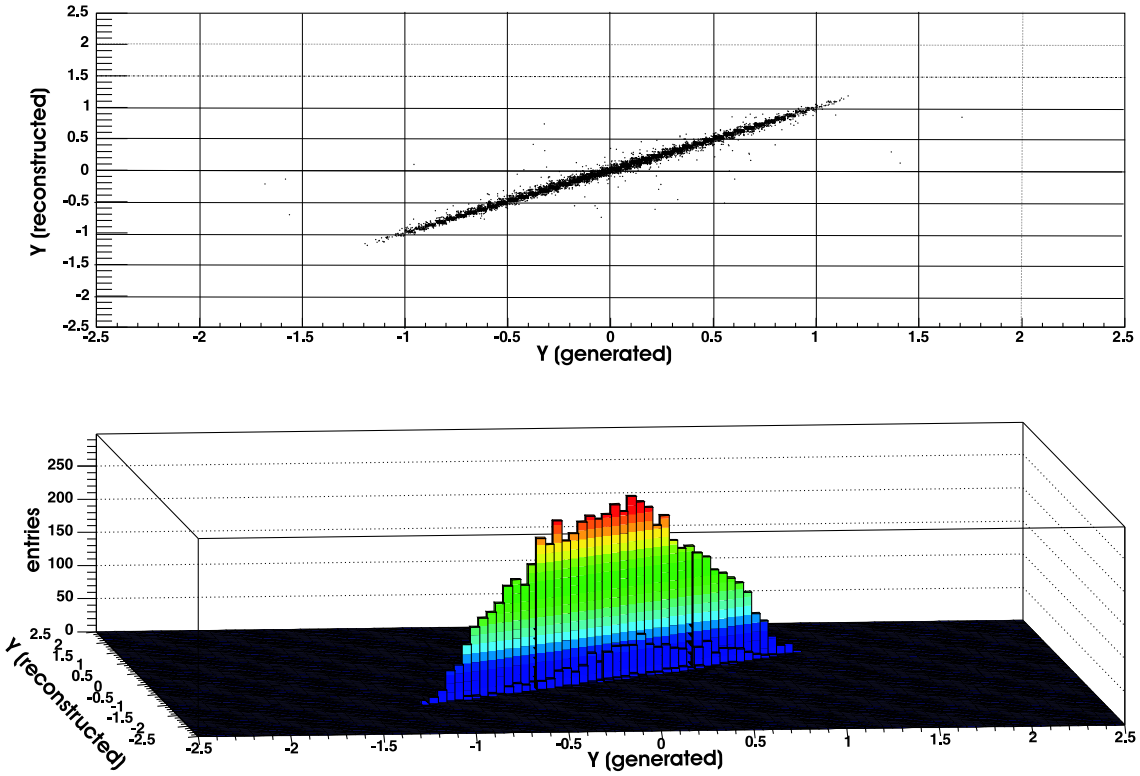

Figure 5.6.2: The generated versus the reconstructed rapidity is plotted for central-central Z bosons. Though the distribution is quite narrow, a correction for accurate counting of Z bosons in the individual rapidity bins is necessary.

The systematic uncertainty determination was repeated for the individual rapidity regions as described in section 5.5. As for the inclusive measurement, the main contribution to the systematic error is the uncertainty of the theoretical NNLO cross section calculation. The results are presented in Table 5.6.3. For central reconstructed Z events, the total systematic uncertainty remains between 4 % to 5 % in all the individual rapidity regions, whereas for Z events with larger rapidities, this uncertainty increases with increasing rapidity up to 8 %.

5.6.2 Differential cross section

The luminosity estimates for the different rapidity bins coincide all with each other within their statistical and systematic errors. The result is presented in Figure 5.6.4. For electrons from the central and the plug calorimeter this is also the case, even though the two rapidity regions above $Y = 1.1$ show higher luminosity values than the others. Possibly, this is due to a calibration asymmetry in energy and/or position for the east- and the west-plug calorimeter. The increase of luminosity in the central rapidity bin ($-0.1 < Y < 0.1$) for central-plug Z bosons is evident in this figure. However, the statistical uncertainty is large and the spacer bars in this region complicate accurate measurements. Figure 5.6.5 shows the combined result of both

rapidity region	detector region	gen. inside rap. region but rec. outside [%]	gen. outside rap. region but rec. inside [%]
$+2.0 < Y < +1.6$	central-plug	5.2 ± 1.0	5.9 ± 1.2
$+1.6 < Y < +1.1$	central-plug	3.0 ± 0.4	3.4 ± 0.4
$+1.1 < Y < +0.6$	central-central	1.4 ± 0.5	2.7 ± 0.6
	central-plug	2.8 ± 0.3	3.8 ± 0.4
$+0.6 < Y < +0.1$	central-central	2.2 ± 0.3	2.9 ± 0.4
	central-plug	6.5 ± 0.8	3.1 ± 0.5
$+0.1 < Y < -0.1$	central-central	8.4 ± 0.8	5.7 ± 0.7
	central-plug	38.8 ± 8.9	18.4 ± 6.1
$-0.1 < Y < -0.6$	central-central	2.4 ± 0.3	2.2 ± 0.3
	central-plug	6.2 ± 0.3	4.1 ± 0.8
$-0.6 < Y < -1.1$	central-central	0.9 ± 0.3	2.2 ± 0.4
	central-plug	3.5 ± 0.4	3.3 ± 0.3
$-1.1 < Y < -1.6$	central-plug	2.6 ± 0.3	4.1 ± 0.5
$-1.6 < Y < -2.0$	central-plug	5.6 ± 1.1	5.2 ± 1.0

Table 5.6.2: The rapidity-corrections with their statistical errors in the different detector and rapidity regions.

	N_{signal}		$\epsilon_{trigger}$		ϵ_{cuts}		σ_{NNLO}	total	
rapidity region	Z cc	Z cp	Z cc	Z cp	Z cc	Z cp	Z cc/cp	Z cc	Z cp
$+2.0 < Y < +1.6$		3.1 %		1.0 %		1.1 %	7.1 %		7.9 %
$+1.6 < Y < +1.1$		2.4 %		0.5 %		0.8 %	5.2 %		5.8 %
$+1.1 < Y < +0.6$	0.5 %	2.0 %	1.2 %	0.5 %	0.3 %	0.3 %	4.1 %	4.3 %	4.6 %
$+0.6 < Y < +0.1$	0.8 %	2.1 %	0.7 %	0.7 %	0.4 %	0.3 %	3.7 %	3.9 %	4.3 %
$+0.1 < Y < -0.1$	1.2 %	2.0 %	0.9 %	2.2 %	0.5 %	0.6 %	3.7 %	4.0 %	4.8 %
$-0.1 < Y < -0.6$	1.1 %	2.3 %	0.7 %	0.7 %	0.4 %	0.4 %	3.7 %	3.9 %	4.4 %
$-0.6 < Y < -1.1$	0.7 %	2.5 %	1.2 %	0.5 %	0.4 %	0.4 %	4.1 %	4.3 %	4.8 %
$-1.1 < Y < -1.6$		2.3 %		0.5 %		0.6 %	5.2 %		5.7 %
$-1.6 < Y < -2.0$		2.7 %		1.0 %		0.7 %	7.1 %		7.7 %

Table 5.6.3: An overview of the considered systematic uncertainties for the individual rapidity regions. The blank entries correspond to non-existing event types.

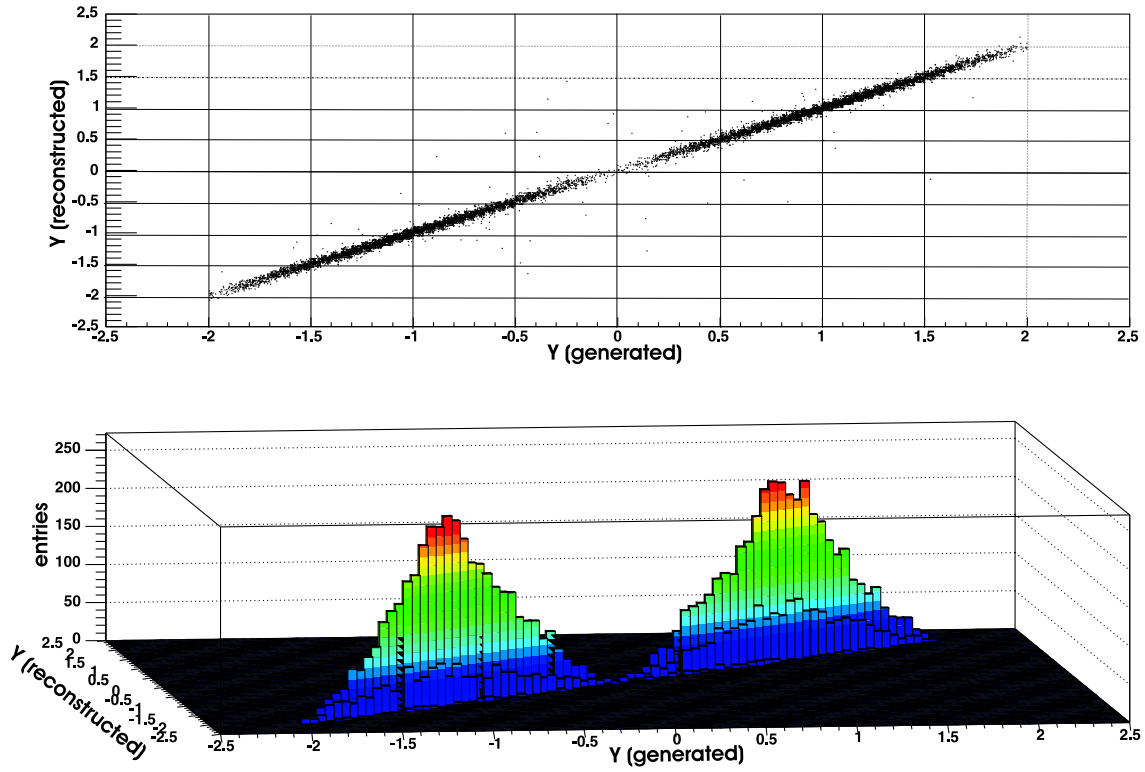

Figure 5.6.3: The generated versus the reconstructed rapidity is plotted for central-plug Z bosons. The double peak structure results from the fact that one electron has to be reconstructed inside the plug calorimeter.

measurements. Here, the increase in the central rapidity bin is much reduced and the luminosity estimate looks more reliable. Additionally, the ratio of the central-plug and the central-central luminosity measurement is plotted in Figure 5.6.6. On average, the counting of central-plug Z bosons leads to 3.4% less luminosity compared to the central-central Z counting. Nevertheless, the only luminosity measurement being outside one standard deviation with respect to all other measurements and the mean is again the rapidity region around $Y = 2$.

Figure 5.6.7 and Figure 5.6.8 show the shape of the differential cross section for on-shell Z boson production in the chosen rapidity bins. Taking the CLC luminosity estimate, the theoretical next-to-next-to-leading order calculations of the differential cross section agree within their errors with our estimates of the Z-rapidity dependence. An exception is the central rapidity region around $\eta = 0$ in the central-plug measurement, where the spacer bars are located. Moreover the statistical uncertainty is large there.

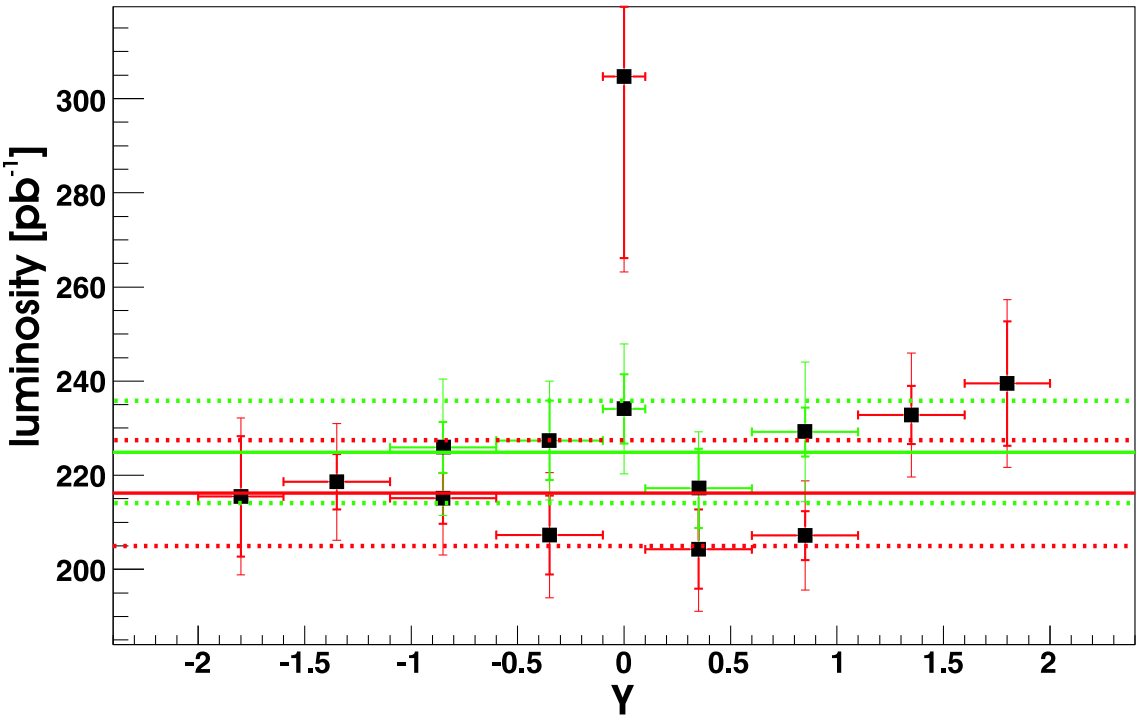

Figure 5.6.4: The measured luminosity in the different rapidity regions. Indicated in red is the luminosity for central-central Z bosons and in green for central-plug. The straight lines represent the mean value of the luminosity, the dotted ones indicate the systematic error on the mean. The statistical error on the individual measurements are shown in bold bars, the statistical plus systematic error are shown as thin error bars.

5.7 Summary

In this chapter the Z boson content of all CDF data between March 2002 and February 2004 was analyzed. This was done to obtain an alternative luminosity estimate with respect to the measurement of the CLC monitors. In total 13953 events were selected, almost 60 % of these from events with two electrons detected in the central calorimeter and about 40 % from events where one electron was measured in the central and the other in the plug calorimeter. Combining all events a total luminosity of $L_{\mathrm{cc/cp}} = 221.7 \pm 2.8\,(\mathrm{stat.}) \pm 11.2\,(\mathrm{sys.})\,\mathrm{pb}^{-1}$ is obtained, using the theoretical NNLO calculations for the Z production cross section. This is in very good agreement with the CLC measurement of $L_{\mathrm{CLC}} = 222.2 \pm 12.9\,\mathrm{pb}^{-1}$. Comparing the errors of both luminosity measurements, it turns out that the accuracies of the two methods are comparable. The systematic error on the luminosity measurement of the counting method is dominated by the uncertainty of the parton distribution function knowledge and thus purely theoretical. In the last part the rapidity-dependence of on-shell Z boson production was studied. This differential measurement became possible since differential next-to-next-to-leading order calculations of the Z production cross section were recently carried out. All luminosity measurements in the different

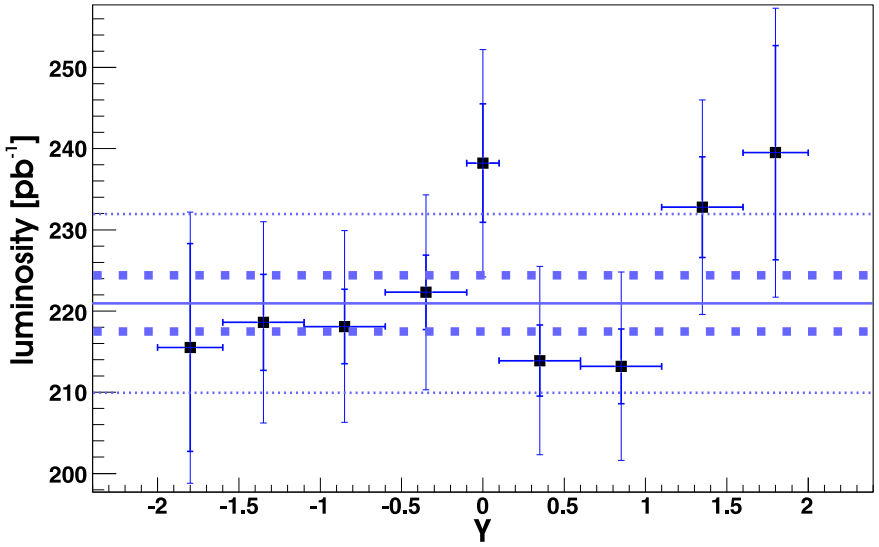

Figure 5.6.5: The combined measured luminosity in the different rapidity regions. The straight line represents the mean value of the luminosity, the dotted thin ones indicate the systematic error on the mean, including the parton distribution function uncertainty, the dotted bold lines indicate the systematic error on the mean, excluding the parton distribution function uncertainty. The statistical error on the individual measurements are shown in bold bars, the statistical plus systematic error are shown as thin error bars.

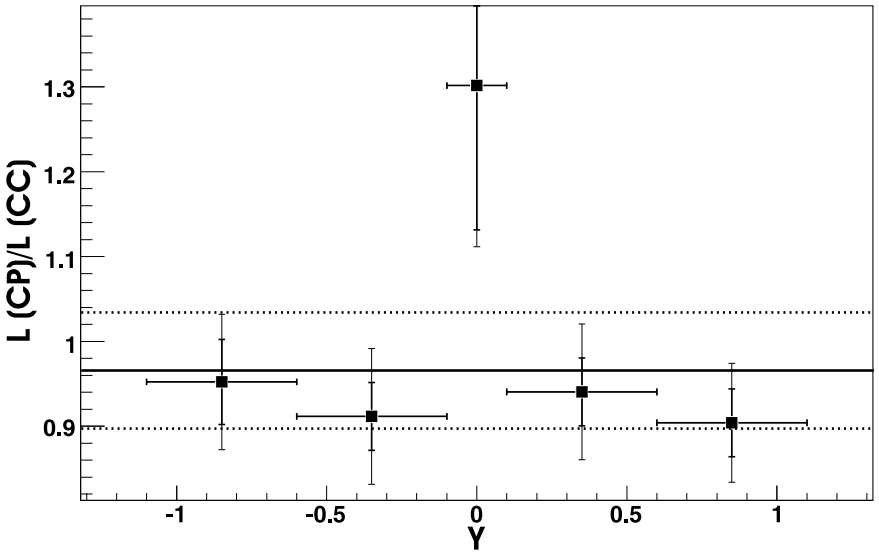

Figure 5.6.6: The ratio of the measured luminosity from Z bosons decaying in a central and a plug electron, and a Z reconstructed from two central electrons as a function of rapidity. The straight line represents the average ratio, the dotted ones indicate the systematic error on the average. The statistical error on the individual measurements are shown in bold bars, the statistical plus systematic error are shown as thin error bars.

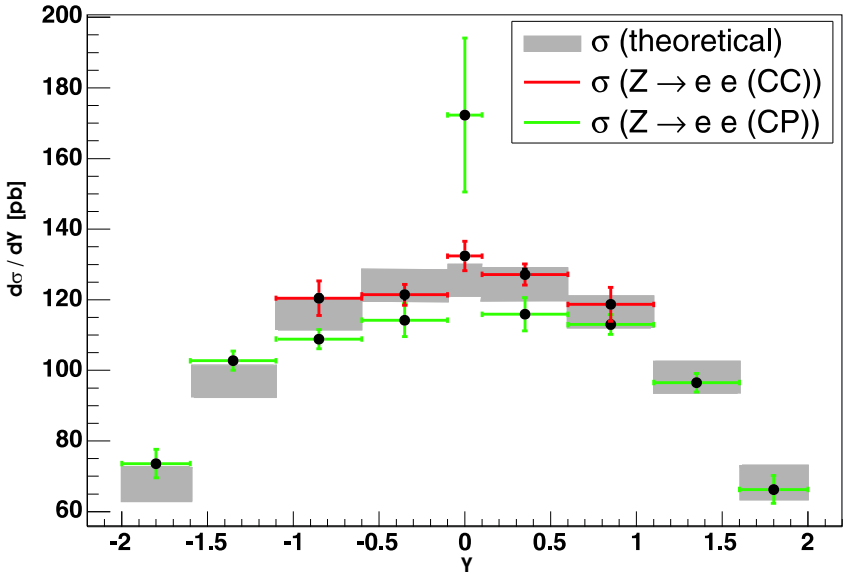

Figure 5.6.7: The differential cross section for on-shell Z boson production over the different rapidity regions. In gray rectangles the theoretical NNLO calculations with their uncertainties as error bars. The measurements and their statistical errors are shown in red (central-central) and green (central-plug).

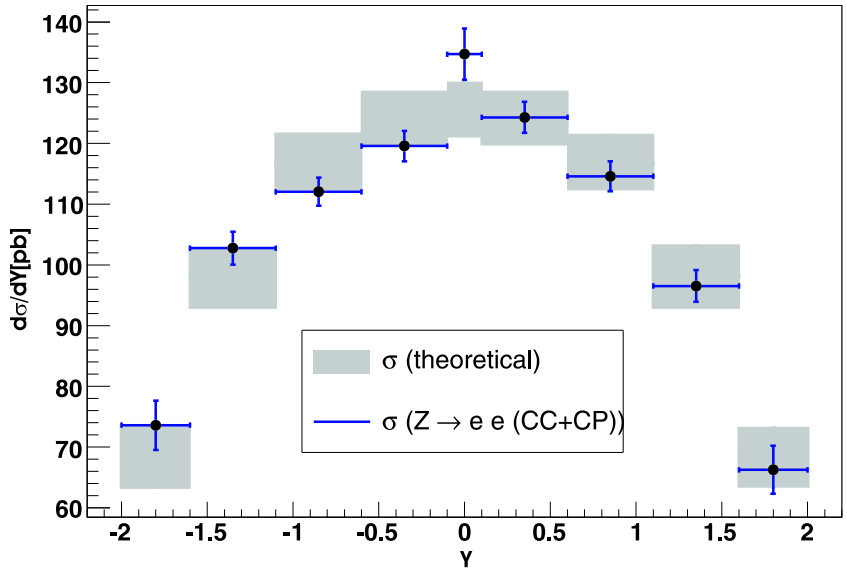

Figure 5.6.8: The differential cross section for on-shell Z boson production over the different rapidity regions. In gray rectangles the theoretical NNLO calculations with their uncertainties as error bars. The combined central-central and central-plug measurements and their statistical errors are shown in blue.

rapidity regions agree with each other within their errors and also agree with the inclusive measurement. The shape of the differential cross section from theory and measurement coincide within their theoretical and statistical uncertainties.

Chapter 6

The counting of Drell-Yan Z and W events at CMS by using their decays to electrons

In this chapter, the experimental counting of the processes pp $\rightarrow$ ZX and pp $\rightarrow$ WX with subsequent leptonic Z and W decays to electrons is studied using the complete CMS detector simulation and analysis scheme. As shown with real CDF data (chapter 5), these reactions can be used to obtain an accurate measurement of the proton-antiproton luminosity or accordingly of the proton-proton luminosity at LHC. The determination of the proton-proton (or parton-parton) luminosity can be factorized into experimental and theoretical problems, which need to be studied and investigated separately. In the following, it is focused exclusively on the experimental constraints related to the CMS detector. The aim of the analysis is to investigate the size of the experimental systematic errors from various sources. A simple and robust signal selection should also guarantee an applicability to the first pp collisions at the LHC. Figure 6.0.1 shows a simulated event in the CMS detector, where a Z boson decays to electrons.

6.1 Event simulation

An event is generated by starting a program called CMKIN. It simulates the kinematics of the physics process by running an event generator like PYTHIA. The output is given in the format of a list of all generated particle types together with their momentum four-vectors. This information is then fed into a program called OSCAR. It is based on GEANT-4 [AGO03] and includes the specific geometry of the CMS detector. OSCAR simulates the interaction of these particles with the detector elements and writes out so-called hits. A hit means that the information of time, position and energy of this process is stored. In a next step, the simulation of the electronic signal generation is performed. This is done via ORCA. ORCA also reconstructs from the electronic signals quantities like energy, momentum etc. for each sub-detector. Finally, it combines all information and reconstructs the physics

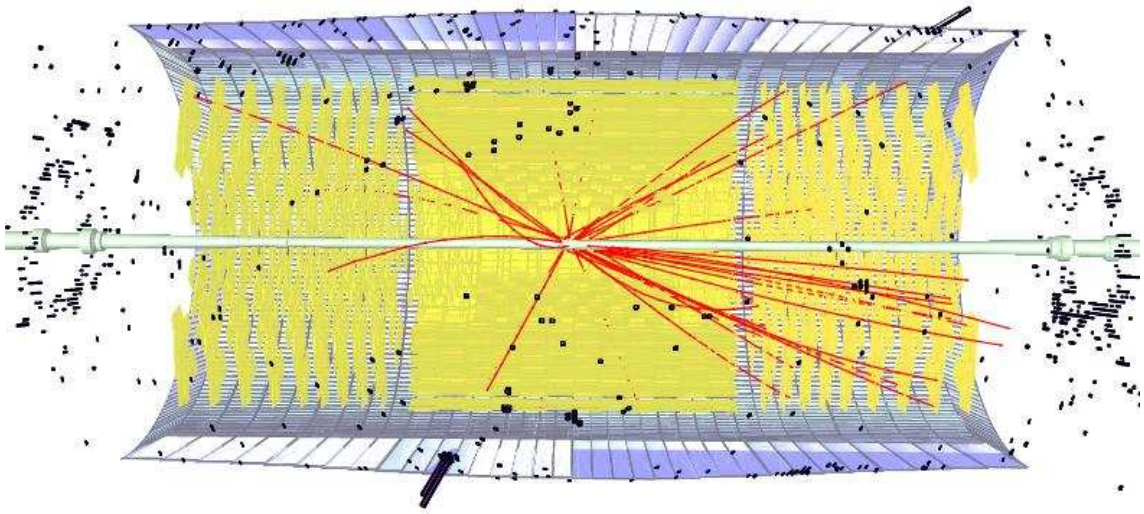

Figure 6.0.1: A Z boson decay into electrons within the CMS detector. Only parts of the tracking system and the electromagnetic calorimeter are displayed. Besides the Z decay also the underlying event and minimum bias events are included.

process, leading to the specific particles like electrons, muons, taus and jets. To allow for fast analysis, a package called PAX [KAP06] was run together with ORCA. It is a set of C++ classes which provides convenient tools to analyze the reconstructed events.

6.1.1 $pp \rightarrow ZX \rightarrow e^+e^-$

About 600000 Drell-Yan events decaying into electrons were generated and reconstructed with ORCA version 8.7.1 using PYTHIA. No restrictions for instance on transverse momentum, rapidity or pseudorapidity were applied on the generator level. Merely, a cut on the minimal Drell-Yan mass of 15 GeV was employed, as can be seen in Figure 6.1.1.

In the following, a study of resonant Z production is carried out. Thus, only generated Drell-Yan events near the Z mass pole are considered, namely $|M_{ee} - 91.2\text{GeV}| <$

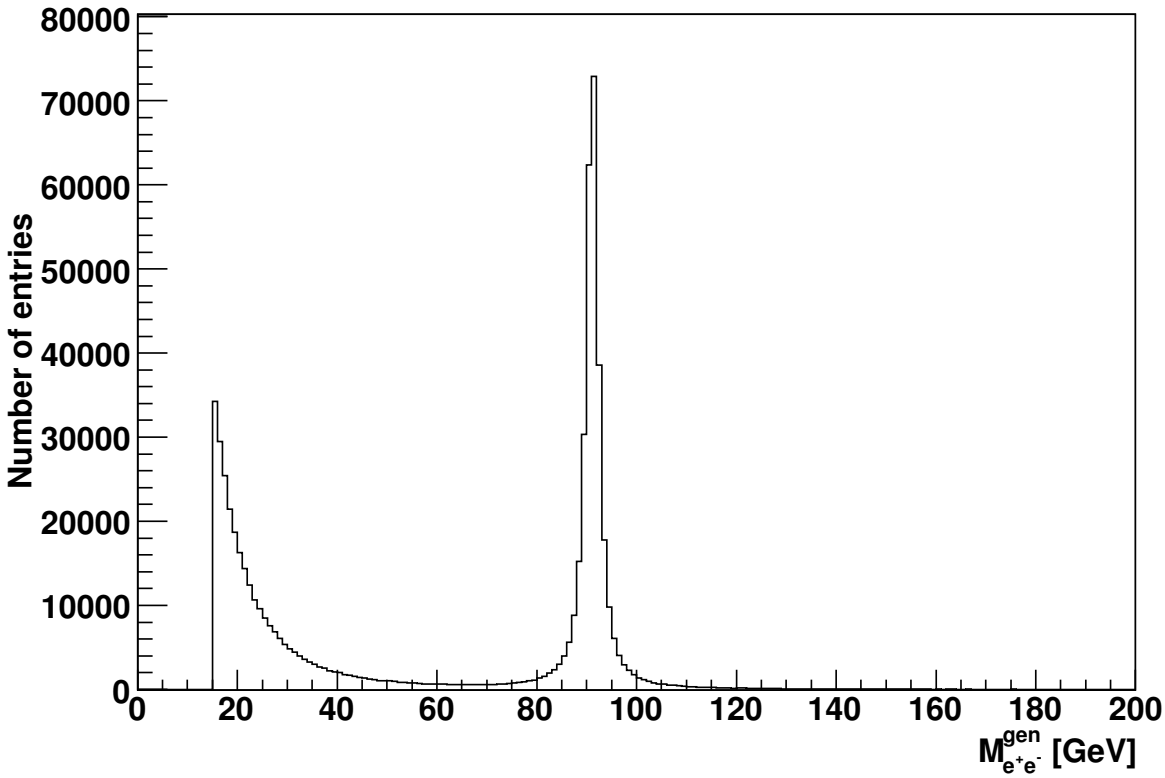

Figure 6.1.1: The generated mass distribution of e^+e^- pairs with a minimal Drell-Yan mass of 15 GeV.

7.5 GeV ($= 3\,\Gamma_Z$). This corresponds to about 50 % of the originally generated events. The events are then separated into three event classes, similar to the procedure in CDF (see section 5.2). The first type, indicated as "BB", requires that the electrons are detected within the acceptance of the barrel calorimeter ($|\eta_{BB}| < 1.4$). The second type, indicated as "BE", demands one electron to be detected inside the barrel calorimeter and the other one in the endcap calorimeter acceptance ($1.6 < |\eta_{BE}| < 2.4$). Finally, the third type, indicated as "EE", requires both leptons to be detected within the endcap acceptance[1]. Figure 6.1.2 illustrates the three cases.

Figure 6.1.3 shows rapidity distributions for the generated Z bosons. Additionally, the reconstructed Z boson rapidity for the three possible decay configurations is presented.

[1]The standard fiducial volume in CMS is defined as $|\eta| < 1.4442$ for the barrel and $1.556 < |\eta| < 2.5$ for the endcaps. Since the event vertex can be shifted by up to ± 15 cm in z-direction, the pseudorapidity of the electron and the pseudorapidity of the crystal it hits are not necessary the same anymore. In order to account for this fact and not be sensitive to border effects, the fiducial volume in this thesis is defined more tightly.

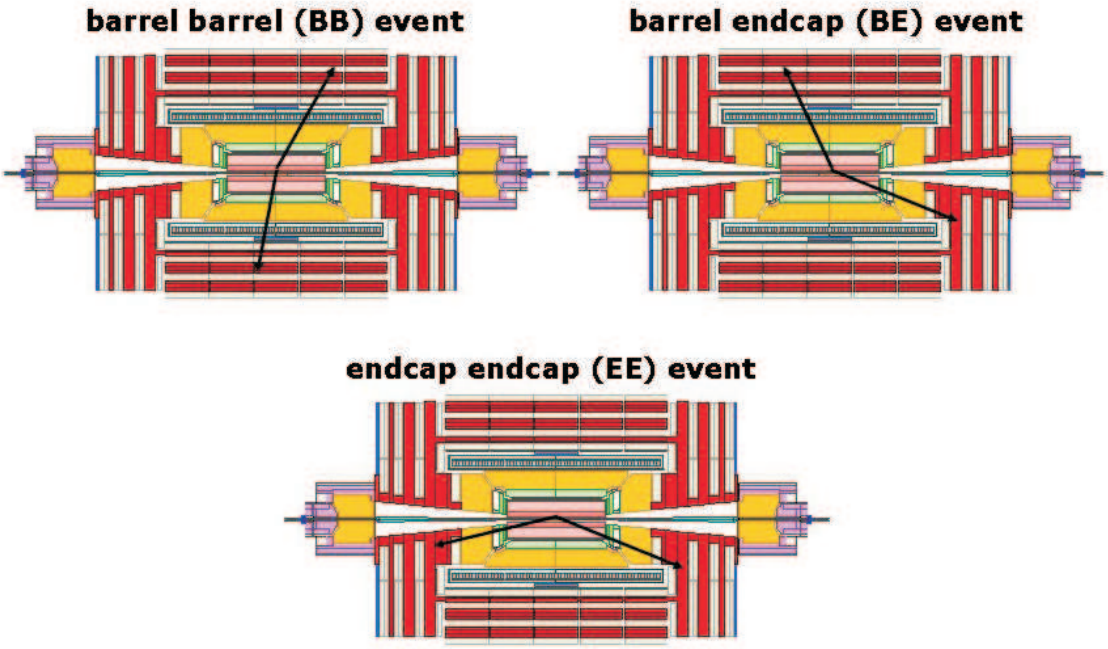

Figure 6.1.2: Schematic view of the three $Z \rightarrow e^+e^-$ event types in CMS. The arrows indicate only the direction of the electrons and not their reach inside the CMS detector.

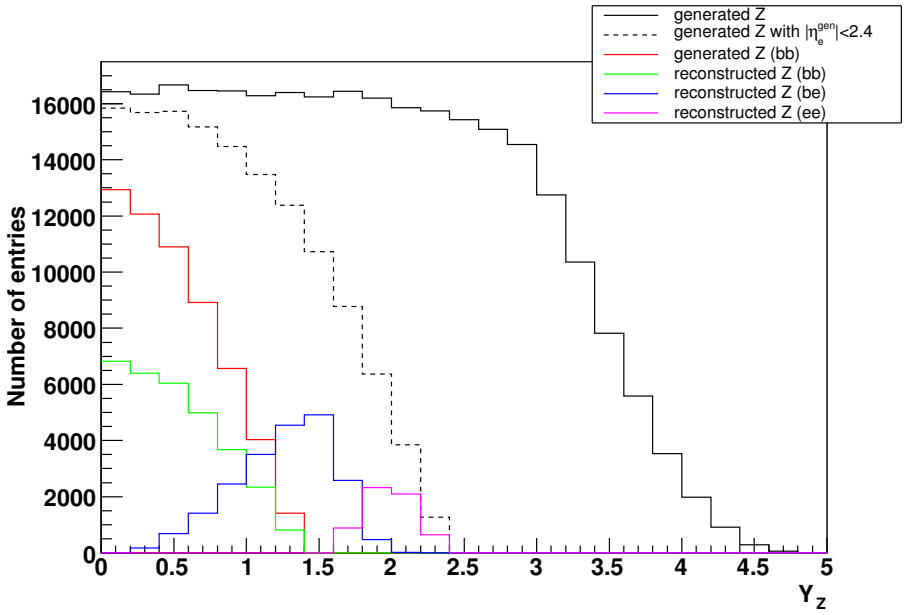

Figure 6.1.3: The rapidity distribution for all generated Z events is presented as a solid black line. The dashed line displays the same events with the additional requirement that the electrons are generated within $|\eta| < 2.4$. The events in red are generated within the barrel acceptance. For comparison, the reconstructed events for BB, BE and EE are plotted in blue, green and magenta.

Comparing the solid and dashed black curve with each other, it becomes apparent that events are lost just because of geometrical detector constraints. Already in the central rapidity bin, 4 % of the events are lost due to uncovered regions at large pseudorapidities. Figure 6.1.4 shows the maximum efficiency achievable versus the rapidity of the Z boson.

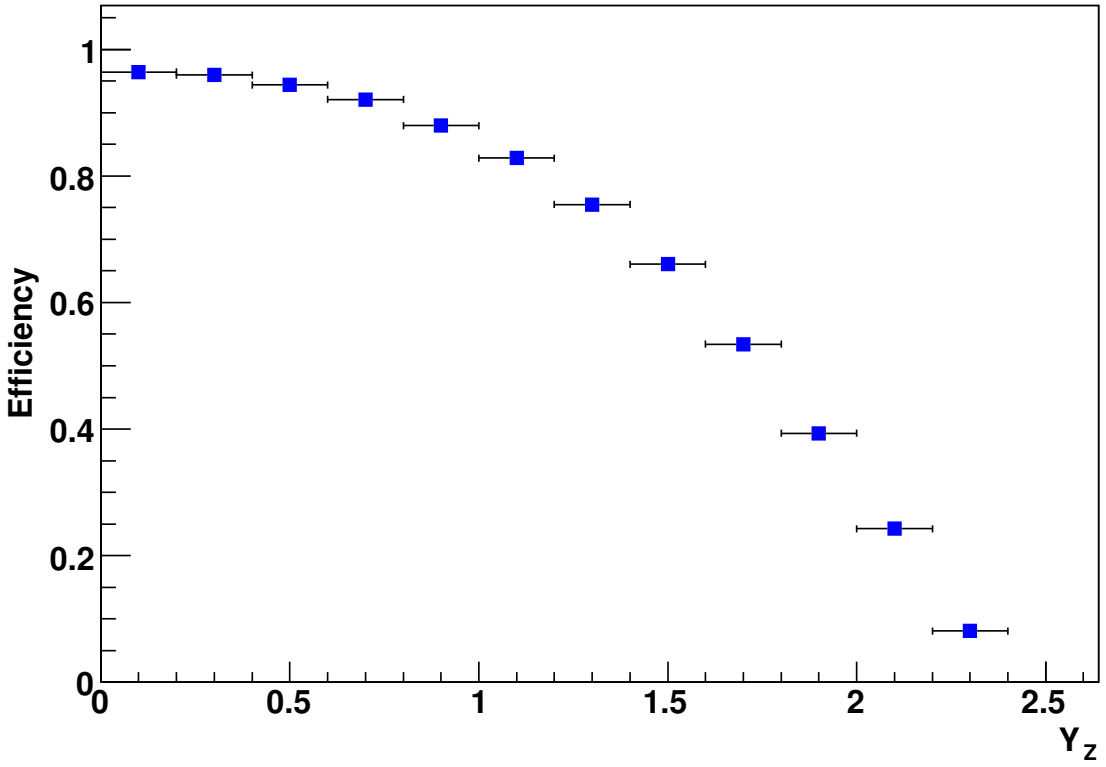

Figure 6.1.4: The maximal possible Z detection efficiency versus the rapidity. The drop in efficiency towards larger rapidities results purely from the geometrical acceptance.

6.1.2 pp → WX → eν

ORCA 8.7.1 was also used to generate about 170000 W events. Again, only resonant W production ($|M_{\mathrm{W}} - 80.4\,\mathrm{GeV}| < 7.5\,\mathrm{GeV}$) is considered as a signal and therefore investigated. Figure 6.1.5 displays the generated mass of the W bosons and Figure 6.1.6 shows the transverse momentum distribution of the W bosons.

Approximately 80 % of the W events feature a generated transverse momentum of below 30 GeV. Figure 6.1.7 exhibits the number of jets per number of events above $E_{\mathrm{T}}^{\mathrm{jet}} = 20\,\mathrm{GeV}$ for a generated W transverse momentum below and above 30 GeV.

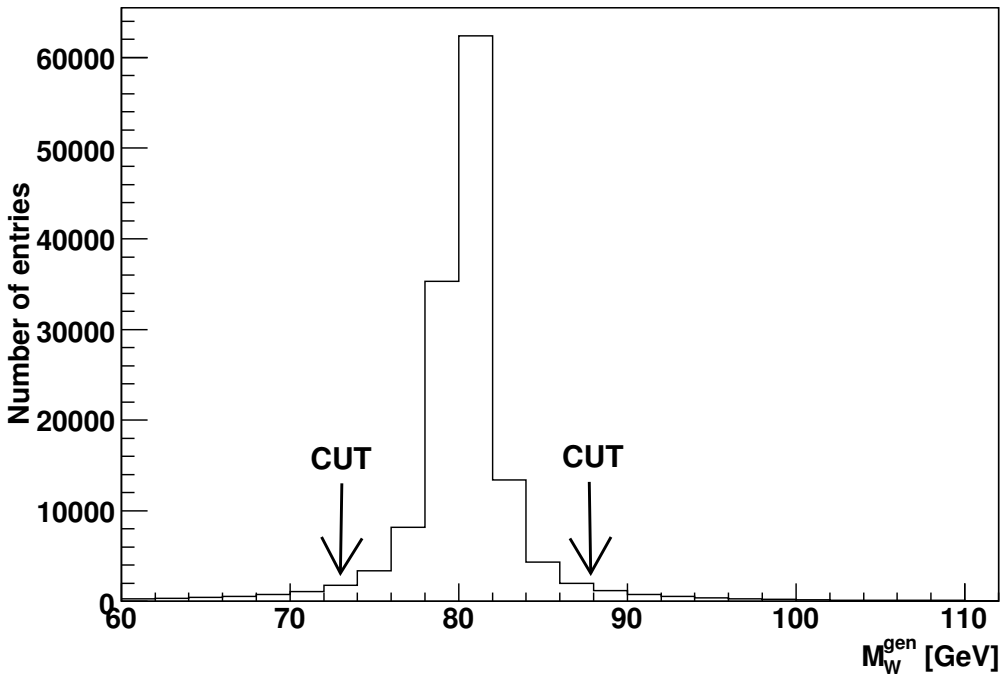

Figure 6.1.5: The generated W boson mass distribution. The cuts indicate the on-shell W bosons ±7.5 GeV around the W mass peak.

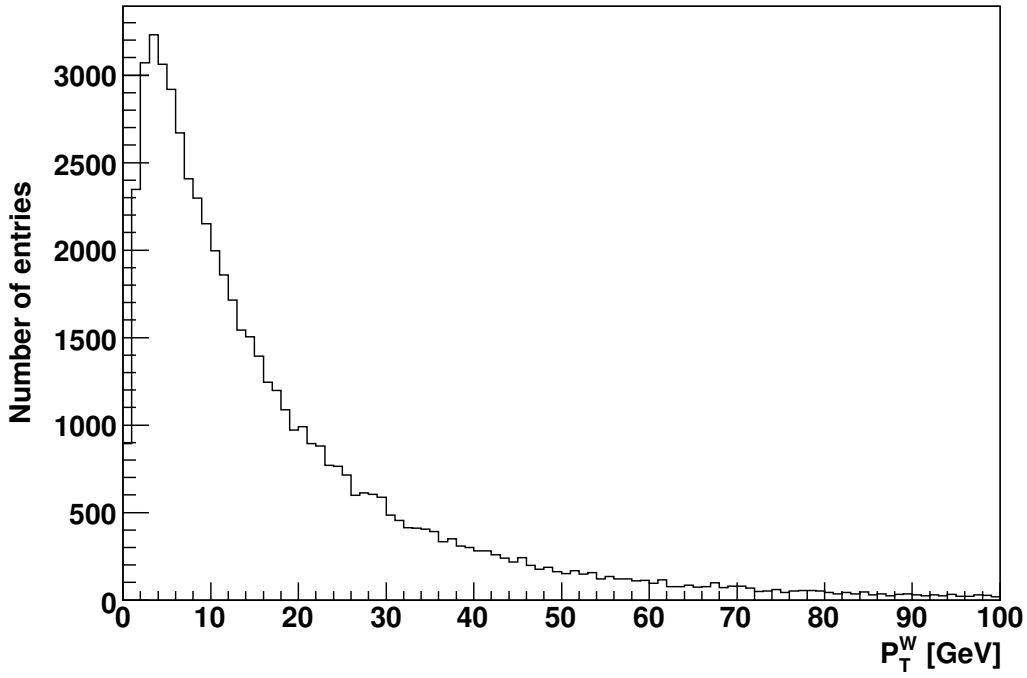

Figure 6.1.6: Distribution of the generated transverse momentum of the W bosons.

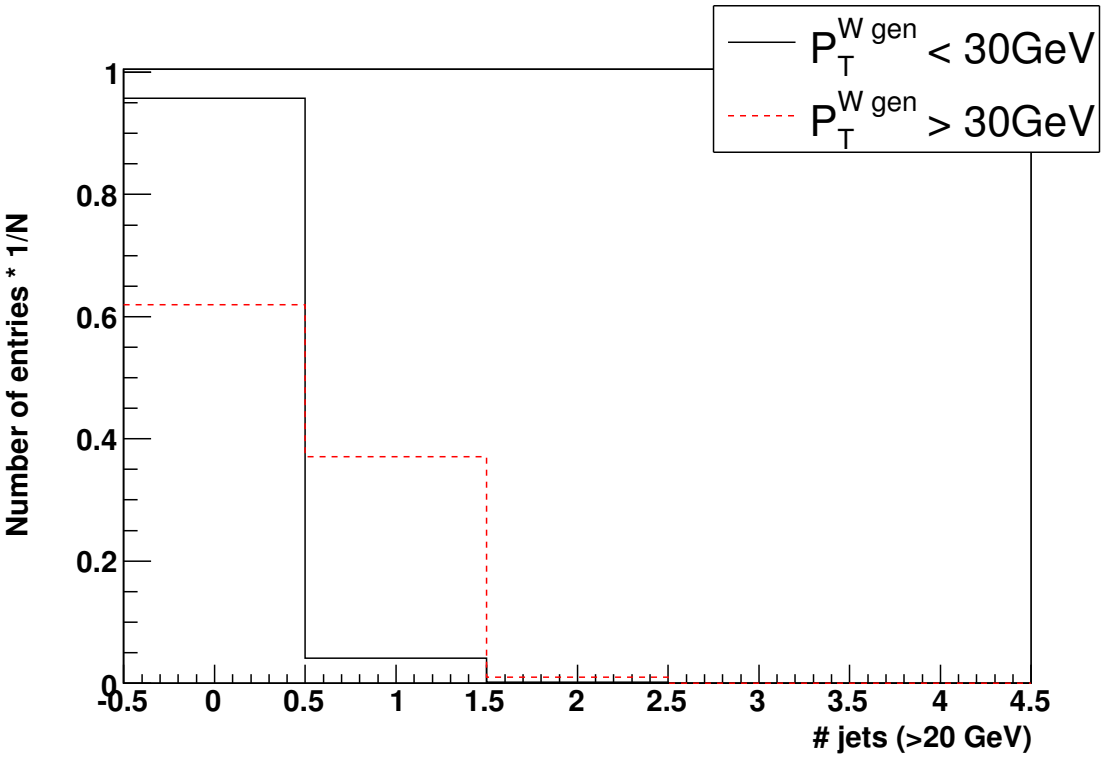

Figure 6.1.7: The jet multiplicity per number of events is shown for jets, which exceed a transverse energy of 20 GeV. Events which have a transverse W momentum below 30 GeV are indicated with a solid black line. Events which feature a transverse W momentum of at least 30 GeV are shown as a dashed red line.

The fraction of "no jet" events[2] for low W transverse momentum is roughly 96 %, whereas it is about 62 % for high W transverse momentum events. This could be a possible way to select W events with low transverse momentum.

In Figure 6.1.8, the sample is divided into W^+ and W^- events. The obviously higher rate of producing a W^+ compared to producing a W^- and also the difference in shape originates from the fact that the proton contains two valence up quarks and only one valence down quark. Consequently, also the distribution of the decay electrons differs from the distribution of the decay positrons. Moreover, the electrons are left-handed and the positrons are right-handed. Due to the nature of the V-A current in the decay of the W boson, the left-handed particles are emitted (in the rest frame of the W) favorably in direction of the incoming quark and the right-handed particles are emitted preferably opposite to the quark direction. At large W rapidities the quark's momentum is on average larger than the one from the antiquark. Hence, the positron is emitted towards smaller pseudorapidities and the electron accordingly towards larger pseudorapidities. This fact is reflected in Figure 6.1.9.

The maximal W selection efficiency as a function of rapidity is calculated for the purpose of estimating the inefficiencies from different sources. On the one hand,

[2] "No jet" events are defined as events containing no jet with $E_T^{jet} > 20\,GeV$.

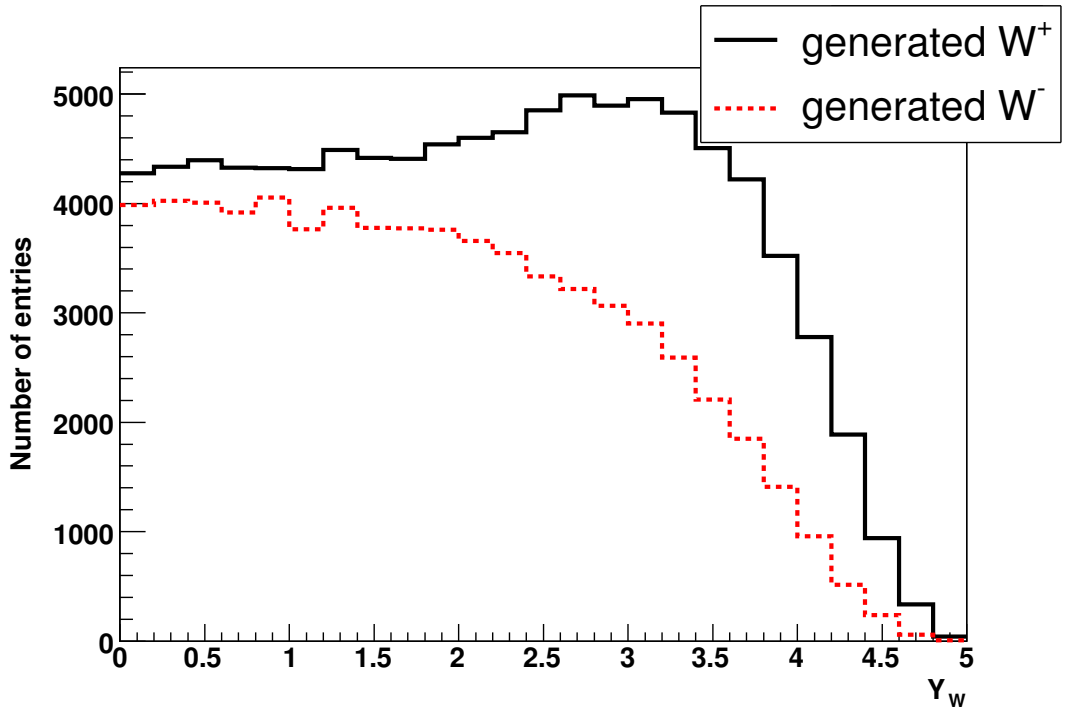

Figure 6.1.8: The rapidity distribution for generated W^+ (solid black line) and W^- (red dashed line) events.

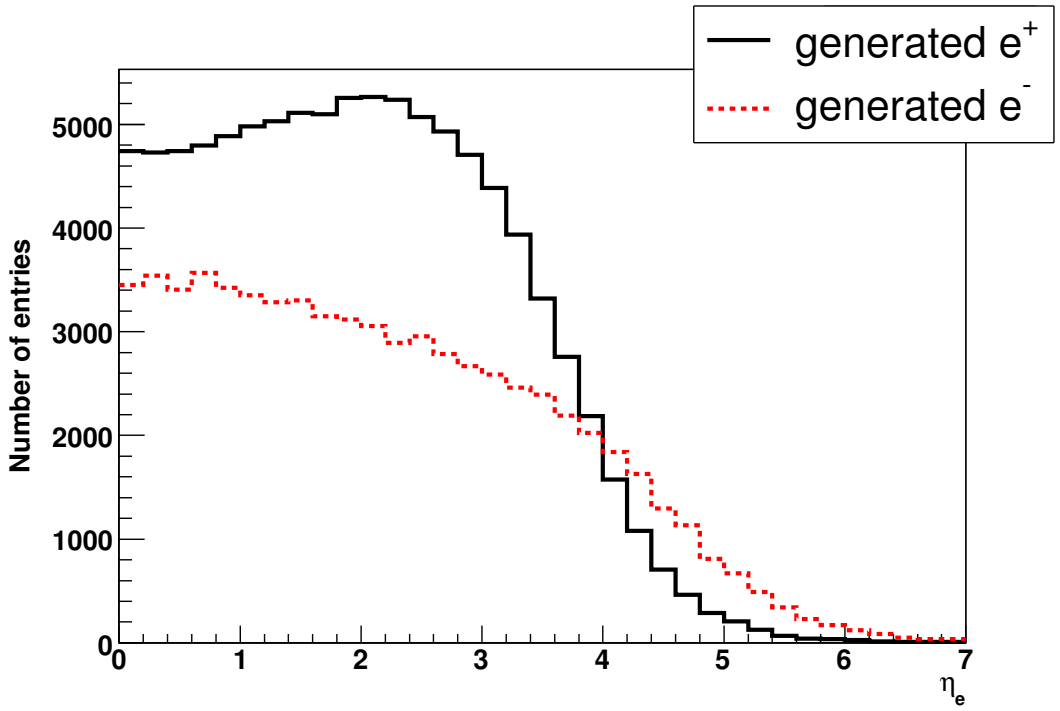

Figure 6.1.9: The pseudorapidity distribution for generated e^+ (solid black line) and e^- (red dashed line).

there are inefficiencies, which are dependent on cuts like the electron identification and the trigger efficiencies, on the other hand, there is the inefficiency from the geometrical design of the detector. Figure 6.1.10 shows the ratio per rapidity interval of $\Delta\eta = 0.2$ of the number of W events with the electron detected inside the barrel acceptance ($|\eta| < 1.4$) to the total number of generated W events.

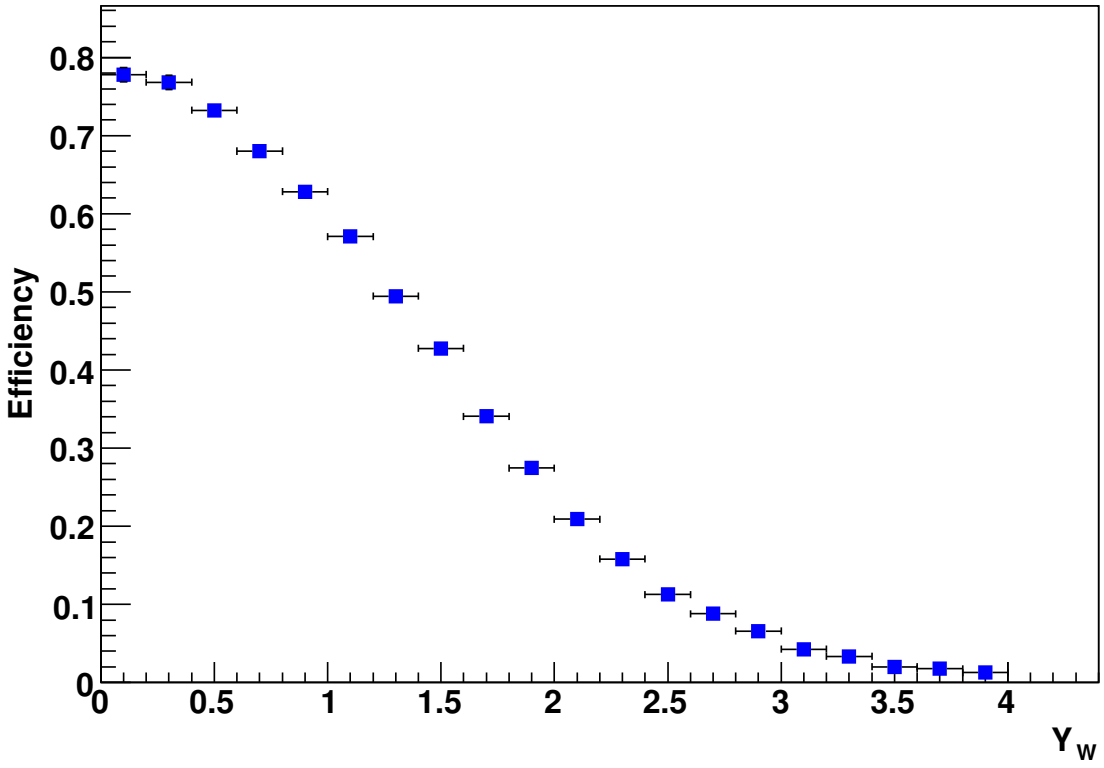

Figure 6.1.10: The maximal efficiency to detect a $W^{\pm}$, where the $e^{\pm}$ is generated within the barrel acceptance of $|\eta| < 1.4$.

6.2 Electron selection

As already seen in chapter 5, the rather high cross section of inclusive $Z \rightarrow e^+e^-$ production at CDF enables to select an almost background-free Z signal after subtraction of the Drell-Yan continuum, which was confirmed by an independent CDF measurement [CDF04]. This was already achieved with three simple selection criteria and a much coarser detector granularity compared to CMS. It is expected to obtain a signal sample with even less contamination of background, since the resolution of almost all relevant sub-detectors is better, the cross section is almost one order of magnitude higher and the electron selection cuts can be much tighter because of this increased statistics.

Since the amount of generated multi-jet Monte Carlo events is not sufficient to precisely estimate this background, these tight selection criteria are necessary to ensure a clean Z signal. The cuts were studied in detail in ref. [DIT04] and essentially pure electrons were obtained. Nevertheless, the selection criteria were tested with several millions of multi-jet events containing one electron (pp $\rightarrow$ jets + e). No single event remained, which corresponds to an upper limit of $\lesssim 2\,\%$ for the multi-jet contamination.

However, despite these advantages in favor of a clean signal sample, the contribution from simultaneous minimum bias events and the underlying event at LHC will be larger compared to the Tevatron. The effect of how much energy will be deposited on average in the calorimeter from these events is difficult to estimate. Still, it should be feasible to measure the energy in detector regions far away from the electrons, once real data is available. For more details see ref. [ACO06].

Electrons for Z events are selected as follows:

- Each electromagnetic supercluster[3] must have a matching track of at least 5 GeV. Track and supercluster are associated, if the track is found in a cone of $\Delta R = \sqrt{(\Delta\phi)^2 + (\Delta\eta)^2} < 0.15$ around the center of the supercluster.
- The transverse energy E_{T} of the supercluster in the electromagnetic calorimeter has to be at least 20 GeV for both, the barrel and the endcap electron candidates.
- The spread of the electromagnetic shower in η-direction with respect to the η of the supercluster position , $\sigma_{\eta\eta}$, has to be smaller than 0.01 for an electron. $\sigma^2_{\eta\eta}$ is defined as $\sum_{5\times5\,\mathrm{crystals}}(\eta_{\mathrm{crystal}} - \eta_{\mathrm{seed}})^2 \frac{E_{\mathrm{crystal}}}{E_{5\times5}}$. The shape of the supercluster should be in agreement with the expected electromagnetic shower shape. Since the magnetic field is pointing along the beam axis, the shower shape will be more extended in the ϕ-direction due to bremsstrahlung while remaining narrow in η. For hadrons, the shower shape is intrinsically wider also in η.
- The ratio of energy deposits from the cluster in the hadronic calorimeter to the associated electromagnetic one is forced to be very small. A value of $\frac{E_{\mathrm{had}}}{E_{\mathrm{em}}}$ must not exceed 0.05. Obviously, hadrons tend to have a larger ratio.
- The electromagnetic energy of a supercluster divided by its track momentum, $\frac{E_{\mathrm{SC}}}{p_{\mathrm{track}}}$, should be larger than 0.9. Additionally, the requirement $|\frac{1}{E_{\mathrm{SC}}} - \frac{1}{p_{\mathrm{track}}}| < 0.02$ has to be valid. The latter relation is equivalent to a cut on the upper part of the $\frac{E_{\mathrm{SC}}}{p_{\mathrm{track}}}$-spectrum but less dependent on the particle's energy. An electron is supposed to have a ratio of close to unity for $\frac{E_{\mathrm{SC}}}{p_{\mathrm{track}}}$. Single pions are efficiently rejected at the lower part of the spectrum. Jets with π^0 $\pi^{\pm}$ content, where the neutral pion deposits its energy in the electromagnetic calorimeter

[3] In order to correct for energy loss by bremsstrahlung in the tracker, individual clusters are merged to a supercluster, if their centers coincide in a distance of $\Delta\phi < 0.8(0.4)$ and $\Delta\eta < 0.06(0.14)$ in the barrel (endcap) calorimeter.

and the charged pion is responsible for the measured track momentum, are found to have larger values than 0.02 for $|\frac{1}{E_{\mathrm{SC}}} - \frac{1}{p_{\mathrm{track}}}|$.

- An electron candidate has to be isolated. The sum of all track's momenta - except the matching track - within a cone of $\Delta R < 0.35$ around the center of the supercluster is divided by the transverse energy of the supercluster. The particle is called isolated, if this ratio does not exceed 0.2. For this, only tracks with a minimal momentum of 1.5 GeV and at least 4 hits in the tracker are considered. Additionally, the tracks have to be closer to the vertex than 0.4 cm in z-direction and closer than 0.1 cm in the transverse direction.

The distributions of all six variables used for the electron selection are shown in Figure 6.2.1. Besides the variable plotted, all other cuts are applied. Table 6.2.1 presents the effect of the individual selection cuts on the efficiency. The requirement for a narrow shower shape in η causes half of the efficiency loss, another quarter is caused by the energy-momentum matching requirement. Though the cut on $\sigma_{\eta\eta}$ involves a 20 % efficiency drop, it is a significant criteria to reject background events. A background estimation from multi-jet events of 3 % ± 3 % is obtained without this cut (corresponding to one reconstructed event), whereas no event is reconstructed if this cut is included, as stated earlier this section.

6.3 Z event selection

Having defined the electrons, the invariant mass of the e^+ e^- pair is calculated by:

$$M_{\mathrm{ee}} = \sqrt{2E_{\mathrm{e}^+}E_{\mathrm{e}^-}(1 - \cos\Delta\theta)} \tag{6.3.1}$$

$E^{\mathrm{e}^\pm}$ is the energy of the electron measured by the electromagnetic calorimeter, and $\Delta\theta$ is the opening angle between the two particles at the vertex. In case three or more electrons are found within one event, only the two superclusters with the highest transverse energy are considered. Figure 6.3.1 shows the number of electron candidates per event.

Besides the electron selection criteria, a Z event is required to have an invariant mass of the electron positron pair close to the reconstructed Z mass peak, $M_{\mathrm{ee}} - 7.5\,\mathrm{GeV} < M_{\mathrm{ee}}^{\mathrm{peak}} < M_{\mathrm{ee}} + 7.5$ GeV. That way, the number of $\mathrm{Z} \to \mathrm{e}^+\mathrm{e}^-$ events can be determined above the Drell-Yan continuum and possible remaining jet events are taken into account.

To compare the trigger (first and higher level) decision with the (offline) Z selection, the trigger efficiency for events which pass the Z selection is shown in Figure 6.3.2 as a function of the Z rapidity. An average trigger efficiency of $\epsilon_{\mathrm{trigger}} = 99.8$ % is obtained for barrel-barrel events and $\epsilon_{\mathrm{trigger}} = 98.5$ % for barrel-endcap events. It follows that almost all events, which are selected offline, also fulfill the trigger requirement.

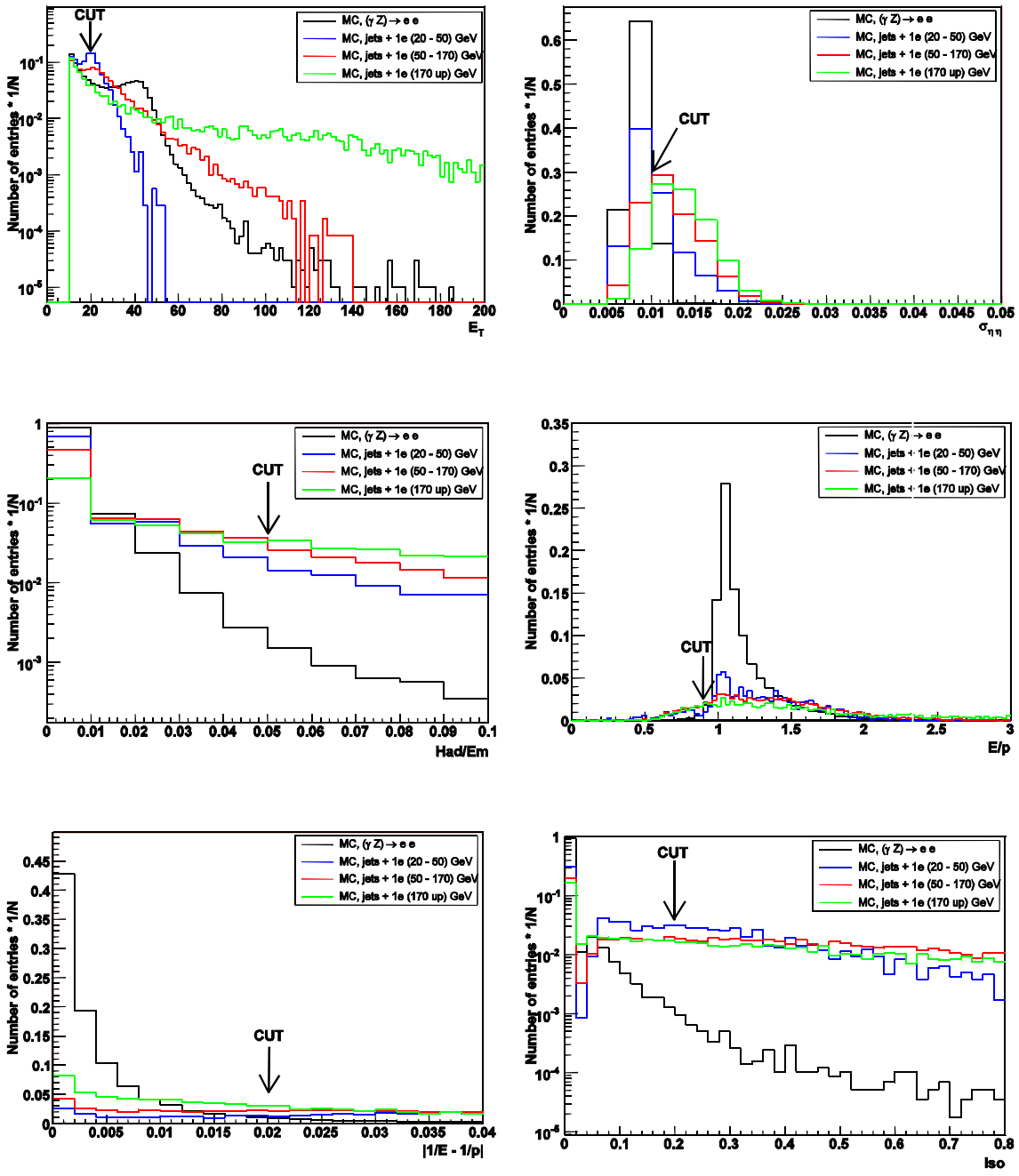

Figure 6.2.1: All selection cuts on the electron variables are shown, namely for the transverse energy (E_{T}, upper left), the shower width in η ($\sigma_{\eta\eta}$, upper right), the ratio of hadronic to electromagnetic energy in the calorimeters ($\frac{E_{\mathrm{had}}}{E_{\mathrm{em}}}$, middle left), the ratio of the supercluster energy to the momentum of the associated track ($\frac{E_{\mathrm{SC}}}{p_{\mathrm{track}}}$, middle right), the absolute value of the difference of the inverse energy and the inverse momentum, ($|\frac{1}{E_{\mathrm{SC}}} - \frac{1}{p_{\mathrm{track}}}|$, lower left) and the track isolation (lower right). All other selection cuts, excluding the cut on the displayed variable, are applied. All plots contain one entry per electron and no requirement of having two electrons is imposed. The processes are not normalized to each other.

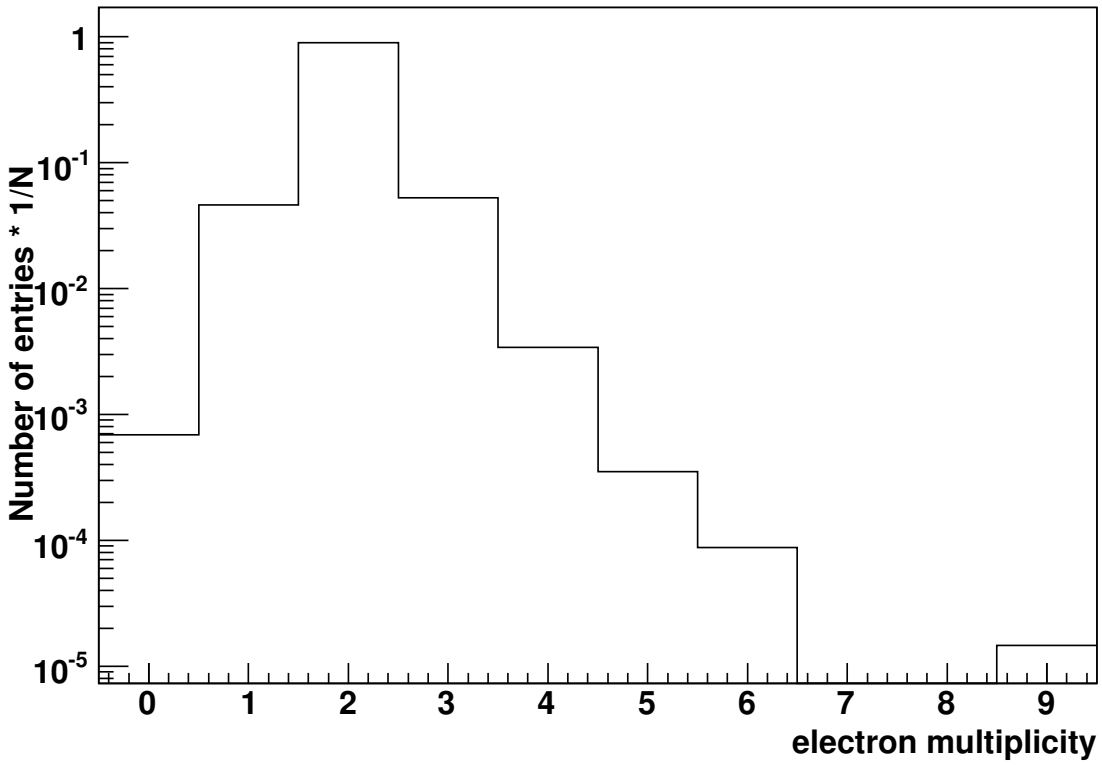

Figure 6.3.1: Number of electron candidates per event

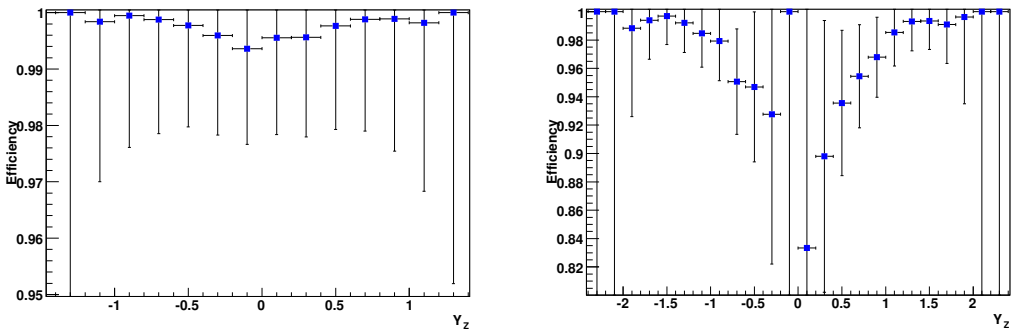

Figure 6.3.2: The L1 + HLT efficiency for Z events, which pass the Z selection criteria. On the left side for Z events where the electrons are both reconstructed in the barrel detector, on the right side for Z events where one electron is reconstructed in the endcap and the other one in the barrel.

cut removed	efficiency increase
E_{T}	3 %
$\sigma_{\eta\eta}$	20 %
$\frac{E_{\mathrm{had}}}{E_{\mathrm{em}}}$	1 %
$\frac{E_{\mathrm{SC}}}{p_{\mathrm{track}}}$	3 %
$\lvert\frac{1}{E_{\mathrm{SC}}} - \frac{1}{p_{\mathrm{track}}}\rvert$	12 %
isolation	2 %

Table 6.2.1: Cuts and corresponding efficiency drop for the applied selection criteria. These numbers are calculated by $1 - \frac{N_{\mathrm{cuts}}^{\mathrm{all}}}{N_{\mathrm{cuts}}^{\mathrm{n-1}}}$, where $N_{\mathrm{cuts}}^{\mathrm{all}}$ is the number of events after all selection cuts are applied and $N_{\mathrm{cuts}}^{\mathrm{n-1}}$ is the number of events after all but the examined selection cut applied.

Figure 6.3.3 shows the generated and reconstructed Z mass peak. As can be seen, the reconstructed mass peak is shifted by approximately 1 GeV towards lower values. A mass peak of 91.18 GeV is found for the generated mass and 90.25 GeV for the reconstructed mass peak, both obtained by a Gaussian fit between 86 GeV and 96 GeV. The mass difference of the reconstructed electron positron pair and the generated one is displayed in Figure 6.3.4. It follows a Gaussian distribution with a sigma of about 2 GeV and an extended tail at the lower part of the spectrum. Actually, this shift is expected, since the superclusters are not completely corrected for energy loss by effects of bremsstrahlung within the tracker. This leads also to an η-dependence of the generated to reconstructed transverse energy ratio for electrons, as shown in Figure 6.3.5.

However, the mass region for the counting of Z boson events around the mass peak is defined quite large, and thus no severe loss of events can be expected due to resolution or calibration effects. Nevertheless, the effects from known and possibly unknown inefficient detector areas need to be investigated in detail. For this reason, the effects from supermodule edges and the gaps between the supermodules with respect to the Z boson reconstruction efficiency is studied. In Figure 6.3.6, the electron efficiency from Z bosons in dependence of the local ϕ angle is presented.

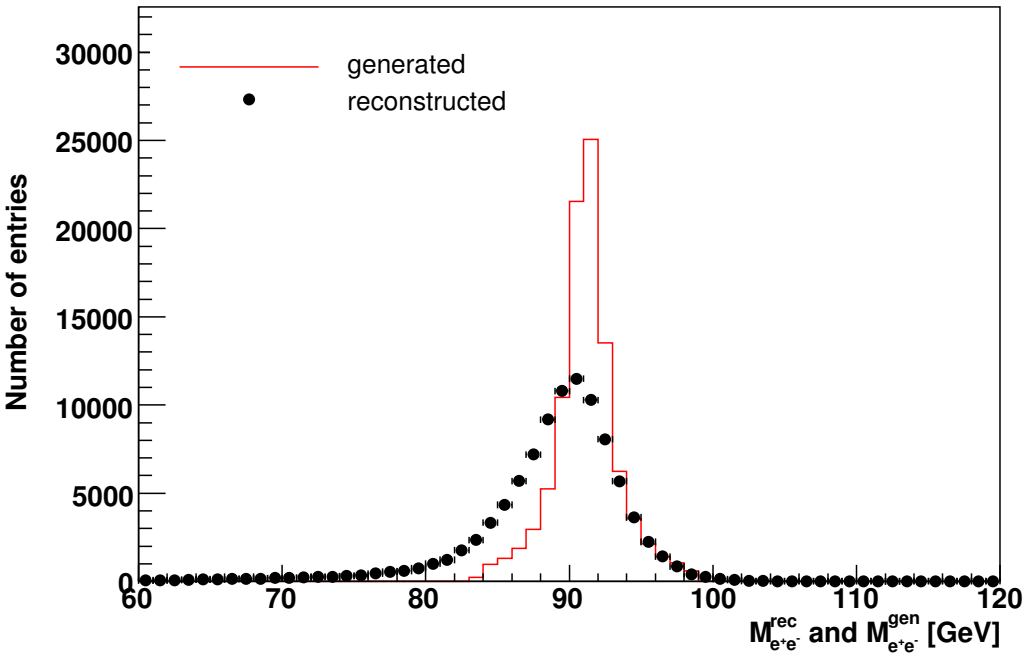

Figure 6.3.3: Generated (red line) and reconstructed (black points with error bars) Z mass distribution after all cuts on the electrons.

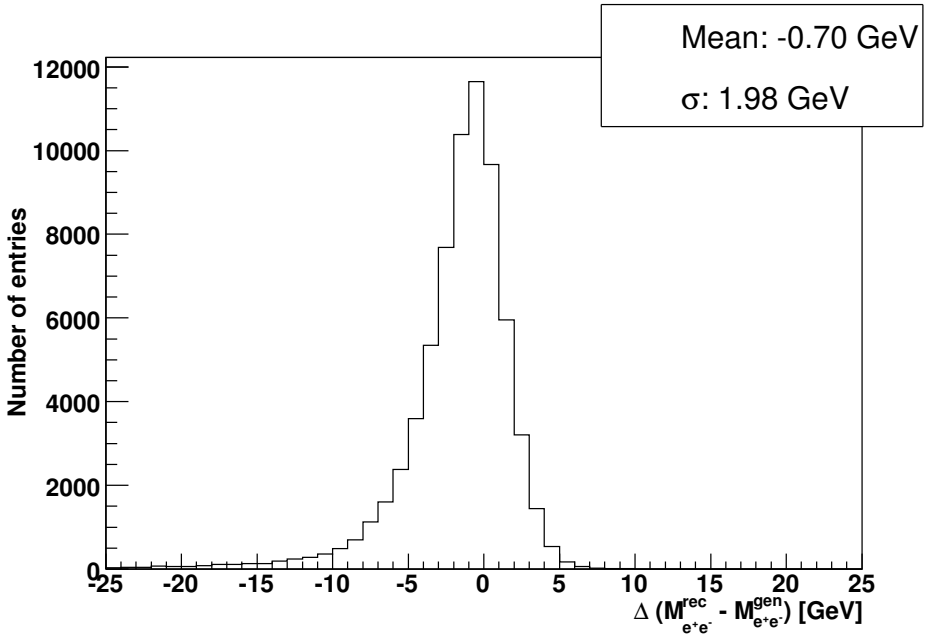

Figure 6.3.4: Difference between the reconstructed electron positron pair mass and the generated mass. The parameters of the Gaussian fit between ± 3GeV are shown.

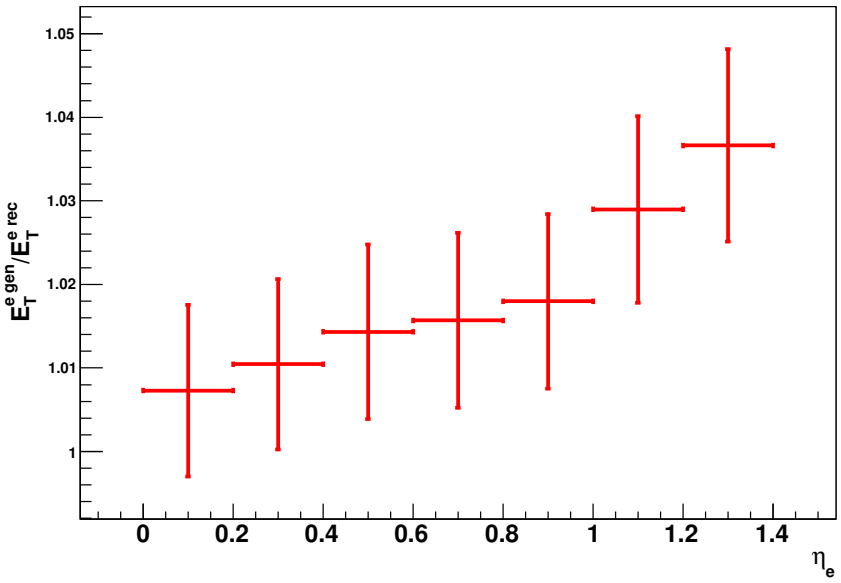

Figure 6.3.5: The ratio of the generated to the reconstructed transverse energy is presented for electrons in the barrel calorimeter, including statistical errors. Whereas the ratio at central pseudorapidities differs less than 1 % from unity, it rises up to 3.5 % at large pseudorapidities.

The efficiency here is defined as the ratio of the number of reconstructed electrons from accepted Z events to the number of electrons belonging to a generated Z event, where the electrons are required to be generated in the barrel region, $|\eta_{e^\pm}^{gen}| < 1.4$. The local ϕ angle means that the nine odd and the nine even numbered supermodules are folded on top of each other. All odd supermodules correspond to the angle 0° to 20° and the even supermodules range from 20° to 40°.

Taking the events from the fiducial volume in ϕ_{local}, the Z reconstruction efficiency is studied as well as a function of η. Figure 6.3.7 shows the result. The gaps between the supermodules are again clearly visible at $\eta \approx 0$, $|\eta| \approx 0.4$, $|\eta| \approx 0.75$ and $|\eta| \approx 1.1$. There is a larger gap in between $|\eta| \approx 1.4$ and $|\eta| \approx 1.6$, where the transition of the barrel and the endcap takes place. The slightly higher Z reconstruction efficiency in the endcap calorimeter reflects the relaxed $\sigma_{\eta\eta}$ cut of 0.03.

An absolute efficiency drop of about 10 % becomes visible in between the supermodules in ϕ. In order to estimate the systematic effect of these detector gaps, the average efficiency is calculated. The uninterrupted blue line in Figure 6.3.6 represents the average efficiency, if the gaps are included. A value of 57.4 % ± 0.2 % is found. Excluding the gap regions, namely ϕ_{local} between 0-1, 19-21 and 38-39 degrees, represented by the interrupted red line, gives an average efficiency of 58.6 % ± 0.2 %. The errors correspond here to the finite number of available Monte Carlo events. Assuming that the electrons are produced homogeneously in ϕ, the corrections for the efficiency loss in the gap region can be determined with a relative accuracy of less

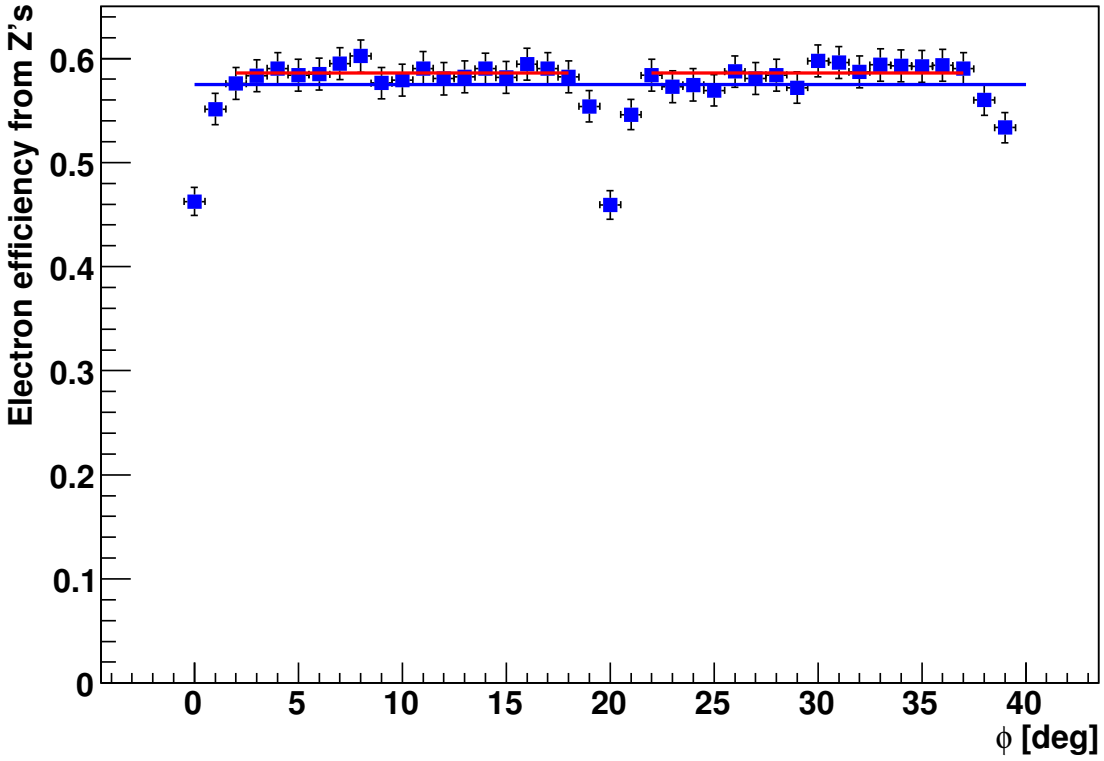

Figure 6.3.6: The electron reconstruction efficiency from $Z \rightarrow e^+e^-$ events as a function of local ϕ in the barrel calorimeter. The average efficiency outside the gap-region (red interrupted line) and over the whole ϕ-range (blue continuous line) are indicated. Their difference is 1.2 %.

than 25 % already with the current statistics. This number is a rough estimate by comparing the minimal efficiency in the gap region with the efficiency of the non-gap regions.

It can be concluded, that with a few 100000 reconstructed $Z \rightarrow e^+e^-$ events it should be possible to bring down the efficiency uncertainty due to the gaps between the supermodules to a $1\,\% - 2\,\%$ level [EHD06], [EDH06]. A further reduction of this uncertainty will be possible, once more statistics is available. This accuracy corresponds to the amount of Z events, which are expected in the first round of LHC data taking. Once LHC has started, a comparison between data and simulation can be carried out by varying cuts on one electron while the electron identification for the other one remains the same. By recording the change in the number of accepted Z events in data and simulation, either these deviations will enter additionally into the systematic uncertainties or will be used to tune the Monte Carlo.

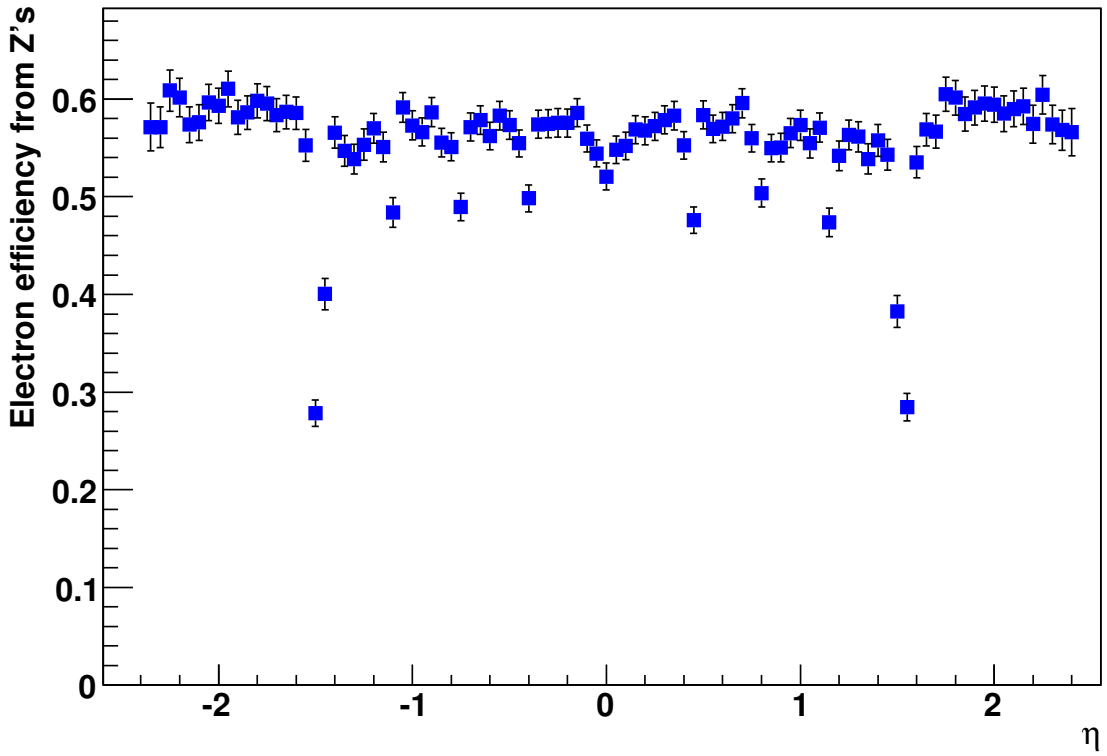

Figure 6.3.7: The electron reconstruction efficiency from $Z \rightarrow e^+e^-$ events as a function of η in the barrel and endcap calorimeter. All electrons which are reconstructed outside the fiducial volume in ϕ do not contribute to this plot.

6.4 W event selection

As described in section 6.2, the electron has to pass a set of selection criteria. There is only one electron allowed in the event. Otherwise the event is discarded, which happens in 10 % of the cases. Figure 6.4.1 exhibits the electron multiplicity per event.

Additionally, there is missing transverse energy of at least 30 GeV required which is associated with the (anti-)neutrino[4]. The transverse mass[5] of the eν-system is defined as

$$M_{\mathrm{T}}^{\mathrm{W}} = \sqrt{2p_{\mathrm{T}}^{\mathrm{e}}p_{\mathrm{T}}^{\nu}(1 - \cos\Delta\phi)}\,, \tag{6.4.1}$$

where $p_{\mathrm{T}}^{\mathrm{e}}$ and p_{T}^{ν} are the transverse momentum of the electron and the neutrino and $\Delta\phi$ is the azimuthal angle between the electron and the neutrino. Finally, the transverse mass is required to be between 60GeV and 100GeV. The transverse momentum

[4]For simplicity, "neutrino" will be used in the following for both neutrino and antineutrino.
[5]In hadron collisions it is impossible to obtain the z-component of the neutrino's momentum.

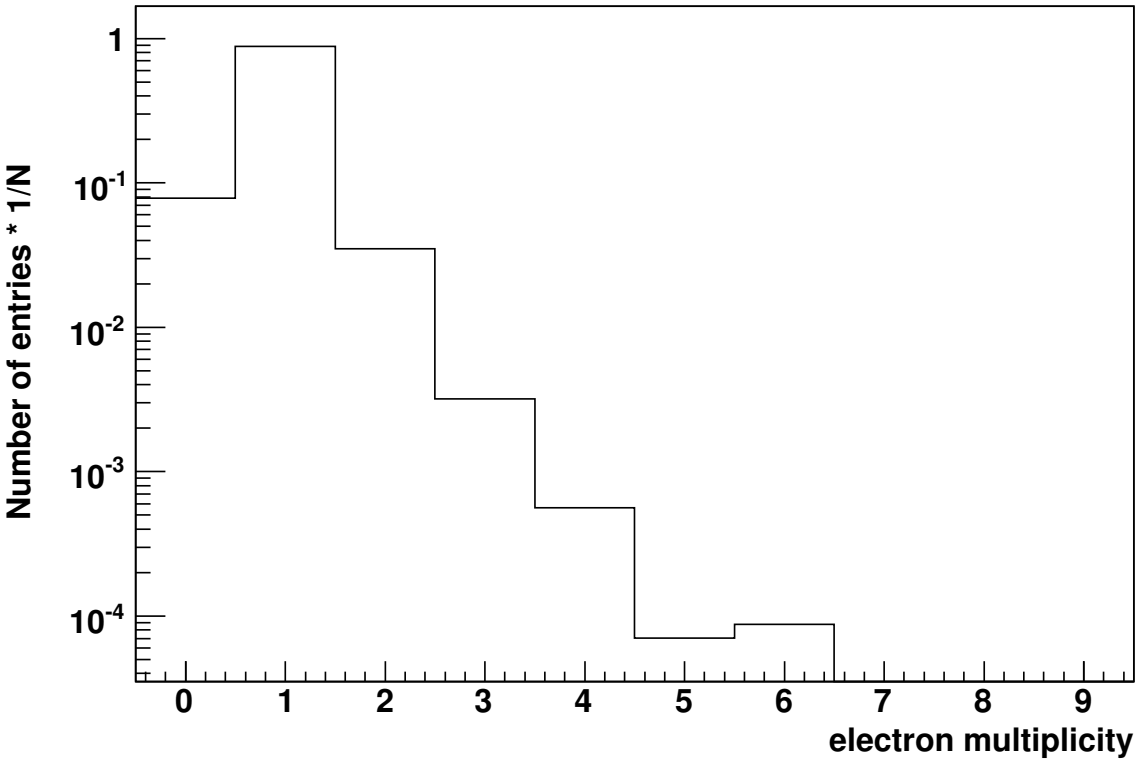

Figure 6.4.1: Number of electron candidates per event.

of the electron can be measured accurately in the electromagnetic calorimeter. Since the neutrino can not be detected directly, a possible way to determine its transverse energy is to calculate the vector sum of all clusters in the calorimeter and accredit the imbalance, called missing transverse energy (MET), to the neutrino. Figure 6.4.2 shows the distribution of the neutrino's generated transverse momentum minus the reconstructed transverse energy for $W \rightarrow e\nu$ events.

On average the reconstructed missing transverse energy is estimated about 20 GeV too low. It is suspected that low energy objects, which are randomly distributed across the detector, are responsible for this bias. Another way to determine the MET is to take the vector sum of the momenta of the hard objects (electrons and jets) only. In the following, this approach is pursued. A reconstructed jet[6] is defined as a jet with a transverse energy of more than 20 GeV and a pseudorapidity of less than 2.4. This energy threshold is a compromise: A too high transverse energy cut would bias the transverse mass distribution for events classified wrongly as zero jet events and therefore be distorted (this is because the W boson can not be assumed to have no transverse momentum, as verified in Figure 6.1.6.). On the other hand,

[6]In the whole analysis uncalibrated jets are used. Definitely, calibrated jets would lead to a more accurate result but it is assumed that these calibrations will not be available at the beginning of data taking.

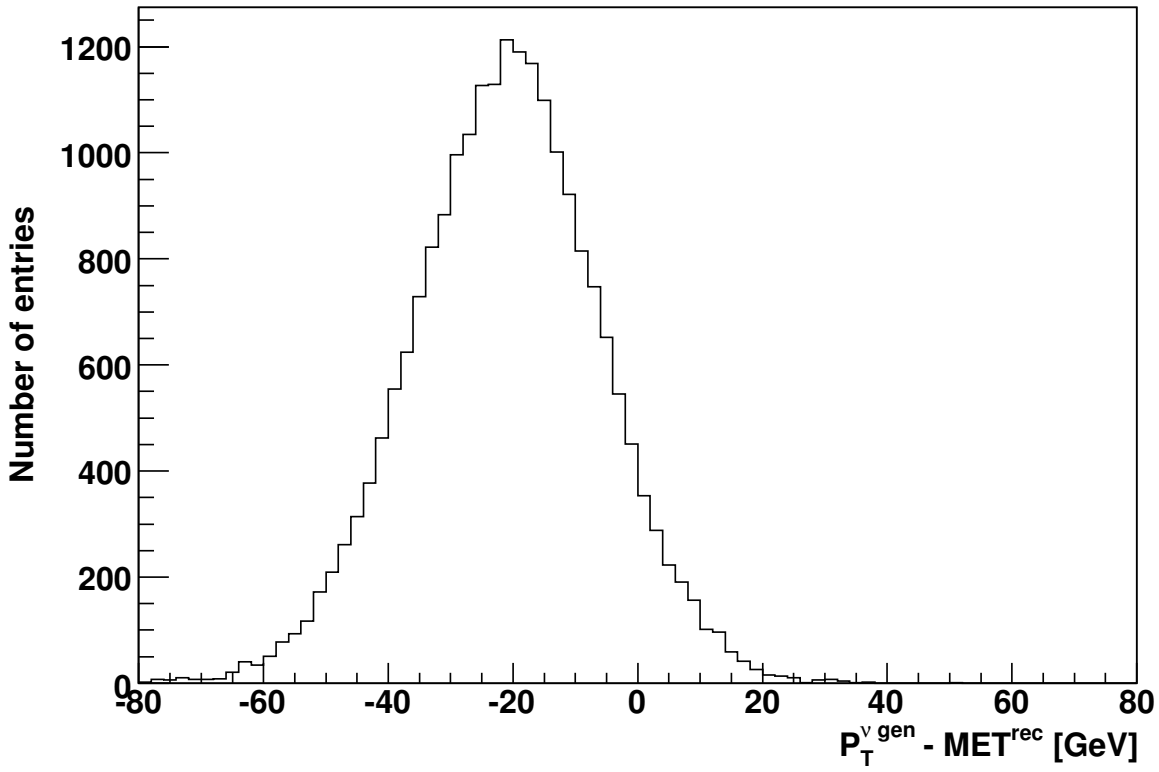

Figure 6.4.2: The difference of the generated transverse momentum and the reconstructed transverse energy of the neutrino for W events decaying into electron and neutrino. The Gaussian distribution has a σ of $\sim$ 17 GeV and a mean value of -20 GeV.

a too low threshold would introduce a large jet scale uncertainty and thus a larger systematic uncertainty, which will be discussed in section 6.4.1. Figure 6.4.3 shows the jet multiplicity per number of events in dependence of the jet transverse energy.

From the transverse momentum sum of these jets and the electron, the missing transverse energy is calculated and then associated with the neutrino. The $W \rightarrow e\nu$ sample is sub-divided into two event types. One sample with jets as defined previously and one sample without jets, i.e. no jet above 20 GeV. For both event types the transverse momentum of the electron and neutrino are presented in Figures 6.4.4, 6.4.5, 6.4.6 and 6.4.7.

The sharp cutoff at 20 GeV for the reconstructed neutrino in the "0-jet" sample results from the requirement, that the reconstructed electron must have at least a transverse energy of 20 GeV. In the case of zero accepted jets it is worth noting, that the absolute value of the reconstructed transverse energy of electrons and neutrinos is the same. Only the direction of the transverse momentum is opposite in ϕ. Having defined how to measure the reconstructed neutrino's transverse energy,

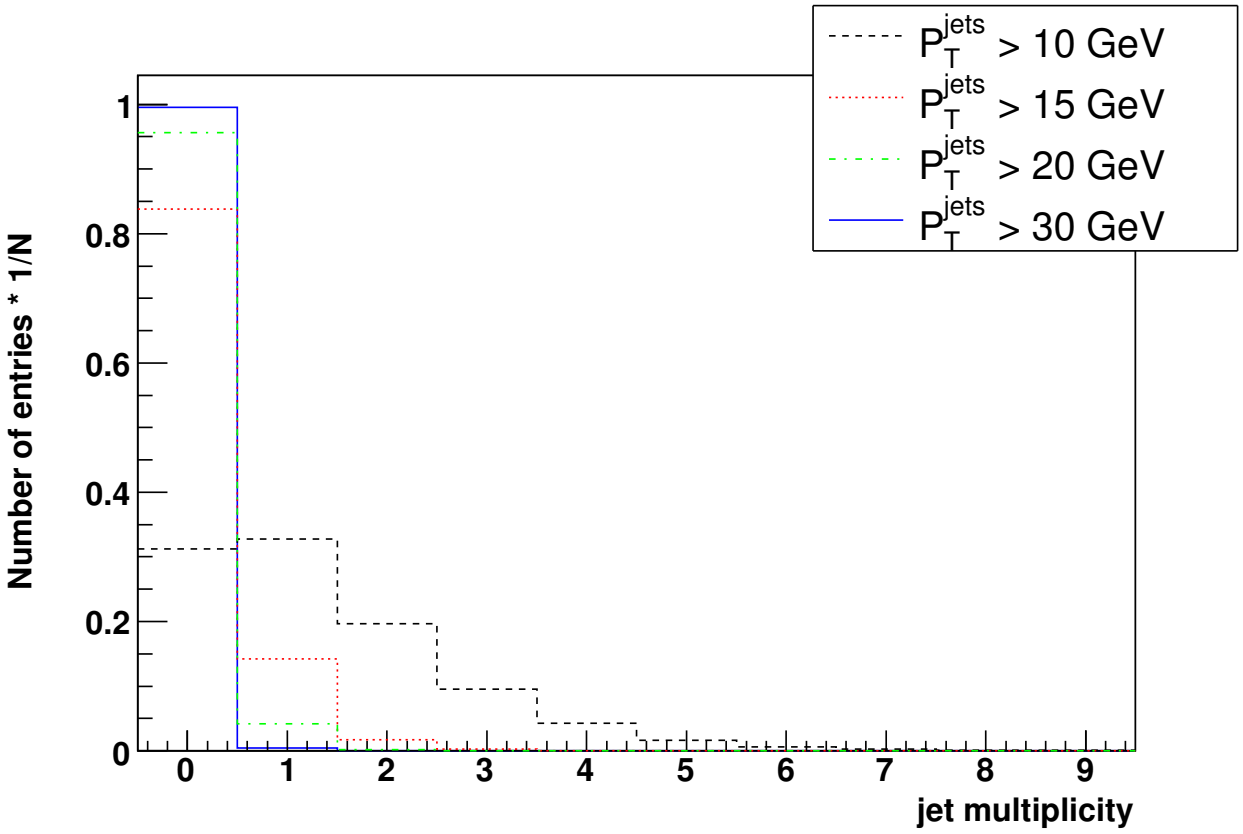

Figure 6.4.3: The jet multiplicity per number of events for different transverse energy cuts on the jets. In black, red, green and blue for jets which exceed a transverse energy of 10 GeV, 15 GeV, 20 GeV and 30 GeV. For example, 95 % of W events have no jet above $E_{\mathrm{T}} = 20\,\mathrm{GeV}$.

Figures 6.4.8 and 6.4.9 show the distribution of the difference of the generated and the reconstructed neutrino transverse energy.

Taking the vector sum of all hard object momenta to define the neutrino's transverse energy apparently introduces no systematic bias. A mean value close to 0 GeV is found in the samples of zero and at least one jet. In the former case a σ of around 6 GeV, in the latter case of about 12 GeV, is obtained by a Gaussian fit around the peak of the distributions. In Figures 6.4.10 and 6.4.11 the generated and reconstructed transverse W mass is presented.

The transverse W mass is reconstructed from the electron and the jet four-momenta. Only events which fulfill the transverse W mass requirement of $60\,\mathrm{GeV} < M_{\mathrm{T}}^{\mathrm{W}} < 100\,\mathrm{GeV}$ are considered for this analysis and for the purpose of counting resonant W events.

The trigger efficiency (first and higher level) for W events, which pass the (offline) selection and are reconstructed in the barrel calorimeter, is shown in Figure 6.4.12 as a function of the W rapidity. The W selection comprises all W events, which are generated in the mass region $|M_{\mathrm{W}}^{\mathrm{gen}} - 80.4\,\mathrm{GeV}| < 7.5\,\mathrm{GeV}$ and where the

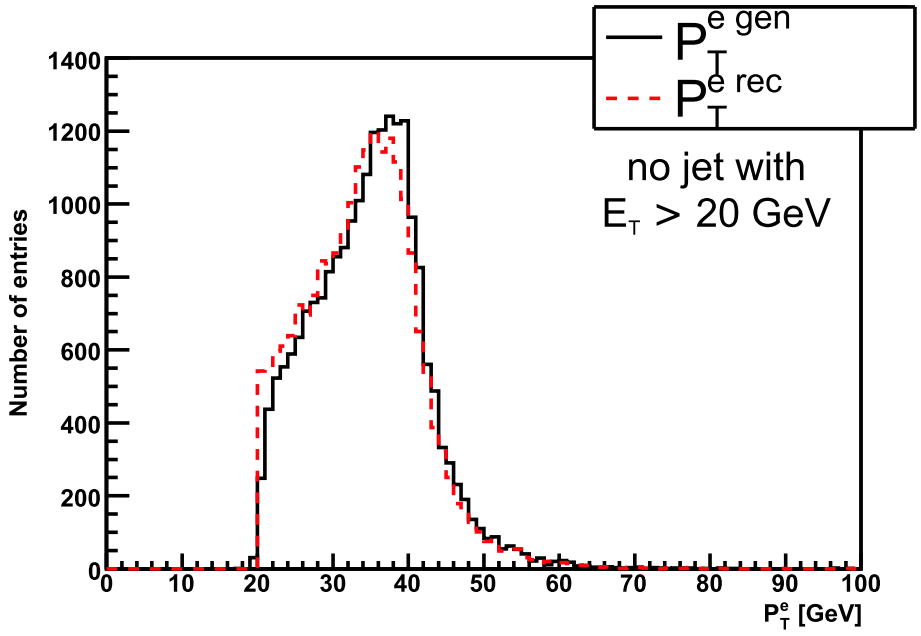

Figure 6.4.4: The transverse momentum of electrons from W decays is shown for events with no jet (above 20 GeV). The solid black line represents the generated and the red dashed line the reconstructed transverse momentum.

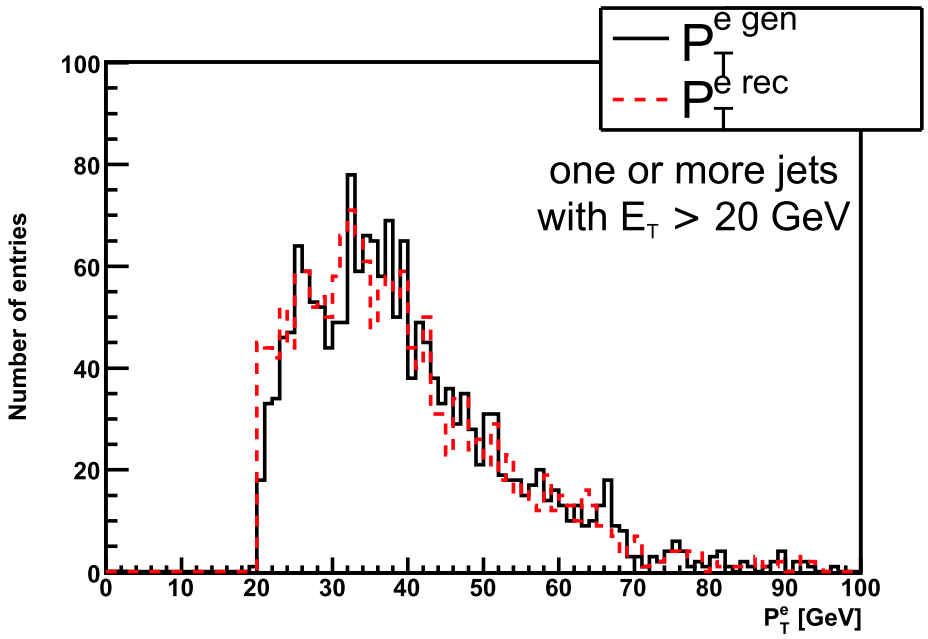

Figure 6.4.5: The transverse momentum of electrons from W decays is shown for events with one or more jets (above 20 GeV). The solid black line represents the generated and the red dashed line the reconstructed transverse momentum.

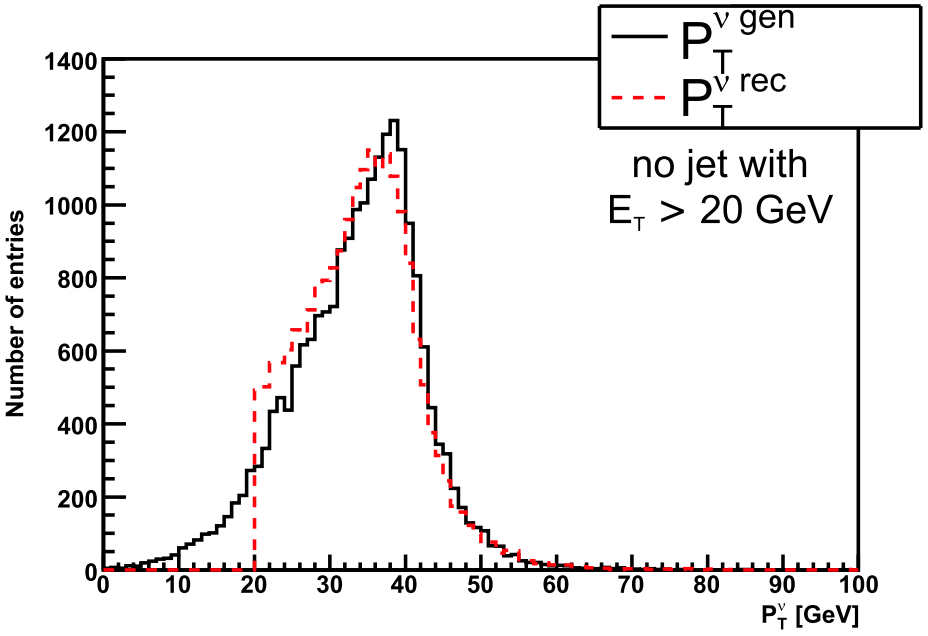

Figure 6.4.6: The transverse momentum of neutrinos is shown for events with no jet (above 20 GeV). The solid black line represents the generated and the red dashed line the reconstructed transverse momentum.

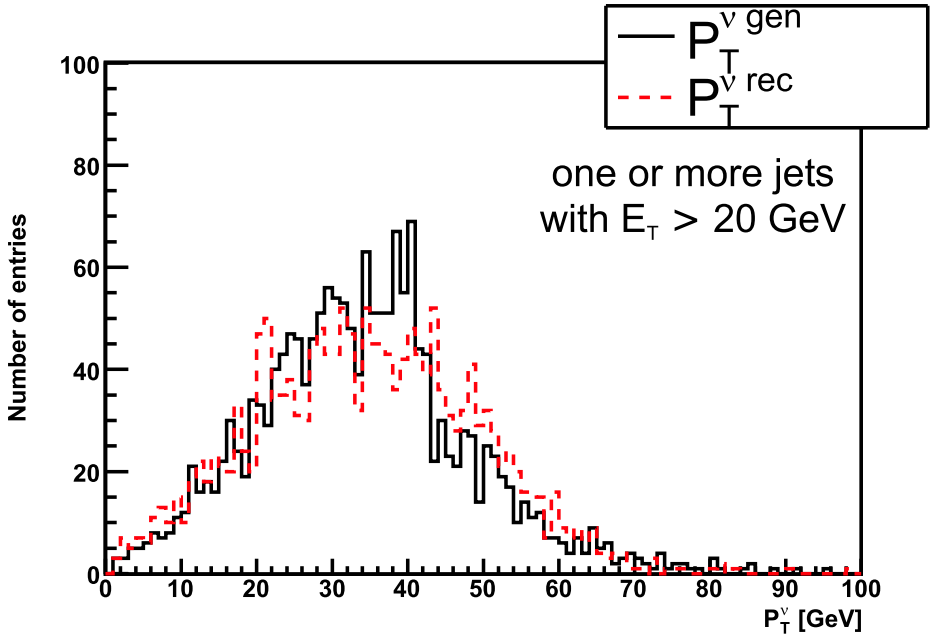

Figure 6.4.7: The transverse momentum of neutrinos is shown for events with one or more jets (above 20 GeV). The solid black line represents the generated and the red dashed line the reconstructed transverse momentum.

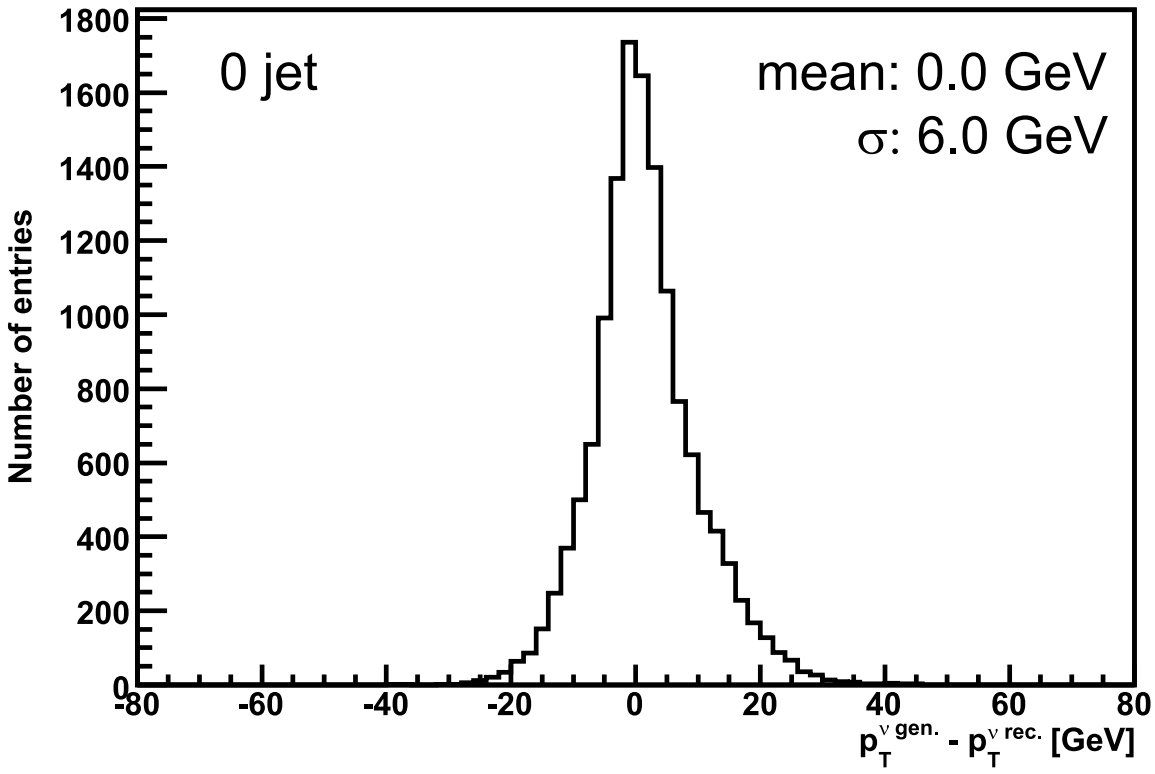

Figure 6.4.8: The distribution of the difference between the generated and the reconstructed transverse momentum of the neutrino for the "0-jet" sample. For these events, the electrons are required to have a transverse momentum between 30 GeV and 50 GeV. The reconstructed neutrino's transverse energy is identical to the one of the electron.

electron is generated with a pseudorapidity of $|\eta_e^{gen}| < 1.4$. In addition, exactly one electron has to be reconstructed in the event and this electron has to fulfill the selection criteria from section 6.2. The ratio of those events, which satisfy the trigger condition and the selection criteria to all offline selected W events, is defined as the trigger efficiency.

Obviously, depending on the rapidity, 10 % to 20 % of the events which are selected with the above criteria are not accepted by the trigger chain. According to ref. [SEE06], the simulation software used for this analysis contains some incorrect Level-1 trigger criteria. For example, too strict isolation cuts have been chosen. This explains the trigger inefficiency at least qualitatively.

6.4.1 Systematic uncertainties

Two sources of systematic uncertainties are studied. First, the uncertainty due to inhomogeneities in the detector geometry and second, the uncertainty related to

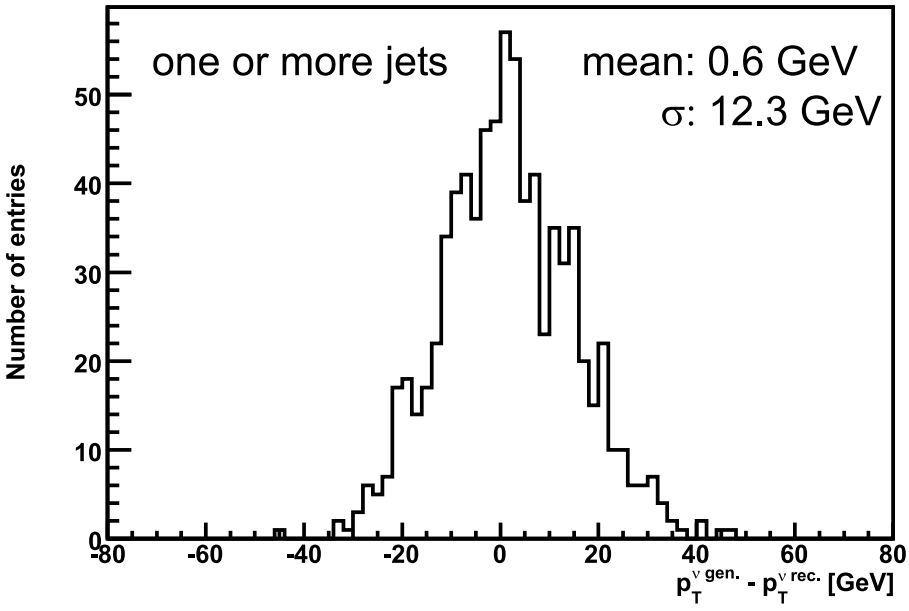

Figure 6.4.9: The distribution of the difference between the generated and the reconstructed transverse momentum of the neutrino for the sample with at least one jet in the event. For these events, the electrons are required to have a transverse momentum between 30 GeV and 50 GeV.

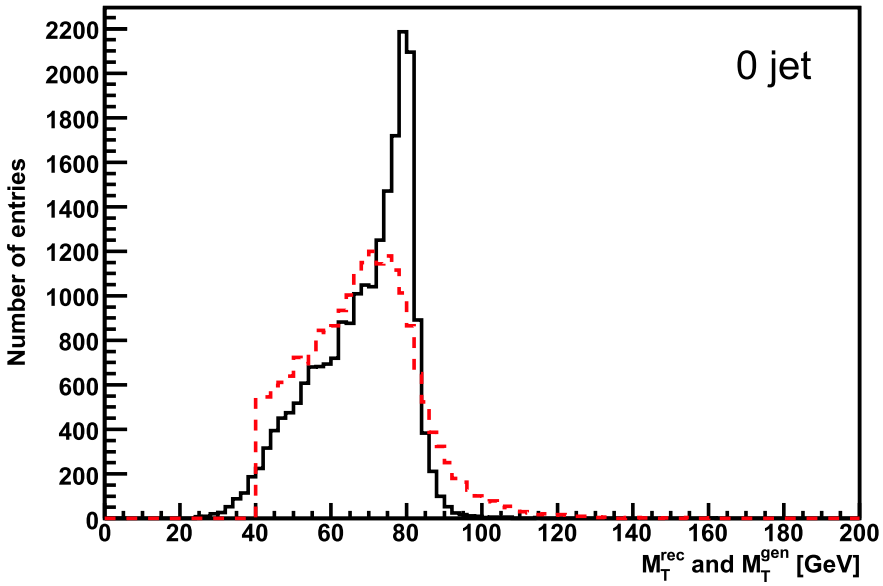

Figure 6.4.10: The transverse W mass is shown for events with no jet (above 20GeV). The solid black line indicates the generated and the dashed red line represents the reconstructed transverse W mass.

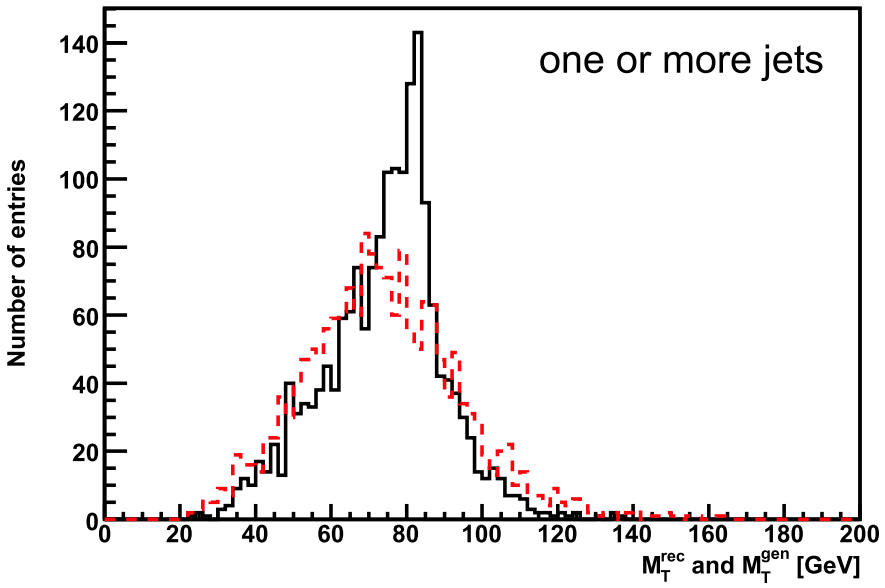

Figure 6.4.11: The transverse W mass is shown for events with one or more jets (above 20 GeV). The solid black line indicates the generated and the dashed red line represents the reconstructed transverse W mass.

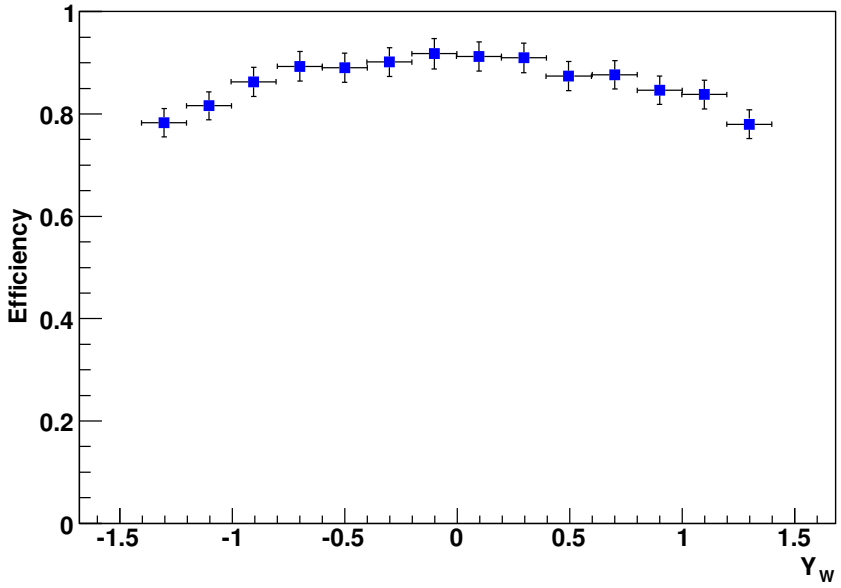

Figure 6.4.12: The trigger efficiency for W events reconstructed in the barrel region as a function of the generated W rapidity.

the jet veto. To start with the detector geometry, Figure 6.4.13 shows the selection efficiency of W events as a function of the electron azimuthal angle across the supermodule boundary.

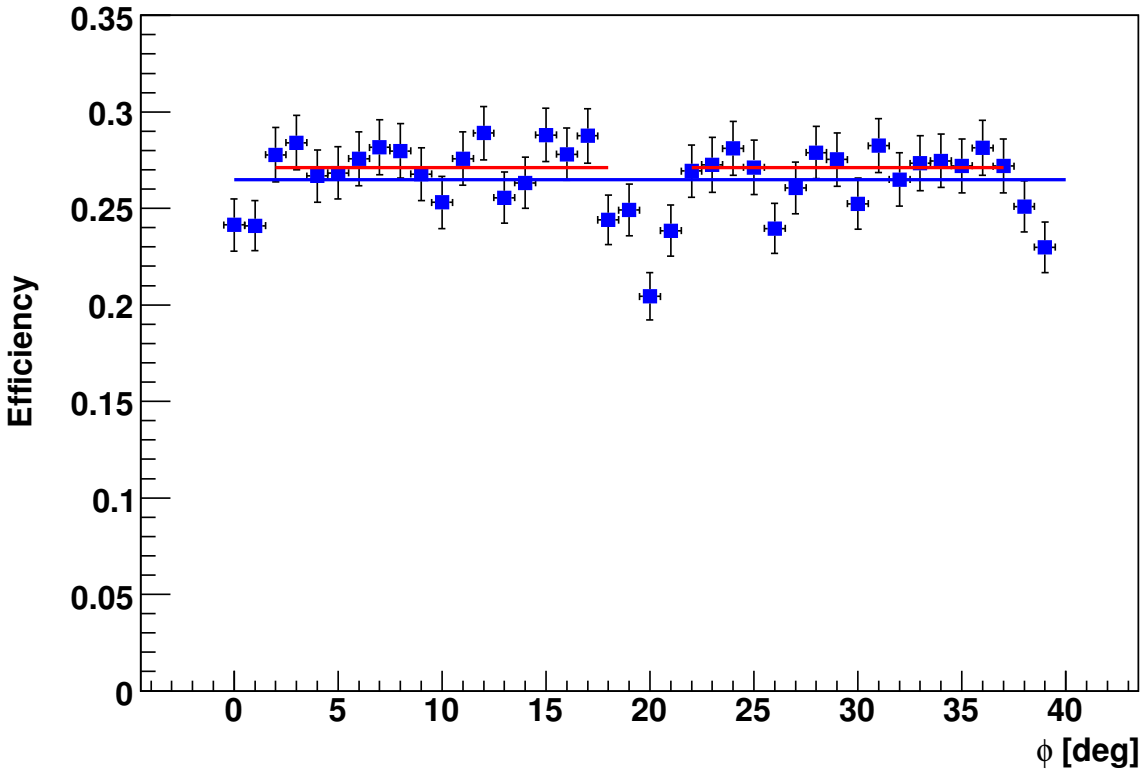

Figure 6.4.13: The reconstruction efficiency for $W \rightarrow e\nu$ events as a function of the reconstructed angle ϕ_{local} of the electron. ϕ_{local} means ϕ modulo 40° and corresponds to the azimuthal coverage of two adjoined supermodules. The drop in efficiency at the supermodule boundaries is clearly visible. The continuous blue line corresponds to the average efficiency over the whole range in ϕ, the interrupted red line corresponds to the average efficiency excluding the less efficient regions. An absolute difference of 0.6 % between both efficiencies is found.

The distribution is similar to the one for Z decays (Figure 6.3.6). Excluding the gap regions, an average efficiency of $27.1\% \pm 0.4\%$ is calculated, while for the whole range in ϕ an efficiency of 26.5 % ± 0.4 % is obtained. The errors are purely of statistical nature. It is to note that no cut on the number of jets per event is applied. Figure 6.4.14 shows the selection efficiency of W bosons as a function of the pseudorapidity.

Due to the very limited statistics, corresponding to only about $5\,\text{pb}^{-1}$, the efficiency drop at the supermodule boundaries is less pronounced in the $W \rightarrow e\nu$ sample compared to the $Z \rightarrow e^+e^-$ sample. Nevertheless, the drop from 27 % to 20 % (i.e. about 25 % relative) at the supermodule boundaries is explicitly apparent. Already with the small statistics available for this study, the efficiency loss due to the gaps

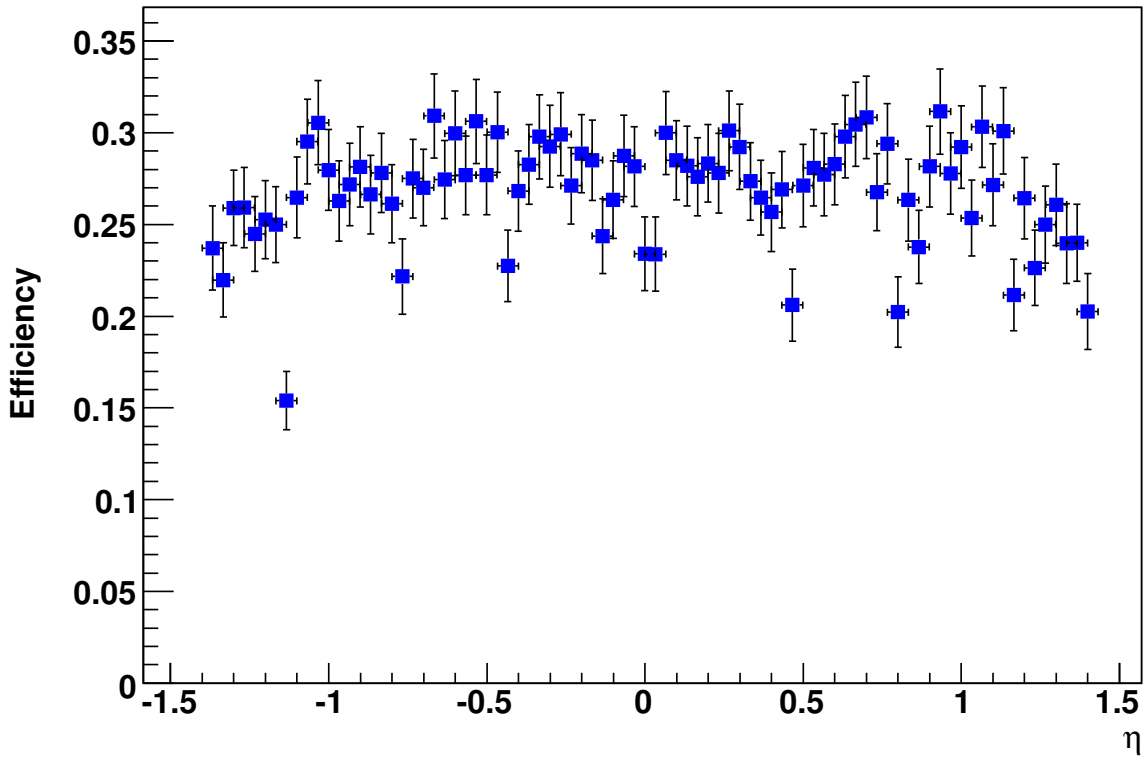

Figure 6.4.14: The reconstruction efficiency of W $\rightarrow$ eν events as a function of the reconstructed pseudorapidity η. No cuts on the jets are applied.

can be determined with a relative accuracy of about 40 %. This number is a rough estimate by comparing the minimal efficiency in the gap region with the efficiency of the non-gap regions. With increased statistics this accuracy will certainly improve drastically.

In the next step, the effect of the scale uncertainty of the absolute calibration on the jet energy is investigated in more detail. For that, the threshold of the transverse energy of the jet is varied and the change in the selection efficiency recorded, as illustrated in Figure 6.4.15.

Taking for example a cut on the transverse jet energy at 20GeV, an absolute efficiency slope of approximately 0.1 % per GeV is measured. This corresponds to a relative uncertainty of roughly 0.4% per GeV (at 25% W selection efficiency). Assuming a jet energy scale uncertainty of 15 % for the LHC startup phase [HEI06], it corresponds to a 3 GeV uncertainty for a jet energy of 20 GeV. Hence, a 1.2 % relative efficiency uncertainty is obtained. Assuming simply a 5 % uncertainty in the jet energy scale, that is after final detector calibration, the relative efficiency uncertainty decreases to merely 0.4 %.

As background, roughly half a million W $\rightarrow$ $\tau\nu$ and Z $\rightarrow$ $\tau\tau$ events were examined. After applying the same selection criteria on these samples, the transverse mass is

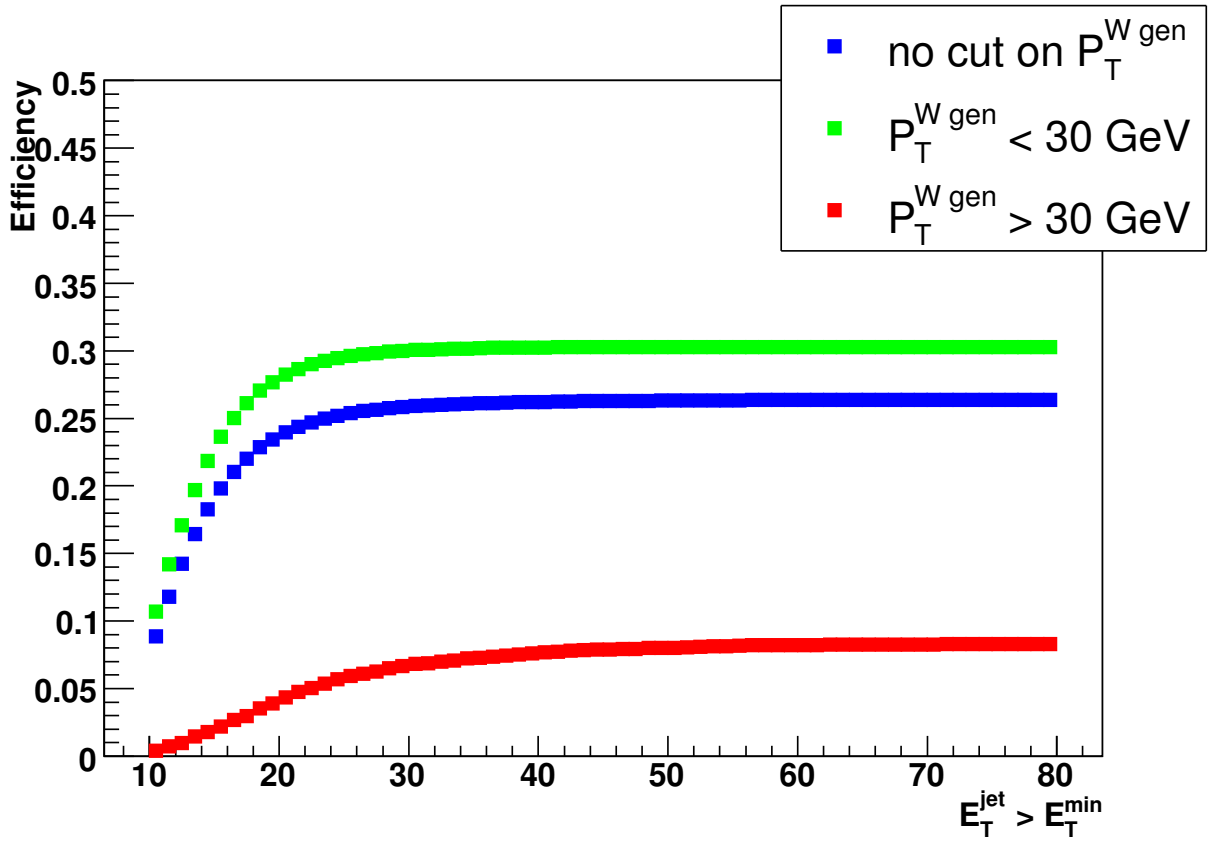

Figure 6.4.15: The efficiency of selecting W events with no jets as a function of the cut on the highest jet transverse energy. In blue (middle line) for all W events. In green (upper line) for events with a generated transverse momentum of the W of less than 30 GeV and in red (lower line) for events with a generated transverse momentum of the W of more than 30 GeV. All electrons must have a transverse energy between 30 GeV and 50 GeV. The abscissa shows the transverse energy for which an event is rejected if its highest jet transverse energy exceeds this value.

reconstructed as can be seen in Figures 6.4.16 and 6.4.17. In addition, the multi-jet background containing one electron (pp $\rightarrow$ jets + e) was tested with the W selection criteria.

For estimating the amount of background inside the signal region, only events with a reconstructed transverse mass between 60 GeV and 100 GeV are considered. A 1.6 % (2.6 %) contamination for no jet (at least one jet) events is found from the W $\rightarrow \tau\nu$ sample. Merely 0.1 % (0.3 %) from Z $\rightarrow \tau\tau$ events. The slightly higher background for events containing jets is expected, since the accuracy to determine the W transverse mass decreases (e.g. see Figure 6.4.11). However, due to the lepton universality and the well known branching ratio of taus decaying into electrons, an accurate control over the background should be possible. With the current Monte Carlo statistics, the background from multi-jet events containing one electron is measured to about 5 % for events with no jet above $E_T = 20$ GeV. This number is

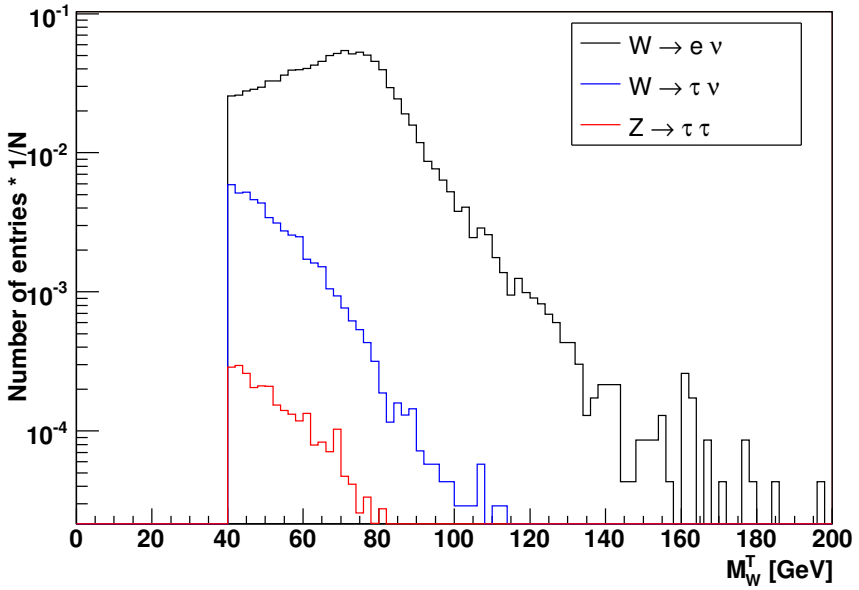

Figure 6.4.16: The reconstructed transverse mass for signal ($W \rightarrow e\nu$) events is shown in black and for background ($W \rightarrow \tau\nu$ and $Z \rightarrow \tau\tau$) events in blue and red, respectively. These events have no jet above 20 GeV. The number of events for the three samples is normalized to the number of signal events expected.

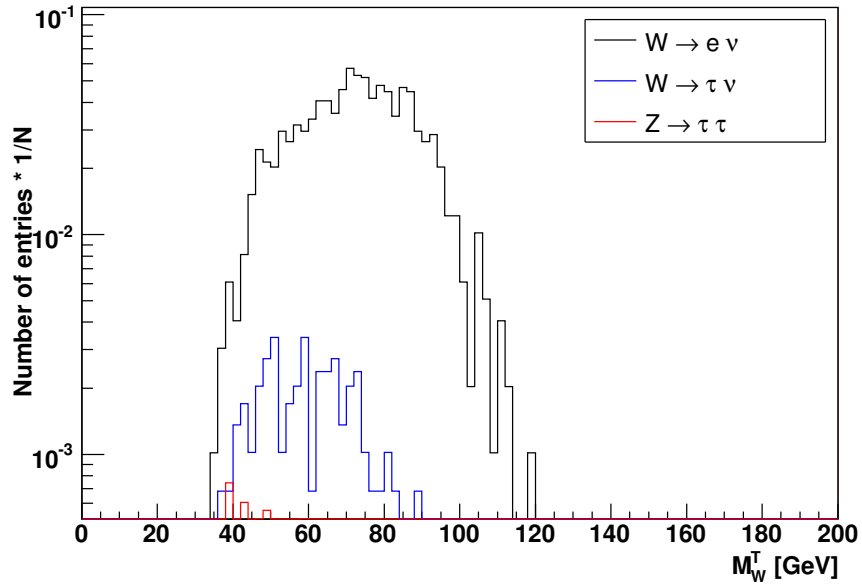

Figure 6.4.17: The reconstructed transverse mass for signal ($W \rightarrow e\nu$) events is shown in black and for background ($W \rightarrow \tau\nu$ and $Z \rightarrow \tau\tau$) events in blue and red, respectively. These events have one or more jets above 20 GeV. The number of events for the three samples is normalized to the number of signal events expected.

based on only two reconstructed events, such that the accuracy of this measurement is quite limited. Concerning the multi-jet background for events with one or more jets above $E_{\mathrm{T}} = 20\,\mathrm{GeV}$, no significant upper limit could be obtained, since the statistics is too low.

6.5 Summary

A selection of $\mathrm{pp} \to \mathrm{ZX}$ and $\mathrm{pp} \to \mathrm{WX}$ events and their decays to electrons was studied. This was pursued using the complete CMS software chain. The selection is based on solid and straightforward electron selection criteria, which are known from other studies, where the selection provided an excellent rejection of fake electrons. Therefore, it should be possible to access almost background-free Z events and W events with only a small background. An upper limit for $\mathrm{pp} \to \mathrm{jets} + \mathrm{e}$ background events in the Z selection of $\lesssim 2\,\%$ is obtained.

A reconstruction efficiency for Z events, where both electrons are detected in the barrel region ($\eta < 1.4$), of almost 60 % is found. With the available statistics of 600000 Drell-Yan Z events (this amount is already expected for the first round of LHC data taking), the simulation indicates an easy identification of geometrical gaps in the barrel electromagnetic calorimeter. Efficiency corrections at this stage are in principle possible at a 1 % to 2 % level and should be further reduced, once more events are available. To study the more complex endcap geometry, larger statistics is needed as well as a close investigation of the potential gaps. Nevertheless, a similar accuracy of counting Z boson events should also be possible for large rapidities. In a next step, effects from miscalibrations and dead or noisy crystals should be analyzed.

To estimate the reconstructed neutrino transverse energy from $\mathrm{W} \to \mathrm{e}\nu$ events, a method using only objects with large transverse momentum in the event is applied. That way, the bias introduced by taking the standard missing transverse energy calculation is reduced considerably. Therefore, the method introduced here is also used to reconstruct the transverse mass of the W boson. The jet energy scale uncertainty on the jet veto was addressed. Only a small effect of about 1 % on the selection efficiency was found.

In conclusion, the current Monte Carlo simulation allows for selecting $\mathrm{pp} \to \mathrm{WX} \to \mathrm{e}\nu$ events with the robust electron selection criteria and indicates that this selection leads to a background from $\mathrm{W} \to \tau\nu$ events of about 2 %, which should be well under control. A very rough backround estimation of $\sim 5\,\%$ from multi-jet events containing one electron is obtained for events with no jet above $E_{\mathrm{T}} = 20\,\mathrm{GeV}$. Background from $\mathrm{Z} \to \tau\tau$ events is negligible. Furthermore, the efficiency can be monitored accurately and the experimental systematic uncertainties for counting $\mathrm{W} \to \mathrm{e}\nu$ events should reach eventually the same accuracy as for the $\mathrm{Z} \to \mathrm{e^+e^-}$ events, which is in the order of 1 %.

Chapter 7

Conclusions and Outlook

For the first time a luminosity determination via the counting of on-shell Z bosons and the use of differential next-to-next-to-leading order (NNLO) cross section calculations was carried out. Two years of CDF data between March 2002 and February 2004 have been analyzed, corresponding to roughly 14000 selected Z boson events and their decays to electrons and positrons. An integrated luminosity of $L_{\text{counting}} = 221.7 \pm 2.8\,(\text{stat.}) \pm 11.2\,(\text{sys.})\,\text{pb}^{-1}$ has been measured, which is in very good agreement with the traditional measurement at CDF of $L_{\text{CLC}} = 222.2 \pm 12.9\,\text{pb}^{-1}$, using Cherenkov Luminosity Counters at large angles. The uncertainties of both measurements are of comparable size. For the counting method the largest uncertainty is purely theoretical, namely the knowledge of the parton distribution functions. Moreover, the rapidity dependence for on-shell Z boson production was analyzed. The theoretical calculations of the differential cross section and the experimental measurements agree within their errors.

For the CMS experiment, a first baseline selection in the channels $\text{pp} \rightarrow \text{ZX} \rightarrow \text{e}^+\text{e}^-$ and $\text{pp} \rightarrow \text{WX} \rightarrow \text{e}\nu$ is presented in order to determine potential uncertainties from detector inhomogeneities. To test the Drell-Yan $\text{Z} \rightarrow \text{e}^+\text{e}^-$ event selection against background, several million multi-jet evens containing one electron ($\text{pp} \rightarrow \text{jets} + \text{e}$) have been analyzed and no single event survived the selection criteria. This corresponds to an upper limit for multi-jet background events of $\lesssim 2\,\%$. The efficiency for Z events, where the electron and positron are both detected at central pseudorapidities ($|\eta| < 1.4$), is found to be about 60 %. Potential gaps in the barrel electromagnetic calorimeter can be well detected and efficiency corrections should be able to be applied with a precision of better than 1 %. In a next step of CMS detector studies the effect from miscalibrations and from possibly dead or noisy crystals should be looked at.

$\text{W} \rightarrow \text{e}\nu$ events were selected and a separation of events with no jet and events with at least one jet was performed. The effect of the jet energy scale uncertainty was addressed and found to be small ($\sim 1\,\%$). The efficiency for events, where the electron/positron is detected in the barrel region, is determined to be about 25 %. Concerning the background, the $\text{W} \rightarrow \tau\nu$ sample showed a $\sim 2\,\%$ contribution. However, due to the lepton universality and the well-known branching ratio from taus

decaying into electrons, no major systematic uncertainty is expected. Background from multi-jet events containing one electron showed a $\sim 5\,\%$ contribution for events with no jet above $E_{\mathrm{T}} = 20\,\mathrm{GeV}$

Overall, this thesis showed the importance of the Drell-Yan process. The luminosity and the cross section shape for on-shell Z bosons could be determined at CDF experiment. A method for counting Drell-Yan events, leading to experimental systematic uncertainties in the order of $1\,\%$, was presented for CMS experiment. In the future, the ETH group will continue studying the Drell-Yan process with regard to CMS detector.

Appendix

Appendix A

List of Figures

1.2.1 Summary table for all fermions. The three generations are indicated in colors and are arranged with increasing mass from top to bottom. 5

1.2.2 Summary table for the properties of the bosons. 5

1.2.3 Summary table for the properties of the forces. 6

1.3.1 The Higgs potential $V = -\mu^2\Phi^\dagger\Phi + \lambda(\Phi^\dagger\Phi)^2$ for $-\mu^2 < 0$. 10

1.3.2 An example of quark-quark scattering by the exchange of a gluon. The colors are indicated. 12

2.1.1 Schematic view of the accelerator chain at Fermilab. 16

2.1.2 The integrated luminosity in inverse pico barn is shown for the years 2002 to 2005. Indicated are also the shutdown periods in the end of 2003 and 2004, where works at the Tevatron, the Recycler and a new neutrino experiment (NUMI) were carried out. 17

2.1.3 The peak luminosities for the different stores from the year 2002 to 2005 are presented in inverse micro barn per second. 18

2.2.1 A sketch of the CDF detector with all its detector components. The length scale indicates its size. 19

2.2.2 The CDF coordinate system with respect to the Tevatron in x, y, z, ϕ and θ. 20

2.2.3 Shown are all components of the CDF tracking system. In addition, the magnet and parts of the calorimeter are also sketched. The range in pseudorapidity is indicated. 21

2.2.4 The geometrical arrangement in the yθ-plane of the three sub-systems of the inner tracking chamber. The z-coordinate is compressed. 22

2.2.5 The rϕ-plane of the COT is presented. The sketch shows one sixth of the east endplate. For each superlayer the average radius (in centimeter), the wire orientation (axial and stereo) and the total number of supercells are given. The zoom shows the sense and field sheet slot geometry. 23

2.2.6 Parts of the detector and the position of the Cherenkov Luminosity Counter are shown. The CLC is located at large pseudorapidities close to the beam-pipe. Primary and secondary particles traversing the detector are indicated. 26

3.1.1 Schematic view of the complete accelerator chain at CERN - from the Linac to the LHC. Other accelerator parts are also shown. 30

3.1.2 Cross section of a standard LHC dipole. 31

3.1.3 The four experiments at LHC. The LHC tunnel lies at a depth varying between 50 and 150 meters. 32

3.2.1 The CMS detector with all its sub-components is displayed in this drawing. 33

3.2.2 A sketch of one quarter of the CMS detector. 33

3.2.3 The CMS pixel detector (barrel and endcaps). 34

3.2.4 Layout of the Silicon Micro-Strip Detector. 35

3.2.5 The light yield temperature dependence for the crystals and the temperature coefficient for the APD's are shown. 36

3.2.6 The arrangement of the CMS ECAL sub-modules, modules and supermodules. 37

3.2.7 Artistic view of the endcap ECAL. The preshower detector is also indicated. 38

3.2.8 The energy resolution as a function of the reconstructed energy in a 3×3 crystal matrix, centered on crystal number 704. 39

3.2.9 Sketch of one quarter of the CMS detector. The HCAL is located in between the magnetic coil and the ECAL and reaches up to rapidities of $|\eta| = 3$. 40

3.2.10 Transverse slice through the CMS detector. Different charged particles are indicated which follow bent trajectories due to the magnetic field. 41

3.2.11 Longitudinal view of one quarter of the CMS muon system. 42

4.0.1 Leading order Feynman diagram for Drell-Yan electron pair production. 45

4.0.2 Next-to-leading order (NLO) contributions for Drell-Yan electron pair production. The electron pair from the γ^*/Z decay is not shown here. 46

4.1.1 The inclusive Drell-Yan lepton pair production cross sections ($p\bar{p} \rightarrow \gamma^*/Z \rightarrow l^+l^-$ and $p\bar{p} \rightarrow W \rightarrow l\nu$) are shown with respect to the center of mass energy. The lines represent the theoretical NNLO calculations for the individual processes, the points with the error bars indicate the measurement of the corresponding experiments and their uncertainties. 48

4.2.1 The LO, NLO and NNLO results for the rapidity distribution of the cross section for on-shell Z bosons at the Tevatron. The error bands indicate the variation of the renormalization and factorization scale in the range $M_Z/2 < \mu < 2M_Z$ [ANA04]. 50

4.2.2 The LO, NLO and NNLO results for the rapidity distribution of the cross section for on-shell Z bosons at the LHC. The error bands indicate the uncertainties from the variation of the renormalization and factorization scale in the range $M_Z/2 < \mu < 2M_Z$ [ANA04]. 51

4.2.3 The region of the parton kinematics x and Q^2 is shown, which is covered by the deep inelastic scattering experiments at HERA and the region accessible with the LHC [STI04]. 54

5.2.1 A schematic view of the two different event types. On the left a Z boson event with both electrons central, on the right a Z boson event with only one electron detected in the central calorimeter and the other one in the plug calorimeter. The electrons are indicated by the black arrows. 60

5.2.2 The normalized distributions for good electron candidates are shown, on the left for central-central electrons, on the right for central-plug electrons. Except for the plotted variable, all the cuts on the other variables are applied. Data is shown as dots, the Monte Carlo prediction as solid line. 61

5.2.3 The invariant mass distribution of central-central electrons for various combinations of their electron quality. The data is shown with its statistical uncertainty as error bars, the simulation as solid line. Those combinations which are used to define the Z signal are highlighted, namely gold-gold, gold-silver and gold-bronze. These combinations are also used to determine the normalization factor between data and simulation. 62

5.2.4 The invariant mass distribution of central-plug electrons with the specific combination of their electron quality. The data is shown with its statistical uncertainty as error bars, the simulation as solid line. Highlighted are the combinations which are used to define the Z signal, namely gold-gold, gold-silver, gold-bronze, silver-silver and silver-bronze. Moreover, the central electron had to be at least golden or silver. These combinations are also used to determine the normalization factor between data and simulation. 63

5.2.5 The invariant mass distribution of accepted electron pairs. The Gaussian fit to the data between 80 GeV and 100 GeV is shown in red for the energy corrected data. The Monte Carlo simulation is normalized to the number of events found within $\pm\, 2\,\sigma$ around the fitted Z mass peak. 65

5.3.1 A sketch of the Z boson mass peak. In red the signal region with Z boson events and background, in blue the sidebands which only contain background events. 66

5.3.2 The bronze-bronze electron combination for central-central and central-plug Z bosons. Data is shown with its error bars and the fit as a solid line. 66

5.3.3 Z boson candidate events for central-central and for central-plug electrons. The fits of the background are indicated in red and blue with a $\frac{\chi^2_{\mathrm{cc}}}{\mathrm{n.d.f.}} = \frac{55}{47}$ and $\frac{\chi^2_{\mathrm{cp}}}{\mathrm{n.d.f.}} = \frac{60}{47}$, respectively. 67

5.3.4 The shape of the Z-reconstruction efficiency as a function of rapidity for central-central and central-plug electrons, only statistical errors are plotted. 67

5.3.5 The distribution from simulation for reconstructed Z bosons which are generated "off-shell". In red the events which are reconstructed in the signal region, in blue those events which are reconstructed in the sidebands. 68

5.3.6 A two-dimensional plot for the reconstructed and generated mass of Z boson candidate events, which are generated "off-shell" but reconstructed inside the counting region. The region for "on-shell" generated Z bosons is located in between the two blue dashed lines. 68

5.3.7 The z-vertex distribution for events boosted into the detector, for data and Monte Carlo simulation. 71

5.3.8 The trigger efficiencies with statistical errors for the electron qualities for the ELECTRON_CENTRAL_18 trigger and the W_NOTRACK trigger as a function of the calorimeter tower number in η. 72

5.5.1 Ratios of the number of counted Z bosons and the corresponding CLC luminosity estimates. Indicated are also the mean values of these ratios and the $\pm$ 5 % line, which is approximately equivalent to the uncertainty of the CLC monitors. The bottom plot shows the ratio between the counting of Z bosons for central-central electrons and central-plug electrons. All error bars are purely statistical. 75

5.5.2 The number of Z bosons for data and simulation per calorimeter tower in the ϕ-direction is shown. 76

5.5.3 The change of the uncorrected invariant mass of two reconstructed electrons originating from Z boson candidate events for different run periods. The lines show the average value for central-central and central-plug electrons, respectively. The statistical uncertainties are shown as error bars. 77

5.5.4 The difference between the uncorrected reconstructed Z boson mass for events with one central electron and one electron in the east-plug (Zcpe) on the one hand and one central electron and one electron in the west-plug (Zcpw) on the other hand, for different run periods. The lines show the average value of approximately 89.1 GeV for central-east-plug and approximately 88.8 GeV for central-west-plug electrons. The error bars indicate the statistical error. 78

5.5.5 The rapidity distribution for Z bosons originating from central-central and central-plug electrons. The data is shown as dots with their statistical error and the Monte Carlo simulation as a blue line. 78

5.5.6 The relative difference in the number of reconstructed Z events between data and simulation per rapidity-bin after all cuts. 79

5.5.7 The transverse momentum of reconstructed Z bosons. The simulation is indicated with a dashed blue line and the data with points and their statistical error as error bars. 79

5.5.8 The relative difference in the number of reconstructed Z events between data and simulation per p_{T}-bin after all cuts. 79

5.5.9 Rapidity distributions for central-central electrons for different p_{T}-regions. From the left to the right - Upper row: (0-5) GeV, (5-10) GeV, (10-15) GeV. Middle row: (15-20) GeV, (20-25) GeV, (25-30) GeV. Lower row: (30-35) GeV, (35-40) GeV , 40 GeV and above. . . . 80

5.5.10 Rapidity distributions for central-plug electrons for different p_{T}-regions. From the left to the right - Upper row: (0-5) GeV, (5-10) GeV, (10-15) GeV. Middle row: (15-20) GeV, (20-25) GeV, (25-30) GeV. Lower row: (30-35) GeV, (35-40) GeV , 40 GeV and above. 81

5.6.1 The z-vertex distributions for the different rapidity regions for events boosted inside the detector. The data is shown as dots with its statistical errors and the simulation as a solid line. 83

5.6.2 The generated versus the reconstructed rapidity is plotted for central-central Z bosons. Though the distribution is quite narrow, a correction for accurate counting of Z bosons in the individual rapidity bins is necessary. 84

5.6.3 The generated versus the reconstructed rapidity is plotted for central-plug Z bosons. The double peak structure results from the fact that one electron has to be reconstructed inside the plug calorimeter. . . . 86

5.6.4 The measured luminosity in the different rapidity regions. Indicated in red is the luminosity for central-central Z bosons and in green for central-plug. The straight lines represent the mean value of the luminosity, the dotted ones indicate the systematic error on the mean. The statistical error on the individual measurements are shown in bold bars, the statistical plus systematic error are shown as thin error bars. 87

5.6.5 The combined measured luminosity in the different rapidity regions. The straight line represents the mean value of the luminosity, the dotted thin ones indicate the systematic error on the mean, including the parton distribution function uncertainty, the dotted bold lines indicate the systematic error on the mean, excluding the parton distribution function uncertainty. The statistical error on the individual measurements are shown in bold bars, the statistical plus systematic error are shown as thin error bars. 88

5.6.6 The ratio of the measured luminosity from Z bosons decaying in a central and a plug electron, and a Z reconstructed from two central electrons as a function of rapidity. The straight line represents the average ratio, the dotted ones indicate the systematic error on the average. The statistical error on the individual measurements are shown in bold bars, the statistical plus systematic error are shown as thin error bars. 88

5.6.7 The differential cross section for on-shell Z boson production over the different rapidity regions. In gray rectangles the theoretical NNLO calculations with their uncertainties as error bars. The measurements and their statistical errors are shown in red (central-central) and green (central-plug). 89

5.6.8 The differential cross section for on-shell Z boson production over the different rapidity regions. In gray rectangles the theoretical NNLO calculations with their uncertainties as error bars. The combined central-central and central-plug measurements and their statistical errors are shown in blue. 89

6.0.1 A Z boson decay into electrons within the CMS detector. Only parts of the tracking system and the electromagnetic calorimeter are displayed. Besides the Z decay also the underlying event and minimum bias events are included. 92

6.1.1 The generated mass distribution of e^+e^- pairs with a minimal Drell-Yan mass of 15 GeV. 93

6.1.2 Schematic view of the three $Z \rightarrow e^+e^-$ event types in CMS. The arrows indicate only the direction of the electrons and not their reach inside the CMS detector. 94

6.1.3 The rapidity distribution for all generated Z events is presented as a solid black line. The dashed line displays the same events with the additional requirement that the electrons are generated within $|\eta| < 2.4$. The events in red are generated within the barrel acceptance. For comparison, the reconstructed events for BB, BE and EE are plotted in blue, green and magenta. 94

6.1.4 The maximal possible Z detection efficiency versus the rapidity. The drop in efficiency towards larger rapidities results purely from the geometrical acceptance. 95

6.1.5 The generated W boson mass distribution. The cuts indicate the on-shell W bosons ±7.5 GeV around the W mass peak. 96

6.1.6 Distribution of the generated transverse momentum of the W bosons. 96

6.1.7 The jet multiplicity per number of events is shown for jets, which exceed a transverse energy of 20 GeV. Events which have a transverse W momentum below 30 GeV are indicated with a solid black line. Events which feature a transverse W momentum of at least 30 GeV are shown as a dashed red line. 97

6.1.8 The rapidity distribution for generated W^+ (solid black line) and W^- (red dashed line) events. 98

6.1.9 The pseudorapidity distribution for generated e^+ (solid black line) and e^- (red dashed line). 98

6.1.10 The maximal efficiency to detect a $W^\pm$, where the $e^\pm$ is generated within the barrel acceptance of $|\eta| < 1.4$. 99

6.2.1 All selection cuts on the electron variables are shown, namely for the transverse energy (E_T, upper left), the shower width in η ($\sigma_{\eta\eta}$, upper right), the ratio of hadronic to electromagnetic energy in the calorimeters ($\frac{E_{had}}{E_{em}}$, middle left), the ratio of the supercluster energy to the momentum of the associated track ($\frac{E_{SC}}{p_{track}}$, middle right), the absolute value of the difference of the inverse energy and the inverse momentum, ($|\frac{1}{E_{SC}} - \frac{1}{p_{track}}|$, lower left) and the track isolation (lower right). All other selection cuts, excluding the cut on the displayed variable, are applied. All plots contain one entry per electron and no requirement of having two electrons is imposed. The processes are not normalized to each other. 102

6.3.1 Number of electron candidates per event 103

6.3.2 The L1 + HLT efficiency for Z events, which pass the Z selection criteria. On the left side for Z events where the electrons are both reconstructed in the barrel detector, on the right side for Z events where one electron is reconstructed in the endcap and the other one in the barrel. 103

6.3.3 Generated (red line) and reconstructed (black points with error bars) Z mass distribution after all cuts on the electrons. 105

6.3.4 Difference between the reconstructed electron positron pair mass and the generated mass. The parameters of the Gaussian fit between ±3GeV are shown. 105

6.3.5 The ratio of the generated to the reconstructed transverse energy is presented for electrons in the barrel calorimeter, including statistical errors. Whereas the ratio at central pseudorapidities differs less than 1 % from unity, it rises up to 3.5 % at large pseudorapidities. 106

6.3.6 The electron reconstruction efficiency from $Z \rightarrow e^+e^-$ events as a function of local ϕ in the barrel calorimeter. The average efficiency outside the gap-region (red interrupted line) and over the whole ϕ-range (blue continuous line) are indicated. Their difference is 1.2 %. . 107

6.3.7 The electron reconstruction efficiency from $Z \rightarrow e^+e^-$ events as a function of η in the barrel and endcap calorimeter. All electrons which are reconstructed outside the fiducial volume in ϕ do not contribute to this plot. 108

6.4.1 Number of electron candidates per event. 109

6.4.2 The difference of the generated transverse momentum and the reconstructed transverse energy of the neutrino for W events decaying into electron and neutrino. The Gaussian distribution has a σ of $\sim 17\,\text{GeV}$ and a mean value of $-20\,\text{GeV}$. 110

6.4.3 The jet multiplicity per number of events for different transverse energy cuts on the jets. In black, red, green and blue for jets which exceed a transverse energy of 10 GeV, 15 GeV, 20 GeV and 30 GeV. For example, 95 % of W events have no jet above $E_{\text{T}} = 20\,\text{GeV}$. 111

6.4.4 The transverse momentum of electrons from W decays is shown for events with no jet (above 20 GeV). The solid black line represents the generated and the red dashed line the reconstructed transverse momentum. 112

6.4.5 The transverse momentum of electrons from W decays is shown for events with one or more jets (above 20 GeV). The solid black line represents the generated and the red dashed line the reconstructed transverse momentum. 112

6.4.6 The transverse momentum of neutrinos is shown for events with no jet (above 20 GeV). The solid black line represents the generated and the red dashed line the reconstructed transverse momentum. 113

6.4.7 The transverse momentum of neutrinos is shown for events with one or more jets (above 20GeV). The solid black line represents the generated and the red dashed line the reconstructed transverse momentum. . . . 113

6.4.8 The distribution of the difference between the generated and the reconstructed transverse momentum of the neutrino for the "0-jet" sample. For these events, the electrons are required to have a transverse momentum between 30GeV and 50GeV. The reconstructed neutrino's transverse energy is identical to the one of the electron. 114

6.4.9 The distribution of the difference between the generated and the reconstructed transverse momentum of the neutrino for the sample with at least one jet in the event. For these events, the electrons are required to have a transverse momentum between 30 GeV and 50 GeV. 115

6.4.10 The transverse W mass is shown for events with no jet (above 20GeV). The solid black line indicates the generated and the dashed red line represents the reconstructed transverse W mass. 115

6.4.11 The transverse W mass is shown for events with one or more jets (above 20 GeV). The solid black line indicates the generated and the dashed red line represents the reconstructed transverse W mass. . . . 116

6.4.12 The trigger efficiency for W events reconstructed in the barrel region as a function of the generated W rapidity. 116

6.4.13 The reconstruction efficiency for W $\rightarrow$ eν events as a function of the reconstructed angle ϕ_{local} of the electron. ϕ_{local} means ϕ modulo 40° and corresponds to the azimuthal coverage of two adjoined supermodules. The drop in efficiency at the supermodule boundaries is clearly visible. The continuous blue line corresponds to the average efficiency over the whole range in ϕ, the interrupted red line corresponds to the average efficiency excluding the less efficient regions. An absolute difference of 0.6 % between both efficiencies is found. 117

6.4.14 The reconstruction efficiency of W $\rightarrow$ eν events as a function of the reconstructed pseudorapidity η. No cuts on the jets are applied. . . . 118

6.4.15 The efficiency of selecting W events with no jets as a function of the cut on the highest jet transverse energy. In blue (middle line) for all W events. In green (upper line) for events with a generated transverse momentum of the W of less than 30 GeV and in red (lower line) for events with a generated transverse momentum of the W of more than 30 GeV. All electrons must have a transverse energy between 30 GeV and 50 GeV. The abscissa shows the transverse energy for which an event is rejected if its highest jet transverse energy exceeds this value. 119

6.4.16 The reconstructed transverse mass for signal (W $\rightarrow$ eν) events is shown in black and for background (W $\rightarrow \tau\nu$ and Z $\rightarrow \tau\tau$) events in blue and red, respectively. These events have no jet above 20GeV. The number of events for the three samples is normalized to the number of signal events expected. 120

6.4.17 The reconstructed transverse mass for signal (W $\rightarrow$ eν) events is shown in black and for background (W $\rightarrow \tau\nu$ and Z $\rightarrow \tau\tau$) events in blue and red, respectively. These events have one or more jets above 20 GeV. The number of events for the three samples is normalized to the number of signal events expected. 120

Appendix B

List of Tables

1.3.1 The weak isospin, the hypercharge and the electric charge for fermions [HAL84]. 7

2.2.1 Overview of the electromagnetic and hadronic calorimeter properties. 24

2.2.2 Estimate of the systematic uncertainties on the luminosity measurement of the CLC in 2004. [ROS04] 27

4.1.1 The largest branching fractions for the Z and W decay modes [PDG06]. 49

4.2.1 Results of the theoretical on-shell Z boson cross section calculations as a function of rapidity (lower and upper bin limits are given) for the Tevatron. The errors on these calculations from PDF uncertainties and scale variations are listed as well as the total (quadratic sum of both) and the relative error. 52

4.2.2 Results of the theoretical on-shell Z boson cross section calculations as a function of rapidity (lower and upper bin limits are given) for the LHC. The errors on these calculations from PDF uncertainties and scale variations are listed as well as the total (quadratic sum of both) and the relative error. 52

5.1.1 The data divided into several time periods. The run numbers and the corresponding CLC luminosity estimates are indicated. 58

5.2.1 Results obtained by the Gaussian fit of the invariant mass distributions for uncorrected and corrected data and simulation. The statistical errors for mass and width are below 100 MeV. 64

5.4.1 The data divided into several time periods. For each period there are two rows indicating events, efficiencies and luminosities for the two cases where on the one hand a Z is reconstructed from two electrons in the central calorimeter (Z cc), and on the other hand a Z is reconstructed from one central electron and one plug electron (Z cp). The corresponding CLC luminosity estimates (in pb^{-1}) are indicated as well. All given errors are of statistical nature. The statistical uncertainty of the CLC measurements are negligible. 74

5.5.1 An overview of the considered systematic errors for the inclusive luminosity measurement ($-2 < Y < +2$). 75

5.6.1 The data divided into several rapidity regions. The rapidity Y, the corresponding efficiencies, the correction factors for the z-vertex cut and the luminosity estimates with their statistical and systematic errors (in pb^{-1}) are indicated for central-central and central-plug Z bosons. 82

5.6.2 The rapidity-corrections with their statistical errors in the different detector and rapidity regions. 85

5.6.3 An overview of the considered systematic uncertainties for the individual rapidity regions. The blank entries correspond to non-existing event types. 85

6.2.1 Cuts and corresponding efficiency drop for the applied selection criteria. These numbers are calculated by $1 - \frac{N_{\text{cuts}}^{\text{all}}}{N_{\text{cuts}}^{\text{n}-1}}$, where $N_{\text{cuts}}^{\text{all}}$ is the number of events after all selection cuts are applied and $N_{\text{cuts}}^{\text{n}-1}$ is the number of events after all but the examined selection cut applied. . . 104

References

[ABB01] B. Abbott et al., DØ Collaboration,
Phys.Rev.Lett. 86 1707 (2001).

[ABE94] F. Abe et al.,
Phys. Rev. D50 pp.5550-5561 (1994).

[ABE98] F. Abe et al., CDF Collaboration,
Phys.Rev.Lett. 81 5754 (1998).

[ACO01] D. Acosta et al.,
Nucl. Instrum. Meth. A 461 540-544 (2001).

[ACO04] D. Acosta et al.,
arXiv:hep-ex/0406078 (2004).

[ACO06] D. Acosta et al.,
CMS AN-2006/040 (2006).

[ADA96] M. R. Adams et al., E665 Collaboration,
Phys.Rev. D 54 3006 (1996).

[ADL00] C. Adloff et al., H1 Collaboration,
Eur.Phys.J. C 13 609 (2000).

C. Adloff et al., H1 Collaboration,
Eur.Phys.J. C 19 269 (2001).

C. Adloff et al., H1 Collaboration,
Eur.Phys.J. C 21 33 (2001).

[AFF01] T. Affolder et al., CDF Collaboration,
Phys.Rev. D 64 032001 (2001).

[AFF04] T. Affolder et al.,
Nucl. Instrum. Meth. A 526 249-299 (2004).

[AGO03] S. Agostinelli et al.,
Nucl. Instrum. Meth. A 506 270-278 (2003).

[ALE03] S. I. Alekhin, Phys. Rev.,
Phys. Rev. D68 014002 (2003).

[AMI94] D. Amidei et al., CDF Collaboration,
Nucl. Instrum. Meth. A350 73 (1994).

[AMO92] N. Amos et al.,
Phys. Rev. Lett. 68 2433 (1992).

[ANA04] C. Anastasiou et al.,
Phys. Rev. D69 094008 (2004).

[ANA05] C. Anastasiou et al.,
Nucl. Phys. B724 197-246 (2005).

[ARN97] M. Arneodo et al., New Muon Collaboration,
Nucl.Phys. B 483 3 (1997).

[ART04] A. Artikov et al.,
arXiv:physics/0403079 (2004).

[AVI99] C. Avila et al.,
Phys. Lett. B445 419 (1999).

[BAL88] L. Balka et al.,
Nucl. Instrum. Meth. A 267 272-546 (1988).

[BER88] S. Bertolucci et al.,
Nucl. Instrum. Meth. A 267 301-314 (1988).

[BEN89] A. C. Benvenuti et al., BCDMS Collaboration,
Phys.Lett. B 223 485 (1989).

A. C. Benvenuti et al., BCDMS Collaboration,
Phys.Lett. B 237 599 (1990).

[BRE00] J. Breitweg et al., ZEUS Collaboration,
Eur.Phys.J. C 12 35 (2000).

C. Chekanov et al., ZEUS Collaboration,
Eur.Phys.J. C 21 443 (2001).

[BRU96] R. Brun and F. Rademakers,
Nucl. Inst. & Meth. in Phys. Re. A 389 81-86 (1996).

[CDF96] CDF Run II Collaboration,
Fermilab-Pub-96-390-E.
www-cdf.fnal.gov/international/upgrades/tdr/tdr.html (1996).

[CDF04] CDF Collaboration,
Recent results: http://www-cdf.fnal.gov/physics/ewk/2004/wzxsec/#ZeePlots.

DØ Collaboration,
Recent results: http://www-d0.fnal.gov/Run2Physics/WWW/results/prelim/EW/E06/E06.pdf.

[CIH95] S. Cihangir et al.,
Nucl. Instrum. Meth. A360 137 (1995).

[CMS94] CMS Collaboration, G. L. Bayatian et al.,
CERN/LHCC 94-38, LHCC/P1 (1994).

[CMS06] CMS Collaboration,
CERN-LHCC-2006-001 (2006).

CMS Collaboration,
CERN-LHCC-2006-021 (2006).

[CMS97] CMS Collaboration,
CERN/LHCC 97-10 (1997).

[CTE04] CTEQ PDF,
JHEP 0207 012 (2002).

[DIS03] G. Dissertori, I. Knowles and M. Schmelling,
Quantum Chromodynamics - High Energy Experiments and Theory.
Oxford Science Publications (2003).

[DIT04] M. Dittmar, A.-S. Giolo-Nicollerat,
CMS IN-2004/036 (2004).

[DIX05] L. Dixon,
private communication.

[DPZ97] M. Dittmar, F. Pauss, D. Zürcher,
Phys. Rev. D56 7284 (1997).

[DYA70] S. D. Drell and T. M. Yan,
Phys. Rev. Lett. 25, 316 (1970).

[ECA97] CMS Collaboration,
CERN/LHCC 97-33 (1997).

[EDH06] G. Dissertori et al.,
CMS AN-2006/054 (2006).

[ELL96] K. Ellis, J. Stirling and B. Webber,
QCD and Collider Physics Cambridge University Press (1996).

[EHD05] J. Ehlers and G. Dissertori,
CDF note 7397 (2005).

[EHD06] G. Dissertori et al.,
CMS NOTE-2006/124 (2006).

[EIC75] E. Eichten et al.,
Phys. Rev. lett. 34 369 (1975).

[GDH04] S. Bucherer, G. Dissertori, A. Holzner,
private communication.

[GGW73] W. Bardeen, H. Fritzsch and M. Gell-Mann,
Scale and Conformal Symmetry in Hadron Physics.
Edited by R. Gatto (Wiley, New York) (1973).

D. Gross and F. Wilczek,
Phys.Rev. D 8 3633 (1973).

S. Weinberg,
Phys.Rev.Lett. 31 494 (1973).

[GRO01] C. Grozis et al.,
Int. J. Mod. Phys. A16S1C:1119-1121 (2001).

[GSW61] S. Glashow,
Nucl.Phys 22 579 (1961).

S. Weinberg,
Phys.Rev.Lett. 19 1264 (1967).

A. Salam,
Elementary Particle Theory.
Edited by N. Svartholm (Almquist and Wiksells, Stockholm) (1969).

[HCA97] CMS Collaboration,
CERN/LHCC 97-31 (1997).

[HAL84] F. Halzen and A. D. Martin et al.,
Quarks & Leptons: An Introductory Course in Modern Particle Physics.
John Wiley & Sons, Inc. (1984).

[HEI06] A. Heister et al.,
CMS NOTE-2006/036 (2006).

[HER05] M. Dittmar et al.,
arXiv:hep-ph/0511119 (2005).

S. Catani et al.,
arXiv:hep-ph/0005114 (1999).

S. Catani et al.,
arXiv:hep-ph/0005025 (2000).

[HHG00] M. J. F. Gunion et al.,
The Higgs Hunter's Guide.
Perseus Publishing, Cambridge, Massachusetts (2000).

[HIG64] P. W. Higgs,
Phys.Rev.Lett. 12 132 (1964).

P. W. Higgs,
Phys.Rev.Lett. 13 508 (1964).

F. Englert and R. Brout,
Phys.Rev.Lett. 13 321 (1964).

G. S. Guralnik, C. R. Hagen and T. W. B. Kibble,
Phys.Rev.Lett. 13 585 (1964).

T. W. B. Kibble,
Phys.Rev. 155 1554 (1967).

[HOL02] A. G. Holzner,
PhD thesis, Dissertation ETH No. 14842 (2002).

[KAP06] S. G. Kappler,
IEEE Trans. Nucl. Sci., vol. 53 no. 2 (2006).

[LHC94] LHC Machine Group,
CERN-2004-003-V-1 (2004).

LHC Machine Group,
CERN-2004-003-V-2 (2004).

LHC Machine Group,
CERN-2004-003-V-3 (2004).

[LYS04] A. v. Lysebettena and P. Verrecchia,
CMS RN-2004/001 (2004).

[MAR04] M. Martinez,
Good Run List version 5.
http://www-cdf.fnal.gov/internal/dqm/goodrun/good.html.

[MDA03] M. Dittmar, A.-S. Nicollerat,
CDF note 6411 (2003).

[MOR91] G. Moreno et al.,
Phys.Rev. D 43 2815 (1991).

[MRS04] MRST PDF,
Phys. Rev. Lett. B531 216 (2002).

[MUO97] CMS Collaboration,
CERN/LHCC 97-32 (1997).

[MUR04] P. Murat,
Stntuple analysis framework.
http://fcdfwww.fnal.gov/~cdfopr/Stntuple/index/index.html.

[NEE91] R. Hamberg, W. L. van Neerven and T.Matsuura,
Nucl. Phys. B 359:343-405 (1991).

[NIC04] A.-S. Giolo-Nicollerat,
PhD thesis, Dissertation ETH No. 15788 (2004).

[PDG05] S. Eidelman et al.,
Phys. Lett. B 529, 1 (2005).

[PDG06] W.-M. Yao et al.,
J. Phys. G 33, 1 (2006).

[PER87] D. H. Perkins,
Introduction to High Energy Physics, Third Edition.
Addison-Wesley Publishing Company, Inc. (1987).

[ROS04] R. Rossin et al.,
Joint Physics Meeting 11/24/04 (2004).

[SAC02] CMS Saclay Group,
CMS IN-2002/012 (2002).

[SEE06] C. Seez,
private communication.

[SJO03] T. Sjostrand,
http://www.thep.lu.se/~torbjorn/Pythia.html.

[SKK04] Y. Ashie et al., Super-Kamiokande Collaboration,
Phys.Rev.Lett 93 101801 (2004).

[STI02] W. J. Stirling et al.,
Phys. Lett. B531, 216 (2002).

[STI04] J. Stirling,
QCD Theory - a status report and review of some developments in the past year.
QCD-ICHEP04 (2004).

[TOW01] R. S. Towell et al., FNAL E866, NuSea Collaboration,
Phys.Rev. D 64 052002 (2001).

[TRA98] CMS Collaboration,
CERN/LHCC 98-6 (1998).

[TRI00] CMS Collaboration,
CERN/LHCC 2000 - 38 (2000).

CMS Collaboration,
CERN/LHCC 2002 - 26 (2002).

[WHI92] L. W. Whitlow et al.,
Phys.Lett. B 282 (1992).

[ZAB05] R. Bruneliere, P. Jarry and A. Zabi,
CMS NOTE-2005/001 (2005).

Acknowledgement

I am indebted to *Prof. Dr. Günther Dissertori* who made it possible to engage in the endeavor and pleasure of making a dissertation. His care and support throughout the thesis and in between the continents was surpassing.

I am especially grateful to *Prof. Dr. Felicitas Pauss* for her enthusiastic commitment to the ETHZ group and to the CMS experiment. Her confidence and faith in all our group members has been always very motivating.

Sincere thanks to *Anne-Sylvie Giolo-Nicollerat* who introduced me to the particular analysis strategies at CDF and CMS. It was always a pleasure to experience her cooperativeness and helpfulness.

Many thanks also to *André Georg Holzner*. He was always around to tackle my CMS software problems. Besides the benefits of our physics discussions, I appreciated him as an enjoyable officemate.

Special thanks goes to *Michael Dittmar* for his experience and support during this sometimes intricate analysis procedure.

I also want to thank *Allan Clark* and the whole *University of Geneva CDF group* for allowing me to stay one year at CDF. Thus, I could enjoy analyzing real data.

My gratitude to *Giovanna Davatz* who frequently supported the social program of this thesis. Thanks to *Alison Lister* with whom I survived and enjoyed the Midwest and also thanks to *Fabian Stöckli* for many coffee meetings including and excluding physics discussions. I would like to thank *Gabriele Kogler*. She was always very helpful and allowed for a hassle-free administrative life. Definitely lots of thanks to *Peter Cwetanski* who oftentimes took care of my recreational activities.

At last, I owe this thesis to my family. They rendered every assistance when needed.